THE UNIVERSITY OF CHICAGO

POLYMER SEMICONDUCTORS FOR BIOELECTRONIC-TISSUE INTERFACES

A DISSERTATION SUBMITTED TO
THE FACULTY OF THE DIVISION OF THE PHYSICAL SCIENCES
IN CANDIDACY FOR THE DEGREE OF
DOCTOR OF PHILOSOPHY

DEPARTMENT OF CHEMISTRY

BY
NAN LI

CHICAGO, ILLINOIS
MARCH 2024

TABLE OF CONTENTS

LIST OF FIGURES

LIST OF TABLES

LIST OF ABBREVIATIONS

AFM	Atomic-force microscopy
BAP	Bioadhesive polymer
BASC	Bioadhesive semiconducting polymer
BDT	Benzodithiophene
BP	Benzophenone
BTz	Benzothiadiazole
CCR7	C-C chemokine receptor type 7
$CDCl_3$	Deuterated chloroform
CDT	Cyclopentadithiophene
CD68	Cluster of differentiation 68
CLIP	Click-to-polymer
CuAAC	Copper-catalyzed azide-alkyne cycloaddition
DAPI	4',6-Diamidino-2-phenylindole
$DCFH_2$-DA	2',7'-Dichlorodihydrofluorescein diacetate
DCM	Dichloromethane
DMF	*N,N*-Dimethylformamide
DMSO	Dimethyl sulfoxide
DPP	Diketopyrrolopyrrole

EA	Ethyl acetate
ECG	Electrocardiogram
ECoG	Electrocorticography
EIS	Electrochemical impedance spectroscopy
EMG	Electromyogram
FBR	Foreign-body response
FBS	Fetal bovine serum
FTIR	Fourier-transform infrared spectroscopy
GIXD	Grazing incidence X-ray diffraction
GM-CSF	Granulocyte-macrophage colony-stimulating factor
GO	Glucose oxidase
HOMO	Highest occupied molecular orbital
IFN	Interferon
IID	Isoindigo
IL	Interleukin
iNOS	Nitric oxide synthase
IPA	Isopropyl alcohol
LED	Light emitting diode

LPS	Lipopolysaccharide
LUMO	Lowest unoccupied molecular orbital
MCP-1	Monocyte chemoattractant protein-1
MD	Molecular dynamics
MeOH	Methanol
MFI	Mean fluorescence intensity
Mn	Number average molecular weight
MTT	3-(4,5-Dimethylthiazol-2-yl)-2,5 diphenyl tetrazolium bromide
Mw	Weight average molecular weight
NDI	Naphthalene diimide
NHS	*N*-hydroxysuccinimide
NMR	Nuclear magnetic resonance
OECT	Organic electrochemical transistors
OEG	Oligo(ethylene glycol)
OFET	Organic field-effect transistors
OPV	Organic photovoltaics
OTS	*n*-Octadecyltrimethoxysilane
Pa	Pascal

PBS	Phosphate-buffered saline
PDMS	Polydimethylsiloxane
PEDOT	Poly(3,4-ethylenedioxythiophene)
PEG	Poly(ethylene glycol)
p-ERK	Phospho-extracellular signal-regulated kinases
PET	Polyethylene terephthalate
p-JNK	Phospho-c-Jun N-terminal Kinase
PMDETA	*N,N,N,N,N*-pentamethyldiethylenetriamine
p-p38	Phospho-p38
PSS	Polystyrene sulfonate
PY	Tetrahydropyran
RBF	Round bottom flask
rDoC	Relative degree of crystallinity
ROS	Reactive oxygen species
r.t.	Room temperature
SAM	Self-assembled monolayer
s.d.	Standard deviation
Se	Selenophene

SEBS	Polystyrene-*block*-poly(ethylene-*ran*-butylene)-*block*-polystyrene
SEM	Scanning electron microscopy
s.e.m.	Standard error of the mean
T	Thiophene
TCE	Trichloroethylene
TFTs	Thin film transistors
THP	Tetrahydro-2-(2-propynyloxy)-2H-pyran
TMO	4-Propargylthiomorpholine 1,1-dioxide
TPU	Thermoplastic polyurethane
TT	Thieno[3,2-b]thiophene
XPS	X-ray photoelectron spectroscopy
1D	One-dimensional
2D	Two-dimensional
α-SMA	α-smooth muscle actin

ABSTRACT

Nan Li: Polymer Semiconductors for Bioelectronic-Tissue Interfaces

Under Direction of Professor Sihong Wang

Bioelectronics are bio-interfacing devices that can be used for interrogating fundamental biological mechanisms and performing electronic diagnosis and therapy. A variety of conventional bioelectronics (to name a few, pacemakers, neurostimulators, cochlear implants, insulin pumps) have been developed to impact and heal millions of people each year. Compared to inorganic metals or silicon, conjugated polymers, which offer broad optoelectronic (light absorption/emission, conducting, semiconducting, etc) properties, have shown tremendous advantages, due to low mechanical modulus, solution processability, and chemical versatility. As a result, conjugated polymers have shown the promise for developing new generations of soft bioelectronics, allowing direct interfacing with biological tissues. To further enable biocompatible bioelectronic-tissue interfaces, the developments of implantable bioelectronics need to encompass a variety of functional properties, intimate contact with dynamic tissues, and suppressed foreign-body response. However, these properties pose significant challenges and remain largely missing for conjugated polymers for bioelectronics.

For my Ph.D. dissertation, I focused on designing functional semiconducting polymers which can greatly expand their chemical and physical properties towards improving the biocompatibility of semiconducting polymer-tissue interface. Based on these designs, I fabricated active transistor devices with biocompatible characteristics for interfacing with biological tissues.

First, to resolve the limitation of conventional methods for functionalizing high-performance semiconducting polymers, I developed the “click-to-polymer” (CLIP) approach as a universal platform to facilely perform both bulk and surface functionalization on the side chain of conjugated polymers. A variety of functional units can be incorporated from this approach with little sacrifice to the electrical performance. Moreover, functional applications including photopatterning and biochemical sensing were demonstrated.

Second, to achieve intimate and robust interfacing with wet biological tissues, I developed bioadhesive polymer semiconductors by creating an interpenetrated double network between newly designed bioadhesive polymers and a redox-active semiconducting polymer. The bioadhesive polymer semiconductor showed significantly improved adhesion on bio-tissues while maintaining a comparable electrical performance to the neat semiconducting polymer. Furthermore, the bioadhesive polymer semiconductor exhibited abrasion resistance, high stretchability, and good biocompatibility, which are highly desirable for stable biointerfaces. I further developed a bioadhesive and stretchable electrochemical transistor for stably capturing electrophysiological signals with adhesive attachment on tissues.

Third, to improve the immune compatibility of semiconducting polymers, I designed new polymer structures with both backbone and side chain engineering. The selenophene incorporation in the backbone suppressed the foreign-body response as evidenced by a decrease of collagen density and immune cell populations, and a downregulation of the pro-inflammatory cytokines. The side chain grafting of immunomodulatory groups via the in-film functionalization approach showed a further suppression of the foreign-body response. Meanwhile, the immune-compatible semiconducting polymers only exhibited a minor decrease in the transistor performance relative to the neat one.

Future perspectives on designing polymer semiconductors for bioelectronic-tissue interfaces are given at last.

ACKNOWLEDGEMENT

First and foremost, I want to express my sincere thanks to my advisor Professor Sihong Wang. Over the past five years, he has given tremendous support and numerous suggestions for my research, without which I cannot achieve any work I have finished. He has shown me how to do good research and how to train myself into a competent researcher in the future. Besides academic study, he also has given me a lot of suggestions and encourage me to trust myself for my future development including awards, postdoctoral positions, independent careers, etc. I want to thank him again for leading me into the field of organic bioelectronics, getting to appreciate the interdisciplinary research, and having the courage to dream bigger and finally make a dream come true. He has set an exemplary model for me to learn from and emulate in my future endeavors.

I want to thank a few other professors who gave me a lot of help during my Ph.D. study. Prof. Stuart Rowan is my pro forma advisor for my Ph.D. study in the Chemistry department. During our annual academic discussions, he gave me a lot of suggestions for my research projects and let me know how to do chemistry-related research in a professional way. I also want to thank Prof. Dmitri Talapin for serving as the committee member for my Ph.D. dissertation defense and giving invaluable support for my projects. I also want to thank Prof. Wenbin Lin, Prof. Luping Yu, and Prof. Dmitri Talapin for serving on my candidacy committee and giving me suggestions. I want to thank Prof. Bozhi Tian, who gave me a lot of help when I started to choose research groups and when I worked on my projects. His generous suggestions and support have inspired me a lot when doing research. I want to thank Prof. Jeffery A. Hubbell, who gave me a lot of generous support and help when working on the material biocompatibility. I also want to thank Prof. Guangbin Dong, who gave me a lot of support at the beginning stage when I entered the University of Chicago and allowed me to do research rotation in his lab. I want to thank Dr. Joeseph Strzalka and Dr. Jie Xu

at Argonne National Laboratory. With their expertise and help on the materials characterization, I was able to complete my research projects in a timely manner.

I want to thank my peer group members and friends in Wang lab. Yahao Dai and Yang Li joined the group around a similar time with me. As the first class of graduate students in Wang lab, they gave me a lot of support and help from the very beginning even before working on a research project. They shared a lot of great understandings with me and gave very important suggestions during the past five years. Besides academic work, they also helped me a lot in my life especially when I came into certain problems. The postdocs in our lab including Dr. Huawei Hu, Dr. Wei Liu, and Dr. Songsong Li gave me a lot of help as well. Thank you for sharing your research and work experience with me, which helped me to form a more complete picture of how they solved the problems they faced and how a principal investigator grew. I want to thank my important collaborators Dr. Seounghun Kang and Dr. Michael J. V. White. They spent a lot of work and gave important suggestions when working together on the biocompatibility project. Their responsive help to my questions and requests made the project to be completed. I need to thank Dr. Joshua Mysona for conducting simulation for my project. I want to thank Yunfei Wang and P. Blake J. St. Onge for helping to collect important data. I also would like to thank Shinya Wai, Cheng Zhang, Naisong Shan, Sean Sutyak, and all the other Wang group members. They really helped me a lot with their expertise and enthusiasm. I want to thank graduate students Qi Su, Shilei Dai, and Ping Cheng who spent two years in the Wang lab. I think you really showed me a good model of how to do research with full efforts and enthusiasm as well as how to make a life-work balance. I also want to thank the undergraduate students I have worked with, including Nickolas De Oliveira, Jiale Xiang, Aidan Ziaja, and Zhichang Liu. Thank you for spending time working with me on some projects and your help definitely matter for finishing certain parts of a research project. I would also like to thank others who have given me help and suggestions, including Dr. Ani Solanki, Dr. Phil Griffin, Dr. Alexadra Filatov, Dr. Yin Fang, Dr. Renhe Li, Dr. Jianchun Wang, Dr. Hongzhang Wang, Dr. Chuangyu Wen, Dr. Mingzhan Wang, Jiuyun Shi, Xiaomin Jiang, Taokun Luo, and a few others.

Last but not least, I want to deeply thank my parents. I am the first generation in my family to achieve a Bachelor of Science and a Ph.D. Although my parents cannot understand the research I worked on, they gave their full support to me. They do not want to give me any burden or pressure and always encourage me to relax more and not be overwhelmed by any failures. With their support, I can focus my efforts on my research projects with no worry on the family. I understand their hard work for the family and the family is always my comfort harbor. I appreciate a lot for what they have done for me. Gradually, I feel that I need to take more responsibilities. So please give me a little more time. I can be your back in a few years.

Attaining a Ph.D. degree is a challenging yet immensely worthwhile endeavor. There were always some hard times when working on the research projects. Therefore, to learn how to deal with failures and frustrations from others and the past is also a crucial aspect of the Ph.D. journey.

Great thanks to all the kind people I had interactions with.

Chapter 1. Conjugated polymers for soft bioelectronics

1.1 Electronic polymers for soft bioelectronics

Biological systems are composed of sophisticated cells and interactions. Ever since the discovery of the electrical stimulation of Galvani's frog leg experiment, increasing amount of research work have been focusing on utilizing electrical stimulation and recording as a type of therapy to treat human diseases[1-3]. Not only do these studies pave the way for understanding fundamental biological behaviors but also revolutionize the human healthcare. Generally, bioelectronics are classified as devices that target at bio-systems to perform recording, stimulation, and actuation functions. A variety of bioelectronic devices including pacemakers, cochlear implants, insulin pumps have been developed and deployed to prolong the lifetime and improve the living quality for millions of patients. For interfacing with neural cells, deep brain stimulators and silicon-based microelectrode arrays such as Utah array and Michigan array have been developed over 3 decades ago, with the potential of treating neurodegenerative, psychiatric, and neuromuscular conditions[4].

However, owing to the soft and dynamic nature of biological tissues, one critical issue that needs to be addressed is the incompatibility of electronic device-tissue interface[5]. Bio-tissues typically have moduli in the range of hundreds of Pa to hundreds of kPa, while conventional electrode technologies employ rigid metals or silicon as the interface materials, which display moduli above 10 GPa. The huge mechanical mismatch results in multi-aspect disadvantages: non-conformable device-tissue interface, inflammatory responses, and impaired device functionality. To mitigate the modulus mismatch, polymer-based materials, which are soft and flexible, have been applied to serve as non-electrical components like the substrate, encapsulation, coating, and dielectrics. Despite the partial resolution of interface issue by the use of non-electrical polymer materials, the active sensing element, namely the conductors and semiconductors, which in a lot of applications need to be exposed on the tissue surface, the problem remains unsolved.

On the other hand, most bioelectrical communications happen in the form of ions, with ion concentration difference building up the electrical potential. Conventional metals typically present compact and well-preserved crystalline structure, so the electrical sensing/stimulation happens at the metal-tissue interface, exhibiting high interfacial impedance. For polymer-based conductors, the amorphous and hydrophilic nature could allow the ion penetration into the bulk, thus effectively lowering the interfacial impedance[6].

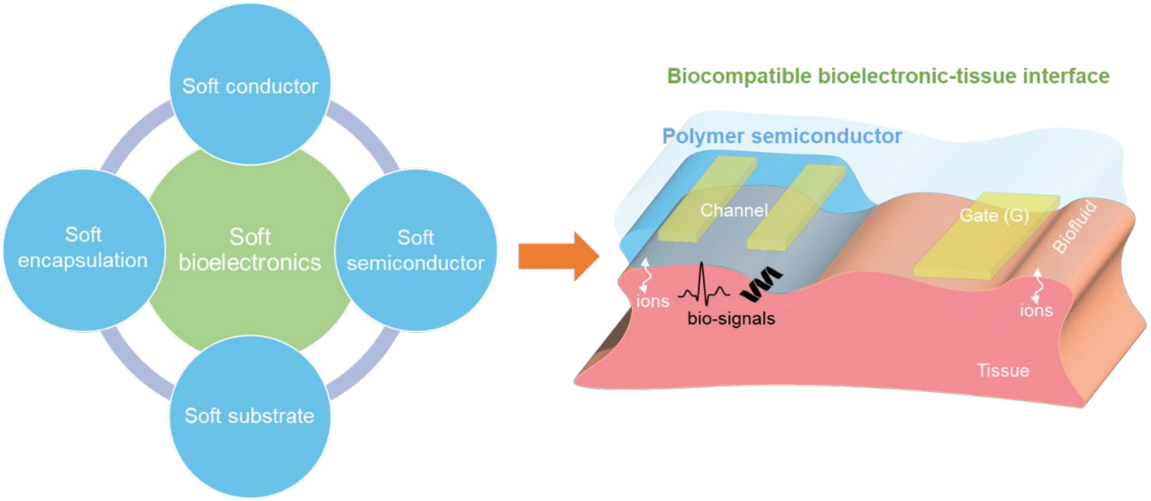

Figure 1-1. Schematics illustrating the development of soft bioelectronics towards biocompatible bioelectronic-tissue interface. The soft components include soft encapsulation, soft substrate, soft conductor, and soft semiconductor.

To develop electrically conducting polymers, Heeger, McDiarmid, and Shirakawa contributed to the discovery and development of chemically doped polyacetylene, which shows metallic conductivity. Since then, conjugated polymers, which are characterized by conjugated backbones of alternating single- and double-bonds with delocalized electrons, are receiving numerous studies because compared to the inorganic counterparts (for example, metals), the semicrystalline to amorphous polymer structure gives rise to softer mechanical modulus and flexibility and have better solution processability.

For instance, the conducting polymer poly(3,4-ethylenedioxythiophene):polystyrene sulfonate (PEDOT:PSS) have been commercialized as aqueous dispersion for more than 2 decades for the use as electrode coating materials or soft conductors[7]. And semiconducting polymers have been developed to exhibit charge carrier mobilities surpassing those of amorphous silicon[8]. They typically show moduli in the range of tens to hundreds of MPa. As a result, conjugated polymers have the potential to replace conventional rigid electrical materials to develop fully soft bioelectronics (**Figure 1-1**).

1.1.1 Chemical designs for conjugated polymers

Conjugated polymers (**Figure 1-2**) are characterized by π-conjugation in the polymer backbone, which allow charge carrier delocalization along the polymer chain[9]. This gives rise to unique semiconducting property as measured by the highest occupied molecular orbital (HOMO), lowest unoccupied molecular orbital (LUMO), and bandgap. Classical types of conjugated polymers are made of hydrocarbons, for examples, polyacetylene, poly(*p*-phenylene), poly(*p*-phenylene vinylene), poly(*p*-phenylene ethynylene), and polyfluorene. Incorporating heteroatoms into the aromatic rings, such as polyaniline, polythiophene, polypyrrole, polycarbazole, can be used to tune the charge transport and light absorption/emission property. More recently, donor-acceptor (D-A) type conjugated polymers have demonstrated a push-pull effect between individual units, promoting a planarized backbone structure and subsequently lowering the bandgap[8]. This, as a result, enhances their charge transport properties. Commonly employed electron acceptors include diketopyrrolopyrrole (DPP), benzothiadiazole (BTz), naphthalene diimide (NDI), and isoindigo

(IID); and commonly employed electron donors include thiophene (T), thieno[3,2-b]thiophene (TT), benzodithiophene (BDT), and cyclopentadithiophene (CDT).

Besides the backbones, side chains on the conjugated core were initially introduced to improve the polymer solubility, enabling the solution processability of conjugated polymers. Therefore, linear alkyl chains or branched alkyl chains were mostly grafted. Later, researchers found that the side chains structures actually influence polymeric packing, and thus the optoelectronic property[10]. To study the side chain influences, varying the alkyl chain length, the position of branching point, and side chains structures have been demonstrated for conjugated polymers, with the latter including oligo(ethylene glycol), siloxane-terminated, fluorinated alkyl chains, hydrogen-bonding group side chains[11]. The side chain designs serve to not only improve the interchain packing and charge carrier transport, but also introduce new functionalities[12].

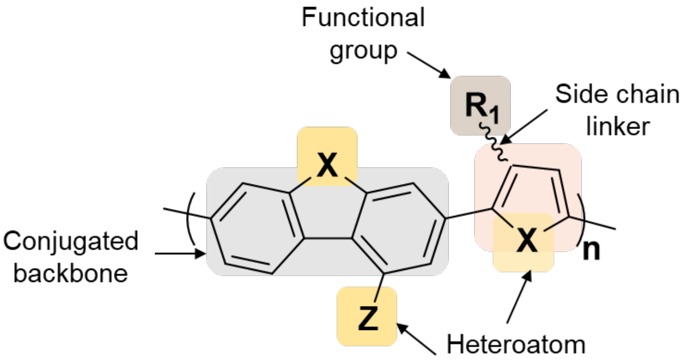

Figure 1-2. General structure of a conjugated polymer.

Replacing alkyl chains with polar chains like glycolated side chains can switch the operation mechanism for electrolyte-gated organic transistors. Rivnay and coworkers compared the polymers with the same polythiophene backbone but one with alkylated side chains (C14, p(a2T-TT)) and one with glycolated side chains (EG3, p(g2T-TT))[13]. They found out that the glycolated side chains can facilitate ion penetration in the bulk film of p(g2T-TT), exhibiting high volumetric capacitance, while p(a2T-TT) only shows interfacial ion doping on the film surface.

The conjugated polymers that are mainly investigated in my dissertation are DPPTT with donor-acceptor backbone of diketopyrrolopyrrole (DPP)-thieno[3,2-b]thiophene (TT) and alkyl side chains, and poly(3,3'-bis(2-(2-(2-methoxyethoxy)ethoxy)ethoxy)-2,2':5',2''-terthiophene) (p(g2T-T)) with polythiophene backbone and oligo(ethylene glycol) side chains (**Figure 1-3**)[14].

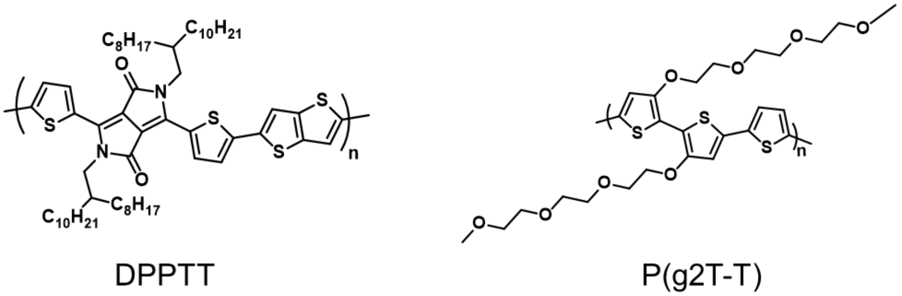

Figure 1-3. Chemical structures of DPPTT and p(g2T-T)

1.1.2 Semiconducting polymers and organic electrochemical transistors

Conjugated polymers, owing to the chemical versatility and therefore broad optoelectronic properties, have found widespread applications, including organic photovoltaics (OPVs)[15], light-emitting diodes (LEDs)[16], thin-film transistors (TFTs)[17], electrochromic[18] and thermoelectric[19] devices, bioimaging[20], and biotherapeutics[21]. For my Ph.D. dissertation, I mainly focused on the study of thin-film transistor applications. Transistors are three-terminal devices and depending on the operation mode, are classified as organic field-effect transistors (OFETs) and organic electrochemical transistors (OECTs).

Semiconducting polymers used in high-performance OFETs typically have alkyl side chains owing to more desired polymeric packing structures. OFETs comprise a gate electrode, a source/drain electrode, a thin semiconductor channel between source and drain electrodes, and an insulating gate dielectric layer[8] (**Figure 1-4**). When a gate voltage (V_g) is applied, charge carriers with opposite charges are induced at the semiconducting polymer-dielectric interface. The charge carriers will flow upon the application of the drain-source voltage (V_d), generating a drain current (I_d). The carrier density is modulated by the V_g and so as the I_d. The figure-of-merit parameters for OFETs are charge carrier mobility (μ), on/off ratio, and threshold voltage (V_t).

OFETs can operate in linear mode or saturation mode depending on V_d and V_g. In the linear regime, $|V_g-V_t| > |V_d|$; while in the saturation regime, $|V_g-V_t| < |V_d|$. Depending on the initial doping state of the semiconductor at $V_g = 0$ V, the transistor can operate either in the accumulation mode or depletion mode. At zero gate voltage, depletion-mode transistors show ON state with a high drain current. After applying the gate voltage, the semiconductor is de-doped and the transistor returns to OFF state. In contrast, accumulation-mode transistors show OFF state at zero gate voltage but are turned ON when a gate voltage is applied.

In an electrolyte-gated FET, the semiconductor and gate are in contact with an electrolyte and the electrolyte serves as the gate dielectric[22]. Ions in the electrolyte can accumulate at the polymer-electrolyte interface to compensate the induced electronic charge carriers in the semiconductor.

As discussed, when polar side chain structures (for instance, ionic groups, oligo(ethylene glycol)) were employed in the semiconducting polymer design, the ions can penetrate into the bulk film to achieve bulk electrochemical doping in the presence of an electrolyte. This class of materials is referred to as redox-active semiconducting polymers and the corresponding transistors are denoted as organic electrochemical transistors (OECTs) (**Figure 1-4**)[23,24]. The Bernards model assumes that after applying the gate voltage, the ions from the electrolyte are injected into the semiconductors to dope the material throughout the volume and hence change the conductivity, capturing the steady-state and transient transport behaviors[25]. Based on the model, the device can be divided into an electronic circuit, which describes the charge flow through source-channel-drain, and an ionic circuit, which describes the ion flow through gate-electrolyte-channel.

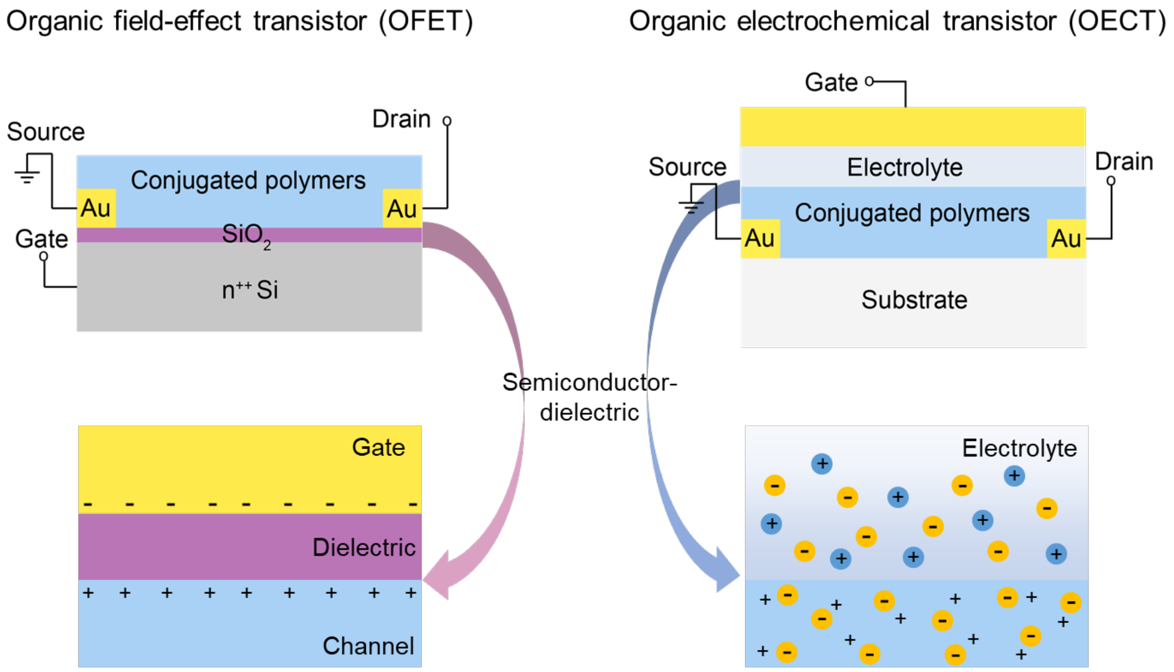

Figure 1-4. Schematics of OFET and OECT and their working mechanisms. Field-effect doping of the conjugated polymer induces charge carrier near the dielectric interface. Electrochemical doping happens throughout the bulk conjugated polymer film.

OECTs provides the capability to transduce a small gate voltage input into a large drain current output. The transconductance (g_m) describes the efficiency of the transduction and is calculated based on equation 1.

$$g_m = \frac{\partial I_d}{\partial V_g} \qquad (1)$$

For OECTs, g_m can also be given by equation 2 shown below,

$$g_m = \begin{cases} -\mu C^* \frac{Wd}{L} V_d, & |V_g - V_t| > |V_d| \\ \mu C^* \frac{Wd}{L} (V_t - V_g), & |V_g - V_t| < |V_d| \end{cases} \quad (2)$$

where *d* is the semiconducting film thickness, and *C** is the capacitance per unit volume of the channel.

Due to the dC^* term, the transconductance of OECTs is several orders of magnitude higher than that of OFETs (for 130 nm-thick PEDOT:PSS channel, the product of dC^*, which is the equivalent capacitance per unit area, is 500 μF/cm^2)[26], which provides OECTs with higher amplification performance compared to other transistor technologies.

1.1.3 Uses of semiconducting polymers and OECTs for tissue interfaces

Semiconducting polymers and transistors especially OECT devices have found multiple applications for tissue interfaces[23]. Due to the mixed electron-ion conduction mechanism and low operation voltage (<1 V), OECTs show promise for directly interfacing with bio-tissues for electrophysiological signal monitoring and biochemical sensing.

For monitoring electrophysiological signals, the OECT is in contact with the electrically active tissues, and the potential difference between the gate and channel will drive the ion injection into the channel and modulate the conductivity (**Figure 1-5A**). For example, Malliaras and coworkers attached the OECT probe composed of PEDOT:PSS to the cortex of a rat brain, and monitored the electrocorticography (ECoG) signals[27]. Due to the built-in amplification, the signal-to-noise ratio of the recording is higher than that from the PEDOT:PSS electrode. This example highlights the amplification capability of OECTs compared to passive electrodes.

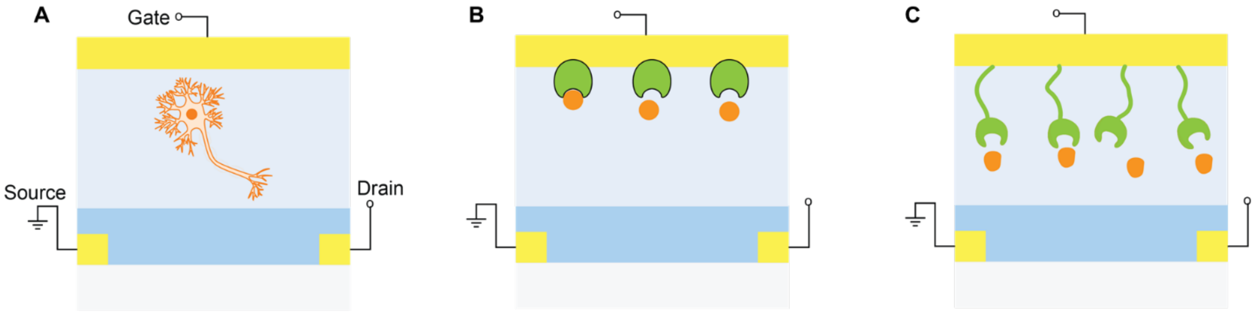

Figure 1-5. Transistors for tissue-interfaced applications. (A) Electrophysiological sensing. (B-C) Biochemical sensing based on immobilization of enzyme-type bioreceptors (B), and affinity based bioreceptors (C).

OECT also find applications in chemical sensing[28,29]. The gate or channel of an OECT device can be functionalized with various bioreceptors to improve the selectivity. For enzyme-type bioreceptors (**Figure 1-5B**), the catalysis of the recognized analytes can either directly transfer charges to the gate (or the semiconducting channel) or generate other mediators that can be redox active so as to modulate the drain current I_d. For non-enzyme type bioreceptors, such as affinity based bioreceptors (antibody, antigen, aptamer) (**Figure 1-5C**), the binding of analyte to the binding site can change the ion distribution so as to change the interfacial impedance between the gate and the electrolyte. For example, Inal and coworkers reported that the nanobody-functionalized gate on an OECT can realize the sensing of antigens even in the range of single molecule[30].

1.1.4 Desired properties of semiconducting polymers for biointerfaces

Biotissues are more complex than being mechanically soft. They exhibit wet and curvilinear surfaces, demonstrate dynamic movements and strains, contribute to sophisticated electrical and chemical communications in the body, and are protected from foreign objects by the immune system[2]. For interfacing semiconducting polymers with biotissues, a variety of functional properties are needed. For example, stretchable, biodegradable, self-healing, bioadhesive, and biocompatible semiconducting polymers for bioelectronics are highly desired for conformable tissue interface for performing stimulation and recording functions in a safe and reliable manner.

Stretchable semiconducting polymers can accommodate the strains in the tissues while maintaining unperturbed electrical property. There have been a number of research works studying stretchable designs[31]. The key molecular design concept is to incorporate strain energy-dissipation mechanisms and maintain efficient charge-transport pathways. Molecular engineering in the semiconducting polymer chains and multicomponent systems have been demonstrated to successfully impart the stretchability to semiconducting polymers.

Biodegradable semiconducting polymers can be degraded after a certain period, eliminating the device removal process. For the degradation of semiconducting polymer chains, incorporating degradable moieties in the backbone is one main strategy. To achieve this, imine bond[32,33], which is degradable by acids, has been most commonly demonstrated.

Self-healing semiconducting polymers can restore the electrical property when subjected to physical damage (i.e., crack formation). Including non-covalent interactions (hydrogen-bonding)[34] in the polymer designs and multicomponent systems[35] have been demonstrated. For most of these examples, external stimuli including heat and vapor treatment are needed to accelerate the self-healing process.

Bioadhesive semiconducting polymers can form stable and intimate adhesion on wet biotissues. The bioadhesion property allows facile attachment of bioelectronic devices on tissue surfaces and facilitates robust recording of physiological signals[36]. However, this is no report or design on developing bioadhesive semiconducting polymers.

Biocompatible semiconducting polymers can mitigate the foreign-body response, which leads to the formation of fibrous capsule formation for implantable bioelectronics. This can be detrimental to the device's function. So far, most of the research works on the biocompatibility of semiconducting polymers focus on in vitro cell viability and adhesion[32,37], which do not necessarily translate to the in vivo suppression of foreign-body response.

1.2 The scope of the dissertation

Although conjugated polymers present promise for soft bioelectronics application, significant challenges persist, particularly concerning effective tissue interfacing. The remainder of the thesis focuses on developing polymer semiconductors for biocompatible bioelectronic-tissue interfaces.

Chapter 2 introduces a universal and facile approach for functionalizing the side chains of conjugated polymers for human-integrated electronics. Specifically, we show that the post-polymerization functionalization using a copper-catalyzed alkyne-azide reaction can be compatible with a variety of functional groups, including immune-modulatory, ion-conducting, photo-responsive, and bio-conjugatory groups.

Chapter 3 presents the development of bioadhesive polymer semiconductors for achieving intimate and robust interfaces with wet bio-tissues for monitoring electrophysiological signals. The bioadhesive polymer semiconductors are created by the formation of a double network between the bioadhesive polymer and a redox-active semiconducting polymer, providing robust tissue adhesion and high charge carrier mobility.

Chapter 4 investigates the immune-compatible designs for semiconducting polymers for bioelectronics. We show that both the backbone selenophene substitution and side chain functionalization with immunomodulatory groups of a semiconducting polymer can suppress the foreign-body response for in vivo implantation. In addition, the immune-compatible semiconducting polymers offer high transistor performance.

Chapter 5 concludes the dissertation and provides future perspective on designing polymer semiconductors for bioelectronic-tissue interfaces.

The works described in the dissertation emphasize the importance of understanding the semiconducting polymer-tissue interface and present the development of effective chemical designs for facilitating biocompatible bioelectronic-tissue interfaces for in vivo applications.

1.3 References

(1) Hong, G.; Lieber, C. M. Novel electrode technologies for neural recordings. *Nat Rev Neurosci* **2019,** *20*, 330.

(2) Feiner, R.; Dvir, T. Tissue–electronics interfaces: from implantable devices to engineered tissues. *Nature Reviews Materials* **2017,** *3*.

(3) Chen, R.; Canales, A.; Anikeeva, P. Neural Recording and Modulation Technologies. *Nat Rev Mater* **2017,** *2*.

(4) Obidin, N.; Tasnim, F.; Dagdeviren, C. The Future of Neuroimplantable Devices: A Materials Science and Regulatory Perspective. *Adv Mater* **2020,** *32*, e1901482.

(5) Liu, S.; Rao, Y.; Jang, H.; Tan, P.; Lu, N. Strategies for body-conformable electronics. *Matter* **2022,** *5*, 1104.

(6) Rivnay, J.; Owens, R. M.; Malliaras, G. G. The Rise of Organic Bioelectronics. *Chemistry of Materials* **2013,** *26*, 679.

(7) Shi, H.; Liu, C.; Jiang, Q.; Xu, J. Effective Approaches to Improve the Electrical Conductivity of PEDOT:PSS: A Review. *Advanced Electronic Materials* **2015,** *1*.

(8) Yang, J.; Zhao, Z.; Wang, S.; Guo, Y.; Liu, Y. Insight into High-Performance Conjugated Polymers for Organic Field-Effect Transistors. *Chem* **2018,** *4*, 2748.

(9) Qiu, Z.; Hammer, B. A. G.; Müllen, K. Conjugated polymers – Problems and promises. *Progress in Polymer Science* **2020,** *100*.

(10) Mei, J.; Diao, Y.; Appleton, A. L.; Fang, L.; Bao, Z. Integrated materials design of organic semiconductors for field-effect transistors. *J Am Chem Soc* **2013,** *135*, 6724.

(11) Yang, Y.; Liu, Z.; Zhang, G.; Zhang, X.; Zhang, D. The Effects of Side Chains on the Charge Mobilities and Functionalities of Semiconducting Conjugated Polymers beyond Solubilities. *Advanced Materials* **2019,** *31*, 1903104.

(12) Liu, Z.; Zhang, G.; Zhang, D. Modification of Side Chains of Conjugated Molecules and Polymers for Charge Mobility Enhancement and Sensing Functionality. *Acc Chem Res* **2018,** *51*, 1422.

(13) Giovannitti, A.; Sbircea, D. T.; Inal, S.; Nielsen, C. B.; Bandiello, E.; Hanifi, D. A.; Sessolo, M.; Malliaras, G. G.; McCulloch, I.; Rivnay, J. Controlling the mode of operation

of organic transistors through side-chain engineering. *Proc Natl Acad Sci U S A* **2016,** *113*, 12017.

(14) Nielsen, C. B.; Giovannitti, A.; Sbircea, D. T.; Bandiello, E.; Niazi, M. R.; Hanifi, D. A.; Sessolo, M.; Amassian, A.; Malliaras, G. G.; Rivnay, J.et al. Molecular Design of Semiconducting Polymers for High-Performance Organic Electrochemical Transistors. *J Am Chem Soc* **2016,** *138*, 10252.

(15) Li, G.; Chang, W.-H.; Yang, Y. Low-bandgap conjugated polymers enabling solution-processable tandem solar cells. *Nature Reviews Materials* **2017,** *2*.

(16) Grimsdale, A. C.; Leok Chan, K.; Martin, R. E.; Jokisz, P. G.; Holmes, A. B. Synthesis of Light-Emitting Conjugated Polymers for Applications in Electroluminescent Devices. *Chemical Reviews* **2009,** *109*, 897.

(17) Klauk, H. Organic thin-film transistors. *Chem Soc Rev* **2010,** *39*, 2643.

(18) Neo, W. T.; Ye, Q.; Chua, S.-J.; Xu, J. Conjugated polymer-based electrochromics: materials, device fabrication and application prospects. *Journal of Materials Chemistry C* **2016,** *4*, 7364.

(19) Wang, S.; Zuo, G.; Kim, J.; Sirringhaus, H. Progress of Conjugated Polymers as Emerging Thermoelectric Materials. *Progress in Polymer Science* **2022,** *129*.

(20) Abelha, T. F.; Dreiss, C. A.; Green, M. A.; Dailey, L. A. Conjugated polymers as nanoparticle probes for fluorescence and photoacoustic imaging. *J Mater Chem B* **2020,** *8*, 592.

(21) Qian, C. G.; Chen, Y. L.; Feng, P. J.; Xiao, X. Z.; Dong, M.; Yu, J. C.; Hu, Q. Y.; Shen, Q. D.; Gu, Z. Conjugated polymer nanomaterials for theranostics. *Acta Pharmacol Sin* **2017,** *38*, 764.

(22) Torricelli, F.; Adrahtas, D. Z.; Bao, Z.; Berggren, M.; Biscarini, F.; Bonfiglio, A.; Bortolotti, C. A.; Frisbie, C. D.; Macchia, E.; Malliaras, G. G.et al. Electrolyte-gated transistors for enhanced performance bioelectronics. *Nat Rev Methods Primers* **2021,** *1*.

(23) Rivnay, J.; Inal, S.; Salleo, A.; Owens, R. M.; Berggren, M.; Malliaras, G. G. Organic electrochemical transistors. *Nature Reviews Materials* **2018,** *3*.

(24) Friedlein, J. T.; McLeod, R. R.; Rivnay, J. Device physics of organic electrochemical transistors. *Organic Electronics* **2018,** *63*, 398.

(25) Bernards, D. A.; Malliaras, G. G. Steady-State and Transient Behavior of Organic Electrochemical Transistors. *Advanced Functional Materials* **2007,** *17*, 3538.

(26) Rivnay, J.; Leleux, P.; Ferro, M.; Sessolo, M.; Williamson, A.; Koutsouras, D. A.; Khodagholy, D.; Ramuz, M.; Strakosas, X.; Owens, R. M.et al. High-performance transistors for bioelectronics through tuning of channel thickness. *Science Advances* **2015,** *1*, e1400251.

(27) Khodagholy, D.; Doublet, T.; Quilichini, P.; Gurfinkel, M.; Leleux, P.; Ghestem, A.; Ismailova, E.; Herve, T.; Sanaur, S.; Bernard, C.et al. In vivo recordings of brain activity using organic transistors. *Nat Commun* **2013,** *4*, 1575.

(28) Marks, A.; Griggs, S.; Gasparini, N.; Moser, M. Organic Electrochemical Transistors: An Emerging Technology for Biosensing. *Advanced Materials Interfaces* **2022,** *9*.

(29) Yao, Y.; Huang, W.; Chen, J.; Liu, X.; Bai, L.; Chen, W.; Cheng, Y.; Ping, J.; Marks, T. J.; Facchetti, A. Flexible and Stretchable Organic Electrochemical Transistors for Physiological Sensing Devices. *Adv Mater* **2023**, DOI:10.1002/adma.202209906 10.1002/adma.202209906, e2209906.

(30) Guo, K.; Wustoni, S.; Koklu, A.; Diaz-Galicia, E.; Moser, M.; Hama, A.; Alqahtani, A. A.; Ahmad, A. N.; Alhamlan, F. S.; Shuaib, M.et al. Rapid single-molecule detection of COVID-19 and MERS antigens via nanobody-functionalized organic electrochemical transistors. *Nat Biomed Eng* **2021,** *5*, 666.

(31) Zheng, Y.; Zhang, S.; Tok, J. B.; Bao, Z. Molecular Design of Stretchable Polymer Semiconductors: Current Progress and Future Directions. *J Am Chem Soc* **2022,** *144*, 4699.

(32) Lei, T.; Guan, M.; Liu, J.; Lin, H.-C.; Pfattner, R.; Shaw, L.; McGuire, A. F.; Huang, T.-C.; Shao, L.; Cheng, K.-T.et al. Biocompatible and totally disintegrable semiconducting polymer for ultrathin and ultralightweight transient electronics. *Proceedings of the National Academy of Sciences* **2017,** *114*, 5107.

(33) Chiong, J. A.; Zheng, Y.; Zhang, S.; Ma, G.; Wu, Y.; Ngaruka, G.; Lin, Y.; Gu, X.; Bao, Z. Impact of Molecular Design on Degradation Lifetimes of Degradable Imine-Based Semiconducting Polymers. *Journal of the American Chemical Society* **2022,** *144*, 3717.

(34) Oh, J. Y.; Rondeau-Gagne, S.; Chiu, Y. C.; Chortos, A.; Lissel, F.; Wang, G. N.; Schroeder, B. C.; Kurosawa, T.; Lopez, J.; Katsumata, T.et al. Intrinsically stretchable and healable semiconducting polymer for organic transistors. *Nature* **2016,** *539*, 411.

(35) Zhang, S.; Cheng, Y. H.; Galuska, L.; Roy, A.; Lorenz, M.; Chen, B.; Luo, S.; Li, Y. T.; Hung, C. C.; Qian, Z.et al. Tacky Elastomers to Enable Tear-Resistant and Autonomous Self-Healing Semiconductor Composites. *Advanced Functional Materials* **2020,** *30*.

(36) Yang, Q.; Wei, T.; Yin, R. T.; Wu, M.; Xu, Y.; Koo, J.; Choi, Y. S.; Xie, Z.; Chen, S. W.; Kandela, I.et al. Photocurable bioresorbable adhesives as functional interfaces between flexible bioelectronic devices and soft biological tissues. *Nat Mater* **2021,** *20*, 1559.

(37) Du, W.; Ohayon, D.; Combe, C.; Mottier, L.; Maria, I. P.; Ashraf, R. S.; Fiumelli, H.; Inal, S.; McCulloch, I. Improving the Compatibility of Diketopyrrolopyrrole Semiconducting Polymers for Biological Interfacing by Lysine Attachment. *Chemistry of Materials* **2018,** *30*, 6164.

Chapter 2. A universal and facile approach for building multifunctional conjugated polymers

2.1 Introduction

Recently, the functional performances of conjugated polymers in electronic devices have witnessed significant improvements. Moreover, conjugated polymers have been demonstrated as the only class of electronic materials that can provide skin-like stretchability[1-5], thereby rendering them prime candidates for human-integrated electronics for health monitoring, disease diagnosis, and medical treatments[6-9]. However, towards realizing such applications of collecting and delivering various types of information from/to human bodies, there have rarely been the designs of conjugated polymers for providing a number of emerging functions, which include, but not limited to, biochemical sensing, chemotherapeutic property, bio/immune-compatibility, micro-patternability, tissue/skin adhesion, stimuli-responsiveness. Currently, the absence of these functional properties poses the major obstacle for taking advantage of the unique properties of conjugated polymers to benefit the development of human-integrated electronics.

As these functional properties are typically afforded by certain functional units, such as bioreceptors, drug motifs, antifouling groups, and photo/thermo-reactive groups, respectively, the most straightforward and effective approach for building these functions into conjugated polymers should be to incorporate these functional units into the molecular designs, such as on the side chains. However, significant challenges arise in the synthesis of these types of molecular structures following the conventional procedure of first incorporating desired functional units during the monomer synthesis and then carrying out the polymerization reaction at the end[10-14]. Since many functional units of the above listed types are either highly sensitive to harsh conditions such as high temperature, high pressure and toxic reagents, or tend to significantly change a monomer's solubility, their attachment on a conjugated monomer either cannot survive through the polymerization reaction or would largely decrease the efficacy of the polymerization. For other functional units that could be compatible with this synthesis procedure, they each require unique design and optimization of the synthesis conditions, which further elevates the technical barrier. So far, the successes along this line for conjugated polymers have only been achieved on a limited number of functional groups of the above-listed types, for example, lysine groups for enhancing cell viability[14], and photochromic groups for optically tunable electrical performance[15].

Alternatively, surface modification on a pre-deposited thin film of conjugated polymers presents another option for incorporating a type of function that mainly relies on surface properties, e.g., chemical sensing, biocompatibility, and adhesion. However, with the lack of suitable reactive sites in the typical designs of conjugated polymers, the viable methods are mostly limited to physical approaches such as coating or adsorption[16,17], which are only applicable to a small portion of functional groups and typically result in poor stability. For the generally preferred modification through covalent assembly, additional pre-treatments (e.g., oxygen plasma activation) to the film surface are often needed for generating reactive groups[18-21], which usually cause undesired side reactions or even degradation to conjugated polymers.

Therefore, to unlock a broad range of desired functionalities for conjugated polymers, it is highly necessary to develop a different synthesis approach that can fully decouple the covalent attachment of functional units with the polymerization reaction. Herein, we report a generalizable molecular design and synthesis approach of using click chemistry as a post-polymerization step to versatilely graft a variety of functional units onto the side chains of high-performance donor-acceptor type semiconducting conjugated polymers[14,22] (**Figure 2-1A**), which we name as the CLIck-to-Polymer (CLIP) method. Specifically, with the criteria of having high reaction efficacy, sufficient compatibility of the clickable site with the cross-coupling (e.g., Stille-coupling) polymerization for donor-acceptor conjugated polymers, a simple reaction procedure, and minimal influence on the charge-carrier transport, we rationally choose the copper-catalyzed azide-alkyne cycloaddition (CuAAC)[23,24] as the click reaction for the CLIP method. To the best of our knowledge, the CuAAC reaction so far has neither been used for the functionalization of a donor-acceptor conjugated polymer, nor achieved high-performance semiconducting property through considering the structure-property relationships[25-28]. Moreover, we hypothesize that the high efficacy and the broad tunable space of the reaction condition of this click chemistry could also allow the versatile use of the CLIP for not only bulk functionalization and but also surface functionalization, by simply swapping the sequence of the click reaction and the thin-film deposition (**Figure 2-1B**), which, to the best of our knowledge, has never been reported before on a single method. This will provide the freedom of choosing the most suitable functionalization approach from the combined considerations of both the nature of the targeted function and the preservation of the electrical performance.

In this work, we demonstrated the versatility of this approach on four types of functional groups (**Figure 2-1A**, bottom) with photo-crosslinkable[29], bio-conjugation[30], immune-modulatory[31], and ionic conducting[32] properties, respectively. From the synthetic perspective, they covered the challenging characteristics of thermal reactivity, solvent incompatibility, and sized volume, as well as serving to solve the challenge from less stable biochemical units. The obtained conjugated polymers with the bulk functionalization of these units still give largely-preserved charge-carrier mobility (above 0.1 $cm^2\ V^{-1}\ s^{-1}$ from three of the four functionalized polymers), while the surface functionalization does not cause any influence on the mobility. To demonstrate the usefulness of this CLIP strategy, we realized two highly desired functions on conjugated polymers: the direct photo-patterning with sub-10 μm resolution enabled by the incorporation of benzophenone groups; and the amplified biomolecular sensing enabled by the incorporation of *N*-hydroxysuccinimide (NHS) ester that can conjugate with enzymatic bioreceptors.

2.2 Experimental section

Materials and characterizations

All the chemicals used in the study were purchased from Sigma-Aldrich and used without further purification. Anhydrous solvents were purchased from either Sigma-Aldrich or Fisher Scientific. 5,5'-Dibromo-3,3'-bis(2-(2-(2-methoxyethoxy)ethoxy)ethoxy)-2,2'-bithiophene was purchased from SunaTech Inc. (CAT# IN1273) and was used as received. Column chromatography was carried out with silica gel for flash chromatography from VWR Scientific.

Microwave polymerization was conducted using a Biotage Initiator +. Nuclei magnetic resonance (NMR) spectra were recorded on a Bruker Avance III HD console spectrometer (^{1}H 400 MHz, ^{13}C 100 MHz) at 293 K. Chemical shifts are given in parts per million (ppm) with respect to tetramethylsilane as an internal standard, and coupling constants (J) are given in Hertz (Hz). Polymer NMR spectra were recorded at 393 K in deuterated 1,1,2,2-tetrachloroethane (TCE-d_2). High-resolution mass spectra (HR-MS) were recorded on an Agilent 6530 LC Q-TOF mass spectrometer using electrospray ionization with fragmentation voltage set at 70 V and processed with an Agilent MassHunter Operating System. Number average molecular weight (M_n), weight average molecular weight (M_w), and polydispersity index (PDI) were evaluated by high temperature size exclusion chromatography (SEC) using 1,2,4-trichlorobenzene and performed on a EcoSEC HLC-8321GPC/HT (Tosoh Bioscience) equipped with a single TSKgel GPC column (GMHHR-H; 300 mm × 7.8 mm) calibrated with monodisperse polystyrene standards. The samples were prepared using 1 mg/mL of sample in trichlorobenzene (TCB), which were allowed to stir at 80 °C for 12 h prior to injection. The analysis of the samples was performed at 180 °C with a flow rate of 1.0 mL/min with injection quantities of 300 μL. The data was collected and integrated using EcoSEC 8321GPC HT software suite. UV-Vis absorption spectra were recorded on the Shimadzu UV-3600 Plus UV-VIS-NIR spectrophotometer. FTIR spectra were recorded on the Shimadzu IRTracer-100 Fourier transform infrared spectrometer. Differential scanning calorimetry (DSC) experiments were performed with a TA Instruments Discovery 2500 differential scanning calorimeter. Thermal gravimetric analysis (TGA) plots were recorded with a TA Instruments Discovery thermogravimetric analyzer. The water contact angle measurement was done with a KRÜSS DSA100 drop shape analyzer. The X-ray photoelectron spectroscopy (XPS) was done with Kratos AXIS Nova with a monochromatic Al Kα X-ray source and a delay line detector (DLD) system. Optical microscope images were captured with a Zeiss Axioscope 5/7/Vario microscope. Grazing-incidence X-ray diffraction (GIXD) was performed at the Advanced Photon Source at Argonne National Laboratory on beamline 8-ID-E[33]. The X-ray energy was 10.92 keV, the incident angle was 0.14°, and the exposure time was 10 s. The area detector (Pilatus 1M, Dectris) was translated vertically for a second exposure. The two images were combined to eliminate gaps due to rows of inactive pixels at the borders between modules using the GIXSGUI package[34] for Matlab and demonstrating that the samples were not damaged by the exposure.

Synthesis of azide-attached DPP monomer (4)

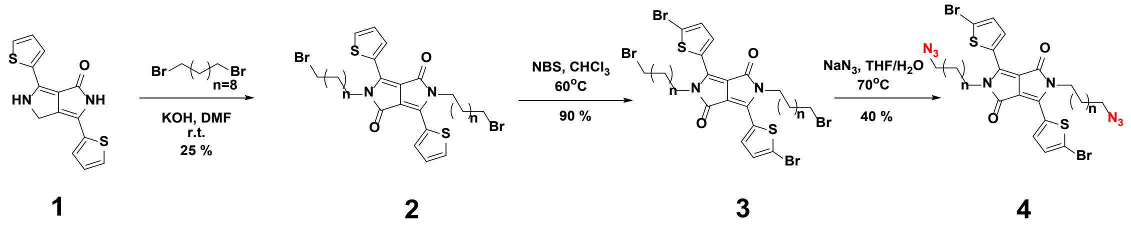

2,5-bis(10-bromodecyl)-3,6-di(thiophen-2-yl)-2,5-dihydropyrrolo[3,4-c]pyrrole-1,4-dione (2).

To a RBF, 3,6-di(thiophen-2-yl)-2,5-dihydropyrrolo[3,4-c]pyrrole-1,4-dione (1) (6.66 mmol, 2 g), 1,10-dibromodecane (16 mmol, 4.8 g), and potassium hydroxide (16 mmol, 0.9 g) were added to 30 mL DMF under nitrogen atmosphere. The mixture was stirred at r.t. overnight, and then was poured to 100 mL water. The solution was extracted with chloroform and washed with water and brine, and then dried over magnesium sulfate. The solvent was removed using rotary evaporation and purified by column chromatography (silica gel, DCM/hexane=1:1, v:v). The final solid was isolated as a red powder (1.2 g, 25 %). ^{1}H NMR (500 MHz, CDCl3) δ 8.93 (dd, *J* = 3.9, 1.1 Hz, 2H), 7.64 (dd, *J* = 5.0, 1.1 Hz, 2H), 7.31 – 7.28 (m, 2H), 4.15 – 3.99 (m, 4H), 3.40 (t, *J* = 6.9 Hz, 4H), 1.92 – 1.79 (m, 4H), 1.74 (d, *J* = 7.8 Hz, 4H), 1.35 (d, *J* = 64.8 Hz, 24H); ^{13}C NMR (126 MHz, $CDCl_3$) δ 161.38, 140.03, 135.29, 130.72, 129.78, 128.64, 107.69, 42.20, 34.08, 32.82, 29.95, 29.50 – 29.10, 28.72, 28.15, 26.84. HRMS (ESI) Calcd for $C_{34}H_{47}Br_2N_2O_2S_2$ [M+H]+ : 737.1440, found 737.1440.

2,5-bis(10-bromodecyl)-3,6-bis(5-bromothiophen-2-yl)-2,5-dihydropyrrolo[3,4-c]pyrrole-1,4-dione (3).

To a RBF with 60 mL chloroform, compound **2** (1.09 mmol, 0.8 g) and *N*-bromosuccinimide (2.23 mmol, 0.4 g) was added. The reaction flask was wrapped with aluminum foil and heated to 60 °C for 3 h. The reaction was cooled to r.t. and washed with water. The organic phase was dried over magnesium sulfate. The solvent was removed using rotary evaporation and purified by column chromatography (silica gel, DCM/hexane=1:1, v:v). The final solid was isolated as a purple powder (0.87 g, 90 %). ^{1}H NMR (500 MHz, $CDCl_3$) δ 8.68 (d, *J* = 4.2 Hz, 2H), 7.23 (d, *J* = 4.2 Hz, 2H), 4.11 – 3.85 (m, 4H), 3.40 (t, *J* = 6.9 Hz, 4H), 1.87 – 1.80 (m, 5H), 1.71 (dt, *J* = 15.4, 7.7 Hz, 4H), 1.42 – 1.27 (m, 24H); ^{13}C NMR (126 MHz, $CDCl_3$) δ 161.02, 138.99, 135.40, 131.68, 131.10, 119.19, 107.79, 42.26, 34.07, 32.82, 29.96, 29.33, 29.12, 28.72, 28.16, 26.79. HRMS (ESI) Calcd for $C_{34}H_{45}Br_4N_2O_2S_2$ $[M+H]^+$: 892.9650, found 892.9644.

2,5-bis(10-azidodecyl)-3,6-bis(5-bromothiophen-2-yl)-2,5-dihydropyrrolo[3,4-c]pyrrole-1,4-dione (4, n = 8).

To a 250 mL RBF with 80 mL THF, compound **3** (0.671 mmol, 0.6 g) was added. Sodium azide (5.37 mmol, 349 mg) in 4 mL water was added. The reaction flask was heated to 70 ºC and stirred for 48 h. After cooling to r.t., the solvent was removed, and the residue was dissolved in 50 mL DCM and was washed with water three times. The organic phase was dried over magnesium sulfate. The solvent was removed using rotary evaporation and purified by column chromatography (silica gel, DCM/hexane=1:1, v:v). The final solid was isolated as a purple powder (0.22 g, 40 %). ^{1}H NMR (500 MHz, $CDCl_3$) δ 8.67 (d, *J* = 4.2 Hz, 2H), 7.23 (d, *J* = 4.2 Hz, 2H), 4.04 – 3.89 (m, 4H), 3.25 (t, *J* = 7.0 Hz, 4H), 1.70 (dt, *J* = 15.5, 7.7 Hz, 4H), 1.59 (dd, *J* = 14.2, 7.0 Hz, 4H), 1.44 – 1.27 (m, 24H); ^{13}C NMR (126 MHz, $CDCl_3$) δ 161.01, 138.97, 135.40, 131.67, 131.10, 119.18, 107.78, 51.49, 42.26, 29.96, 29.36, 29.12, 28.84, 26.75. HRMS (ESI) Calcd for $C_{34}H_{45}Br_2N_8O_2S_2$ $[M+H]^+$: 819.1468, found 819.1468.

2,5-bis(6-azidohexyl)-3,6-bis(5-bromothiophen-2-yl)-2,5-dihydropyrrolo[3,4-c]pyrrole-1,4-dione (4, n = 4).

^{1}H NMR (400 MHz, $CDCl_3$) δ 8.67 (d, *J* = 4.2 Hz, 2H), 7.24 (d, *J* = 4.2 Hz, 2H), 4.05 – 3.94 (m, 4H), 3.27 (t, *J* = 6.8 Hz, 4H), 1.74 (d, *J* = 6.4 Hz, 4H), 1.67 – 1.58 (m, 4H), 1.44 (dt, *J* = 6.9, 3.4 Hz, 8H). ^{13}C NMR (101 MHz, $CDCl_3$) δ 161.01, 138.94, 135.48, 131.74, 130.98, 119.28, 107.77, 51.34, 42.03, 29.86, 28.74, 26.37. HRMS (ESI) Calcd for $C_{26}H_{29}Br_2N_8O_2S_2$ $[M+H]^+$: 707.0216, found 707.0219.

Synthesis of DPPTT-10a and DPPTT-20a

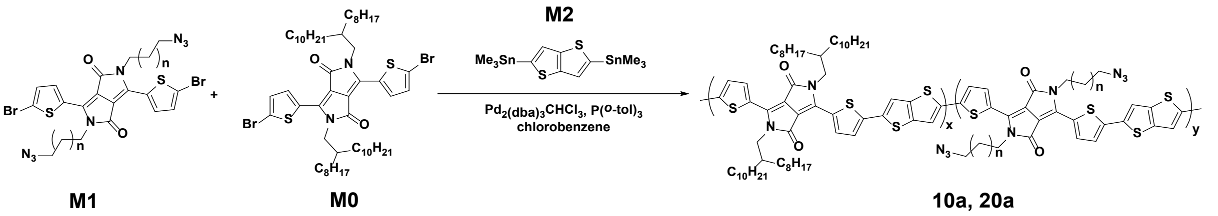

To a mixture of **M1** (0.109x mmol, x eq., x=0.1, 0.2), **M0** (0.109-0.109x mmol, (1.0-x) eq.), 2,5-bis(trimethylstannyl)-thieno[3,2-b]thiophene (**M2**, 51 mg, 0.109 mmol, 1.0 eq.), $Pd_2(dba)_3$ $CHCl_3$ (2.2 mg, 0.0022 mmol, 0.02 eq.), and P(*o*-tol)$_3$ (2.6 mg, 0.0087 mmol, 0.08 eq.) was added 2 mL of chlorobenzene in a nitrogen filled glovebox. The reaction vial was sealed and submitted to a microwave reactor with the following temperature profile: 1 minute at 100 °C, 2 minutes at 120 °C, 2 minutes at 140 °C, 3 minutes at 160 °C and 40 minutes at 180 °C. After the reaction was cooled down, 10 mol% of trimethyl(phenyl)stannane were added and the crude polymer solution was heated again to 1 minute at 100 °C, 1 minute at 120 °C, 2 minutes at 140 °C and 3 minutes at 160 °C. To complete the end-capping of the polymer, 10 mol% of bromobenzene were added and the reaction vessel submitted one last time to microwave heating (1 minute at 100 °C, 1 minute at 120 °C, 2 minutes at 140 °C and 3 minutes at 160 °C). The crude polymer was then precipitated into methanol, filtered, loaded to a Soxhlet thimble and washed successively with hexane, acetone (each for 24 h). The polymer was finally collected from the thimble with chloroform. The chloroform solution was then concentrated and precipitated into methanol. The polymer fibers were collected by filtration and dried under high vacuum for 24 h to give the final polymers 10a, 20a. Polymer NMR spectra were recorded at 393 K in deuterated 1,1,2,2-tetrachloroethane (TCE-*d*$_2$)

Synthesis of g2T-10a

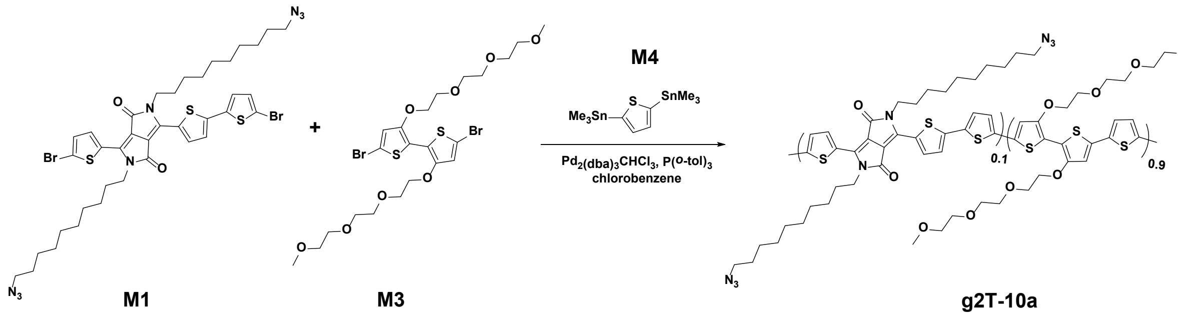

To a mixture of **M1** (0.1 eq., 0.0086 mmol, 7 mg), **M3** (0.9 eq., 0.0774 mmol, 50 mg), 2,5-bis(trimethylstannyl)thiophene (**M2**, 35.3 mg, 0.086 mmol, 1.0 eq.), $Pd_2(dba)_3$ $CHCl_3$ (1.8 mg, 0.0017 mmol, 0.02 eq.), and $P(o\text{-tol})_3$ (2.1 mg, 0.0069 mmol, 0.08 eq.) was added 2 mL of chlorobenzene in a nitrogen filled glovebox. The reaction vial was sealed and submitted to a microwave reactor with the following temperature profile: 1 minute at 100 °C, 2 minutes at 120 °C, 3 minutes at 140 °C, and 20 minutes at 160 °C. After the reaction was cooled down, 10 mol% of trimethyl(phenyl)stannane were added and the crude polymer solution was heated again to 1 minute at 100 °C, 2 minutes at 120 °C, and 3 minutes at 140 °C. To complete the end-capping of the polymer, 10 mol% of bromobenzene were added and the reaction vessel was submitted one last time to microwave heating (1 minute at 100 °C, 2 minutes at 120 °C, and 3 minutes at 140 °C). The crude polymer was then precipitated into methanol, filtered, loaded to a Soxhlet thimble and washed successively with hexane, acetone (each for 24 h). The polymer was finally collected from the thimble with chloroform. The chloroform solution was then concentrated and precipitated into methanol. The polymer fibers were collected by filtration and dried under high vacuum for 24 h to give the final polymer g2T-10a. The NMR spectrum of g2T-10a was recorded at r.t. in $CDCl_3$.

Bulk CLIP method

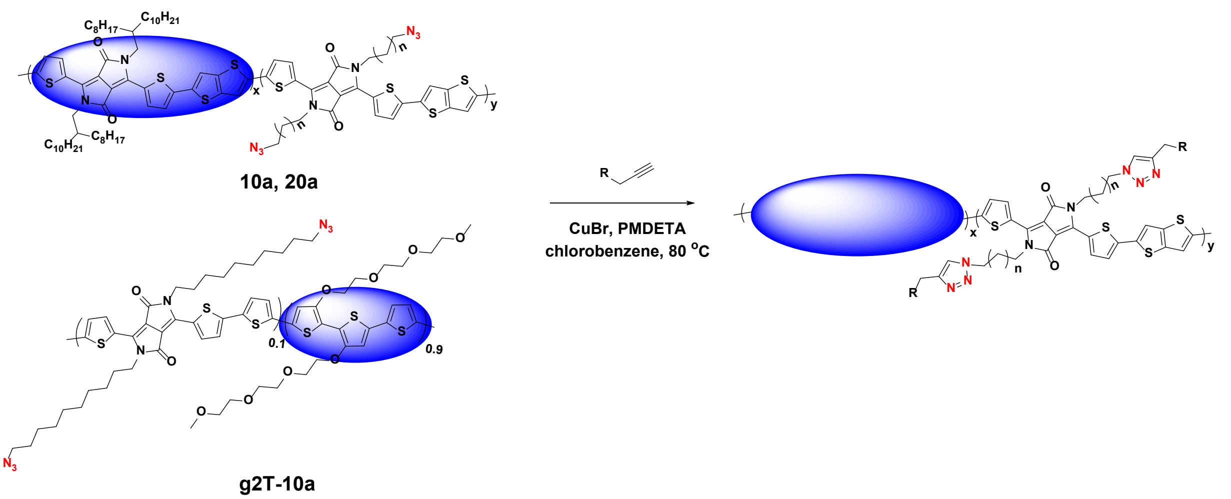

A mixture of azide-modified conjugated polymers (i.e., C6-10a, C6-20a, C10-10a, C10-20a or g2T-10a; with the amount of 10 mg, 1.0 eq.), alkyne-modified functional group (i.e., alkyne-PY, alkyne-PEG2000, alkyne-BP, alkyne-PEG5-*N*-hydroxysuccinimidyl ester, in 3.0 eq.), CuBr (in 3.0 eq.), and *N,N,N,N,N*-pentamethyldiethylenetriamine (PMDETA, in 3.0 eq.) were added to a 4 mL vial. The vial was sealed with a septum and degassed with nitrogen gas before anhydrous chlorobenzene (2 mL) added. The reaction was stirred at 80 °C for 3 hours. Then the solution was precipitated into methanol (100 mL), stirred for 30 min and filtered through a Soxhlet thimble. The CLIP product was washed by Soxhlet with methanol or acetone and the polymer was extracted with $CHCl_3$. The $CHCl_3$ fraction was concentrated down to 1 mL and precipitated into methanol (10 mL) and filtered. The polymer fibers were collected by filtration and dried under high vacuum for 24 h to give the final functional polymers. Polymer NMR spectra were recorded at 393 K in deuterated 1,1,2,2-tetrachloroethane (TCE-d_2)

Device fabrication and characterization

The thin-film transistors (TFTs) are based on bottom-contact/bottom-gate structure. The *n*-octadecyltrimethoxysilane (OTS)-treated Si/SiO_2 (300 nm) substrates[35] are cleaned by toluene. After that, the source/drain gold electrodes (50 nm) are patterned via thermal evaporation with a metal shadow mask. The channel length (*L*) and width (*W*) are 200 μm and 4 mm, respectively. The gold surface is then modified by submerging the substrates in 30 mL IPA with 10-μL 2,3,4,5,6-pentafluorothiophenol to form a SAM layer. The substrates are gently rinsed with IPA and blow-dried with nitrogen gas. The polymer solution (5 mg/mL in chlorobenzene) was then spin-coated at 1000 rpm for 60 s, followed by annealing at 150 °C for one hour in nitrogen atmosphere. All of the electrical characteristics of the semiconducting layer were measured using Keithley 4200 (Keithley Instruments Inc, Cleveland, OH, USA) under an ambient environment .

The organic electrochemical transistors (OECTs) were fabricated similar to the literature previously reported[36]. Briefly, the glass substrates are cleaned with acetone, isopropyl alcohol, and water. After that, the source/drain gold electrodes (50 nm) are patterned via thermal evaporation with a metal shadow mask. The channel length (*L*) and width (*W*) are 200 μm and 4 mm, respectively. Then the polymer solution (5 mg/mL in chloroform) was spin-coated at 1000 rpm, followed by annealing at 110 °C for 30 min in nitrogen atmosphere. The electrolyte was PBS solution dropped on top of the transistors. The gate electrode was gold which was immersed in the electrolyte. The electrical characteristics of the semiconducting layer were measured using Keithley 4200 (Keithley Instruments Inc, Cleveland, OH, USA) under an ambient environment.

Surface CLIP method

The surface CLIP follows the general procedure. C10-10a and C10-20a films are first spin-coated on OTS-treated silicon substrate and annealed at 150 °C for one hour. The solution of alkyne-PEG2000 (4 mg, 2 μmol) was dissolved in DMF (0.5 mL) and mixed with a solution of $CuSO_4$ (10 μL, 0.1 M, 1 μmol) and sodium ascorbate (20 μL, 0.1 M, 2 μmol) in water. The reaction mixture was placed on the film surface surrounded with a PDMS well and incubated at room temperature overnight. The surface was rinsed with H_2O and DMF and finally dried with nitrogen gas.

Direct photo-patterning for 10BP conjugated polymer

The C10-10BP polymer (5 mg/mL in chlorobenzene) is spin-coated on OTS-modified silicon oxide substrate at 1000 rpm for 60 s. The polymer film is first annealed at 140 °C for 30 minutes to remove solvent and boost the relative crystallinity. The obtained film thickness is around 30-40 nm. Then the conjugated polymer film is exposed to UV light (365 nm, 2.6 mW/cm^2, Spectrolinker XL-1000) with selected areas for a given period. After immersing the film in chloroform (also a good solvent for dissolving C10-10BP polymer) for 30 s with gentle shaking, the film is blow-dried by nitrogen gas, and then baked at 170 °C for 30 minutes inside glove box in order to fully remove the trapped solvent in the polymer network and further increase the relative crystallinity.

OECT glucose sensing

For the sensing experiment, glucose oxidase dissolved in PBS (pH 7.4) (3 mg/mL) was incubated on the device channel area for two hours and then rinsed with DI water. Glucose was dissolved as stock solutions in PBS. Current-voltage characteristics of the devices were recorded using a Keithley 4200 under an ambient environment. After a steady baseline was obtained for the drain current, the glucose stock solution (4 μL each time) was injected to the electrolyte gently. For all the experiments, the volume of the electrolyte solution was kept at 0.4 mL and drain current changes in response to subsequent additions of increasing concentrations of glucose solutions into the electrolyte were monitored as a function of time.

2.3 Results and discussion

2.3.1 Synthesis and characterization of CLIP based side chain functionalization

In our proposed CLIP method, the first key step is to attach the azide group onto the side chains of conjugated monomers (e.g., the acceptor units for the synthesis of donor-acceptor polymers, as shown in **Figure 2-1A**) during the monomer synthesis process, which serves as the click site for the later CuAAC reaction with a functional group modified with the alkyne group. For most types of functional groups, such alkyne modification can be achieved under compatible, mild conditions[37-41]. To reduce potentially unfavorable influences of bulky functional groups on the packing structure of conjugated polymers, we introduced a linear alkyl linker between the clickable site and the backbone. Since the azide group will neither be activated under the typical conditions of the polymerization reaction (e.g., the Stille-coupling reaction with the temperature range of 180-200 °C), nor influence the monomer's solubility, the subsequent polymerization can still be carried out as usual.

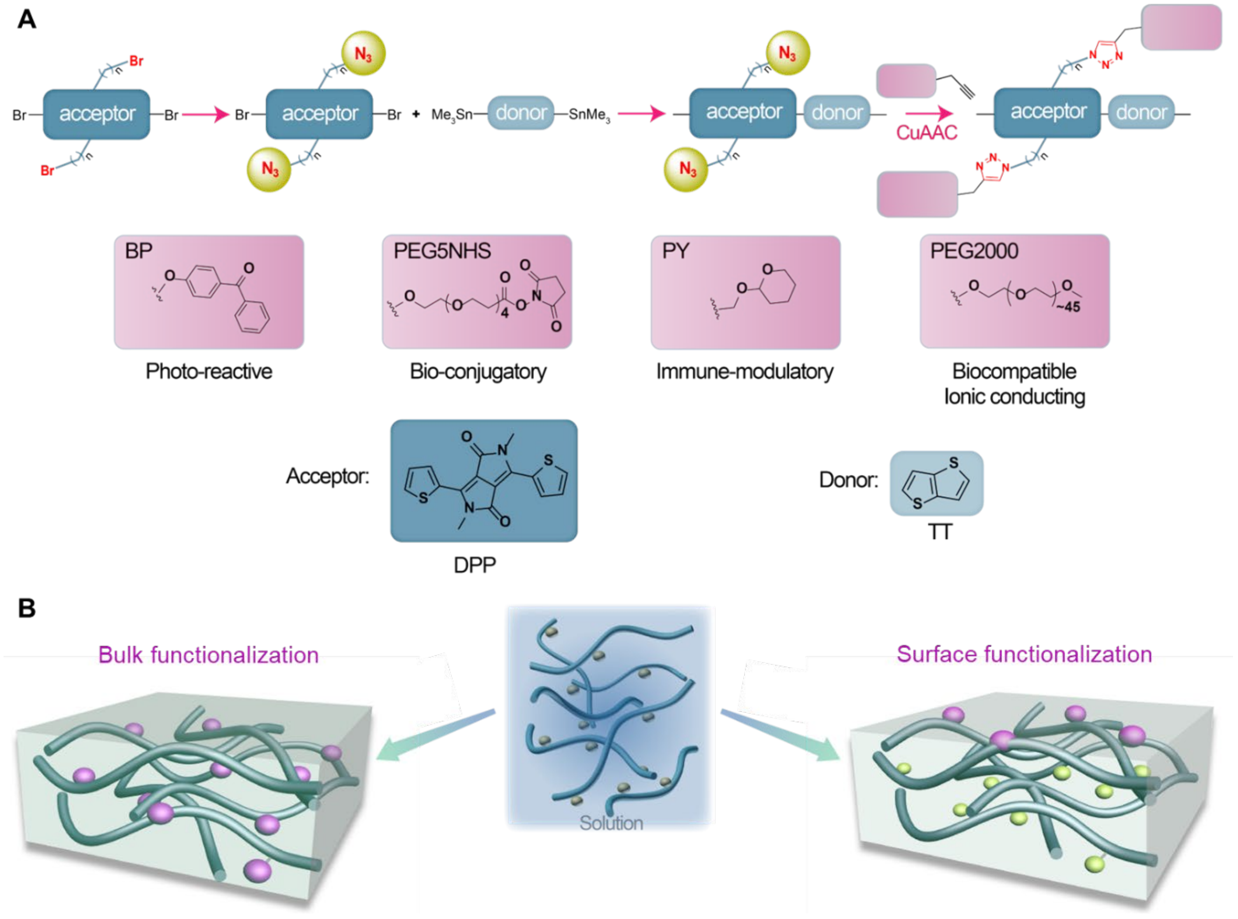

Figure 2-1. Scheme for CLIP synthesis. (A) Synthesis scheme and the demonstrated functional groups and backbone structures. (B) Both bulk and surface functionalization can be achieved from one general conjugated polymer precursor.

Bulk functionalization in the solution state

With the donor-acceptor backbone of diketopyrrolopyrrole-thieno[3,2-b]thiophene (DPPTT) used as the model system, we first demonstrate the bulk functionalization process and characterize the obtained polymers (**Figure 2-2A**). We synthesized DPP monomers with azide-substituted side chains in two different alkyl-linker lengths—six and ten carbons, which were further taken to co-polymerize with DPP units of conventional branched alkyl side chains in two ratios of 1:9 and 2:8.

The reason of copolymerization with branched alkyl chains is to balance the desired functionality and the good solution-processability of the modified polymers. It should be noted that by adding some solubilizing side chains onto the donor (TT) units, the fraction of the functionalized DPP units could be further increased while still keeping sufficient solubility. Through the same polymerization condition, the four types of azide-substituted polymers, namely C6-10a (i.e., six-carbon alkyl linker and 10 % azide-substituted DPP units), C6-20a, C10-10a, C10-20a, all have lower molecular weights than the DPPTT polymer only with branched alkyl side chains (**Table 2-1**), which should come from the slight decrease in the solubility caused by the partial replacement of branched side chains with linear side chains. Subsequently, the four types of functional units as shown in **Figure 2-1A**, i.e., tetrahydropyran (PY), poly(ethylene glycol) 5-*N*-hydroxysuccinimide ester (PEG5NHS), benzophenone (BP), and poly(ethylene glycol)-2000-kDa (PEG2000), were grafted onto the polymers via the CuAAC click reaction. The successes of our CLIP method were verified by Fourier-transform infrared spectroscopy (FTIR, **Figure 2-2B**) and nuclear magnetic resonance (NMR, **Figure 2-2C**) results, which all clearly show the existence of the azide groups after the polymerization reaction, and the subsequent disappearance of the azide after the click reaction.

Table 2-1. Conjugated polymers characteristics

Polymers	M_n (kDa)	M_w (kDa)	PDI	X_n*	Yield (%)
DPPTT	39	93	2.4	39	86
C10-10a	28	37	1.3	28	80
C10-20a	15	19	1.3	16	72
C6-10a	32	52	1.6	33	71
C6-20a	13	14	1.1	14	65

*number-average degree of polymerization.

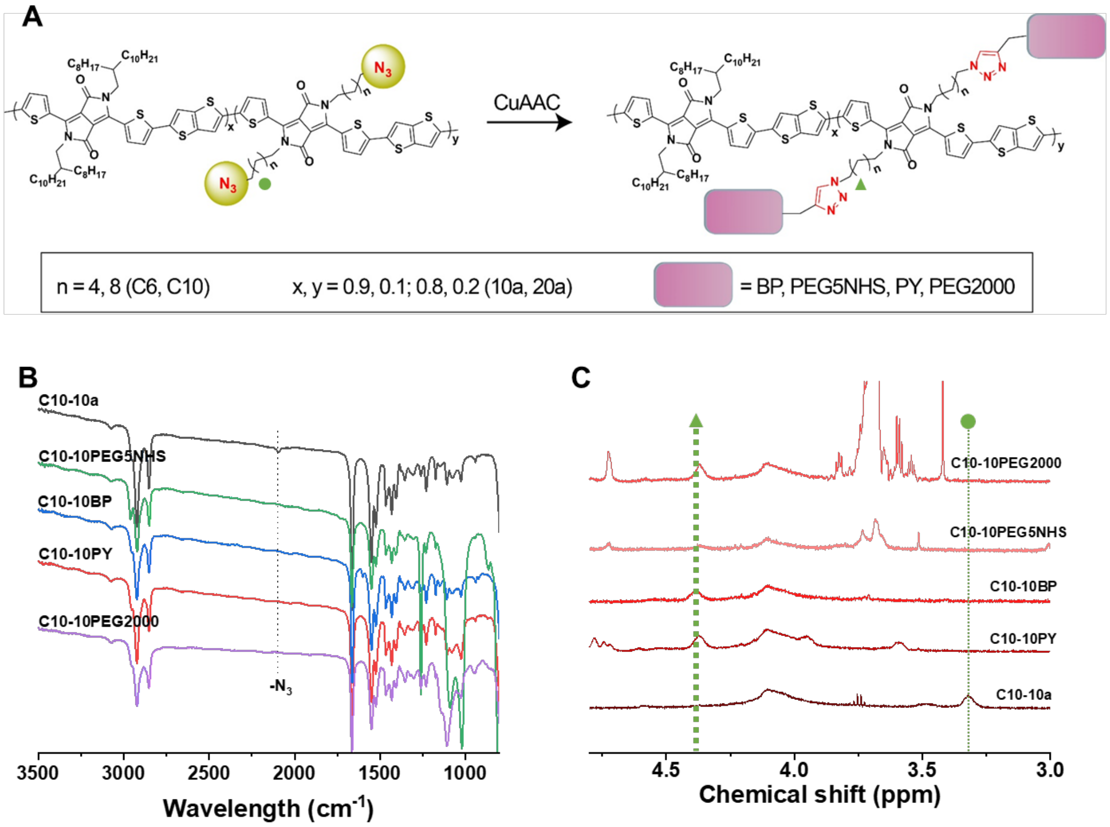

Figure 2-2. Characterizations of conjugated polymers with bulk functionalization through the CLIP method. (A) Reaction scheme for the use of the CuAAC click reaction for functionalizing four types of units on azide-functionalized DPPTT conjugated polymer, with two different alkyl linker lengths (n = 4, 8, respectively) and two copolymerization ratios (y = 0.1, 0.2, respectively) to the number of repeating units. (B) FTIR spectra illustrating the azide peak. (C) High-temperature ^{1}H NMR spectra for the representative polymers before and after the click reaction. The green line labeled with a circle (●) stands for the proton peak adjacent to azide group in starting polymer as indicated in (A). The green line labeled with a triangle (▲) stands for the proton peak adjacent to triazole group in functionalized polymer as indicated in (A).

Surface functionalization on conjugated polymers

Compared to the bulk functionalization, the surface functionalization on a pre-deposited thin film can avoid the disruption to the polymer's packing structures by sizable functional groups. For enabling the CuAAC click reaction on such surfaces, the azide groups as the clickable sites need to be effectively exposed on the surfaces, which is indeed satisfied by the edge-on packing orientation of the deposited C10-10a and C10-20a films (**Figure 2-5A**). However, with the much lower amount of the azide group available on the surface as compared to that from the fully solubilized polymers, sufficiently high reaction efficiency is highly needed. For this, we chose *N,N*-dimethyl formamide (DMF) as the solvent for the click reaction, which offers good wettability to these conjugated polymer films, thus facilitating the transport of the reactant molecules to the surface (**Figure 2-3A**). Under this condition, we carried out the surface functionalization on a C10-10a film with the unit of PEG2000. After the reaction at room temperature overnight followed by a thorough rinse to fully remove the excess reagents, we observed a decrease of the water contact angle from 98° to 67°, which suggests the successful grafting of the PEG2000 chain (**Figure 2-3B**). This was further verified through the X-ray photoelectron spectroscopy (XPS) characterization, which shows the appearance of the C 1s peak (**Figure 2-3C**) and the increased intensity of the O 1s peak, both corresponding to the formed C-O bond. To further exclude the possibility of physical absorption, a control experiment was carried out with the same reaction condition but without the catalyst for the click reaction, which gave little change in the contact angle or the XPS spectrum.

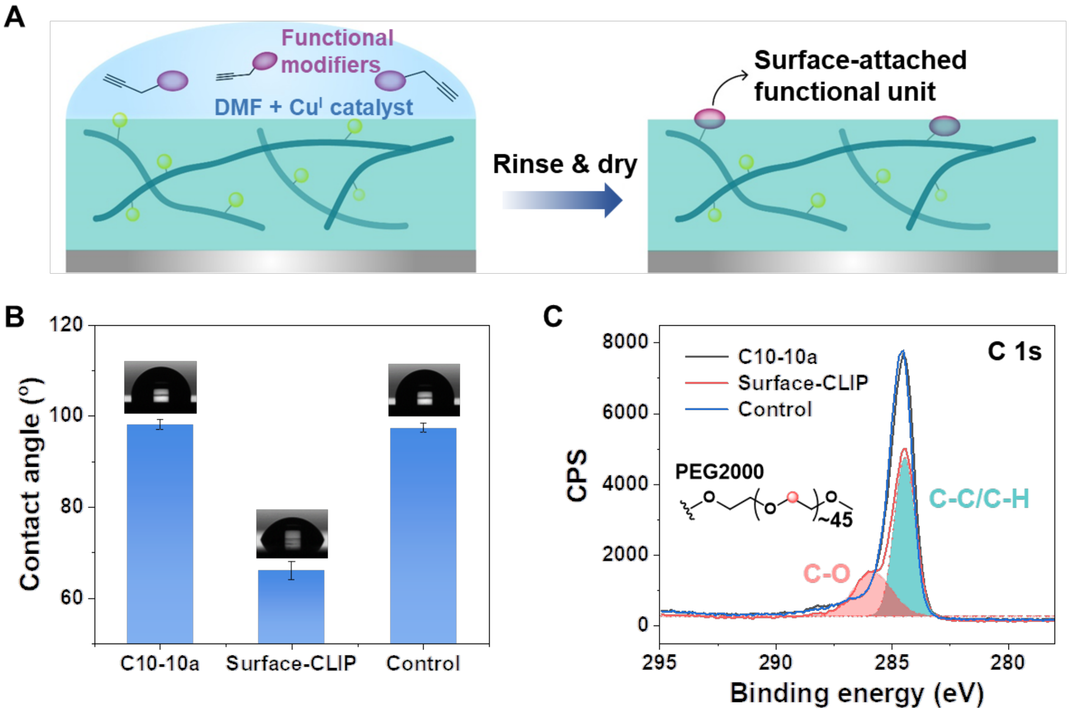

Figure 2-3. Characterizations of conjugated polymers with surface functionalization through the CLIP method. (A) Schematic images showing the process for performing the surface CLIP on a deposited film from an azide-modified conjugated polymer (i.e., C10-10a in the demonstrated experiment). (B) Water contact angles on C10-10a film, the film modified with PEG2000 by the surface CLIP process, and the control film obtained from a C10-10a film going through the same surface CLIP process but without the CuI catalyst. (C) XPS spectra showing the changes of the C 1s peaks from the three films in (B).

2.3.2 Electrical and structural characterization

To evaluate the influence of side-chain functionalization made by the CLIP method on the polymers' electrical performance, we fabricated field-effect transistor (FET) devices to characterize the charge-carrier mobility, which are in the bottom-gate bottom-contact device structure with SiO_2/n^{++}-Si as the gate dielectric and gate electrode, and gold as the source/drain electrodes. The semiconducting properties were evaluated in both linear and saturation regimes.

The linear mobility (μ_{lin}) is calculated via equation 3,

$$\mu_{lin} = \left(\frac{\partial I_d}{\partial V_g}\right)\frac{L}{WC_iV_d} \text{ , when } |V_g\text{-}V_t| > |V_d| \qquad (3)$$

where L and W are the channel length and width, respectively; C_i is the gate-channel capacitance per unit area (for 300 nm SiO_2 dielectric, C_i is 11.5 nF/cm^2).

The saturation mobility (μ_{sat}) is calculated via equation 4.

$$\mu_{sat} = \left(\frac{\partial\sqrt{|I_d|}}{\partial V_g}\right)^2\frac{2L}{WC_i} \text{ , when } |V_g\text{-}V_t| < |V_d| \qquad (4)$$

In general, all the obtained polymers give ideal transfer and output characteristics, as represented by the polymer with PY-functionalization on C10-10a (**Figure 2-4, A and B**). Compared to the unfunctionalized DPPTT polymer with 100 % branched-alkyl side chains, there is only some minor decrease in mobilities (**Figure 2-4C**) resulting from the side-chain modifications with the azide group alone and the four types of functional units. Such changes in mobility could be the combined effects of the changes in the packing structure, the molecular weight, and the deposited film morphology. The extent of such influences is dictated by both the side-chain structure (i.e., the alkyl-breaker length) and the molar ratio in the co-polymerization. As shown in **Figure 2-4C**, the CLIP of the functional group PY on C10-10a results in slightly less decrease in mobility than on C6-10a.

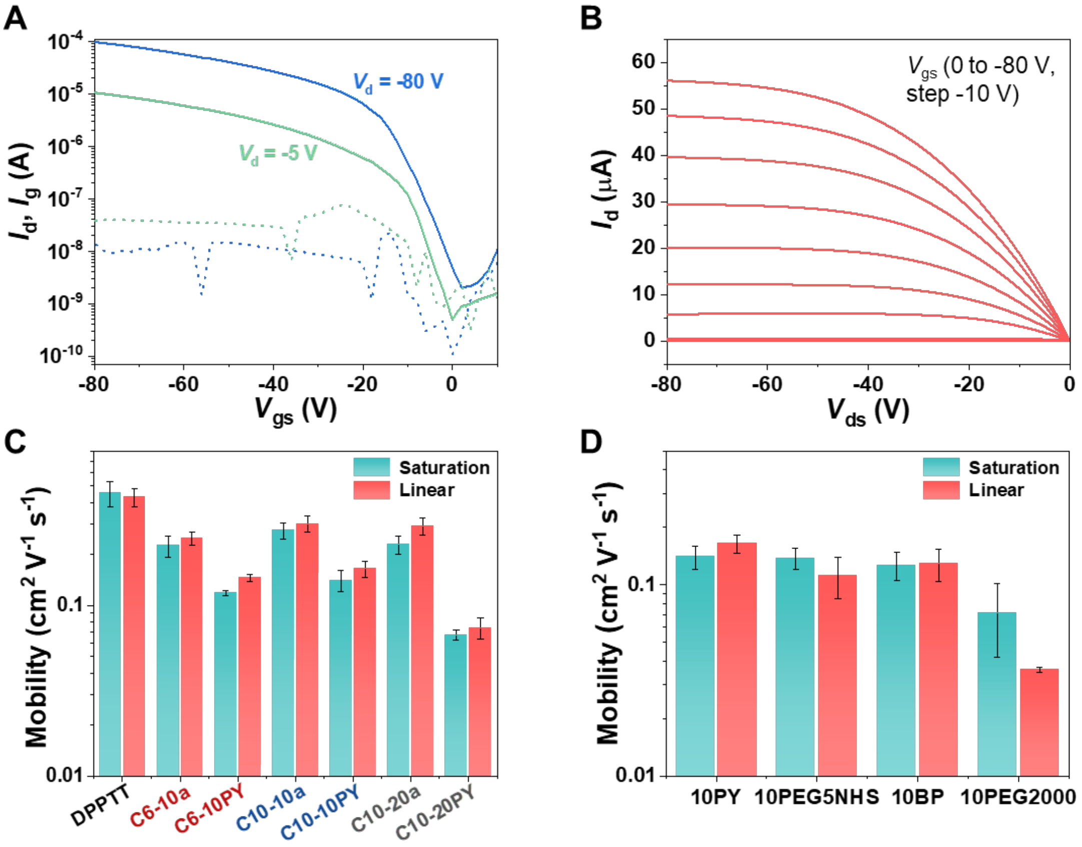

Figure 2-4. OFET characterization of bulk-functionalized conjugated polymers. (A) Typical transfer characteristic obtained from the functionalized polymer C10-10PY. I_d, drain current, represented by solid lines; I_g, gate current, represented by the dashed line; V_{gs}, the gate-source voltage. (B) Typical output characteristic from C10-10PY. (C) Saturation and linear charge-carrier mobilities from the unfunctionalized DPPTT polymer, azide-modified polymers (C6-10a, C10-10a, C10-20a) and the further obtained PY-functionalized polymers (C6-10PY, C10-10PY, C10-20PY). C6 and C10 stand for the alkyl linker lengths of 6-carbon and 10-carbon, respectively; 10a/PY and 20a/PY stand for the side-chain modification with the azide/PY group in the molar ratio of 10 % and 20 % respectively. (D) Saturation and linear charge-carrier mobilities from the

four polymers with the four functional units functionalized on C10-10a, respectively. The error bars in (C) and (D) represent the standard deviation obtained from at least six measurements.

To study the structure-property relationship, from **Figure 2-5, A and B**, the longer alkyl linker (C10 vs C6) reduces the steric hindrance from the functional group to the polymers' packing ordering, as shown by the crystallinities measured from grazing incidence X-ray diffraction (GIXD) and aggregation level characterized by ultraviolet-visible (UV-Vis) (**Figure 2-5C**). For the C10 polymers, on the other hand, the increase of the functionalization ratio from 10 % to 20 % (i.e., the resulted polymer of C10-20PY) leads to lower mobility, which should also come from the elevated disruption to the packing structure. Besides, the decreased molecular weights of the functionalized polymers could also be a reason for the decrease in mobility[42], which in the future could be improved by enhancing the solubility of the monomers and resulted polymers through introducing additional solubilizing groups to the backbone[43].

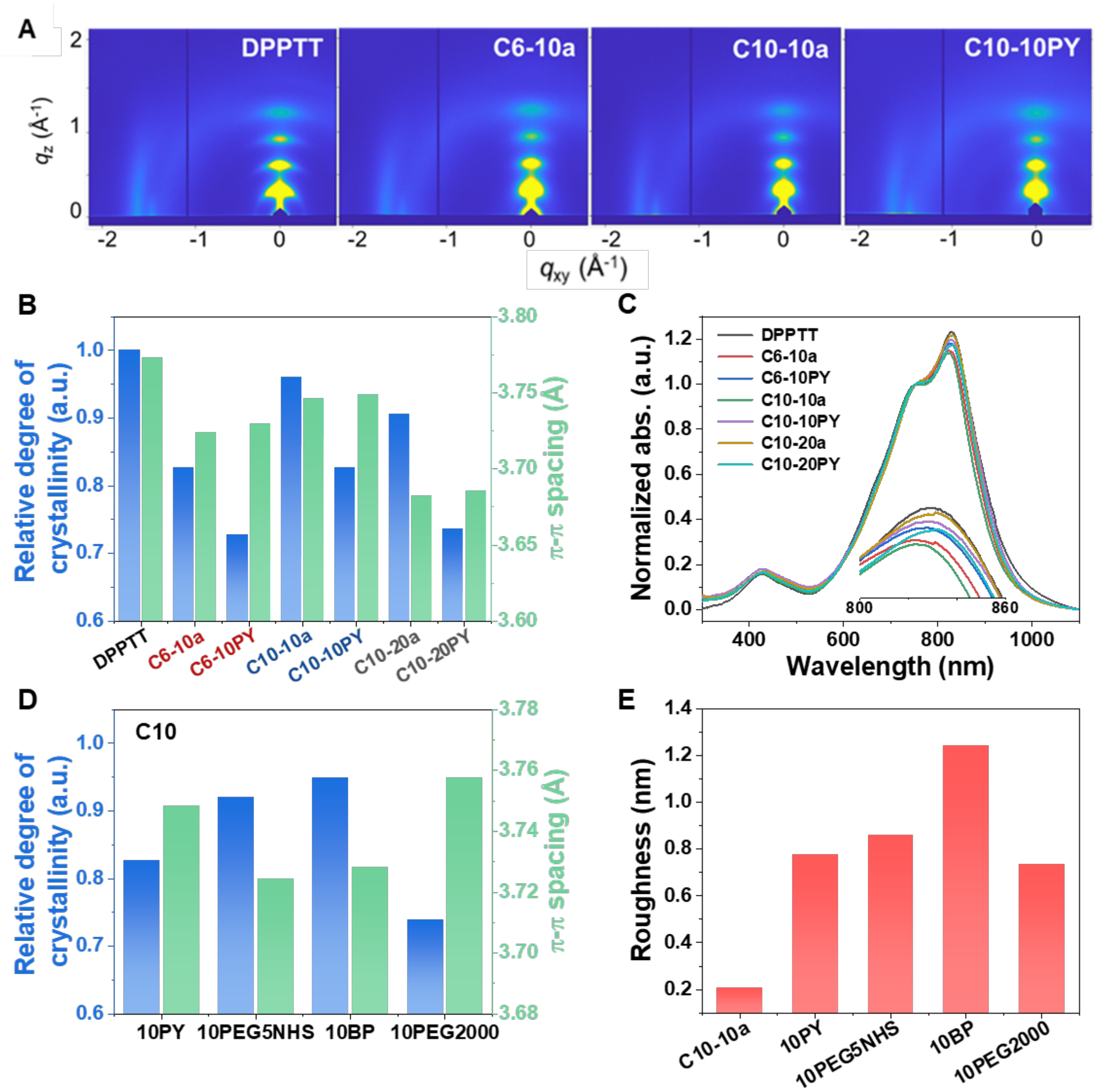

Figure 2-5. Structural characterization of bulk-functionalized conjugated polymers. (A) 2D GIXD images. (B) Relative degrees of crystallinity and π-π spacings comparing DPPTT polymer, azide-modified polymers and the further obtained PY-functionalized polymers. (C) Normalized UV-Vis absorption spectra. (D) Relative degrees of crystallinity and π-π spacings comparing the four functional units functionalized on C10-10a. (E) Root-mean-square roughness of C10-10a and these four types of functionalized polymers, as determined from atomic-force microscopy (AFM) topological images.

The further expanded comparison of the other three types of functional groups, i.e., namely PEG5NHS, BP and PEG2000, together with PY, functionalized on C10-10a polymer all achieve mobility above 0.1 $cm^2 V^{-1} s^{-1}$ except PEG2000 (**Figure 2-4D**). In general, the primary influence from the types of functional group should be the different steric hindrance effects in disrupting the packing structure (**Figure 2-5D**). Expectedly, PEG2000 as the bulkiest group results in the most substantial decrease in mobility. Moreover, it is observed that the functionalization overall leads to increased surface roughness of the deposited thin film as compared to C10-10a (**Figure 2-5E**), which could be another factor causing the slight decrease of mobilities. Overall, benefiting from the minimal influence on the polymerization efficacy and the tunability of the side-chain structure, the functionalization to conjugated polymers using the CLIP method can largely preserve the electrical performance.

To demonstrate the unprecedented synthesis capability given by the CLIP strategy, we made an experimental comparison to the use of the conventional pre-polymerization functionalization approach for the synthesis of the 10PEG2000 polymer, in which the PEG2000 unit is first grafted onto the DPP monomers prior to the polymerization (**Figure 2-6A**). With such a functionalized monomer, the obtained polymer from the same Stille-coupling reaction indeed has a much lower molecular weight, together with a very low mobility around 0.001 $cm^2 V^{-1} s^{-1}$ (**Figure 2-6, B and C**), which should come from the substantial decrease of the reactivity of the functionalized DPP monomer as a result of the substitution of such a bulky and polar group. This comparison clearly shows that the CLIP method provides the unparalleled capability in functionalizing conjugated polymers without affecting the synthesis outcomes.

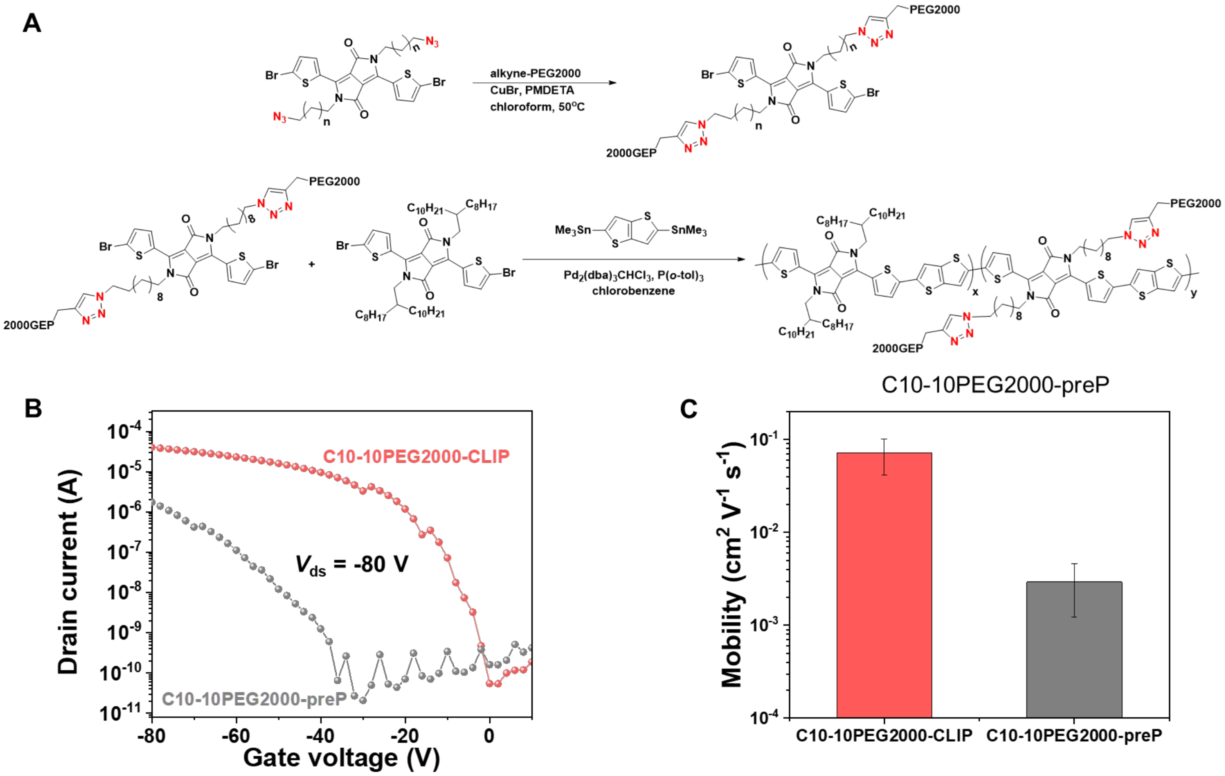

Figure 2-6. Comparison of pre-polymerization synthesis and the CLIP synthesis for C10-10PEG2000 polymer. (A) Synthesis scheme for the pre-polymerization process. (B) Transfer curves from the TFT devices made from these two polymers, which are labeled as C10-10PEG2000-preP, and C10-10PEG2000-CLIP. (C) Comparison of the mobilities from both methods.

On the other hand, for surface functionalization with PEG2000, the measurement of its charge-carrier mobility in OTFTs indeed proves that such surface functionalization causes negligible influence on the electrical performance (**Figure 2-7**), so that the mobility is almost one order of magnitude higher than that from its bulk-functionalized counterpart.

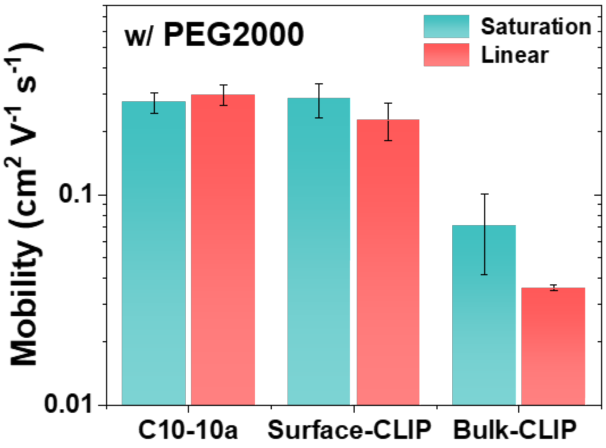

Figure 2-7. OFET characterization comparing surface-functionalized and bulk-functionalized conjugated polymers with PEG2000.

2.3.3 Direct photopatterning with benzophenone group

Among the four types of functional units incorporated in this work, the benzophenone group can enable interchain crosslinking (**Figure 2-8A**) for the functionalized conjugated polymer through the photo-initiated reaction with an adjacently-located C-H bond[44] (**Figure 2-8B**) under mild-UV (365 nm) exposure. This will impart solvent resistance to pre-annealed (at 140 °C for 30 min) 10BP films when the UV exposure time is longer than 5 minutes (under the 365-nm wavelength and 2.6-mW/cm^2 intensity), as verified by the immersion test in chloroform (**Figure 2-8C**). This could thus enable one-step direct photolithography for the patterning of the conjugated polymer film, by using a photomask to limit the UV exposure to selected areas. As conjugated polymers are generally not compatible with the solvents of normal photoresists and developers, their patterning into small feature sizes has been one of the major challenges for using them to fabricate functional circuits. Among all the potential options, the direct photo-patterning through imparting a conjugated polymer with photo-crosslinkable property is the most ideal choice for the simplicity in fabrication. So far, the very few reports about the direct photo-patterning of a semiconducting polymer are through the use of azide crosslinking reaction, by either blending an azide-containing crosslinker[45] (e.g., bis(fluorophenyl azide)) or attaching the azide group onto the polymer side chain[46,47]. However, since the azide crosslinking chemistry requires the use of deep-UV light (i.e., with the wavelength of 254 nm) and a relatively high exposure dose, detrimental effects could be caused for conjugated polymers, as verified by the UV-exposure experiment on our C10-10a polymer that also has the azide group. Alternatively, the benzophenone photo-crosslinking chemistry that is incorporated to conjugated polymers for the first time should be more benign for preserving the electrical performance after the direct photo-patterning.

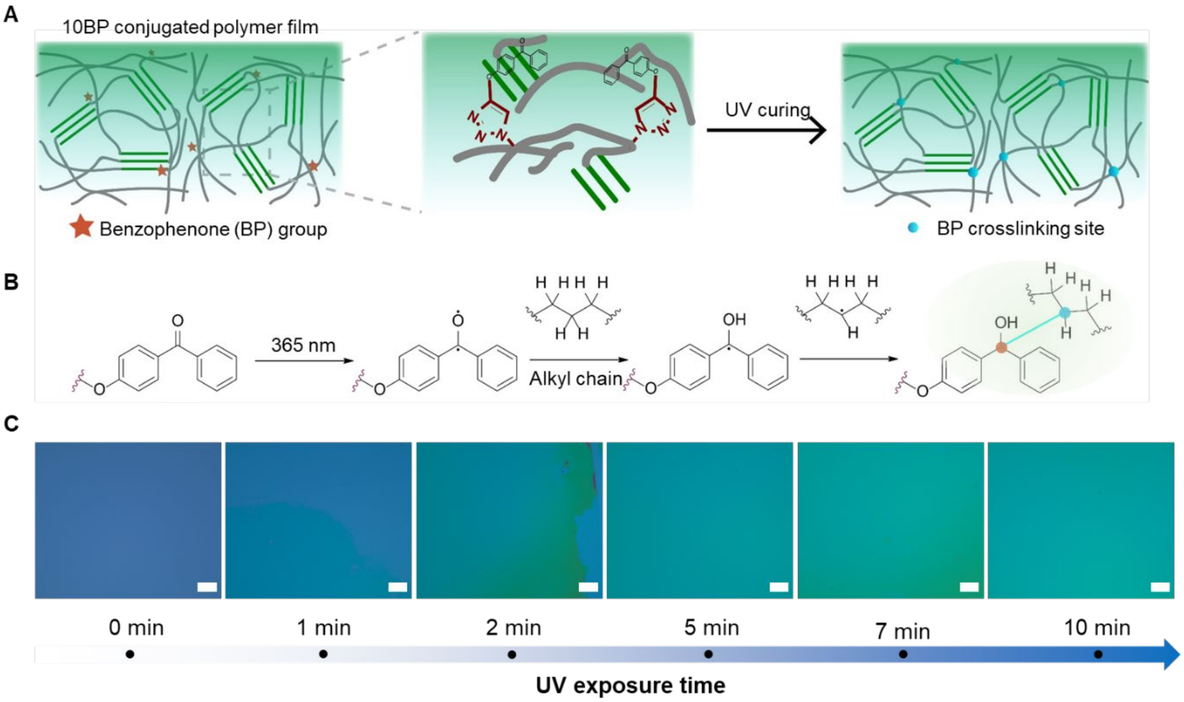

Figure 2-8. Study of direct photo-patterning of 10BP conjugated polymer films. (A) Schematic illustration of the UV photo-crosslinking process (365 nm) for conjugated polymer with benzophenone group. (B) Proposed photo-initiated interchain crosslinking reaction of the benzophenone group. (C) Chloroform-immersion test of C10-10BP films after the UV exposure

with varied time lengths. Before the UV exposure, the films are first annealed at 140 °C for 30 minutes. Scale bar: 500 μm.

We then carried out a systematic study of the crosslinking conditions to realize the full preservation of electrical performance from 10BP films after the direct photolithography process (**Figure 2-9A**). Through testing varied UV exposure durations all followed by a post-bake step (at 170 °C for 30 min) to fully remove the development solvent (i.e., chloroform) from the film, we found that a UV exposure time equal or longer than 10 min can ensure the full preservation of the charge-carrier mobility (**Figure 2-9B**) after the solvent removal of the unexposed areas. Consequently, the mobility of ~0.2 $cm^2\ V^{-1}\ s^{-1}$ is obtained from the patterned films of conjugated polymers. Under this photo-patterning condition, we further demonstrated the transfer of pre-designed patterns from masks to 10BP films through the one-step photolithographic process, which can indeed work well for complicated geometries and achieve a resolution below 10 μm (**Figure 2-9C**). It can be envisaged that this CLIP-based incorporation of benzophenone group can be adopted to other designs of conjugated polymers, so as to obtain photo-patternable polymer semiconductors with even higher mobility.

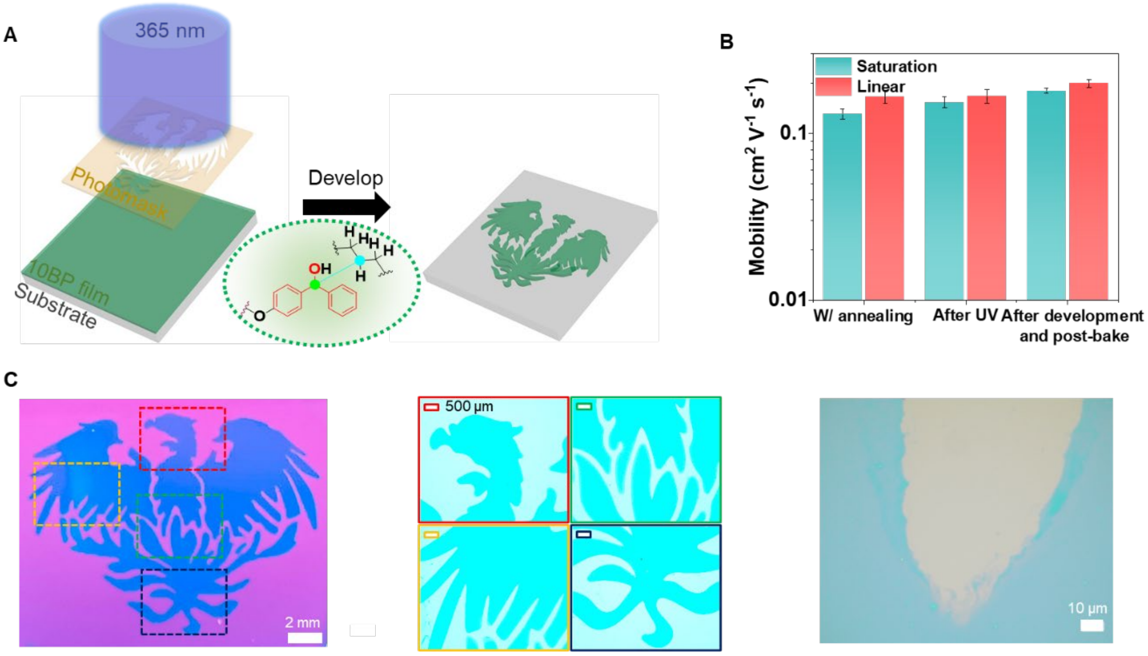

Figure 2-9. Direct photo-patterning of 10BP conjugated polymer films enabled by the CLIP functionalization of benzophenone group. (A) Photo-patterning schematics. (B) Charge-carrier mobility comparison of pre-annealed (at 140 ºC for 30 min), UV-exposed (365 nm, 2.6 mW/cm^2, for 10 minutes), and after chloroform development and post-bake (at 170 ºC for 30 min). The error bars represent the standard deviation obtained from at least six measurements. (C) Optical microscopy images of photo-patterned 10BP films.

2.3.4 Biochemical sensing with NHS ester group

The NHS ester, another group that gets functionalized onto conjugated polymers using the CLIP method, can serve to impart conjugated polymers with selective sensing to targeted biomolecules, through having the bio-conjugation reaction with the primary amine group in protein/polypeptide-type bioreceptors. Since biochemical sensing is one of the major approaches for health monitoring and disease diagnosis, imparting such functions to conjugated polymers is highly desirable for their use in human-integrated electronics. So far, although there have been a few examples of using conjugated polymers as the channel layer in transistor-type sensors that can uniquely offer built-in amplifications for achieving higher sensitivity, the specificity was imparted by either non-covalent physical absorption method[16], which lacks the long-term robustness; or through complicated surface treatment methods[48,49] such as templating and plasma deposition, which are only applicable to a narrow range of bioreceptors.

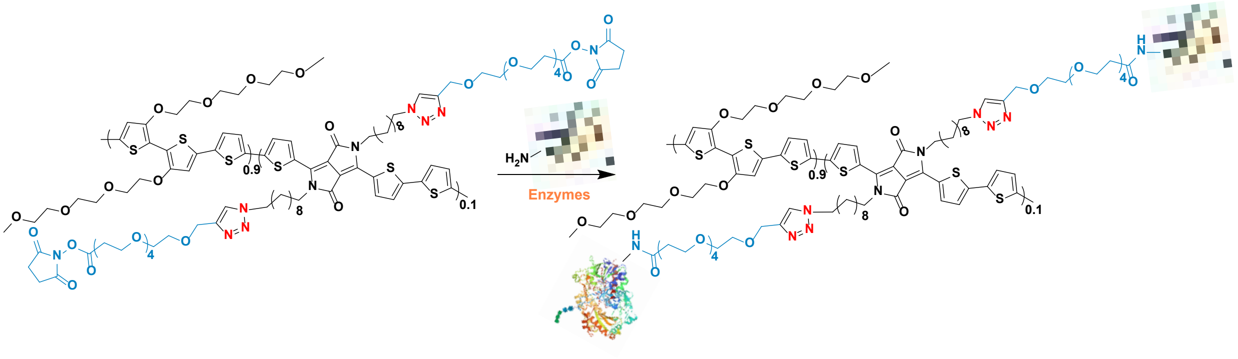

Figure 2-10. Reaction scheme of the covalent bioconjugation of glucose oxidase (GO) enzyme on g2T-NHS polymer.

To demonstrate this biochemical sensing function offered by the functionalized NHS ester group, we chose to immobilize the glucose oxidase (GO) enzyme as the bioreceptor for the sensing of glucose. Recently, based on the mixed electronic-ionic conducting property of conjugated polymers, organic electrochemical transistors (OECTs) have been developed as a very promising device platform for biosensing, which can provide even higher amplification to sensing signals than normal field-effect transistors[50-52]. In order to adopt the functionalization of NHS ester group to conjugated polymers for OECT operations, we copolymerized the azide-attached DPP monomer with the glycolated 2,2’-bithiophene (g2T) monomer[36,53], in the ratio of 1 to 9 (**Figure 2-10**), so as to achieve the desired ionization potential and aqueous-swelling property for OECT operation. Using this polymer, namely g2T-NHS, the glucose sensor was fabricated (**Figure 2-11A**) through first depositing the semiconducting film onto patterned gold source/drain electrodes on a glass substrate, and then treating the channel area with the solution of GO enzyme for 2 hours to achieve the covalent immobilization of this bioreceptor. The gating is made with the extended configuration of having another piece of gold film on the side of the channel, which gets bridged to the channel by the added analyte solution. When there is glucose in the solution, its oxidation under the catalysis of the GO enzyme will transfer electrons to the channel layer, thus de-doping the p-type conjugated polymer[16] (**Figure 2-11A**, right).

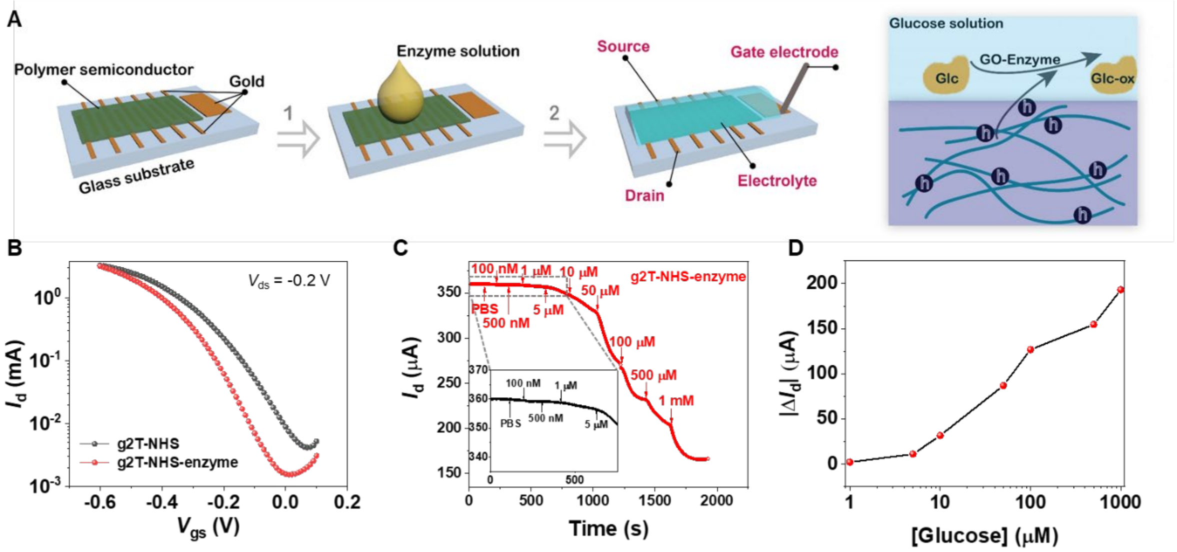

Figure 2-11. Biochemical sensing to glucose from conjugated polymers enabled by covalent grafting of enzymatic bioreceptors. (A) Fabrication process of the enzymatic sensor based on OECT device design, and the recognition mechanism to glucose at the surface of the GO enzyme-modified channel layer (right). Glc: glucose; Glc-ox, glucono-1,5 lactone. (B) Transfer curves from the OECT sensor devices with GO-enzyme-modified g2T-NHS (labeled as g2T-NHS-enzyme) and pristine g2T-NHS as the channel layer, respectively. (C) Real-time current response (V_{gs} = -0.2 V, V_{ds} = -0.05 V) of an as-fabricated glucose sensor with g2T-NHS-enzyme to the stepwise

addition of glucose in different concentrations. (D) Drain current ($|\Delta I_d|$) response to glucose concentrations in the range of 1 μM to 1000 μM.

As shown in **Figure 2-11B**, the enzyme immobilization on the semiconducting channel only causes small shift to the threshold voltage of the OECT operation in phosphate-buffered saline (PBS) solution. The sensing performance to glucose was characterized by adding glucose in controlled concentrations into the PBS solution. When the concentration of the added glucose was equal to or greater than 1 μM, a stepwise decrease of the current was observed (**Figure 2-11C**). The extent of the current decrease exhibits good correlation with the added glucose concentration (**Figure 2-11D**). In contrast, when only the PBS solution was added, there was no change in the current, suggesting the specificity to glucose as afforded by the enzyme. As a control, the device made from the pristine NHS-functionalized semiconducting film showed no response to glucose, which verifies that the sensing function is indeed afforded by the GO enzyme. Since the conjugation chemistry to the NHS ester group has broad applicability to other types of protein or polypeptide based bioreceptors (including both enzymes and antibodies), this material design and synthesis concept based on the CLIP method opens up the avenue of covalently functionalizing bioreceptors on mechanically soft, potentially stretchable, conjugated polymers for realizing biochemical sensing at bio-interfaces with specificity and biocompatibility.

2.4 Conclusion

In summary, we established a new synthesis strategy, the CLIP method, for largely expanding the synthesizable molecular designs of conjugated polymer, towards incorporating a wide range of emerging functions. Through enabling the use of a click reaction as a post-polymerization step for the functionalization of side chains, this CLIP method is shown to be facile and highly versatile for different functional units and for both bulk and surface functionalization. This method is successfully utilized to covalently graft four different types of functional groups onto the side chains of conjugated polymers, which, otherwise, are all highly challenging to be incorporated. Two of the developed polymers are further taken to realize two highly desirable functions on conjugated polymers: direct photo-patternability, and biochemical sensing with specificity. Additional functionalities that can be incorporated by the approach can become highly valuable topics for future investigations on the expanded uses of conjugated polymers. Through innovative incorporation of click chemistry to the design and synthesis paradigm of high-performance conjugated polymers, we anticipate that this synthesis strategy will greatly enlarge the molecular design space and thus enrich the functional properties of conjugated polymers. This will satisfy the need of their developments towards the far-reaching application area of human-integrated electronics.

2.5 Appendix

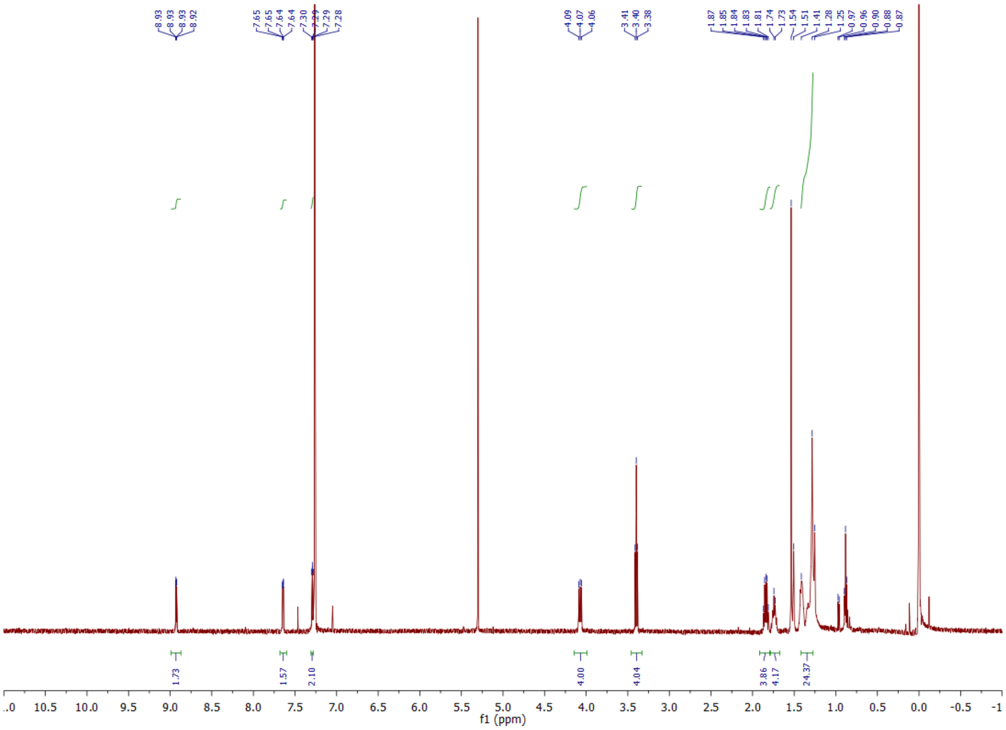

Figure 2-12. ^{1}H NMR spectrum of compound 2

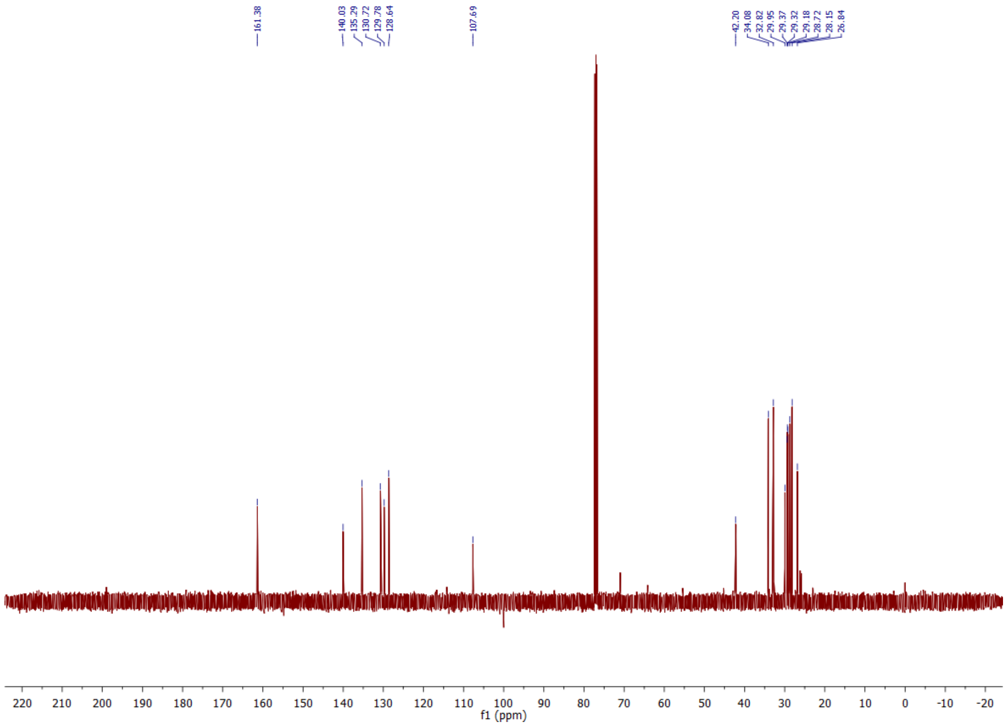

Figure 2-13. ^{13}C NMR spectrum of compound 2

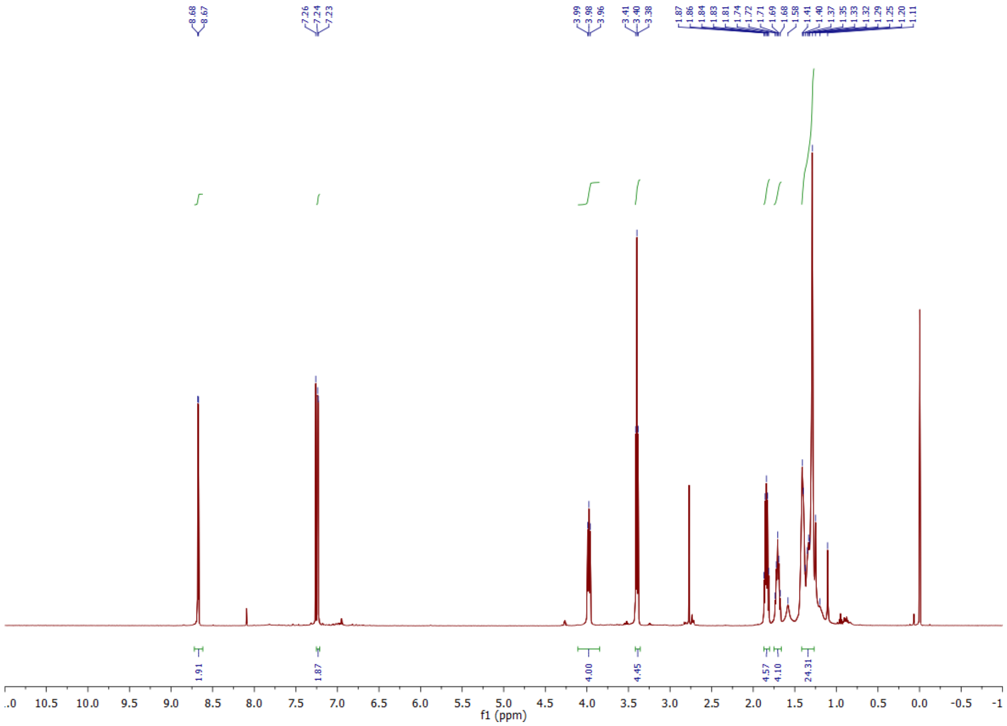

Figure 2-14. ^{1}H NMR spectrum of compound 3

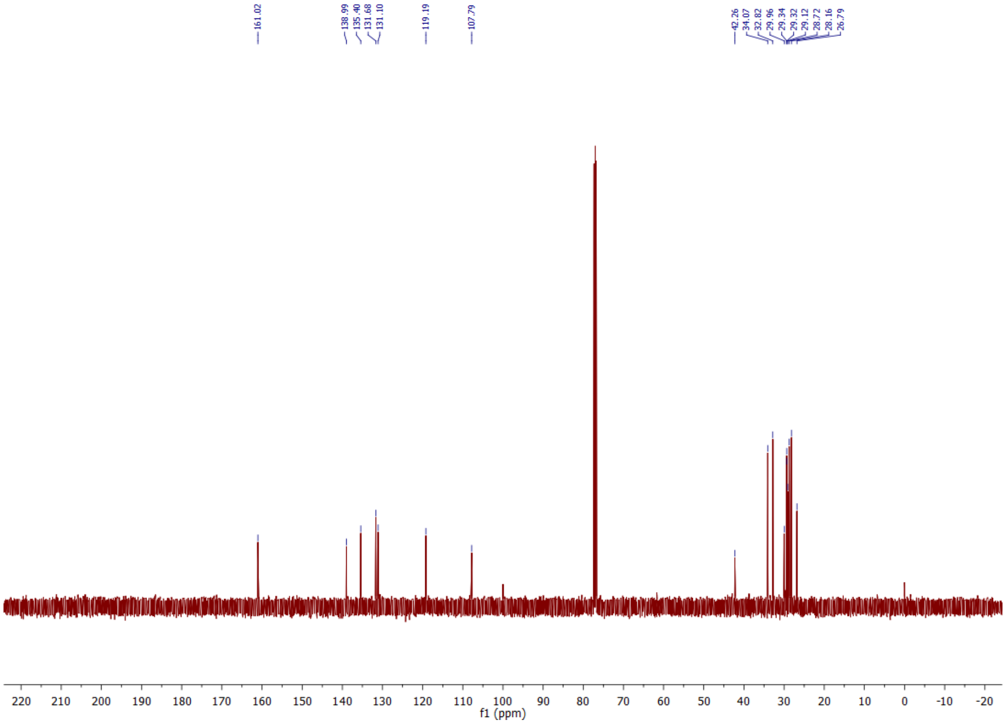

Figure 2-15. ^{13}C NMR spectrum of compound 3

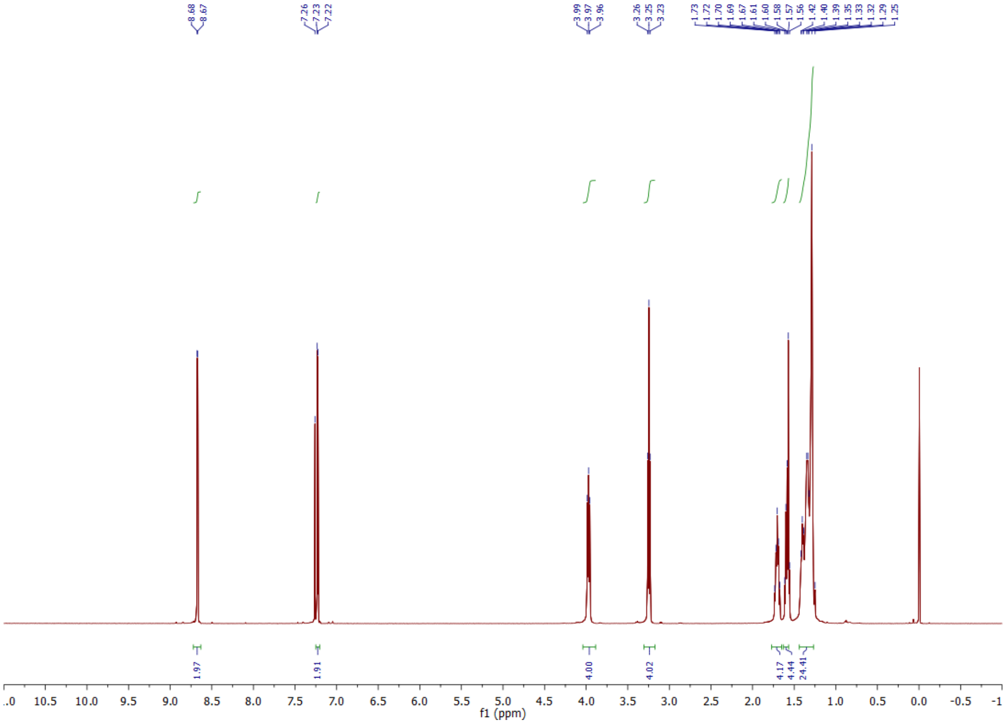

Figure 2-16. ^{1}H NMR spectrum of compound 4, n = 8

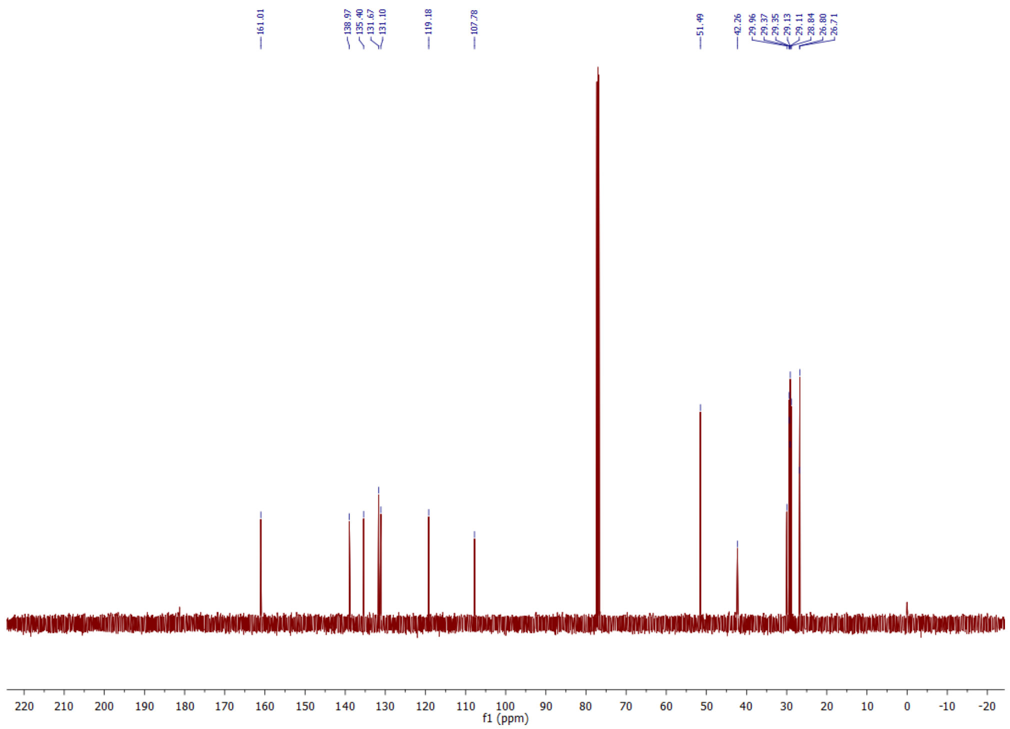

Figure 2-17. ^{13}C NMR spectrum of compound 4, n = 8

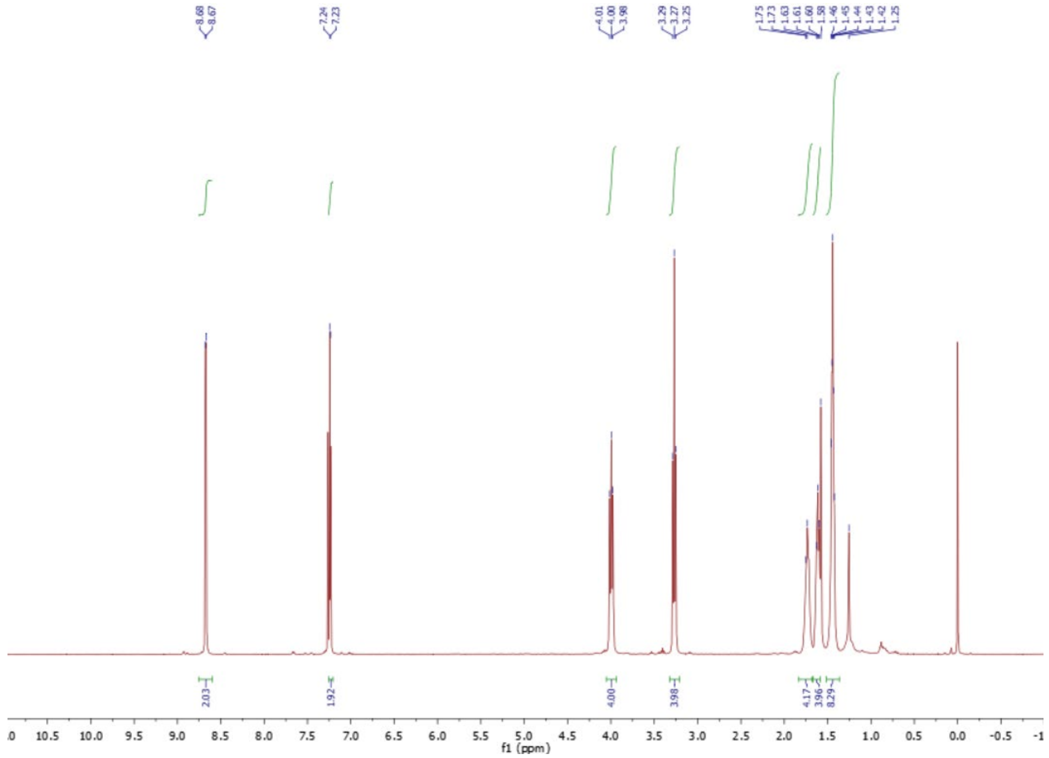

Figure 2-18. ^{1}H NMR spectrum of compound 4, n = 4

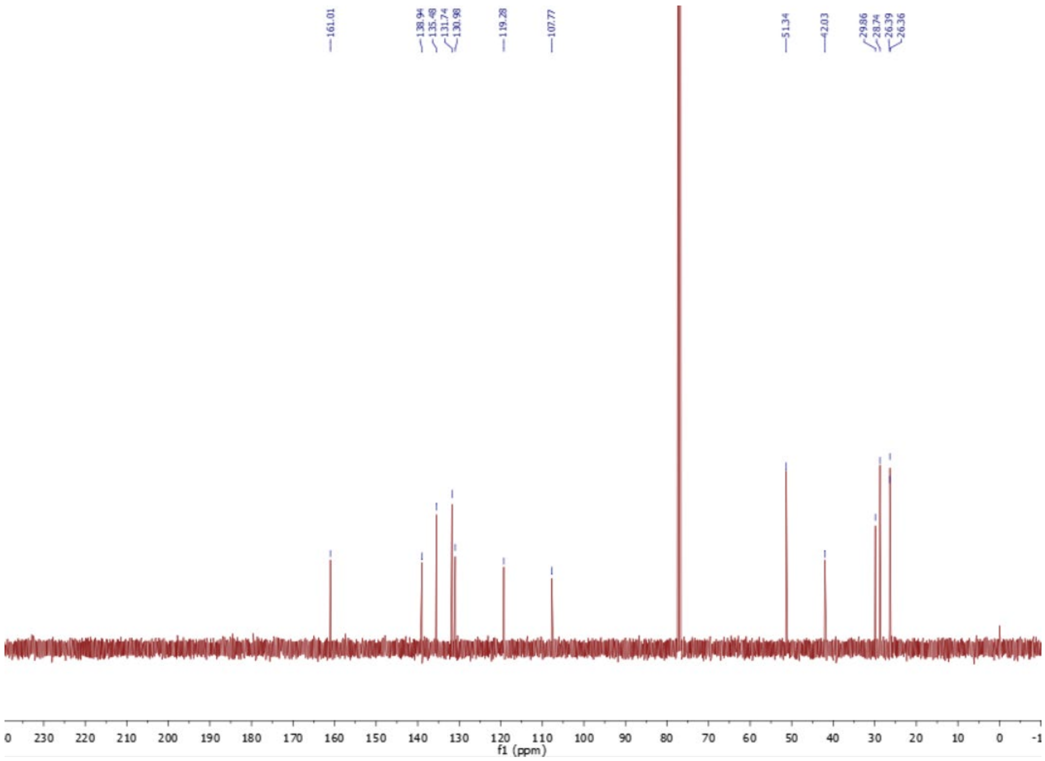

Figure 2-19. ^{13}C NMR spectrum of compound 4, n = 4

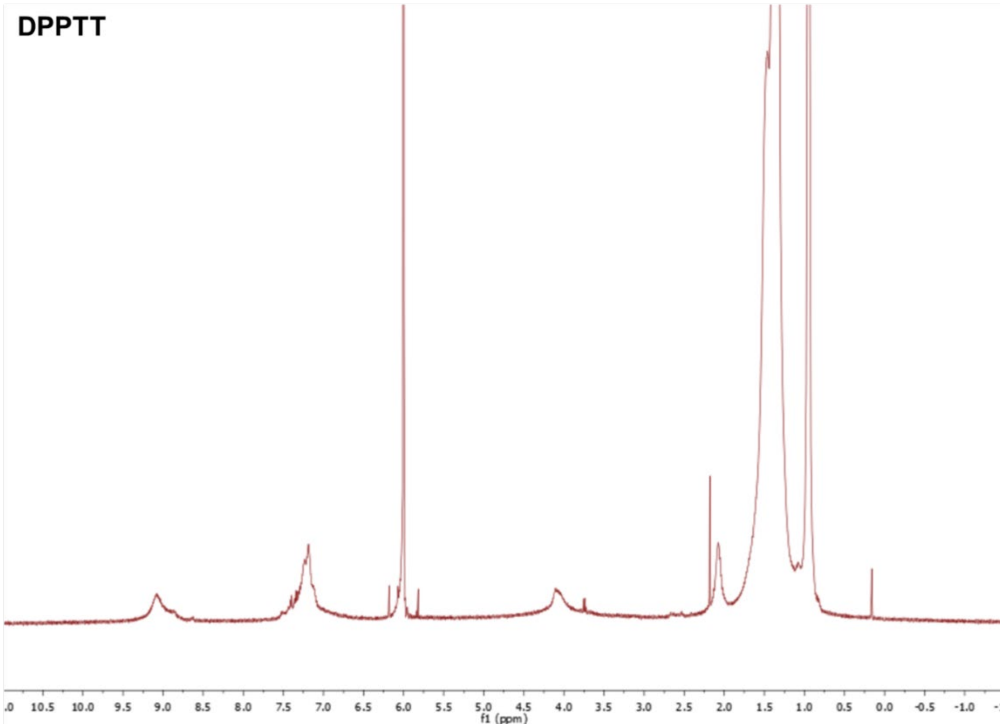

Figure 2-20. ^{1}H NMR spectrum of polymer DPPTT

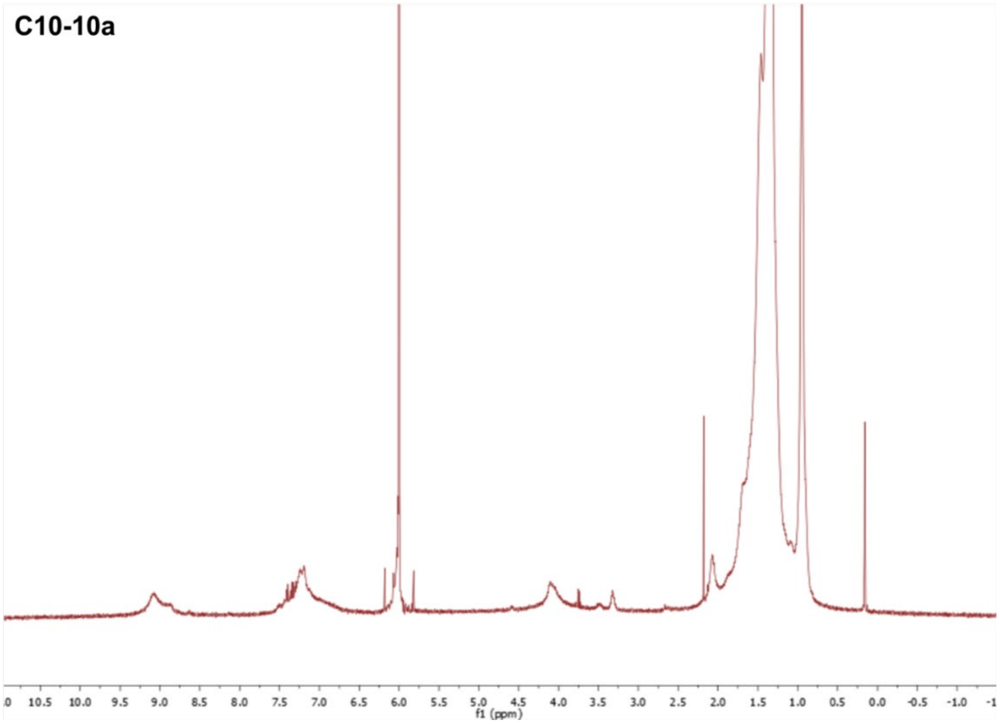

Figure 2-21. ^{1}H NMR spectrum of polymer C10-10a

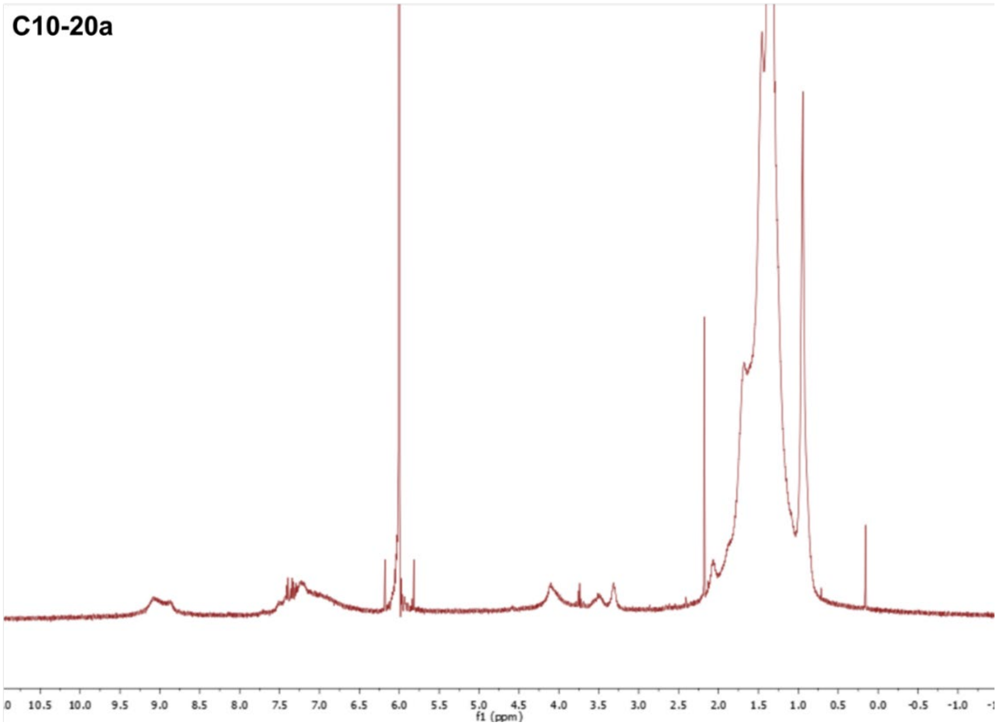

Figure 2-22. ^{1}H NMR spectrum of polymer C10-20a

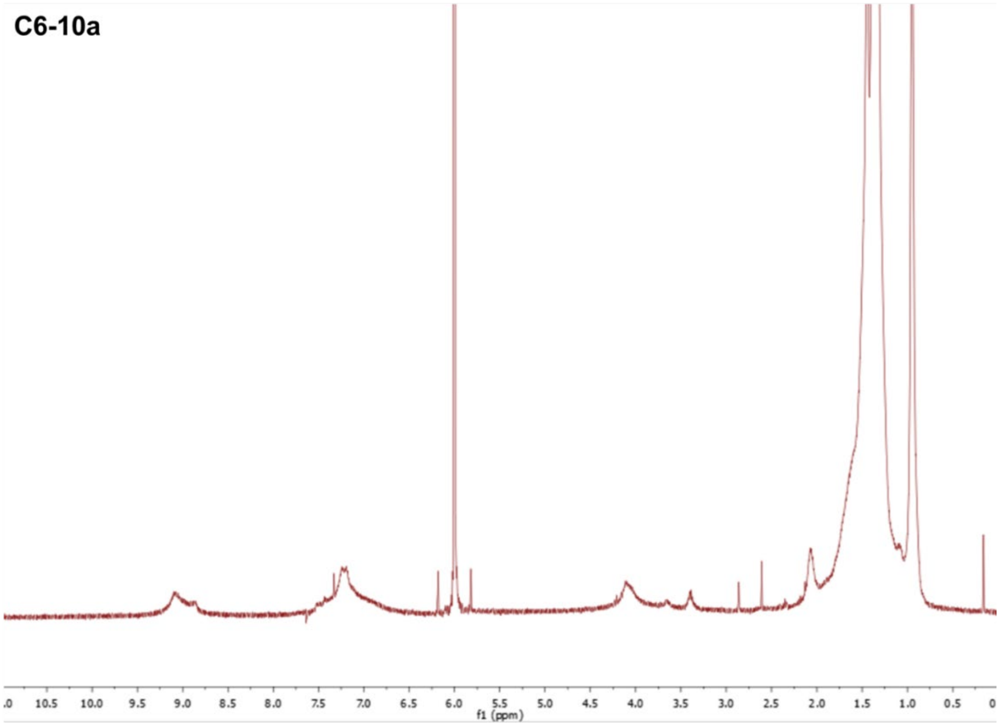

Figure 2-23. ^{1}H NMR spectrum of polymer C6-10a

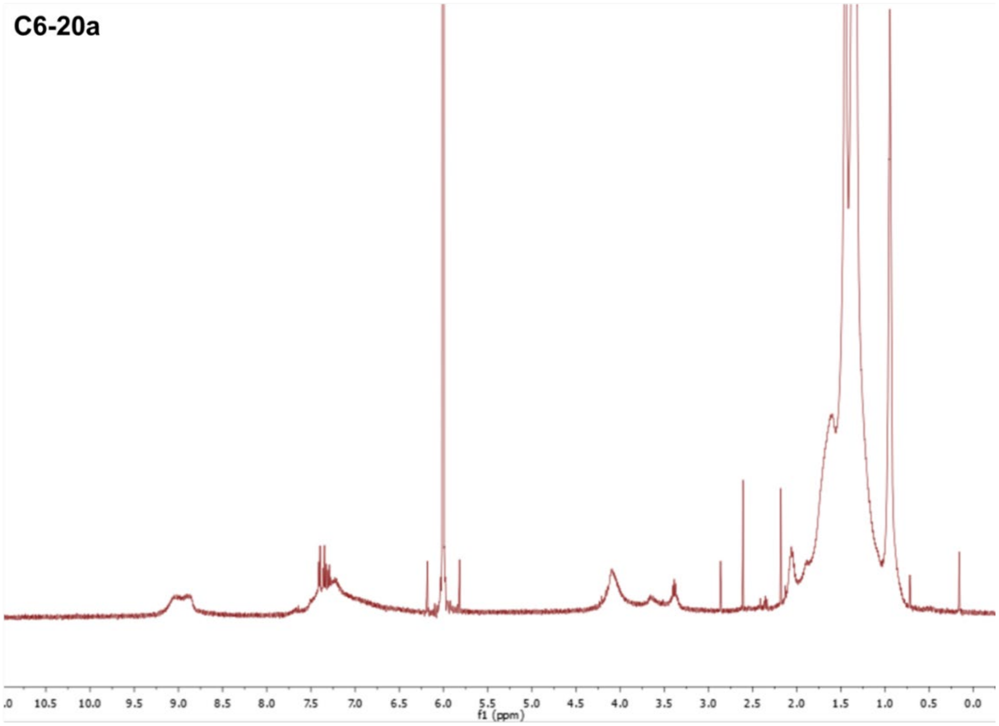

Figure 2-24. ^{1}H NMR spectrum of polymer C6-20a

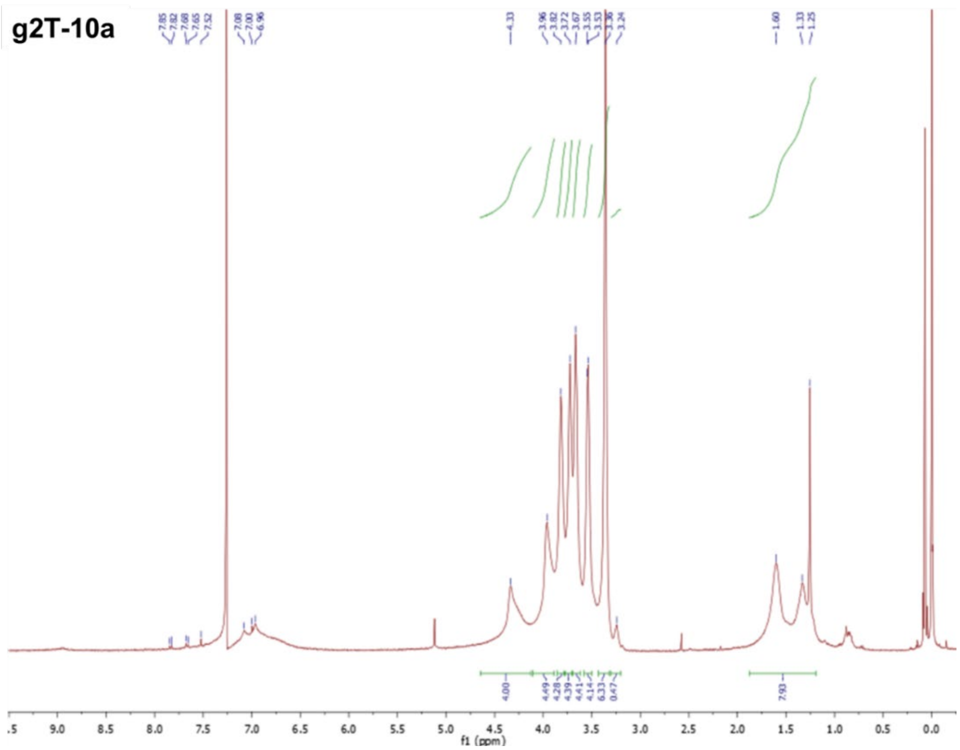

Figure 2-25. ^{1}H NMR spectrum of polymer g2T-10a

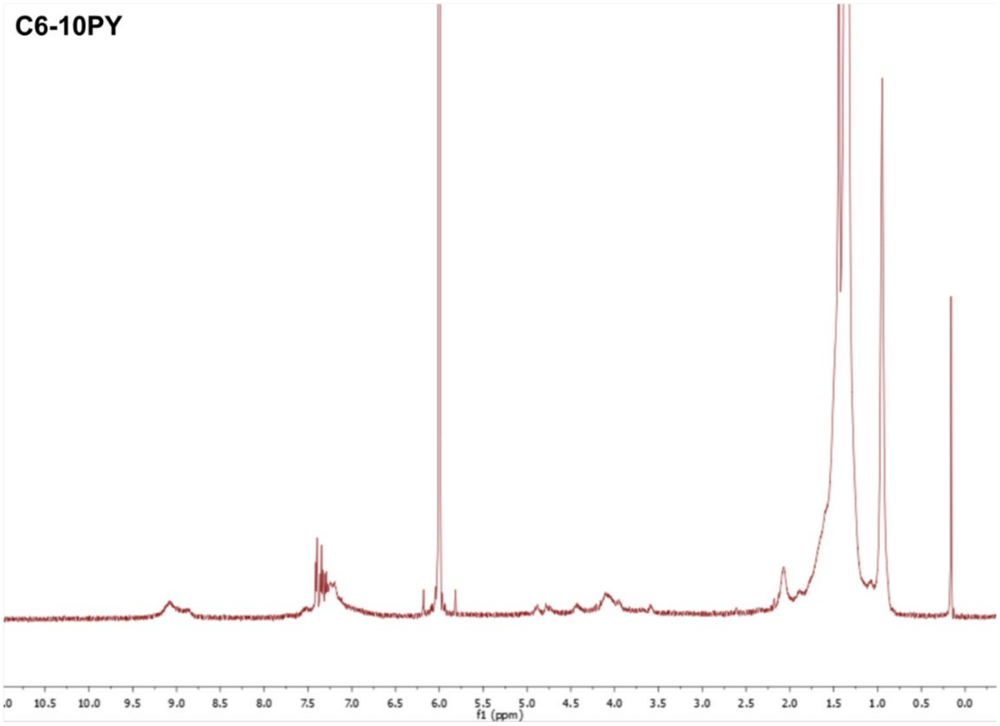

Figure 2-26. ^{1}H NMR spectrum of polymer C6-10PY

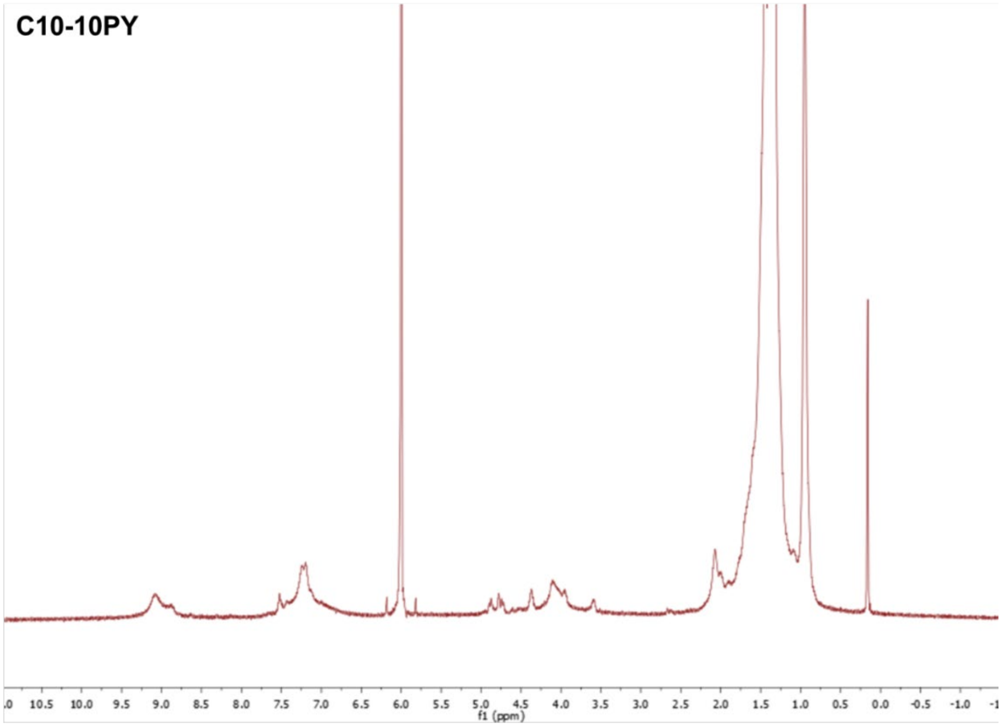

Figure 2-27. ^{1}H NMR spectrum of polymer C10-10PY

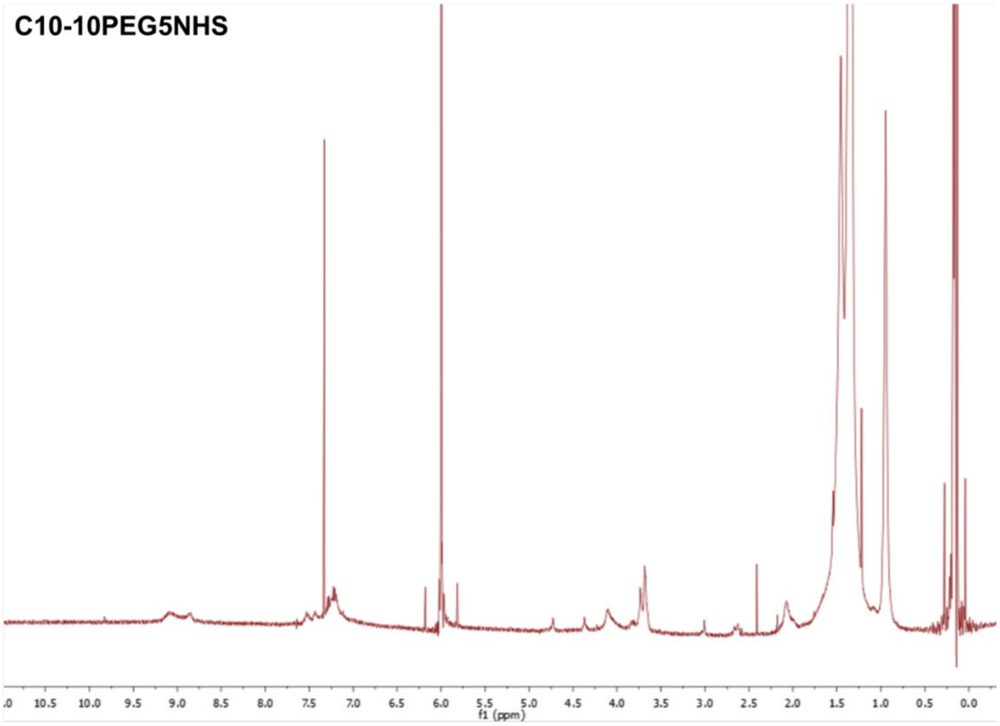

Figure 2-28. ^{1}H NMR spectrum of polymer C10-10PEG5NHS

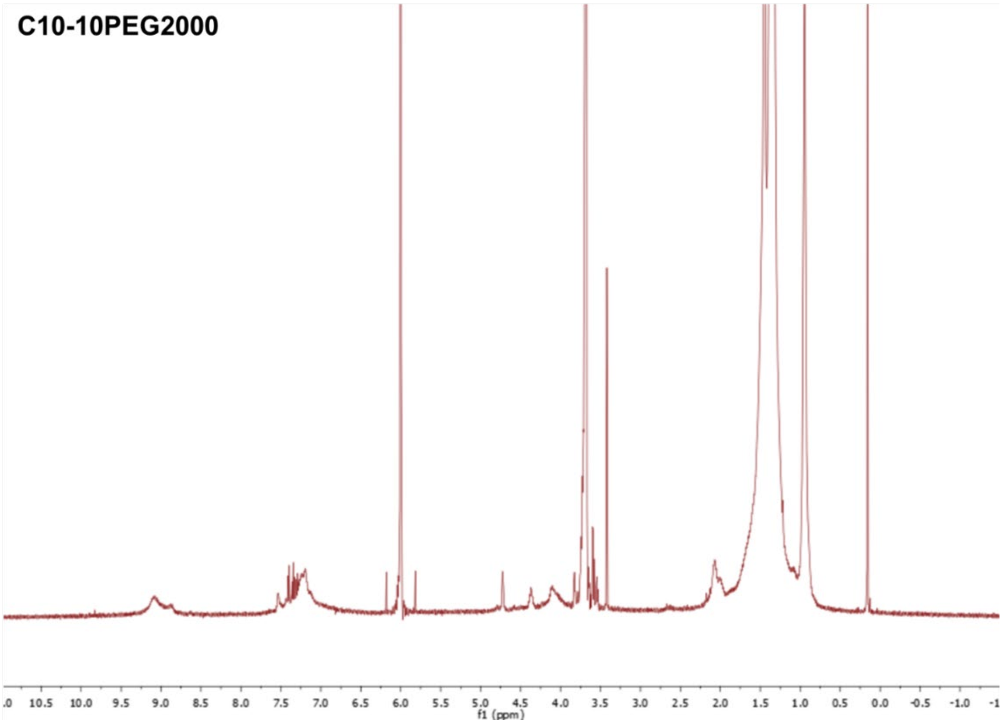

Figure 2-29. ^{1}H NMR spectrum of polymer C10-10PEG2000

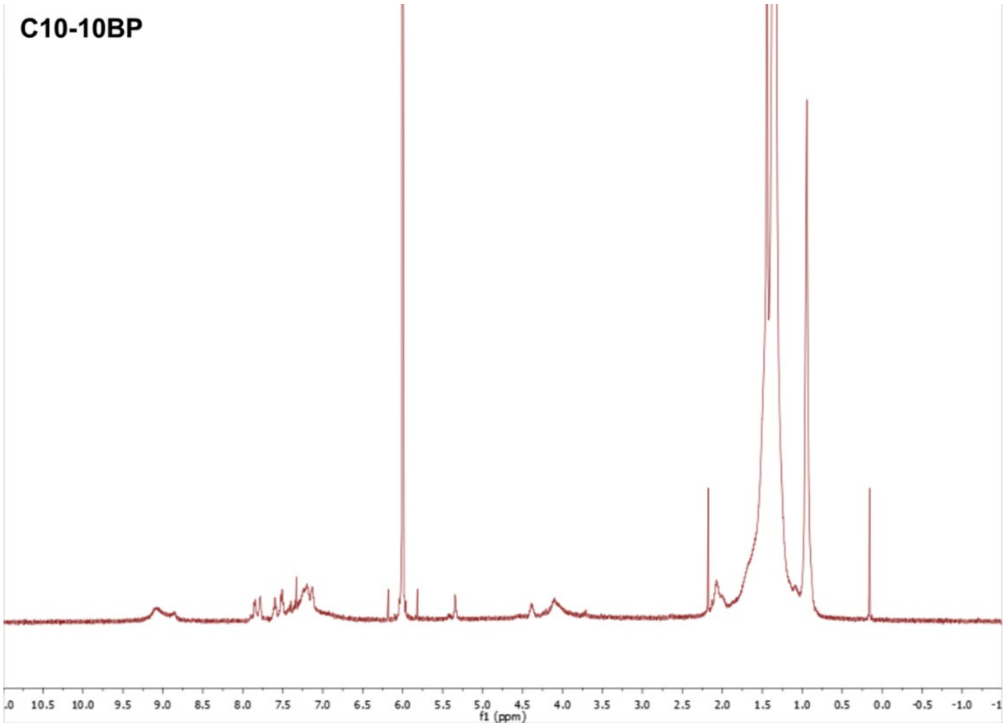

Figure 2-30. ^{1}H NMR spectrum of polymer C10-10BP

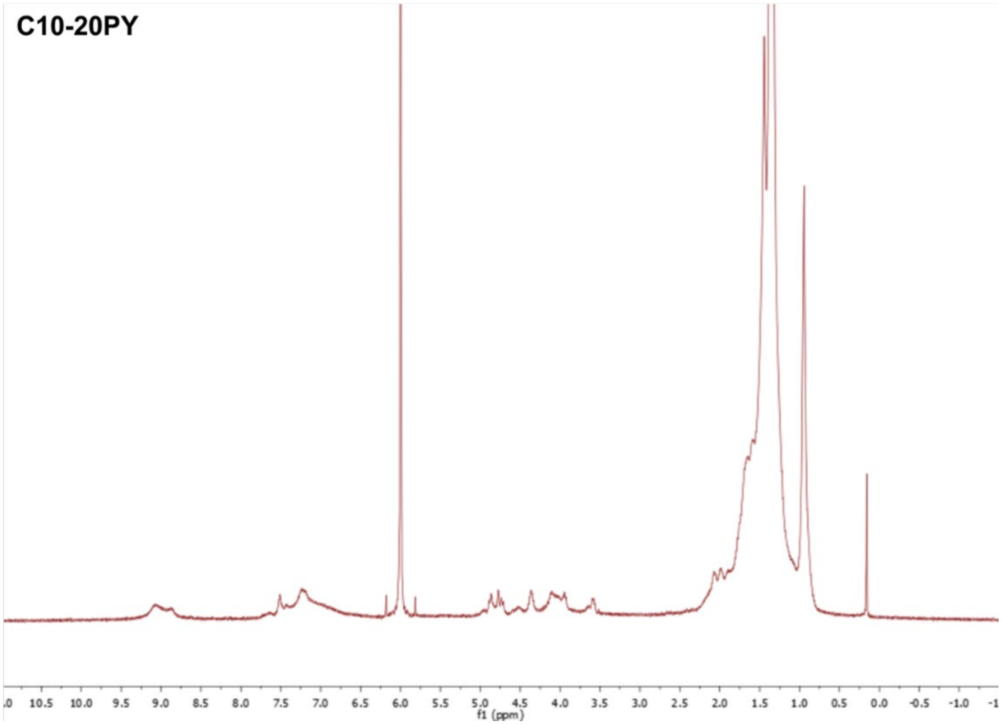

Figure 2-31. ^{1}H NMR spectrum of polymer C10-20PY

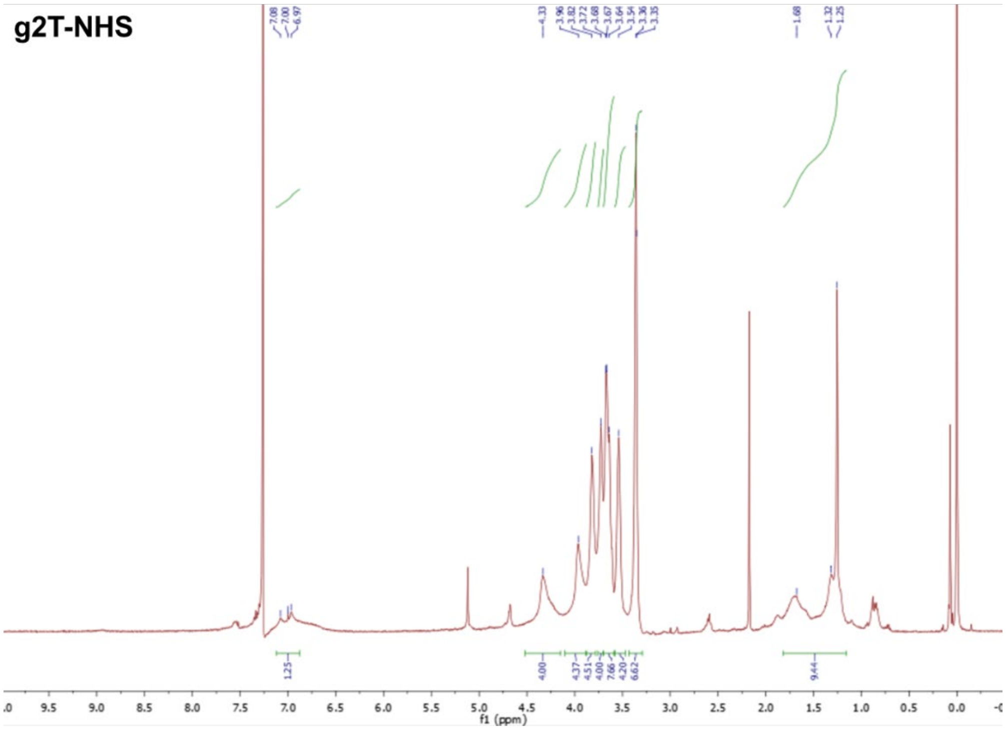

Figure 2-32. ^{1}H NMR spectrum of polymer g2T-NHS

2.6 References

(1) Someya, T.; Bao, Z.; Malliaras, G. G. The rise of plastic bioelectronics. *Nature* **2016,** *540*, 379.

(2) Xu, J.; Wang, S.; Wang, G.-J. N.; Zhu, C.; Luo, S.; Jin, L.; Gu, X.; Chen, S.; Feig, V. R.; To, J. W. F.et al. Highly stretchable polymer semiconductor films through the nanoconfinement effect. *Science* **2017,** *355*, 59.

(3) Wang, S.; Xu, J.; Wang, W.; Wang, G. N.; Rastak, R.; Molina-Lopez, F.; Chung, J. W.; Niu, S.; Feig, V. R.; Lopez, J.et al. Skin electronics from scalable fabrication of an intrinsically stretchable transistor array. *Nature* **2018,** *555*, 83.

(4) Wang, S.; Oh, J. Y.; Xu, J.; Tran, H.; Bao, Z. Skin-Inspired Electronics: An Emerging Paradigm. *Acc Chem Res* **2018,** *51*, 1033.

(5) You, I.; Kong, M.; Jeong, U. Block Copolymer Elastomers for Stretchable Electronics. *Accounts of chemical research* **2019,** *52*, 63.

(6) Khodagholy, D.; Gelinas, J. N.; Thesen, T.; Doyle, W.; Devinsky, O.; Malliaras, G. G.; Buzsaki, G. NeuroGrid: recording action potentials from the surface of the brain. *Nat. Neurosci.* **2015,** *18*, 310.

(7) Liu, Y.; Liu, J.; Chen, S.; Lei, T.; Kim, Y.; Niu, S.; Wang, H.; Wang, X.; Foudeh, A. M.; Tok, J. B. H.et al. Soft and elastic hydrogel-based microelectronics for localized low-voltage neuromodulation. *Nat. Biomed. Eng* **2019,** *3*, 58.

(8) Park, S.; Heo, S. W.; Lee, W.; Inoue, D.; Jiang, Z.; Yu, K.; Jinno, H.; Hashizume, D.; Sekino, M.; Yokota, T.et al. Self-powered ultra-flexible electronics via nano-grating-patterned organic photovoltaics. *Nature* **2018,** *561*, 516.

(9) Dorfman, K. D.; Adrahtas, D. Z.; Thomas, M. S.; Frisbie, C. D. Microfluidic opportunities in printed electrolyte-gated transistor biosensors. *Biomicrofluidics* **2020,** *14*, 011301.

(10) Du, W.; Ohayon, D.; Combe, C.; Mottier, L.; Maria, I. P.; Ashraf, R. S.; Fiumelli, H.; Inal, S.; McCulloch, I. Improving the Compatibility of Diketopyrrolopyrrole Semiconducting Polymers for Biological Interfacing by Lysine Attachment. *Chemistry of Materials* **2018,** *30*, 6164.

(11) Yang, Y.; Liu, Z.; Chen, L.; Yao, J.; Lin, G.; Zhang, X.; Zhang, G.; Zhang, D. Conjugated Semiconducting Polymer with Thymine Groups in the Side Chains: Charge Mobility Enhancement and Application for Selective Field-Effect Transistor Sensors toward CO and H2S. *Chem. Mater.* **2019,** *31*, 1800.

(12) Gasperini, A.; Wang, G.-J. N.; Molina-Lopez, F.; Wu, H.-C.; Lopez, J.; Xu, J.; Luo, S.; Zhou, D.; Xue, G.; Tok, J. B. H.et al. Characterization of Hydrogen Bonding Formation and Breaking in Semiconducting Polymers under Mechanical Strain. *Macromolecules* **2019,** *52*, 2476.

(13) Lin, Y. C.; Chen, C. K.; Chiang, Y. C.; Hung, C. C.; Fu, M. C.; Inagaki, S.; Chueh, C. C.; Higashihara, T.; Chen, W. C. Study on Intrinsic Stretchability of Diketopyrrolopyrrole-Based pi-Conjugated Copolymers with Poly(acryl amide) Side Chains for Organic Field-Effect Transistors. *ACS Appl Mater Interfaces* **2020,** *12*, 33014.

(14) Yang, Y.; Liu, Z.; Zhang, G.; Zhang, X.; Zhang, D. The Effects of Side Chains on the Charge Mobilities and Functionalities of Semiconducting Conjugated Polymers beyond Solubilities. *Adv. Mater.* **2019,** *31*, e1903104.

(15) Tian, J.; Fu, L.; Liu, Z.; Geng, H.; Sun, Y.; Lin, G.; Zhang, X.; Zhang, G.; Zhang, D. Optically Tunable Field Effect Transistors with Conjugated Polymer Entailing Azobenzene Groups in the Side Chains. *Adv. Funct. Mater.* **2019,** *29*, 1807176.

(16) Pappa, A. M.; Ohayon, D.; Giovannitti, A.; Maria, I. P.; Savva, A.; Uguz, I.; Rivnay, J.; McCulloch, I.; Owens, R. M.; Inal, S. Direct metabolite detection with an n-type accumulation mode organic electrochemical transistor. *Sci. Adv.* **2018,** *4*, eaat0911.

(17) Pappa, A.-M.; Inal, S.; Roy, K.; Zhang, Y.; Pitsalidis, C.; Hama, A.; Pas, J.; Malliaras, G. G.; Owens, R. M. Polyelectrolyte Layer-by-Layer Assembly on Organic Electrochemical Transistors. *ACS Applied Materials & Interfaces* **2017,** *9*, 10427.

(18) Shen, H.; Zou, Y.; Zang, Y.; Huang, D.; Jin, W.; Di, C.-a.; Zhu, D. Molecular antenna tailored organic thin-film transistors for sensing application. *Materials Horizons* **2018,** *5*, 240.

(19) Piro, B.; Wang, D.; Benaoudia, D.; Tibaldi, A.; Anquetin, G.; Noel, V.; Reisberg, S.; Mattana, G.; Jackson, B. Versatile transduction scheme based on electrolyte-gated organic field-effect transistor used as immunoassay readout system. *Biosens. Bioelectron.* **2017,** *92*, 215.

(20) Khan, H. U.; Roberts, M. E.; Johnson, O.; Forch, R.; Knoll, W.; Bao, Z. In situ, label-free DNA detection using organic transistor sensors. *Adv. Mater.* **2010,** *22*, 4452.

(21) Wang, Y.; Gong, Q.; Miao, Q. Structured and functionalized organic semiconductors for chemical and biological sensors based on organic field effect transistors. *Materials Chemistry Frontiers* **2020,** *4*, 3505.

(22) Yang, J.; Zhao, Z.; Wang, S.; Guo, Y.; Liu, Y. Insight into High-Performance Conjugated Polymers for Organic Field-Effect Transistors. *Chem* **2018,** *4*, 2748.

(23) Pickens, C. J.; Johnson, S. N.; Pressnall, M. M.; Leon, M. A.; Berkland, C. J. Practical Considerations, Challenges, and Limitations of Bioconjugation via Azide-Alkyne Cycloaddition. *Bioconjug. Chem.* **2018,** *29*, 686.

(24) Tang, W.; Becker, M. L. "Click" reactions: a versatile toolbox for the synthesis of peptide-conjugates. *Chem. Soc. Rev.* **2014,** *43*, 7013.

(25) Zhang, Y.; Park, A. M.; McMillan, S. R.; Harmon, N. J.; Flatté, M. E.; Fuchs, G. D.; Ober, C. K. Charge Transport in Conjugated Polymers with Pendent Stable Radical Groups. *Chem. Mater.* **2018,** *30*, 4799.

(26) Chan, E. W. C.; Baek, P.; Barker, D.; Travas-Sejdic, J. Highly functionalisable polythiophene phenylenes. *Polymer Chemistry* **2015,** *6*, 7618.

(27) Hsu, L.-C.; Kobayashi, S.; Isono, T.; Chiang, Y.-C.; Ree, B. J.; Satoh, T.; Chen, W.-C. Highly Stretchable Semiconducting Polymers for Field-Effect Transistors through Branched Soft–Hard–Soft Type Triblock Copolymers. *Macromolecules* **2020,** *53*, 7496.

(28) Bunz, U. Adventures of an Occasional Click Chemist. *Synlett* **2013,** *24*, 1899.

(29) Dorman, G.; Prestwich, G. D. Benzophenone Photophores in Biochemistry. *Biochemistry* **1994,** *33*, 5661.

(30) Koniev, O.; Wagner, A. Developments and recent advancements in the field of endogenous amino acid selective bond forming reactions for bioconjugation. *Chem. Soc. Rev.* **2015,** *44*, 5495.

(31) Vegas, A. J.; Veiseh, O.; Doloff, J. C.; Ma, M.; Tam, H. H.; Bratlie, K.; Li, J.; Bader, A. R.; Langan, E.; Olejnik, K.et al. Combinatorial hydrogel library enables identification of materials that mitigate the foreign body response in primates. *Nat Biotechnol* **2016,** *34*, 345.

(32) Zhang, H.; Li, C.; Piszcz, M.; Coya, E.; Rojo, T.; Rodriguez-Martinez, L. M.; Armand, M.; Zhou, Z. Single lithium-ion conducting solid polymer electrolytes: advances and perspectives. *Chem. Soc. Rev.* **2017,** *46*, 797.

(33) Jiang, Z.; Li, X.; Strzalka, J.; Sprung, M.; Sun, T.; Sandy, A. R.; Narayanan, S.; Lee, D. R.; Wang, J. The dedicated high-resolution grazing-incidence X-ray scattering beamline 8-ID-E at the Advanced Photon Source. *J Synchrotron Radiat* **2012,** *19*, 627.

(34) Jiang, Z. GIXSGUI: a MATLAB toolbox for grazing-incidence X-ray scattering data visualization and reduction, and indexing of buried three-dimensional periodic nanostructured films. *J. Appl. Crystallogr.* **2015,** *48*, 917.

(35) Chortos, A.; Lim, J.; To, J. W.; Vosgueritchian, M.; Dusseault, T. J.; Kim, T. H.; Hwang, S.; Bao, Z. Highly stretchable transistors using a microcracked organic semiconductor. *Adv. Mater.* **2014,** *26*, 4253.

(36) Nielsen, C. B.; Giovannitti, A.; Sbircea, D. T.; Bandiello, E.; Niazi, M. R.; Hanifi, D. A.; Sessolo, M.; Amassian, A.; Malliaras, G. G.; Rivnay, J.et al. Molecular Design of Semiconducting Polymers for High-Performance Organic Electrochemical Transistors. *J Am Chem Soc* **2016,** *138*, 10252.

(37) Li, Z.; Hao, P.; Li, L.; Tan, C. Y.; Cheng, X.; Chen, G. Y.; Sze, S. K.; Shen, H. M.; Yao, S. Q. Design and synthesis of minimalist terminal alkyne-containing diazirine photo-crosslinkers and their incorporation into kinase inhibitors for cell- and tissue-based proteome profiling. *Angew. Chem. Int. Ed. Engl.* **2013,** *52*, 8551.

(38) Spicer, C. D.; Davis, B. G. Selective chemical protein modification. *Nat Commun* **2014,** *5*, 4740.

(39) Parker, C. G.; Pratt, M. R. Click Chemistry in Proteomic Investigations. *Cell* **2020,** *180*, 605.

(40) Li, N. S.; Gossai, N. P.; Naumann, J. A.; Gordon, P. M.; Piccirilli, J. A. Efficient Synthetic Approach to Linear Dasatinib-DNA Conjugates by Click Chemistry. *Bioconjug. Chem.* **2016,** *27*, 2575.

(41) Fantoni, N. Z.; El-Sagheer, A. H.; Brown, T. A Hitchhiker's Guide to Click-Chemistry with Nucleic Acids. *Chem. Rev.* **2021**, DOI:10.1021/acs.chemrev.0c00928 10.1021/acs.chemrev.0c00928.

(42) Pei, D.; Wang, Z.; Peng, Z.; Zhang, J.; Deng, Y.; Han, Y.; Ye, L.; Geng, Y. Impact of Molecular Weight on the Mechanical and Electrical Properties of a High-Mobility Diketopyrrolopyrrole-Based Conjugated Polymer. *Macromolecules* **2020,** *53*, 4490.

(43) Niu, W.; Wu, H.-C.; Matthews, J. R.; Tandia, A.; Li, Y.; Wallace, A. L.; Kim, J.; Wang, H.; Li, X.; Mehrotra, K.et al. Synthesis and Properties of Soluble Fused Thiophene Diketopyrrolopyrrole-Based Polymers with Tunable Molecular Weight. *Macromolecules* **2018,** *51*, 9422.

(44) Prestwich, G. D. a. G. D. Benzophenone Photophores in Biochemisty. *Biochemistry* **1994**, DOI:10.1021/bi00185a001, 10.1021/bi00185a001,.

(45) Png, R. Q.; Chia, P. J.; Tang, J. C.; Liu, B.; Sivaramakrishnan, S.; Zhou, M.; Khong, S. H.; Chan, H. S.; Burroughes, J. H.; Chua, L. L.et al. High-performance polymer semiconducting heterostructure devices by nitrene-mediated photocrosslinking of alkyl side chains. *Nat Mater* **2010,** *9*, 152.

(46) Kim, H. J.; Han, A. R.; Cho, C.-H.; Kang, H.; Cho, H.-H.; Lee, M. Y.; Fréchet, J. M. J.; Oh, J. H.; Kim, B. J. Solvent-Resistant Organic Transistors and Thermally Stable Organic Photovoltaics Based on Cross-linkable Conjugated Polymers. *Chem. Mater.* **2011,** *24*, 215.

(47) Mueller, C. J.; Klein, T.; Gann, E.; McNeill, C. R.; Thelakkat, M. Azido-Functionalized Thiophene as a Versatile Building Block To Cross-Link Low-Bandgap Polymers. *Macromolecules* **2016,** *49*, 3749.

(48) Knopfmacher, O.; Hammock, M. L.; Appleton, A. L.; Schwartz, G.; Mei, J.; Lei, T.; Pei, J.; Bao, Z. Highly stable organic polymer field-effect transistor sensor for selective detection in the marine environment. *Nat Commun* **2014,** *5*, 2954.

(49) Palazzo, G.; De Tullio, D.; Magliulo, M.; Mallardi, A.; Intranuovo, F.; Mulla, M. Y.; Favia, P.; Vikholm-Lundin, I.; Torsi, L. Detection beyond Debye's length with an electrolyte-gated organic field-effect transistor. *Adv. Mater.* **2015,** *27*, 911.

(50) Bai, L.; Elosegui, C. G.; Li, W.; Yu, P.; Fei, J.; Mao, L. Biological Applications of Organic Electrochemical Transistors: Electrochemical Biosensors and Electrophysiology Recording. *Frontiers in chemistry* **2019,** *7*, 313.

(51) Rivnay, J.; Inal, S.; Salleo, A.; Owens, R. M.; Berggren, M.; Malliaras, G. G. Organic electrochemical transistors. *Nature Reviews Materials* **2018,** *3*.

(52) Khau, B. V.; Scholz, A. D.; Reichmanis, E. Advances and opportunities in development of deformable organic electrochemical transistors. *Journal of Materials Chemistry C* **2020,** *8*, 15067.

(53) Inal, S.; Malliaras, G. G.; Rivnay, J. Benchmarking organic mixed conductors for transistors. *Nat Commun* **2017,** *8*, 1767.

Chapter 3. Bioadhesive polymer semiconductors for intimate biointerfaces

3.1 Introduction

Integrating biocompatible electronic devices with living biological tissues is emerging as a promising avenue for achieving the real-time measurement of biological signals with high spatiotemporal resolutions for biological studies and health monitoring[1-3]. An overarching goal for the development of bioelectronic devices is to achieve conformable and stable interfacing between the sensing surface and the tissue[4-6]. This requires soft and stretchable properties on devices for adapting to curvilinear tissue surfaces, combined with stable bonding between the electrical sensing surface and the tissue. Progress has been made in the development of stretchable bioelectronic materials and devices[7-12]. However, for interface bonding[13] that necessitates the adhesion property of electronic materials to wet tissue surfaces, there are only limited successes. Although there have been adhesives developed in the liquid[13] or solid[14] format for electronic applications, they only serve as non-electrical adhesive functions and suffer from several challenges: complicated usage, potential biocompatibility issue, swelling induced issue, and bio-signal degradation from a thick adhesive layer. Therefore, imparting the intrinsically bioadhesive property to the functional layer can overcome most of the problems. So far, successes towards this goal have been limited to conductors[15-18], which can only be used for passive sensing that has moderate sensitivity.

To realize higher sensitivity, transistor-based active sensing devices are the more advanced option that can provide built-in amplification[19,20]. For bio-interfaced sensing, organic electrochemical transistors (OECTs)[21-24] based on semiconducting polymers are one of the more promising options with a number of advantages, including high amplification, low operation voltage, intrinsic compatibility with ion-based biological events, and the possibility of achieving tissue-like stretchability. The sensing function of an OECT is achieved by directly attaching its semiconducting channel to the tissue surface, so that a biopotential or targeted biochemical signal can electrostatically modulate the bulk conductivity of the channel[25-28]. Since such bio-signal transduction is essentially determined by the microscopic distance between the semiconducting channel and a tissue surface[4], neither the conventional periphery fixation through suturing or stapling, nor applying a separate adhesive can give the most conformable and stable contact between the semiconducting polymers and tissue surfaces. Instead, the more desired interfacing is to have the semiconducting channel directly adhere to the tissue surface.

We report the design of a BioAdhesive polymer SemiConductor (BASC) film that can form robust and rapid adhesion (**Figure 3-1**) with bio-tissues under gentle pressure, while providing high charge-carrier mobility. This is achieved through a double-network structure formed by a semiconducting polymer and a separate tissue-adhesive polymer. Although there have been reports of tissue-adhesive polymers and hydrogels[14, 29-31], none of these is suitable for the creation of bioadhesive semiconductor films. First, as semiconducting polymers typically having long side chains, it is a challenge to ensure the accessibility of the bioadhesive groups on the film surface. Second, the bioadhesive polymer needs to have co-processibility with semiconducting polymers that are typically soluble in organic solvents. To achieve good electrical performance, the obtained morphology needs to both keep continuous charge transport pathways and have only a moderate level of aqueous swellability.

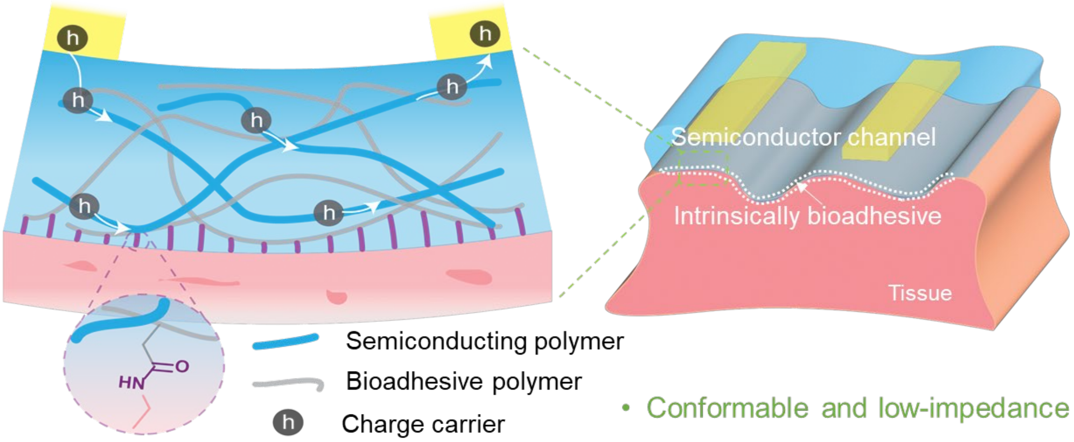

Figure 3-1. Direct adhesive attachment achieved by a bioadhesive polymer semiconducting (BASC) channel and a wet tissue surface. The double-network design of the BASC contains a semiconducting polymer and an adhesive polymer achieving covalent bonding with tissue surfaces.

3.2 Experimental section

Materials and characterizations

The chemicals used in the study, including tetra(ethylene glycol), acryloyl chloride, triethylamine, succinic anhydride, 4-dimethylaminopyridine (DMAP), *N*-hydroxysuccinimide (NHS), 2,5-bis(trimethylstannyl)thiophene, trimethyl(phenyl)tin, bromobenzene, 2-hydroxy-2-methyl-propiophenone, anhydrous dichloromethane (DCM), anhydrous chloroform, and anhydrous chlorobenzene were purchased from Sigma-Aldrich and used without further purification. Tetraethylene glycol dimethylacrylate was purchased from Polysciences Inc. 1-ethyl-3-(3-dimethylaminopropyl)carbodiimide hydrochloride (EDC) was purchased from Oakwood Chemical. 5,5'-Dibromo-3,3'-bis(2-(2-(2-methoxyethoxy)ethoxy)ethoxy)-2,2'-bithiophene was purchased from SunaTech Inc. SEBS was obtained from Asahi Kasei. The thermoplastic polyurethane (TPU) was obtained from BASF.

Microwave polymerization was conducted using a Biotage Initiator +. Nuclei magnetic resonance (NMR) spectra were recorded on a Bruker Avance III HD console spectrometer (^{1}H 400 MHz, ^{13}C 100 MHz) at 293 K. Chemical shifts are given in parts per million (ppm) with respect to tetramethylsilane as an internal standard, and coupling constants (J) are given in Hertz (Hz). High-resolution mass spectra (HR-MS) were recorded on an Agilent 6530 LC Q-TOF mass spectrometer using electrospray ionization with fragmentation voltage set at 70 V and processed with an Agilent MassHunter Operating System. Number average molecular weight (M_{n}), weight average molecular weight (M_{w}), and polydispersity index (PDI) were evaluated by Tosoh EcoSEC size exclusion chromatography system (GPC) using DMF + 0.01 M LiBr as eluent (50 ºC) calibrated with polystyrene standards. The UV-Vis absorption spectra were recorded on the Shimadzu UV-3600 Plus UV-VIS-NIR spectrophotometer. The water contact angle measurement was done with a KRÜSS DSA100 drop shape analyzer. Differential scanning calorimetry (DSC) experiments were performed with a TA Instruments Discovery 2500 differential scanning calorimeter. The atomic force microscope (AFM) imaging was done with the Bruker Multimode 8 AFM. The scanning electron microscope (SEM) imaging was done with the FEI Quanta 650 FEG SEM. The depth-profiling X-ray photoelectron spectroscopy (XPS) was done with Kratos AXIS Nova with a monochromatic Al Kα X-ray source and a delay line detector (DLD) system with Ar1000+ with 10 keV to etch. Grazing-incidence X-ray diffraction (GIXD) was performed at the Advanced Photon Source at Argonne National Laboratory on beamline 8-ID-E.

Synthesis of bioadhesive monomers

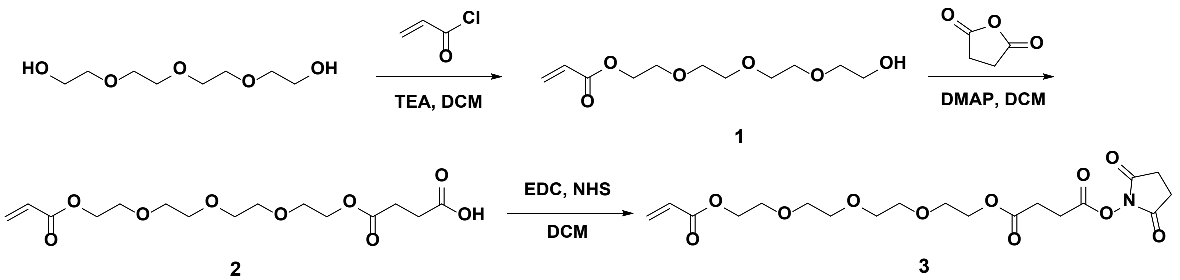

2-(2-(2-(2-hydroxyethoxy)ethoxy)ethoxy)ethyl acrylate (1)

To a round bottom flask (RBF) with a stirring bar, tetra(ethylene glycol) (103 mmol, 20 g) and triethylamine (41.2 mmol, 4.2 g) were added to 30 mL anhydrous DCM under nitrogen atmosphere with an ice bath. Acryloyl chloride (20.6 mmol, 1.86 g) was added dropwise under stirring. Then the mixture was stirred at room temperature (r.t.) overnight. After that, the solid was filtered and the solution was washed with water. The product was extracted with DCM. The solvent was removed using rotary evaporation and purified by column chromatography (silica gel, EA/MeOH=95:5, v:v). The final product was isolated as a colorless oil (4.8 g, 94 %). ^{1}H NMR (400 MHz, $CDCl_3$) δ 6.40 (dd, *J* = 17.3, 1.4 Hz, 1H), 6.13 (dd, *J* = 17.3, 10.4 Hz, 1H), 5.81 (dd, *J* = 10.4, 1.4 Hz, 1H), 4.30 (dd, *J* = 5.5, 4.2 Hz, 2H), 3.76 – 3.67 (m, 4H), 3.67 – 3.61 (m, 8H), 3.58 (dd, *J* = 5.3, 3.8 Hz, 2H), 2.66 (s, 1H); ^{13}C NMR (101 MHz, $CDCl_3$) δ 166.16, 131.03, 128.26, 72.52, 70.66, 70.59, 70.55, 70.35, 69.13, 63.65, 61.73. HRMS (ESI) Calcd for C11H21O6 [M+H]+ : 249.1333, found 249.1334.

3,17-dioxo-4,7,10,13,16-pentaoxaicos-1-en-20-oic acid (2)

To a RBF with a stirring bar, **1** (16 mmol, 4 g), succinic anhydride (32 mmol, 3.2 g), and DMAP (1.1 mmol, 138 mg) were added to 40 mL anhydrous DCM under nitrogen atmosphere. The mixture was stirred at r.t. overnight. After that, the solution was washed with 1M HCl and brine successively. The product was extracted with DCM. The solvent was removed using rotary evaporation and purified by column chromatography (silica gel, EA/MeOH=95:5, v:v). The final product was isolated as a colorless oil (3.9 g, 70 %). ^{1}H NMR (400 MHz, $CDCl_3$) δ 6.43 (dd, *J* = 17.3, 1.4 Hz, 1H), 6.15 (dd, *J* = 17.3, 10.4 Hz, 1H), 5.84 (dd, *J* = 10.4, 1.4 Hz, 1H), 4.31 (dd, *J* = 5.5, 4.2 Hz, 2H), 4.28 (dd, *J* = 5.5, 4.1 Hz, 2H), 3.78 – 3.73 (m, 2H), 3.73 – 3.69 (m, 2H), 3.69 – 3.62 (m, 8H), 2.96 (t, *J* = 7.1 Hz, 2H), 2.84 (s, 4H), 2.78 (t, *J* = 7.0 Hz, 2H); ^{13}C NMR (101 MHz, $CDCl_3$) δ 176.31, 172.06, 166.21, 131.08, 128.25, 70.70, 70.53, 70.46, 69.09, 68.99, 63.86, 63.63, 29.16, 28.97. HRMS (ESI) Calcd for C15H25O9 [M+H]+ : 349.1494, found 349.1495.

2,5-dioxopyrrolidin-1-yl (13-oxo-3,6,9,12-tetraoxapentadec-14-en-1-yl) succinate (3)

To a RBF with a stirring bar, **2** (5.7 mmol, 2 g) and NHS (6.3 mmol, 0.73 g) were added to 40 mL anhydrous DCM under nitrogen atmosphere. The mixture was stirred at 0 ºC for 30 min. then EDC (6.3 mmol, 0.98 g) in DCM was added to the solution dropwise. The reaction was stirred at r.t. overnight. After that, the solution was washed with brine. The product was extracted with DCM. The solvent was removed using rotary evaporation and purified by column chromatography (silica gel, EA). The final product was isolated as a colorless oil (1.9 g, 75 %). ^{1}H NMR (400 MHz, $CDCl_3$) δ 6.43 (dd, *J* = 17.3, 1.3 Hz, 1H), 6.15 (dd, *J* = 17.3, 10.4 Hz, 1H), 5.85 (dd, *J* = 10.4, 1.3 Hz, 1H), 4.36 – 4.29 (m, 2H), 4.29 – 4.23 (m, 2H), 3.80 – 3.73 (m, 2H), 3.73 – 3.63 (m, 10H), 2.66 (s, 4H); ^{13}C NMR (101 MHz, $CDCl_3$) δ 170.97, 168.90, 167.69, 166.16, 131.01, 128.29, 70.62, 70.58, 69.12, 68.94, 64.18, 63.68, 28.67, 26.27, 25.57. HRMS (ESI) Calcd for C19H28NO11 [M+H]+ : 446.1657, found 446.1647.

Synthesis of polymer p(g2T-T)

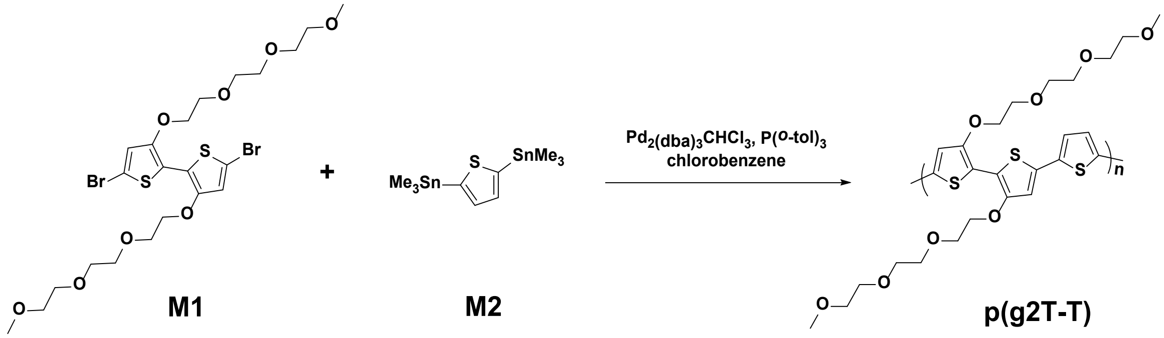

To a mixture of 5,5'-dibromo-3,3'-bis(2-(2-(2-methoxyethoxy)ethoxy)ethoxy)-2,2'-bithiophene (**M1**, 100 mg, 0.155 mmol, 1.0 eq.), 2,5-bis(trimethylstannyl)thiophene (**M2**, 63.8 mg, 0.155 mmol, 1.0 eq.), $Pd_2(dba)_3$ $CHCl_3$ (3.2 mg, 0.0031 mmol, 0.02 eq.), and P(*o*-tol)$_3$ (3.8 mg, 0.0124 mmol, 0.08 eq.) was added 2 mL of chlorobenzene in a nitrogen-filled glovebox. The reaction vial was sealed and submitted to a microwave reactor with the following temperature profile: 2 minutes at 80 °C and 5 minutes at 100 °C. After the reaction was cooled down, 10 mol% of trimethyl(phenyl)stannane were added and the crude polymer solution was heated again to 2 minutes at 80 °C. To complete the end-capping of the polymer, 10 mol% of bromobenzene were added and the reaction vessel was submitted one last time to microwave heating (2 minutes at 80 °C). The crude polymer was then precipitated into methanol, filtered, loaded to a Soxhlet thimble and washed successively with hexane, acetone (each for 24 h). The polymer was finally collected from the thimble with chloroform. The solvent was then removed using rotary evaporation and the polymer was obtained as a blue solid. The NMR spectrum of p(g2T-T) was recorded at r.t. in $CDCl_3$.

Semiconducting film fabrication

The glass substrates were treated with a *n*-octadecyltrimethoxysilane (OTS) layer on the surface[32]. P(g2T-T) polymer was dissolved in chloroform with a concentration of 5 mg/mL. For non-adhesive semiconducting polymer films, the polymer solution was directly spin-coated on the OTS-treated glass substrate at a spin speed of 1,000 r.p.m. for 1 min in a nitrogen-filled glovebox. The polymer film was finally annealed at 110 ºC for 5 min. For preparing the bioadhesive semiconductor precursor solution, a certain amount of well-dissolved p(g2T-T) polymer solution in 5 mg/mL was mixed with desired amounts of ACTEGCOOH or ACTEGNHS monomers, 0.5 wt% of 2-hydroxy-2-methyl-propiophenone (as the photoinitiator) and 0.5 wt% of tetraethylene glycol dimethylacrylate (as the crosslinker) in chloroform. For preparing BASC polymer, the weight ratio of p(g2T-T) to ACTEGCOOH to ACTEGNHS is 1-20-20. The mixture was allowed to stir for 20 min at 60 ºC before spin-coating. The polymer solution was spin-coated on the OTS-treated glass substrates at a spin speed of 1,000 r.p.m. for 1 min in a nitrogen-filled glovebox. The film was then photo-polymerized under 365 nm UV light for 5 min, followed by annealing at 110 ºC for 5 min in a nitrogen-filled glovebox. For adhesion and mechanical characterizations of the semiconducting films, stretchable substrates were fabricated by dissolving TPU in THF with a concentration of 60 mg/mL and then drop-casting the solution on a clean glass substrate to obtain a uniform TPU film (thickness around 70 μm) after the complete evaporation of the solvent in room temperature. The semiconducting polymer precursor solution was spin-coated on the TPU substrates at a spin speed of 1,000 r.p.m. for 1 min in a nitrogen-filled glovebox. The polymer film then was photocured under 365 nm UV light for 5 min, followed by annealing at 110 ºC for 5 min in the glovebox. The TPU film can be peeled off from the glass substrate.

OECT fabrication for the characterization of electrical performance

First, a glass substrate was cleaned with acetone, isopropyl alcohol, and water, successively. After that, the source/drain gold electrodes (60-nm thick) are patterned via e-beam evaporation with a metal shadow mask. The channel length (*L*) and width (*W*) are 200 μm and 4 mm, respectively.

The semiconducting polymer films were transferred onto the channel area using a PDMS stamp. The electrolyte of 0.1 M NaCl solution was dropped on top of the channel. The gate electrode was served by Ag/AgCl. The performance of the fabricated OECTs were measured using Keithley 4200 under an ambient environment.

Electrochemical characterization

The electrochemical measurements were done using the PalmSens electrochemical workstation. The polymer solution was spin-coated on gold electrode as the working electrode. The exposed gold area was encapsulated with the epoxy resin. The EIS measurements were performed in either 0.1 M NaCl solution or 1X PBS solution, with Ag/AgCl as the reference electrode and Pt as the counter electrode. The EIS spectrum was obtained over a range of 10 kHz to 0.1 Hz with an AC 10 mV sine wave and a DC offset of 0.2 V. The analysis of the EIS data was carried out using Multitrace 4.5 software. And the volumetric capacitance was averaged from 3 samples. The mobility was calculated based on the equation $g_{\mathrm{m}} = \frac{Wd}{L}\mu C^{*}(V_{\mathrm{th}} - V_{\mathrm{g}})$, where d is the film thickness, μ is the charge-carrier mobility, C^* is the capacitance of the channel per unit volume, and V_{th} is the threshold voltage.

Mechanical characterization

For rheology measurement, the adhesive semiconductor precursor solution was drop-casted on a clean glass substrate and was fully polymerized under 365 nm UV light in a nitrogen-filled glovebox. The samples were then annealed at 110 °C for 10 min to fully remove the residue solvent. The final film was cut into a circular shape with a diameter of 10 mm and a thickness around 0.8 mm. The rheology test was done with TA Instruments ARES-G2 shear rheometer at room temperature.

For adhesion tests, the semiconducting polymer films were prepared on TPU substrates according to the process described above. The TPU substrates were then cut into a rectangular shape with a length/width of 80 mm/6 mm. The semiconducting polymer occupies one end with an average length/width of 10 mm/6 mm.

The surfaces of synthetic materials including PDMS, TPU, glass, and gold were treated with primary amine groups according to procedures reported in literature[33].

The bio-tissues were purchased from local markets. Generally, the bio-tissues were cut into rectangular pieces and rinsed with 0.1X PBS solution and pre-dried gently with Kimwipe to remove excess water on the surface. The bio-tissues were fixed to a glass substrate at one end with Kapton tape. The bioadhesive polymers on TPU substrates were adhered to the bio-tissue surface by gently pressing of ~ 5 kPa for 1 min. All the samples were stored in a sealed bag at 4-8 ºC for 2 h before the mechanical test.

The interfacial toughness was tested by the 180° peel test with a Zwick-Roell zwickiLine Z0.5 materials testing instrument. All tests were conducted with a constant peeling speed of 0.5 %/s. Interfacial toughness was calculated from the plateau force and the width of the adhered area following the corresponding ASTM standard. The shear strength was tested by the lap-shear test with a Zwick-Roell zwickiLine Z0.5 materials testing instrument. All tests were conducted with a constant tensile speed of 0.5 %/s. Shear strength was calculated by dividing the maximum force by the adhered area following the corresponding ASTM standard. The tensile strength was tested by the tensile test with a Zwick-Roell zwickiLine Z0.5 materials testing instrument. All tests were conducted with a constant tensile speed of 0.5 %/s. Tensile strength was calculated by dividing the maximum force by the adhered area following the corresponding ASTM standard.

Film-on-water (FOW) test

To prepare the thin film samples, polystyrene sulfonate (PSS, 3 wt%) aqueous solution was first spin-coated on the silicon wafer as a sacrificial layer and then the semiconductor polymer solution was spin-coated on top. The films were patterned into the dogbone or rectangular shape using ultrafast laser patterning and then released from water. Details of the tensile stage setup can be found in the previous publication[34]. Briefly, the film was unidirectionally deformed at a strain rate of 0.04 mm/s until film fracture. Elastic modulus was obtained from the slope of the linear fit based on the elastic region from the stress-strain curve using the first 1 % strain. For the fracture toughness measurement, notched and unnotched polymer films were prepared and tested with the pure shear method. Both materials were laser-etched into an I shape with a 2 mm * 16 mm rectangular gauge, and two 2 mm * 20 mm rectangular pads. For a notched sample, an 8 mm-long notch was introduced to its center along the width direction. A strain rate of 0.02 s^{-1} was performed for the tensile test of all samples. The critical displacement for stable crack propagation was identified from the force-displacement curve of notched samples.

In vitro biocompatibility

RAW 264.7 cells, a mouse macrophage cell line, was obtained from ATCC (Cat# TIB-71) and were cultured according to instructions. RAW 264.7 cell line was routinely checked for mycoplasma contamination. For sample preparation, the BASC films were supported on SEBS substrates. p(g2T-T) film is prepared in the same way and is tested as a control sample. RAW 264.7 cells were cultured into a 48-well plate (50,000 cells per well) that was pre-coated with the films (*n* = 5) and incubated in a cell incubator for 24 h. The cells were carefully washed using PBS and conducted MTT assay for measuring the cell viability. For the live/dead staining, the cells pre-incubated with the films were carefully washed using PBS and stained using LIVE/DEAD assay (Thermofisher) in a cell incubator for 15 min. The fluorescence images were taken using EVOSTM M7000 imaging system (Invitrogen).

In vivo biocompatibility

Male C57BL/6 (age 8 weeks) were purchased from Charles River Laboratory. All the animal experiments performed in this research were approved by the Institutional Animal Care and Use Committee of the University of Chicago.

The elastomer SEBS-1221 substrate with a thickness of 1 mm were prepared by drop-casting the SEBS solution in toluene onto a clean glass substrate. The adhesive polymer samples were prepared by spin-coating adhesive precursor solution in chloroform on oxygen plasma treated SEBS substrates at a spin speed of 1,000 r.p.m. for 1 min in a nitrogen-filled glovebox. The polymer films were then photocured under 365 nm UV light for 5 min, followed by annealing at 110 ºC for 5 min in a nitrogen-filled glovebox. The other side of SEBS substrate was coated with the adhesive polymer in the same way. The adhesive polymer-coated SEBS substrates were then punched into circular disks with a diameter of 6 mm with biopsy. Before implantation, all the disks were sterilized with 70 % ethanol solution and UV light for 20 min each. Anaesthesia was maintained using a nose cone. The back hair was removed. The subcutaneous space was accessed by a 1-2 cm skin incision per implant in the center of the animal's back. To create space for implant placement, blunt dissection was performed from the incision towards the animal's shoulder blades. The sample was placed in the subcutaneous pocket created above the incision ($n = 5$). The incision was closed with interrupted sutures. After one month post the implantation, the animals were killed by CO_2 inhalation. The implanted samples were excised and collected for biocompatibility analysis.

Histological analysis (trichrome staining)

The mice skin samples were harvested at scheduled end point and incubated in 2 % PFA for 2 days at 4 °C. The fixed skin samples were conducted paraffin embedding process and sectioned at 5 μm thickness. Trichrome staining was conducted by Human Tissue Resource Center, the University of Chicago. The slides were imaged by EVOS FL Auto (Life Technologies).

Immunofluorescence analysis

The paraffin embedded skin samples were sectioned at 5 μm, and the slides were performed with deparaffination process. The slides were incubated in perm/blocking buffer (0.3 % Triton X-100, 1 % BSA in PBS) for 3 h at room temperature. The slides were washed using 1X PBS 3 times and incubated in primary antibody solution (0.1 % tween 20 in PBS) for overnight at 4 ℃. The primary antibodies information: Anti-alpha smooth muscle Actin antibody (EPR5368, abcam) and CD68 Monoclonal Antibody (FA-11, Invitrogen). The slides were washed using 1X PBS 3 times and incubated in secondary antibody solution (0.1 % tween 20 in PBS) for 3 h at room temperature. Secondary antibody information: Donkey anti-Rat IgG (H+L) Alexa FluroTM 594 Secondary Antibody and Goat anti-Rabbit IgG Alexa FluorTM 647 Secondary Antibody (Invitrogen). Then, the slides were washed using 1X PBS 3 times and stained using DAPI. The stained skin slides were covered with mounting solution and dried for overnight in dark place. The slides were imaged by Olympus confocal microscopy system.

Fabrication of fully-bioadhesive OECT sensors

BAP adhesive precursors in chloroform were spin-coated on the tip area of oxygen plasma treated TPU substrates followed by curing at 365-nm light for 5 min and annealing at 110 ºC for 5 min in a nitrogen-filled glovebox. The prepared substrates were stretched biaxially (stretched along one major direction at 80 % strain, and along the other direction for around 30 % strain) and fixed to a glass substrate. Then a PET shadow mask was attached to each substrate with openings for gate, source and drain electrodes sitting on the adhesive area. SEBS 1052 solution in toluene with a concentration of 10 mg/mL was spin-coated on the open channel as the bottom encapsulation layer. After that, the titanium/gold electrodes were fabricated through e-beam evaporation to achieve a thickness of 5 nm/80 nm. Then the mask was carefully removed. The fixed substrate was slowly released to its original shape so microcracked gold electrodes were obtained. Then, BASC films were transferred to the channel area and the gate area to serve as both the channel and gate materials. The device was flipped and the BAP adhesive precursors in chloroform were spin-coated on backside of the tip area on the TPU substrate followed by curing at 365-nm light for 5 min and annealing at 110 °C for 5 min in a nitrogen-filled glovebox. Thin SEBS 1052 films (~570 nm) were transferred with a PDMS stamp to encapsulate the exposed gold electrodes. Finally, the completed device was released from the glass substrate.

Fabrication of the non-bioadhesive OECT sensor

A TPU substrate was stretched biaxially (stretched along one major direction at 80 % strain, and along the other direction for around 30 % strain) and fixed to a glass substrate. A PET shadow mask was attached to the substrate. Then SEBS 1052 solution in toluene with a concentration of 10 mg/mL was spin-coated on the open channel as the bottom encapsulation layer. After that, titanium/gold electrodes were fabricated through e-beam evaporator with a thickness of 5 nm/80 nm. Then the mask was carefully removed. The fixed substrate was slowly released to its original shape so microcracked gold electrodes are obtained. Neat semiconducting polymer p(g2T-T) films were transferred to the channel area and the gate area to serve as both the channel and gate materials. Thin SEBS 1052 films (~570 nm) were transferred with a PDMS stamp to encapsulate the exposed gold electrodes. The device was finally released from the glass substrate.

Fabrication of the passive electrode sensor

A TPU substrate was stretched biaxially (stretched along one major direction at 80 % strain, and along the other direction for around 30 % strain) and fixed to a glass substrate. A PET shadow mask was attached to the substrate. Then SEBS 1052 solution in toluene with a concentration of 10 mg/mL was spin-coated on the open channel as the bottom encapsulation layer. After that, titanium/gold electrodes were fabricated through e-beam evaporator with a thickness of 5 nm/80 nm. Then the mask was carefully removed. The fixed substrate was slowly released to its original shape so microcracked gold electrodes are obtained. PEDOT:PSS (PH1000) blending with 1/1 weight ratio of hydrophilic polyurethane (HydroMed D4) was spin-coated on top of the electrode to lower the interfacial impedance with bio-tissues[35]. Silicon rubber adhesive was blade-coated to encapsulate the exposed gold electrodes. The device was finally released from the glass substrate.

Ex vivo ECG measurement

Isolated rat hearts were prepared following the method described previously[36]. An adult rat (males, 300-400 g body weight, purchased from Charles River Laboratory) was heparinized and anaesthetized using open-drop exposure of isoflurane in a bell jar configuration. The heart was removed and placed in ice cold HBSS buffer, and the aorta was cannulated in preparation for use in a Langendorff set-up. Oxygenated HEPES-buffered Tyrode’s solution was perfused through the cannulated aorta after passing through a heating coil and bubble trap (Radnoti). The heart was placed in a water-jacketed beaker (Fisher Scientific) to maintain a temperature of 37 °C. The perfusion pressure was maintained at 80-100 mmHg. The sinoatrial node along with the atria were removed to lower the atrioventricular node pace. The perfusion and left ventricular pressure were monitored using a BP-100 probe (iWorx) connected to the perfusion line and a water-filled balloon (Radnoti) inserted into the LV, respectively. For ECG recordings, a fully-bioadhesive (or non-bioadhesive) OECT sensor was positioned on the ventricular wall and the source-drain voltage was powered by a Keithley 2450 SourceMeter. Gentle pressure was applied on the back of the OECT device for 20 s to make sure adhesion formation. The output signals were connected to a C-ISO-256 preamplifier (iWorx). All signals (perfusion, left ventricular pressure and ECG) were amplified using an IA-400D amplifier (iWorx) and interfaced with a computer using a Digitate 1550 digitizer with Clampex software (Molecular Devices).

In vivo EMG measurement

The sciatic nerve surgery followed methods described previously[36]. In short, an adult rat (10-24 weeks, males, purchased from Charles River Laboratory) was deeply anaesthetized with isoflurane (3-4 %). The fur was removed from the hindquarters using surgical clippers and hair removal cream. An incision across the midline was made in the skin, and the fascial plane was opened between the gluteus maximus and the anterior head of the biceps femoris, exposing the sciatic nerve. The nerve was extruded using sutures and was stimulated by bipolar silver wire electrodes (0.003 µm, A-M Systems). Biphasic electrical impulses (durations of cathodic phase, anodic phase and inter-phase interval: 0.2 ms) were generated by a potentiostat (SP-200, BioLogic) controlled with EC-Lab software. After cutting the skin open, the bioadhesive transistor was attached to the gastrocnemius medialis (GM) muscle with gentle pressure applied for 20 s. For EMG recordings, the output was connected to a C-ISO-256 preamplifier (iWorx). The EMG signal was amplified using an IA-400D amplifier (iWorx) and interfaced with a computer using a Digidata 1550 digitizer with Clampex software (Molecular Devices).

3.3 Results and discussion

3.3.1 Synthesis and characterization of bioadheisve semiconducting polymers

We designed a brush-architectured BioAdhesive Polymer (BAP) (**Figure 3-2**) for forming a double-network film with a semiconducting polymer. This bioadhesive polymer has a polyethylene backbone with long linear side chains terminated with two types of functional units in a controlled ratio: carboxylic acid (COOH) and *N*-hydroxysuccinimide (NHS) ester. The COOH group provides water-absorption for temporarily drying the tissue surface and forms electrostatic interactions with tissue surfaces. The NHS ester group, as the primary contributor to bio-adhesion, covalently bonds with the primary amine groups on the tissue surface[14, 29]. To allow the effective exposure of these groups on the film surface when blending with a semiconducting polymer, a key innovation in our design is the extension of the side chain length by inserting tetra(ethylene glycol) (TEG) structure. This structure is selected for its moderate level of polarity for providing a suitable level of swelling, which, on the one hand, can help to drain the fluid on the tissue surface and facilitate ion transport, and on the other hand, won't cause exaggerated swelling and volume expansion.

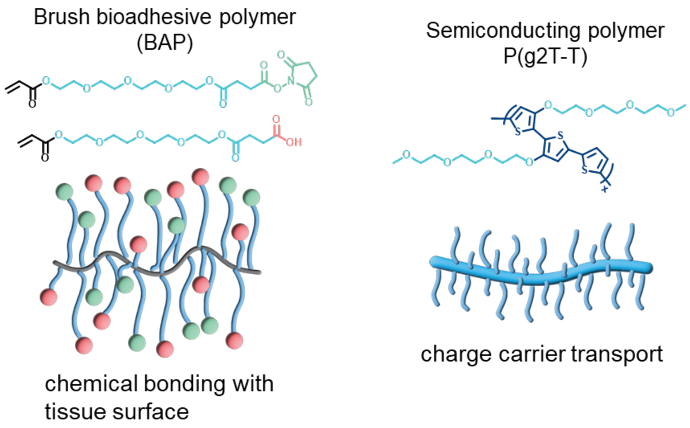

Figure 3-2. Chemical structures of the brush bioadhesive polymer (BAP) and the semiconducting polymer p(g2T-T).

The semiconductor phase is served by a type of redox-active polymer semiconductor, p(g2T-T), which has shown high performance in OECT devices for biosensing functions[37,38]. For the preparation of the double-network film, we blend p(g2T-T) with the two types of acrylate monomers (COOH-terminated and NHS ester-terminated, respectively) in a controlled ratio (**Table 3-1**) in chloroform. We then spin-coat the blended solution on a substrate to form thin films, and further polymerize and crosslink the bioadhesive monomers in the films under UV light (**Figure 3-3**). Such an in-situ polymerization process not only solves the co-solubility issue, but also controls the phase separation scale for achieving better percolation connectivity of the p(g2T-T) phase. The obtained bioadhesive semiconductor further enables us to fabricate a fully-bioadhesive and stretchable OECT sensor, and realize tissue-interfaced sensing (e.g., electrophysiological recording on a wet heart) with stable bonding and built-in signal amplification.

Table 3-1. Summary of adhesive polymer compositions

	p(g2T-T)	ACTEGCOOH	ACTEGNHS
BASC	1	20	20
BASC-COOH	1	40	0
BASC-NHS	1	0	40
BAP	0	20	20
BAP-COOH	0	40	0
BAP-NHS	0	0	40

*The values show the weight ratios.

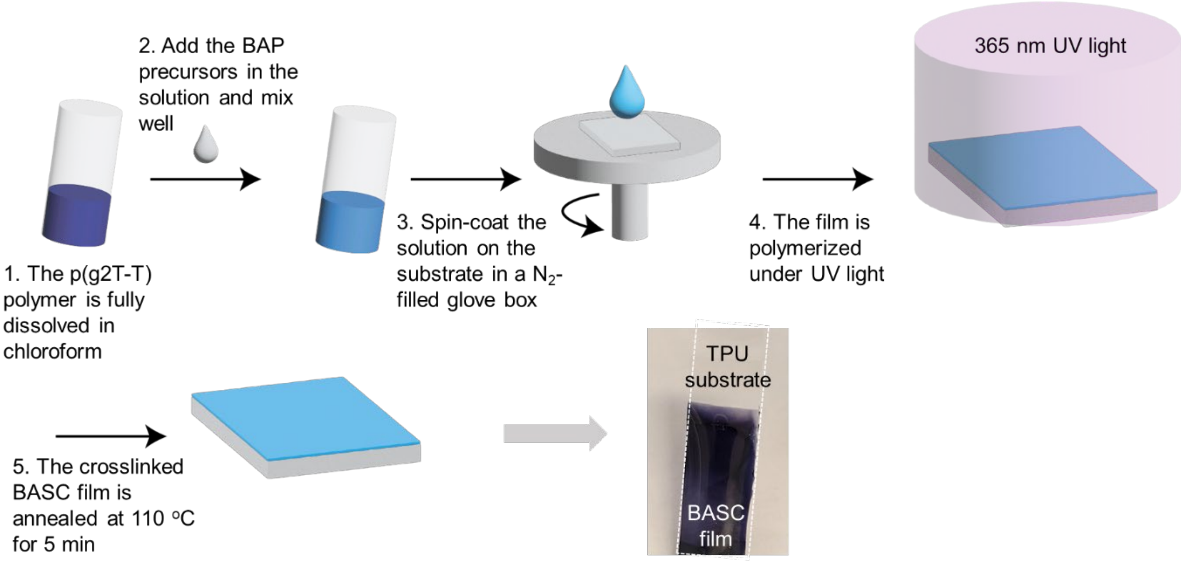

Figure 3-3. Procedure for preparing the BASC film.

When the BAP is blended with p(g2T-T) to form BASC films through spin-coating processes, the p(g2T-T) phase self-assembles into interconnected nanofibril structures, as evidenced by atomic force microscopy (AFM) images (**Figure 3-4A**) for the top and bottom surfaces of a film with the blending ratio of 1:40 (in mass) for p(g2T-T)-to-BAP. In the thickness direction, depth-profiling XPS shows an increasing fraction of p(g2T-T) from the top to the bottom surface (**Figure 3-4C**).

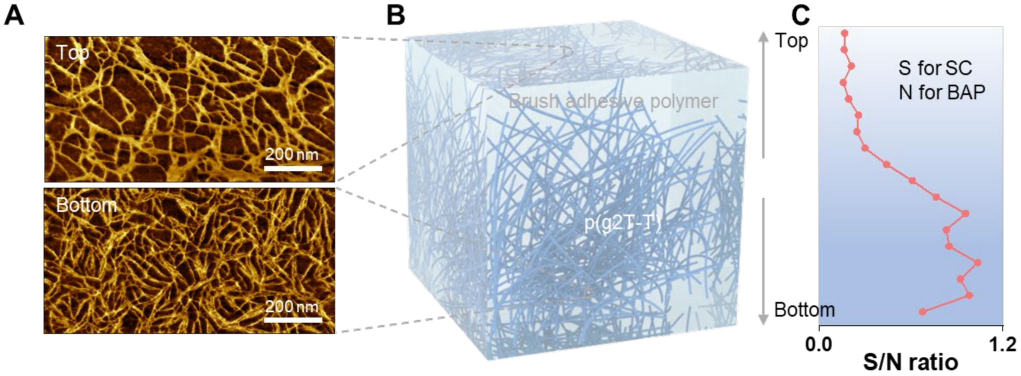

Figure 3-4. Morphological characterization of the BASC.

Figure 3-4, continued. (A) AFM phase images showing the top and bottom surfaces of the BASC film. (B) 3D schematic morphology of the BASC film. (C) XPS depth-profiling illustrating the S/N ratio.

This high ratio of BAP is chosen to ensure sufficient surface density of NHS ester groups for high adhesive property, as validated further below. Such a dominant amount of BAP in the BASC film also renders the BASC film with similar mechanical properties to BAP, as featured by a low modulus and viscoelasticity (**Figure 3-5**). These tissue-like mechanical properties are crucial for achieving conformal physical contact with tissue surfaces[39], and adhesion.

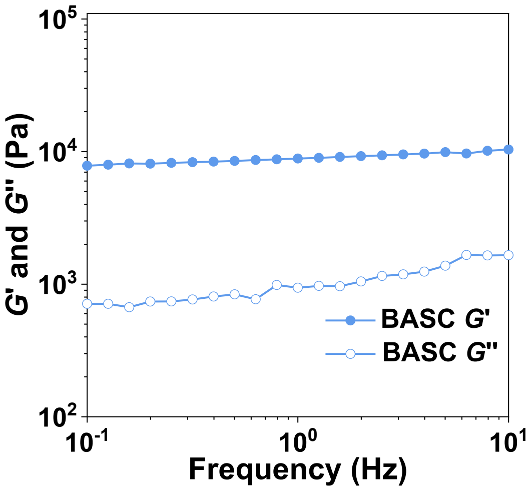

Figure 3-5. Rheological measurement of the BASC polymer in the dry state.

3.3.2 Adhesion property

According to our hypothesis, when the BASC is in contact with the tissue surface, the brush-type BAP phase starts to absorb and remove water on the tissue surface. To validate this, we first investigate the water absorption and swelling behavior of a neat brush BAP. After soaking in phosphate-buffered saline (PBS) solution, the mass of BAP increases by ~20 % after 2 min from rapid water absorption, which is followed by slow absorption over the next 24 hours (**Figure 3-6A**). This is also reflected by the volumetric swelling, with a lateral expansion ratio of ca. 1.05 (**Figure 3-6B**). Comparatively, the 1:1 blending of the more hydrophilic COOH group and less hydrophilic NHS ester group renders the BAP with a moderate level of water absorption and swelling, which stands between the levels of the two brush polymers with only COOH or NHS ester terminated side chains (namely BAP-COOH and BAP-NHS, respectively). The water absorption behaviors of these three brush-architectured polymers are all much milder than poly(acrylic acid) (**Figure 3-6C**), which could come from different film morphologies and porosities (**Figure 3-6D**) from the two different polymer architectures (i.e., brush vs. non-brush)[40,41]. Overall, the moderate level of water absorption for BAP is beneficial for the stability of electrical performance from BASC films.

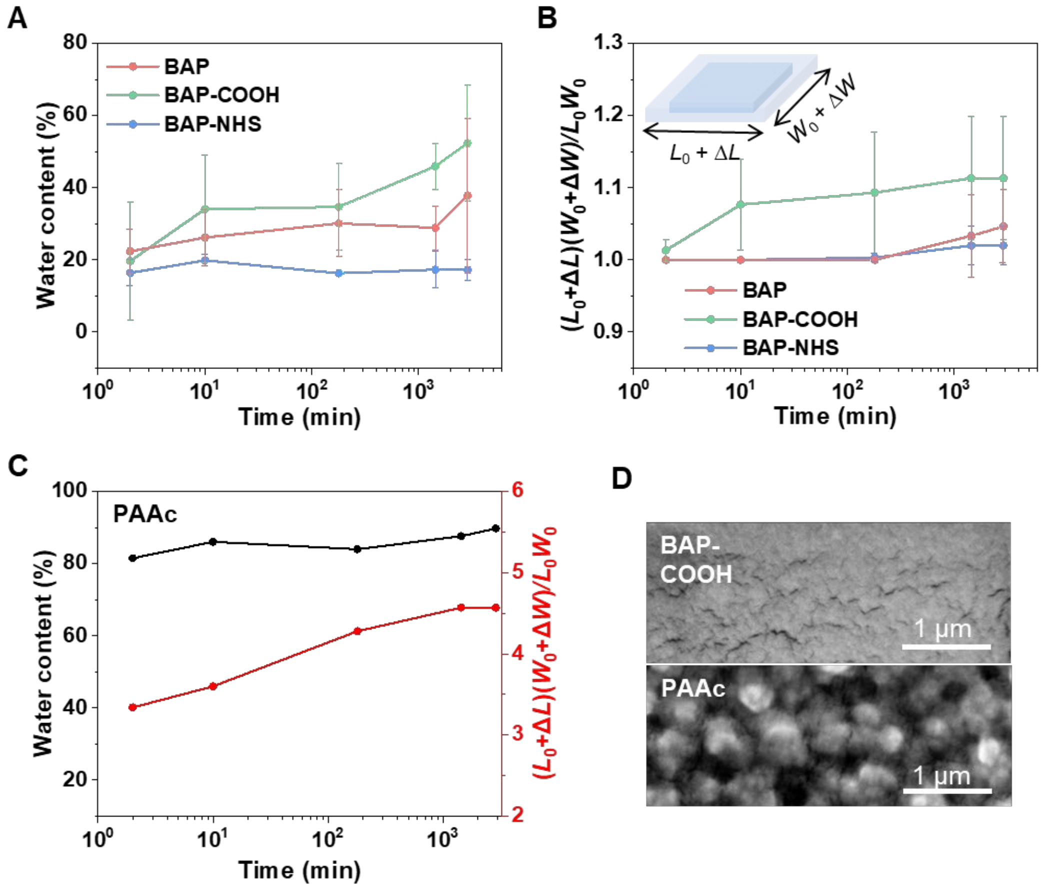

Figure 3-6. Water absorption and surface morphology. (A-B) Water content measured through gravimetric analysis (A) and dimensional swelling (B) of the BAPs with three types of side-chain designs when soaked in PBS solution over time. (C) Water content and dimensional swelling of PAAc in PBS solution. (D) SEM images showing the microscale features of a BAP-COOH film and a PAAc film in the dry state.

We next study the adhesion behavior of BASC films through 180-degree peel, lap-shear, and tensile tests on various synthetic materials and bio-tissues, by first holding these films (supported on thermoplastic polyurethane (TPU) substrates) to the different surfaces with gentle pressure (around 5 kPa) for 1 min (**Figure 3-7A**). On amine-treated glass surfaces, which can form covalent interaction with NHS ester, BASC films display much stronger and tougher adhesion than neat p(g2T-T) films, with an over 40-fold increase in the interfacial toughness, which achieves even higher level than the BAP film (**Figure 3-7B**). Tests of BASC films with other blending ratios manifest the general trend of higher adhesion from higher ratios of BAP in the film. On several other synthetic surfaces (i.e., gold, TPU, PDMS), BASC films also form much stronger adhesion than neat p(g2T-T) films.

With the side chain design of the BAP playing the key role in the adhesion property of BASC films, we further compare the BAP (1:1 ratio of COOH and NHS ester) with three polymers with the same backbone but different side chains: BAP-COOH, BAP-NHS, and regular PAAc. Comparisons are also made on the three blended semiconducting films (namely BASC-COOH, BASC-NHS, and SC-PAAc) from each of these polymers with p(g2T-T) in the ratio of 1:40. Through testing on amine-functionalized glass surfaces, several observations can be made. First, among the three types of brush BAPs and the resulting BASCs, the higher amount of NHS ester gives higher adhesion, which proves that the adhesion is mainly provided by the NHS group. Second, the three BASCs built with the three brush BAPs all provide comparable or higher adhesion properties with their corresponding BAPs. In contrast, blending of PAAc with p(g2T-T) results in a decrease of adhesion by about 90 % (**Figure 3-7C**). This validates our design hypothesis for BAP, that long side chains are needed for overcoming the shielding effect from the long side chains of p(g2T-T) on the adhesive groups.

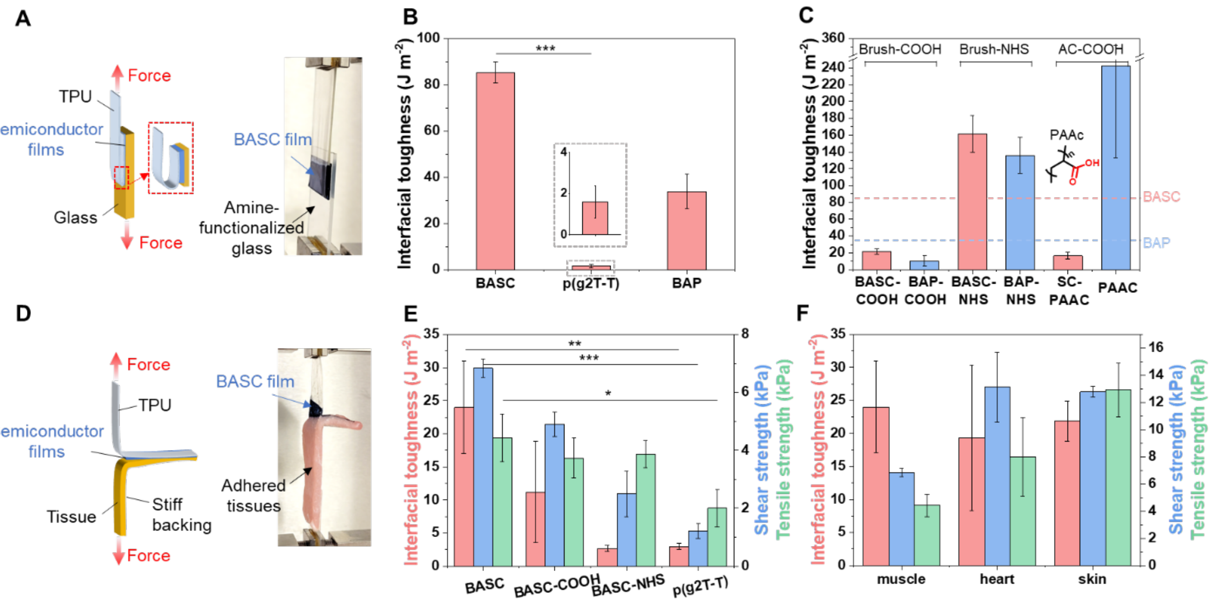

Figure 3-7. Adhesive properties of the BASC films. (A) 180-degree peel test (ASTM D3330) for interfacial toughness measurement on rigid substrates. (B) Interfacial toughness of the adhesion between a BASC film and an amine-functionalized, dry glass substrate, in comparison to a neat p(g2T-T) film, and a BAP film. (C) On amine-functionalized glass substrates, interfacial toughness achieved by BASC films and BAP (including PAAc) films with different types of side chains. (D) 180-degree peel test (ASTM F2256) for interfacial toughness measurement on bio-tissues. (E) Interfacial toughness, shear strength, and tensile strength of the adhesion between wet porcine muscle tissues and a BASC film, a BASC-COOH film, a BASC-NHS film, and a neat p(g2T-T) film, respectively. (F) Interfacial toughness, shear strength, and tensile strength achieved by BASC films on various wet tissue surfaces. Values represent the mean and the standard deviation ($n = 3$). Statistical significance and P values are determined by two-sided Student's t-test: $*P<0.05$; $**P<0.01$.

We then characterize the adhesion performance of BASC films on wet tissue surfaces (**Figure 3-7D**). As shown for porcine muscle surfaces, BASC films achieve an interfacial toughness of ~24

J m-2, a shear strength of ~7 kPa, and a tensile strength of ~4.4 kPa, which are, ca. 10-fold increase than that from neat p(g2T-T) films for interfacial toughness (**Figure 3-7E**). These adhesion properties are achieved with an equal ratio of brush COOH and NHS ester side chains, and are higher than those with COOH or NHS ester only side chains (i.e., BASC-COOH and BASC-NHS) or other unbalanced mixing ratios of the two groups. Such a trend of the side-chain influence is different from the behaviors on dry amine-glass surfaces, which manifests the importance of hydrophilic COOH groups for absorbing water in establishing adhesion on wet tissue surfaces. The BASC film can also be applied to various wet tissues, including the heart, skin, spleen, with high interfacial toughness, high shear strength, and high tensile strength (**Figure 3-7F**).

3.3.3 Electrical and structural characterization

Designed as a semiconductor, the electrical performance of BASC films was characterized in OECT devices. The OECT's transfer curve with an on/off ratio of 10^4 indicates ideal semiconducting performance from the BASC film (**Figure 3-8A**), which is on par with p(g2T-T). As calculated from the transconductance (g_m), the obtained charge-carrier mobility of the BASC film approaches 1 $cm^2 V^{-1} s^{-1}$, which is comparable to that of the neat p(g2T-T) film (**Figure 3-8B**). This is given by the percolated charge-transport pathway formed by the p(g2T-T) phase in the BASC film. On the device level, the maximum transconductance, as the key figure-of-merit for OECT performance, the BASC film displays a slight increase compared to the p(g2T-T) film, which should come from a much higher thickness (1.9 μm) of the BASC film than that (35 nm) of the neat p(g2T-T) film. On the other hand, the measurement of the OECT response speed of these semiconducting films shows that the higher thickness of the BASC film does not lead to a slower response to the gating compared to the neat p(g2T-T) film, as ions can transport very efficiently in the blended BAP.

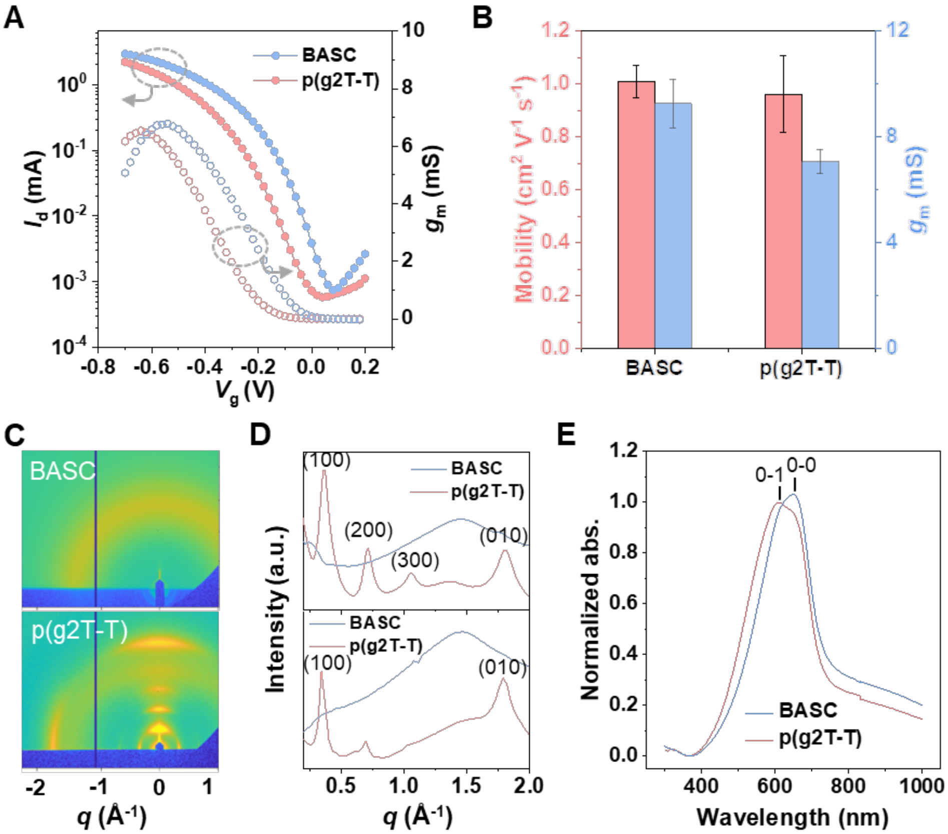

Figure 3-8. Electrical and structural characterizations of the BASC film. (A) Transfer curves from a BASC film and a p(g2T-T) film serving as the OECT channel (V_g: gate voltage, I_d: drain current, V_d: drain voltage, g_m: transconductance). (B) Charge-carrier mobility and g_m for the BASC and p(g2T-T) films. Values represent the mean and the standard deviation (n = 5). (C) 2D GIXD patterns of the BASC and p(g2T-T) films. (D) 1D linecuts in the out-of-plane direction (top) and in-plane direction (bottom) of a BASC and a p(g2T-T) film. (E) Normalized UV-vis absorption of a BASC and a p(g2T-T) film.

We carried out GIXD and UV-vis spectroscopy (**Figure 3-8C**) to study interchain packing morphology of the p(g2T-T) phase in the film. The GIXD results (**Figure 3-8D**) reveal that blending with the brush-architected BAP almost completely suppresses the long-range crystallization, which could decrease the modulus of the p(g2T-T) phase. However, the UV-vis absorption spectroscopies show that the p(g2T-T) phase in the BASC film has a higher level of short-range aggregation than the neat film, as represented by the ratios between 0-0 and 0-1 optical transition peaks (**Figure 3-8E**). At the molecular level, this explains the well-maintained mobility from the BASC film.

For the direct interfacing of a semiconducting polymer with a bio-tissue surface for sensing biophysical or biochemical signals, the other two important interface factors that influence the recorded signal amplitudes are interfacial impedance and the separation distance between the recording and tissue surfaces. For the interfacial impedance, we compared the electrochemical impedance spectroscopy (EIS) measurements of the BASC and surface coating with BAP and commercia adhesive product and state-of-the-art hydrogel adhesive in literature. The results shown in **Figure 3-9** do show that our double-network BASC design gives lower impedance than applying a separate adhesive at the interface.

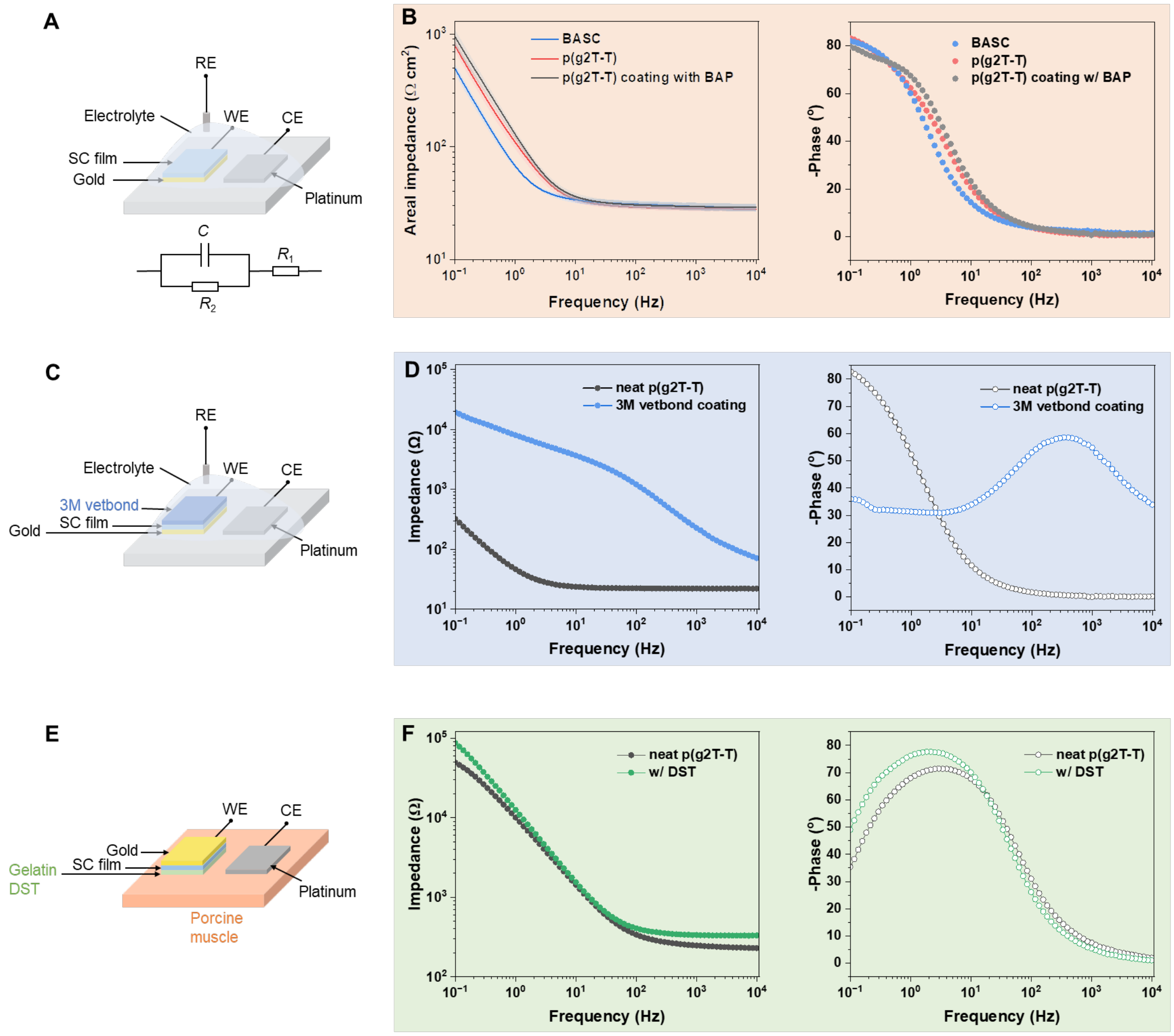

Figure 3-9. EIS impedance comparison. (A) Schematic diagram showing the EIS measurement setup and the simplified Randles equivalent circuit diagram utilized for characterizing the surface impedances. The working electrode (WE) is semiconducting-film-coated gold; the counter electrode (CE) is platinum; the reference electrode (RE) is Ag/AgCl. The electrolyte is PBS solution. (B) EIS areal impedance and phase spectrum of a BASC film, a p(g2T-T) film, and a bilayer p(g2T-T) film coated with a BAP layer (thickness of ~2.5 μm). (C) EIS measurement setup for 3M vetbond tissue adhesive as a coating layer on p(g2T-T) film. The tissue adhesive was applied on p(g2T-T) film as a thin layer. Upon contact with water, the adhesive cures. The EIS

measurement was done in PBS solution with a Pt counter electrode and an Ag/AgCl reference electrode. (D) Comparison of the EIS impedance and phase measurement results for 3M vetbond tissue adhesive coated on the p(g2T-T) film. (E) EIS measurement setup for gelatin-based double-sided tape (DST) as a coating layer on p(g2T-T) film. The measurements were carried out by attaching the WE (supported by an SEBS1052 substrate) and Pt CE to a wet porcine muscle. Specifically, the dry gelatin DST (made following the literature[14]; dry thickness ~200 µm) was attached to the tissue surface and waited for the adhesive to hydrate. Then the semiconductor film was then attached to the top side of the DST layer. The reason for doing the impedance measurement on porcine muscle here is that attaching the dry gelatin DST on the p(g2T-T) film cannot guarantee conformable and stable contact, therefore performing such impedance measurement in PBS solution may not give very reliable results. (F) Comparison of the EIS impedance and phase measurement results for gelatin-based DST coated on the p(g2T-T) film.

More importantly, our BASC design helps to keep the closest distance between the semiconducting film and the tissue surface during recording. To semi-quantitatively assess the effect of using separate adhesion layers in increasing the distance between the device and tissue surfaces[42-45], we coated our BAP polymer in two different thicknesses (3.8 µm and 300 µm) onto a pair of p(g2T-T)-based recording electrodes (**Figure 3-10A**). This layout emulates the channel and the gate in OECT devices. To show the recording capability, AC signals were applied through another pair of gold electrodes that are attached to the top surface of the BAP coating layer, which was fully soaked with PBS solution. As shown in **Figure 3-10B**, the BAP layers with thickness increased from 3.8 µm to 300 µm leads to significant decreases in the potential sensed between the two p(g2T-T) electrodes, which shows major signal decay caused by the use of a separate adhesive layer.

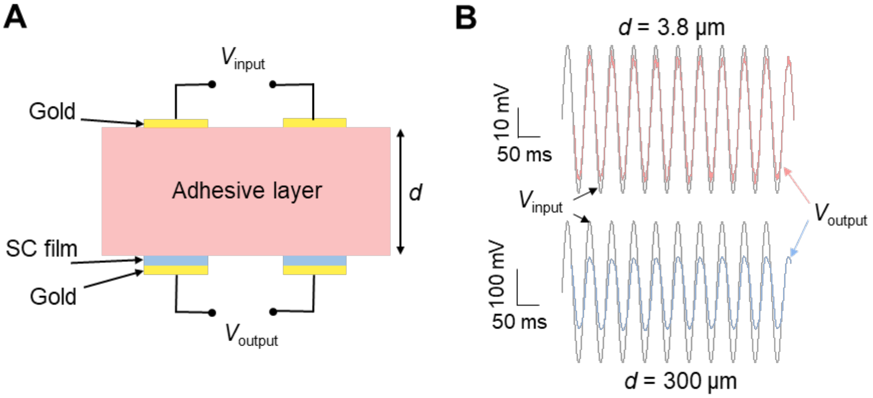

Figure 3-10. Electrical characterization of the separation distance between the recording and tissue surfaces. (A) Schematic diagram showing the setup for characterizing the influence of the device-tissue distance caused by the use of a separate bioadhesive layer. (B) AC signal input (grey) and acquired signals between the p(g2T-T) electrodes that are covered with a layer of BAP with two different thicknesses. The thin adhesive layer ($d = 3.8$ μm) decreases the signal amplitude by 15 % while the thick adhesive layer ($d = 300$ μm) decreases the amplitude by 50 %.

3.3.4 Abrasion resistance, stretchability, and biocompatibility

When a polymer semiconductor is interfaced with bio-tissues, several other properties, including abrasion resistance, stretchability, and biocompatibility, are important to the robustness and long-term stability of the interface and the function. During insertion and/or attachment of a device into/onto bio-tissues, physical abrasion can occur on the device surface (**Figure 3-11A**). With conjugated polymers typically having relatively low stretchability and toughness, the films are generally susceptible to abrasions[46]. Our BASC film shows abrasion-resistance, which should come from the ultrasoft and viscoelastic properties of the film. To characterize this, we used a piece of polytetrafluoroethylene (PTFE)-covered glass to slide back and forth on a BASC film under a pressure of 1 kPa. After 1,000 cycles of such surface sliding, the BASC film remains mostly intact in appearance under an optical microscope and electrical performance in an OECT device (**Figure 3-11, B and C**). In comparison, a neat p(g2T-T) film was damaged by the surface abrasion processes. To better mimic the abrasion during device implantation processes, we also carried out the comparison using porcine skin, which gives a similar trend. The brief tissue contact during typical abrasion processes would not be sufficient for BASC films to generate adhesion with the tissue surfaces and further create higher frictional force.

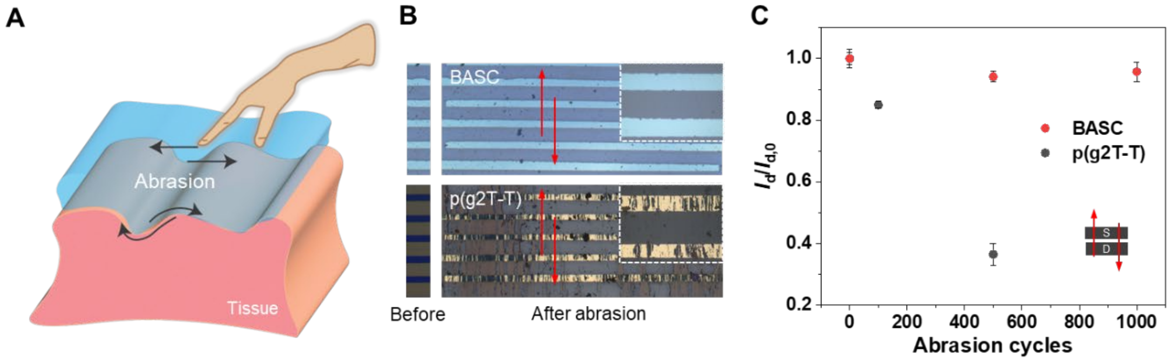

Figure 3-11. Abrasion resistance of BASC films. (A) Schematic diagram illustrating physical abrasions that can happen on the surfaces of implantable devices. (B) Photographs showing a BASC film and a p(g2T-T) film before and after abrasion by a PTFE-covered glass plate under 1 kPa for 500 cycles. The arrows indicate the direction of the abrasion. (C) Changes of OECT on-current from the two films after the abrasion cycles along the charge transport direction. Values represent the mean and the standard deviation (*n* = 4-5).

As both p(g2T-T) and the BAP gel are highly stretchable[10], the resulting BASC films also have high stretchability (**Figure 3-12A**), which benefits conformability to curvilinear tissue surfaces and robustness under tissue deformations. From the optical microscopy and AFM images, the BASC film can be stretched to 100 % strain without forming any cracks (**Figure 3-12B**). Instead, strain-induced alignment of the p(g2T-T) nanofibers is observed. When tested in OECT devices, the BASC film displays highly stable electrical performance during stretching to 100 % strain, even after 100 repeated cycles (**Figure 3-12C**).

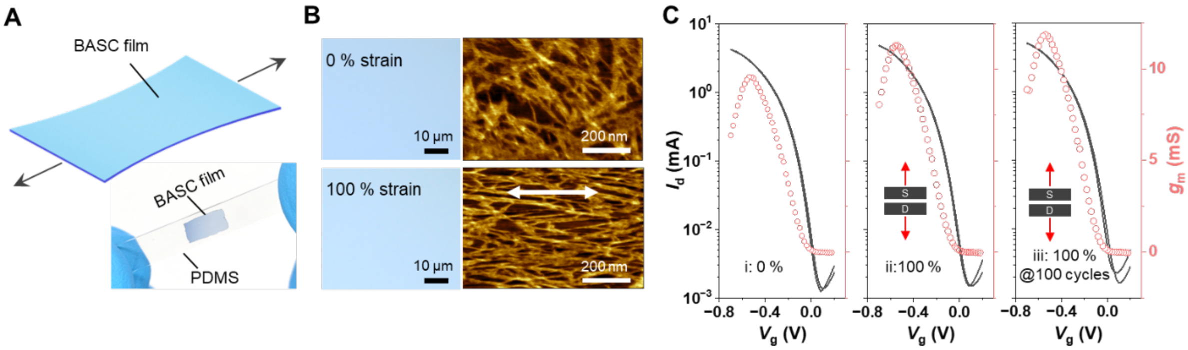

Figure 3-12. Stretchability of BASC films. (A) Schematic illustrating a BASC film under stretching. The bottom photograph shows a stretched BASC film on a PDMS substrate at 100 % strain. (B) Optical microscopy and AFM images showing a BASC film stretched to 100 % strain without forming cracks. (C) Transfer curves of BASC films in the pristine state, and stretched to 100 % strain for 1 and 100 cycles, which were measured with V_d = -0.6 V.

When a device is interfaced with tissue, the foreign-body response (FBR) is one of the main factors that limit the longevity[47,48], which is influenced by the modulus and the surface chemistry of an implant. We first show through in vitro cell culture that the BASC has minimal cytotoxicity (**Figure 3-13A**). We then study the FBR behavior of our BASC films by laminating them on both sides of SEBS (polystyrene-*block*-poly(ethylene-*ran*-butylene)-*block*-polystyrene) substrates and implanting subcutaneously in mice. After one-month implantation, fibrotic capsules formed around the BASC samples are thinner than those formed around SEBS control samples, as shown by Masson's trichrome staining results (**Figure 3-13B**). Besides, immunofluorescence imaging of FBR-related biomarkers (i.e., α-SMA and CD68) shows lower amounts of fibroblasts and macrophages deposited on the BASC surface than those on the SEBS samples (**Figure 3-13B**).

These results collectively show that BASC films have better biocompatibility than SEBS, which further elevates the promise for directly interfacing with bio-tissues through implantable devices.

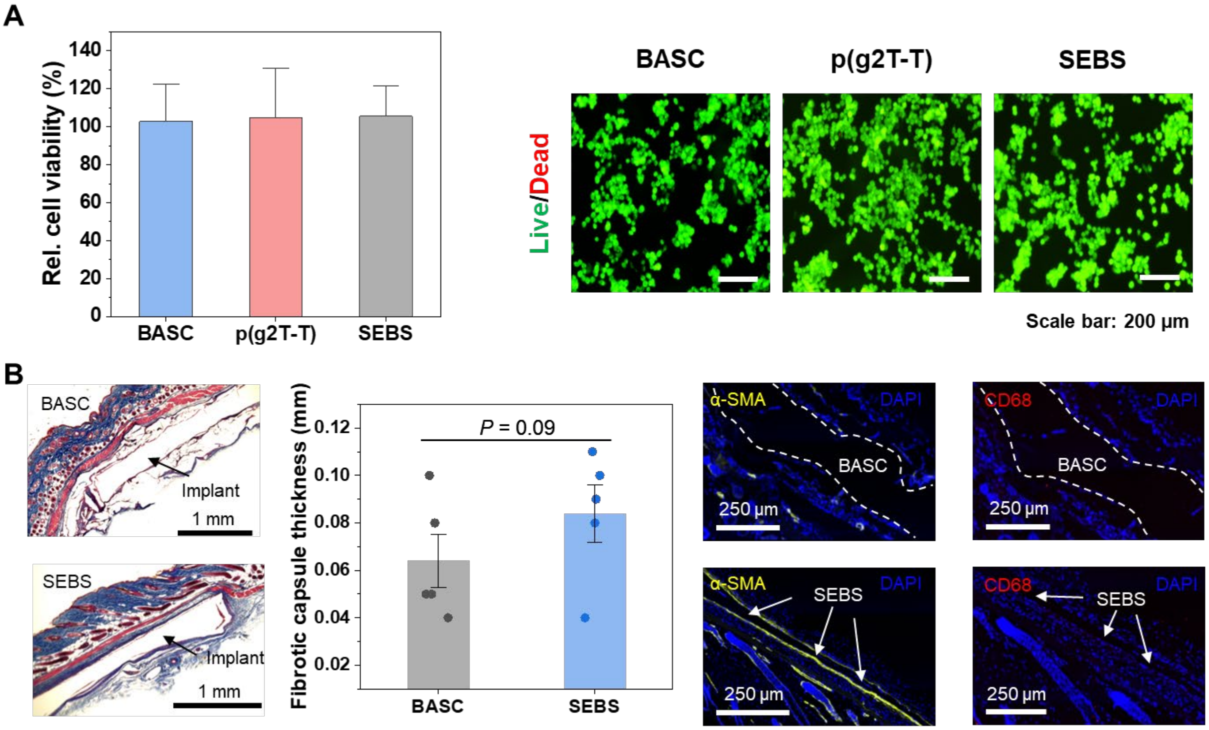

Figure 3-13. Biocompatibility study of BASC. (A) In vitro cell viability study. Left, MTT; right, Live/Dead staining. (B) Masson's trichrome staining of surrounded tissues of a subcutaneously implanted BASC film and a SEBS film (control) after one month in mice and calculated fibrotic capsule thickness. Immunofluorescence staining of α-SMA for fibroblasts (yellow) and CD68 for macrophages (red). Statistical significance and *P* values are determined by two-sided Student's t-test.

3.3.5 Bioadhesive transistors for tissue interfaces

We designed and fabricated an OECT-based sensor (**Figure 3-14A**) using BASC films as both the semiconducting channel and the redox-active gate. The surrounding area is occupied by the substrate, which is covered by our BAP film. With the use of microcrack-based stretchable gold

(**Figure 3-14B**) as the electrodes[49,50] and thin SEBS layers (~570-nm thick) as the encapsulation for the interconnects and the bottom side of the electrodes, the OECT sensor is also stretchable. An as-fabricated fully-bioadhesive OECT displays ideal transfer behavior at 0 % strain and when stretched to 50 % strain and forms strong adhesion when attached to the surface of a wet porcine muscle.

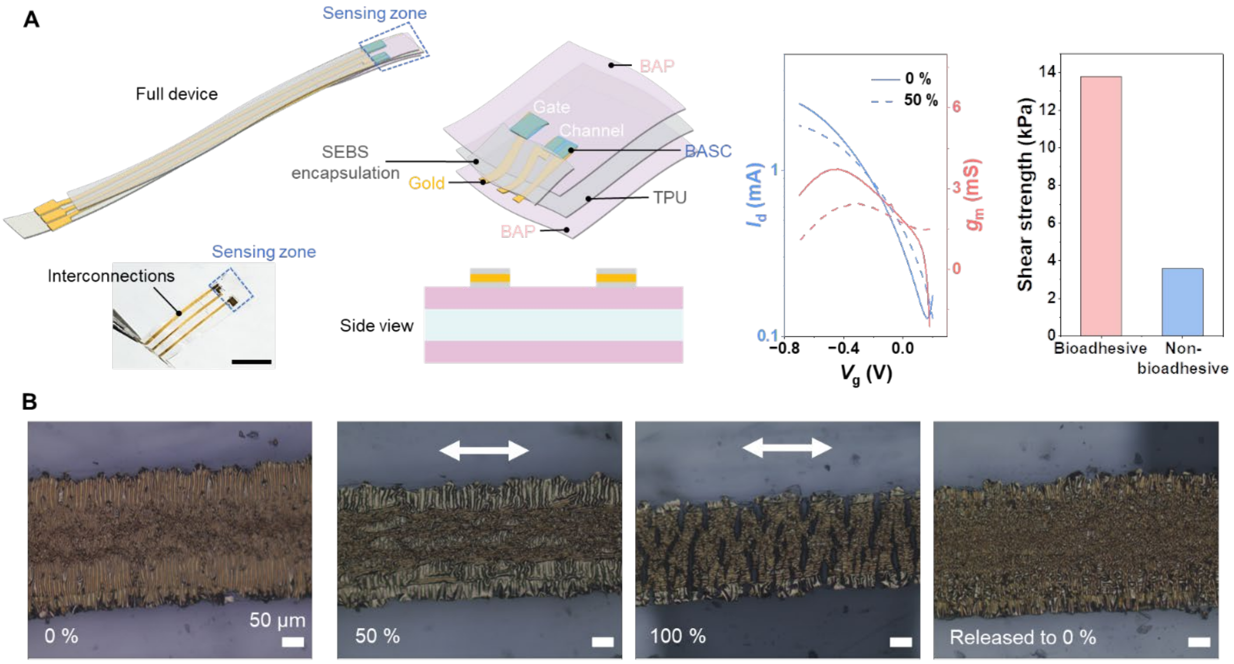

Figure 3-14. Schematics of the bioadhesive OECT. (A) Stretchability and adhesion test of the bioadhesive OECT. (B) Photographs showing stretchability test of the gold electrode.

We further demonstrate the benefit of the bioadhesive property of the OECT sensor on epicardial electrocardiogram (ECG) recording from an isolated rat heart (**Figure 3-15A**). The bioadhesive OECT can be conveniently adhered to the wet heart surface by gently pressing for 20 s. During the recording process, the bioadhesive and stretchable properties, working in conjunction, help the OECT to well accommodate the heart beating, thereby maintaining spatially stable and conformable contact on the heart (**Figure 3-15B**). Even under external mechanical perturbation (e.g., pulling), stable attachment is still maintained. The ECG recording from both the left ventricle (LV) and right ventricle (RV) surfaces also remain stable (**Figure 3-15D**). In comparison, for a non-bioadhesive OECT (**Figure 3-15C**), which can only stay on the heart surface through capillary force from the fluid, gradual drifting and complete detachment can happen as a result of either heart beating or external perturbation (e.g., pulling) (**Figure 3-15E**). This significantly affects the quality and stability of ECG recording.

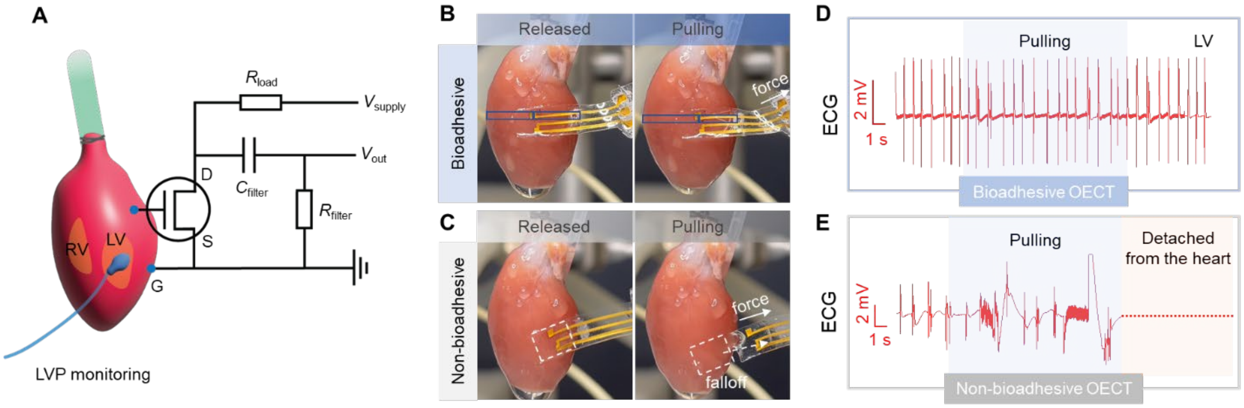

Figure 3-15. *Ex vivo* monitoring of ECG signals on an isolated rat heart. (A) Schematic showing the use of the OECT sensor for ECG recording on a heart surface, and the circuit diagram. (B) Photographs show a fully-bioadhesive OECT attached to an isolated rat heart surface maintaining stable contact during mechanical agitation. (C) Comparison of a non-bioadhesive OECT, for which capillary-based attachment cannot maintain conformable and stable contact. (D) ECG signals recorded by the fully-bioadhesive OECT on the LV. (E) ECG recording by the non-bioadhesive OECT, which ceased after the device detachment from the heart.

We also demonstrate the in vivo use of the bioadhesive OECT on under-skin electromyogram (EMG) recording from the gastrocnemius medialis (GM) muscle of a live rat, for which the OECT can also form stable adhesion by gentle pressing (**Figure 3-16A**). During electrical stimulation of the sciatic nerve for triggering leg movements, EMG signals corresponding to each stimulation can be stably recorded without being affected by mechanical perturbation (e.g., pulling) (**Figure 3-16, B and D**), which is in stark contrast with the non-bioadhesive OECT (**Figure 3-16, C and E**). Furthermore, we also validated the benefits of such direct tissue adhesion as compared to suturing or a separate adhesive layer, in low invasiveness, and/or higher signal amplitude and stability. Such benefits couple with the built-in amplification ability of OECT-based active sensor, as illustrated by the comparison with a PEDOT:PSS-based passive recording device.

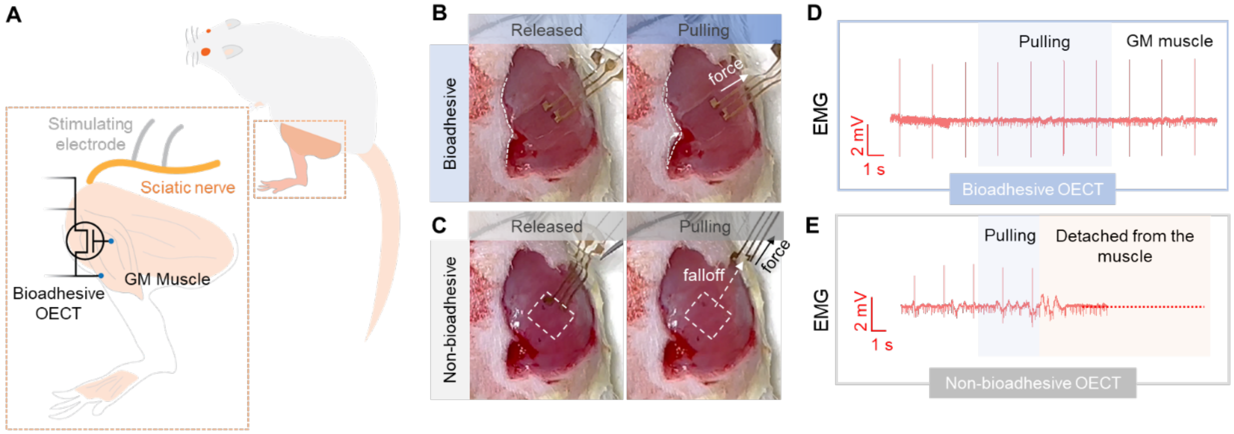

Figure 3-16. *In vivo* monitoring of EMG signals on rat muscles. (A) Schematic showing the use of the OECT sensor for EMG recording on the GM muscles upon stimulation of the sciatic nerve. (B) Photographs showing a fully-bioadhesive OECT attached to the GM muscle maintaining stable contact during mechanical agitation. (C) Comparison of a non-bioadhesive OECT, for which capillary-based attachment cannot maintain conformable and stable contact. (D) EMG signals recorded by the fully-bioadhesive OECT on the GM muscle. (E) EMG signals recorded by the non-bioadhesive OECT on the GM muscle, which ceased after the device detached from the muscles.

3.4 Conclusion

Through designing a new brush-architectured bioadhesive polymer and a double-network morphology with redox-active semiconducting polymers, we successfully imparted bioadhesive properties to semiconducting polymer films, which also combine high electrical performance, tissue-like stretchability, anti-abrasion property, and biocompatibility. These properties, working together, greatly enhance tissue conformability, operation stability, biocompatibility, and signal quality for the use of transistor technology for interfacing with biological systems.

3.5 Appendix

^{1}H NMR spectrum (400 MHz, $CDCl_3$) of compound 1

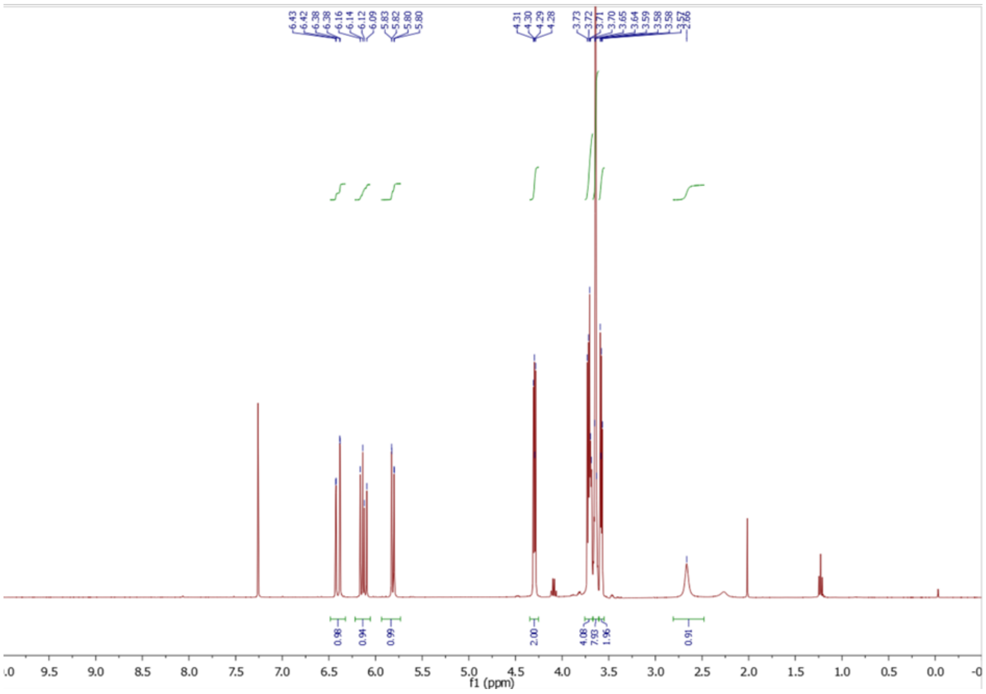

Figure 3-17. ^{1}H NMR spectrum for compound 1

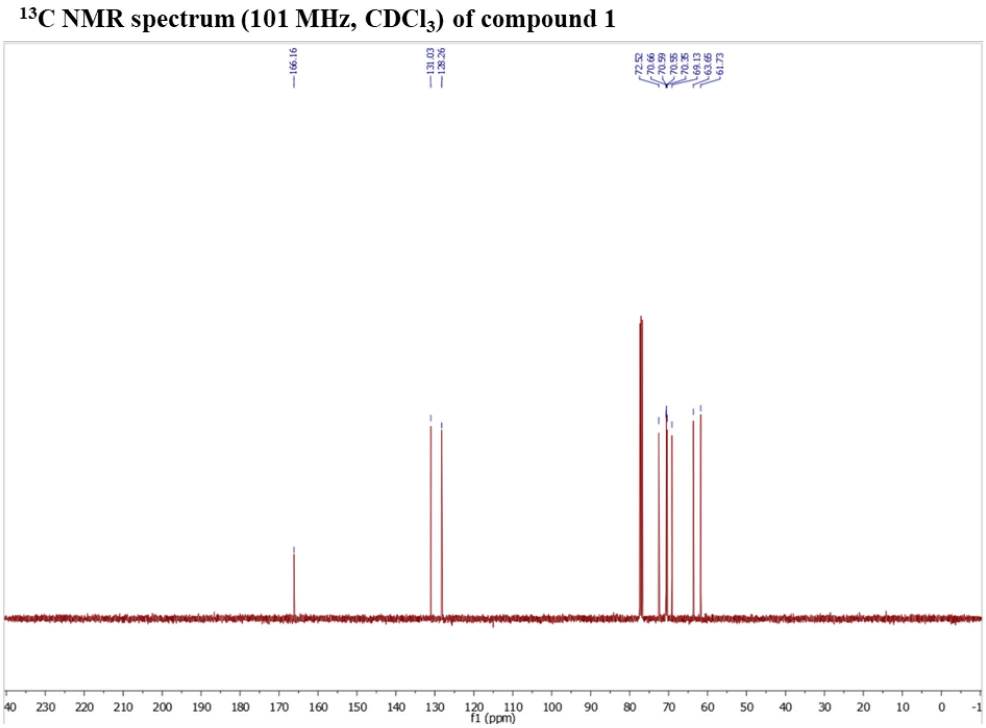

Figure 3-18. ^{13}C NMR spectrum for compound 1

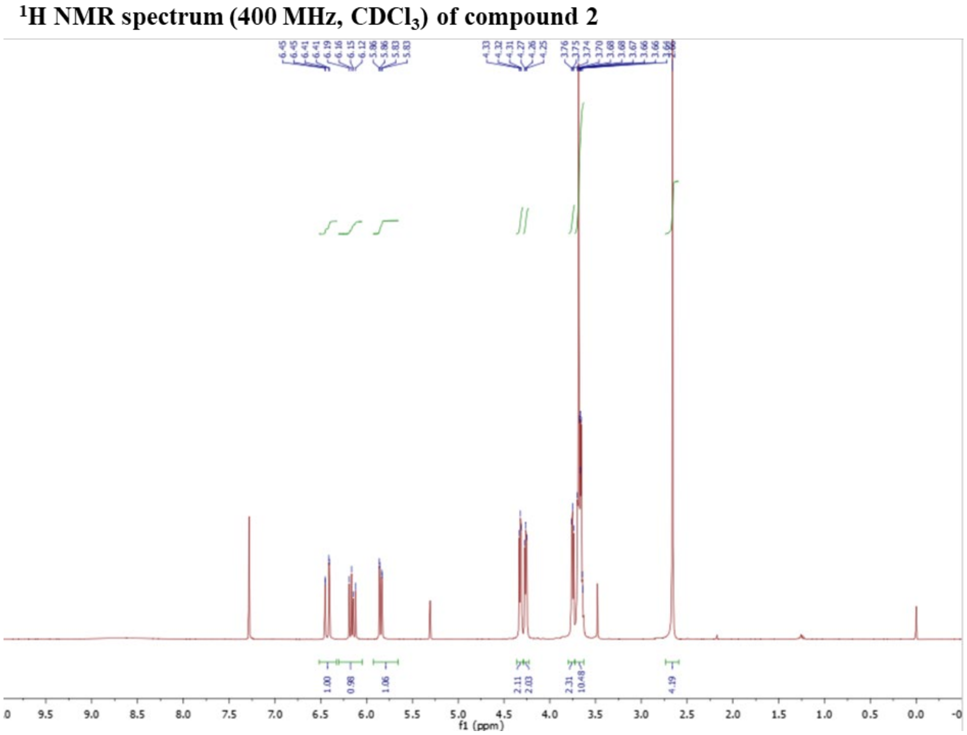

Figure 3-19. ^{1}H NMR spectrum for compound 2

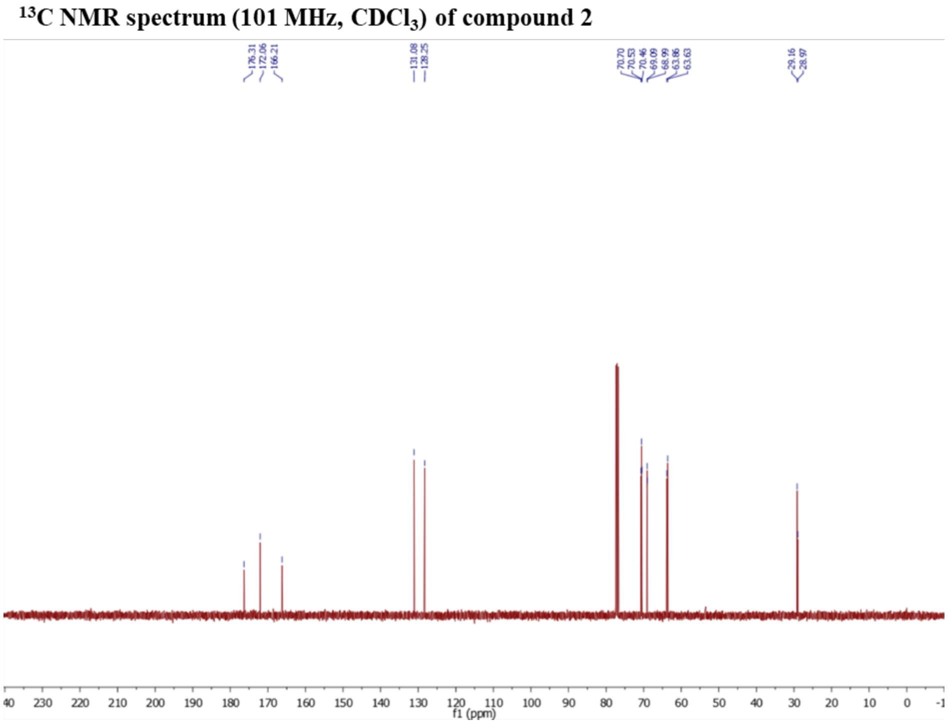

Figure 3-20. ^{13}C NMR spectrum for compound 2

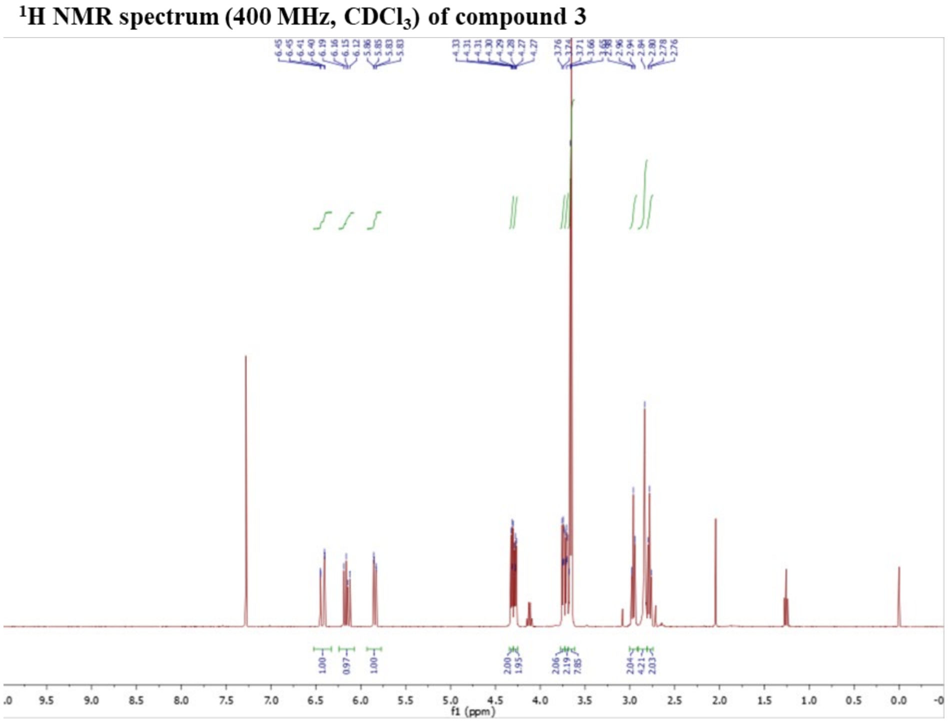

Figure 3-21. ^{1}H NMR spectrum for compound 3

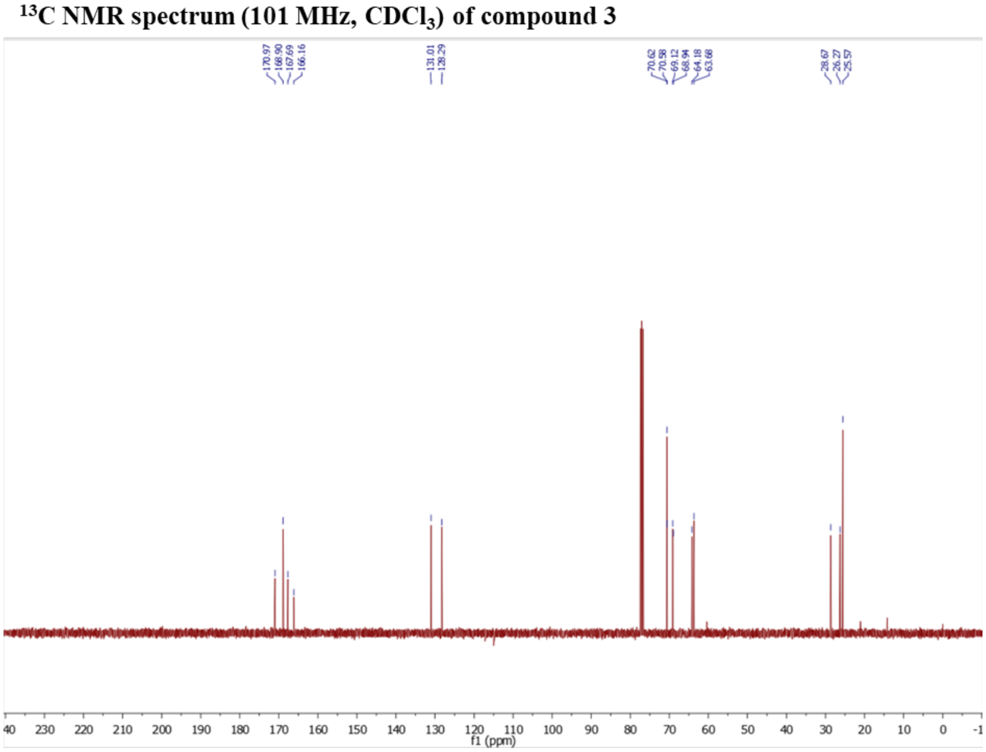

^{13}C NMR spectrum (101 MHz, $CDCl_3$) of compound 3

Figure 3-22. ^{13}C NMR spectrum for compound 3

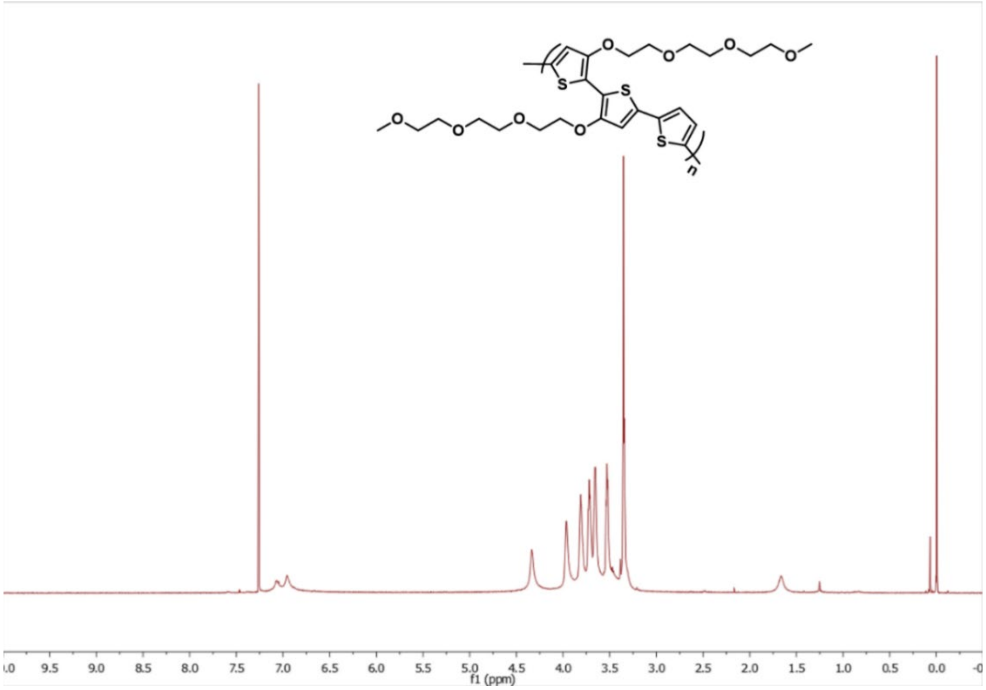

Figure 3-23. ^{1}H NMR spectrum of polymer p(g2T-T)

3.6 References

(1) Sunwoo, S.-H.; Ha, K.-H.; Lee, S.; Lu, N.; Kim, D.-H. Wearable and Implantable Soft Bioelectronics: Device Designs and Material Strategies. *Annual Review of Chemical and Biomolecular Engineering* **2021,** *12*, 359.

(2) Yuk, H.; Lu, B.; Zhao, X. Hydrogel bioelectronics. *Chem Soc Rev* **2019,** *48*, 1642.

(3) You, I.; Mackanic, D. G.; Matsuhisa, N.; Kang, J.; Kwon, J.; Beker, L.; Mun, J.; Suh, W.; Kim, T. Y.; Tok, J. B.-H.et al. Artificial multimodal receptors based on ion relaxation dynamics. *Science* **2020,** *370*, 961.

(4) Rivnay, J.; Wang, H.; Fenno, L.; Deisseroth, K.; Malliaras, G. G. Next-generation probes, particles, and proteins for neural interfacing. *Science Advances* **2017,** *3*, e1601649.

(5) Liu, S.; Rao, Y.; Jang, H.; Tan, P.; Lu, N. Strategies for body-conformable electronics. *Matter* **2022,** *5*, 1104.

(6) Yuk, H.; Wu, J.; Zhao, X. Hydrogel interfaces for merging humans and machines. *Nature Reviews Materials* **2022,** *7*, 935.

(7) Xu, J.; Wang, S.; Wang, G.-J. N.; Zhu, C.; Luo, S.; Jin, L.; Gu, X.; Chen, S.; Feig, V. R.; To, J. W. F.et al. Highly stretchable polymer semiconductor films through the nanoconfinement effect. *Science* **2017,** *355*, 59.

(8) Wang, S.; Xu, J.; Wang, W.; Wang, G. N.; Rastak, R.; Molina-Lopez, F.; Chung, J. W.; Niu, S.; Feig, V. R.; Lopez, J.et al. Skin electronics from scalable fabrication of an intrinsically stretchable transistor array. *Nature* **2018,** *555*, 83.

(9) Jiang, Y.; Zhang, Z.; Wang, Y. X.; Li, D.; Coen, C. T.; Hwaun, E.; Chen, G.; Wu, H. C.; Zhong, D.; Niu, S.et al. Topological supramolecular network enabled high-conductivity, stretchable organic bioelectronics. *Science* **2022,** *375*, 1411.

(10) Dai, Y.; Dai, S.; Li, N.; Li, Y.; Moser, M.; Strzalka, J.; Prominski, A.; Liu, Y.; Zhang, Q.; Li, S.et al. Stretchable Redox-Active Semiconducting Polymers for High-Performance Organic Electrochemical Transistors. *Advanced Materials* **2022,** *34*, 2201178.

(11) Yan, Z.; Xu, D.; Lin, Z.; Wang, P.; Cao, B.; Ren, H.; Song, F.; Wan, C.; Wang, L.; Zhou, J.et al. Highly stretchable van der Waals thin films for adaptable and breathable electronic membranes. *Science* **2022,** *375*, 852.

(12) Sim, K.; Ershad, F.; Zhang, Y.; Yang, P.; Shim, H.; Rao, Z.; Lu, Y.; Thukral, A.; Elgalad, A.; Xi, Y.et al. An epicardial bioelectronic patch made from soft rubbery materials and capable of spatiotemporal mapping of electrophysiological activity. *Nature Electronics* **2020,** *3*, 775.

(13) Yang, Q.; Wei, T.; Yin, R. T.; Wu, M.; Xu, Y.; Koo, J.; Choi, Y. S.; Xie, Z.; Chen, S. W.; Kandela, I.et al. Photocurable bioresorbable adhesives as functional interfaces between flexible bioelectronic devices and soft biological tissues. *Nat Mater* **2021,** *20*, 1559.

(14) Yuk, H.; Varela, C. E.; Nabzdyk, C. S.; Mao, X.; Padera, R. F.; Roche, E. T.; Zhao, X. Dry double-sided tape for adhesion of wet tissues and devices. *Nature* **2019,** *575*, 169.

(15) Wang, X.; Sun, X.; Gan, D.; Soubrier, M.; Chiang, H.-Y.; Yan, L.; Li, Y.; Li, J.; Yu, S.; Xia, Y.et al. Bioadhesive and conductive hydrogel-integrated brain-machine interfaces for conformal and immune-evasive contact with brain tissue. *Matter* **2022,** *5*, 1204.

(16) Han, I. K.; Song, K. I.; Jung, S. M.; Jo, Y.; Kwon, J.; Chung, T.; Yoo, S.; Jang, J.; Kim, Y. T.; Hwang, D. S.et al. Electroconductive, Adhesive, Non-Swelling, and Viscoelastic Hydrogels for Bioelectronics. *Adv Mater* **2022**, DOI:10.1002/adma.202203431 10.1002/adma.202203431, e2203431.

(17) Deng, J.; Yuk, H.; Wu, J.; Varela, C. E.; Chen, X.; Roche, E. T.; Guo, C. F.; Zhao, X. Electrical bioadhesive interface for bioelectronics. *Nat Mater* **2021,** *20*, 229.

(18) Li, S.; Cong, Y.; Fu, J. Tissue adhesive hydrogel bioelectronics. *J Mater Chem B* **2021,** *9*, 4423.

(19) Torricelli, F.; Adrahtas, D. Z.; Bao, Z.; Berggren, M.; Biscarini, F.; Bonfiglio, A.; Bortolotti, C. A.; Frisbie, C. D.; Macchia, E.; Malliaras, G. G.et al. Electrolyte-gated transistors for enhanced performance bioelectronics. *Nat Rev Methods Primers* **2021,** *1*.

(20) Marks, A.; Griggs, S.; Gasparini, N.; Moser, M. Organic Electrochemical Transistors: An Emerging Technology for Biosensing. *Advanced Materials Interfaces* **2022,** *9*.

(21) Rivnay, J.; Inal, S.; Salleo, A.; Owens, R. M.; Berggren, M.; Malliaras, G. G. Organic electrochemical transistors. *Nature Reviews Materials* **2018,** *3*.

(22) Paulsen, B. D.; Tybrandt, K.; Stavrinidou, E.; Rivnay, J. Organic mixed ionic–electronic conductors. *Nature Materials* **2020,** *19*, 13.

(23) Chen, J.; Huang, W.; Zheng, D.; Xie, Z.; Zhuang, X.; Zhao, D.; Chen, Y.; Su, N.; Chen, H.; Pankow, R. M.et al. Highly stretchable organic electrochemical transistors with strain-resistant performance. *Nat Mater* **2022,** *21*, 564.

(24) Jimbo, Y.; Sasaki, D.; Ohya, T.; Lee, S.; Lee, W.; Arab Hassani, F.; Yokota, T.; Matsuura, K.; Umezu, S.; Shimizu, T.et al. An organic transistor matrix for multipoint intracellular action potential recording. *Proceedings of the National Academy of Sciences* **2021,** *118*, e2022300118.

(25) Spyropoulos, G. D.; Gelinas, J. N.; Khodagholy, D. Internal ion-gated organic electrochemical transistor: A building block for integrated bioelectronics. *Science Advances* **2019,** *5*, eaau7378.

(26) Cea, C.; Spyropoulos, G. D.; Jastrzebska-Perfect, P.; Ferrero, J. J.; Gelinas, J. N.; Khodagholy, D. Enhancement-mode ion-based transistor as a comprehensive interface and real-time processing unit for in vivo electrophysiology. *Nat Mater* **2020,** *19*, 679.

(27) Bidinger, S. L.; Keene, S. T.; Han, S.; Plaxco, K. W.; Malliaras, G. G.; Hasan, T. Pulsed transistor operation enables miniaturization of electrochemical aptamer-based sensors. *Science Advances* **2022,** *8*, eadd4111.

(28) Guo, K.; Wustoni, S.; Koklu, A.; Diaz-Galicia, E.; Moser, M.; Hama, A.; Alqahtani, A. A.; Ahmad, A. N.; Alhamlan, F. S.; Shuaib, M.et al. Rapid single-molecule detection of COVID-19 and MERS antigens via nanobody-functionalized organic electrochemical transistors. *Nat Biomed Eng* **2021,** *5*, 666.

(29) Li, J.; Celiz, A. D.; Yang, J.; Yang, Q.; Wamala, I.; Whyte, W.; Seo, B. R.; Vasilyev, N. V.; Vlassak, J. J.; Suo, Z.et al. Tough adhesives for diverse wet surfaces. *Science* **2017,** *357*, 378.

(30) Xue, B.; Gu, J.; Li, L.; Yu, W.; Yin, S.; Qin, M.; Jiang, Q.; Wang, W.; Cao, Y. Hydrogel tapes for fault-tolerant strong wet adhesion. *Nat Commun* **2021,** *12*, 7156.

(31) Ma, Z.; Bourquard, C.; Gao, Q.; Jiang, S.; De Iure-Grimmel, T.; Huo, R.; Li, X.; He, Z.; Yang, Z.; Yang, G.et al. Controlled tough bioadhesion mediated by ultrasound. *Science* **2022,** *377*, 751.

(32) Chortos, A.; Lim, J.; To, J. W. F.; Vosgueritchian, M.; Dusseault, T. J.; Kim, T.-H.; Hwang, S.; Bao, Z. Highly Stretchable Transistors Using a Microcracked Organic Semiconductor. *Advanced Materials* **2014,** *26*, 4253.

(33) Inoue, A.; Yuk, H.; Lu, B.; Zhao, X. Strong adhesion of wet conducting polymers on diverse substrates. *Science Advances* **2020,** *6*, eaay5394.

(34) Zhang, S.; Ocheje, M. U.; Luo, S.; Ehlenberg, D.; Appleby, B.; Weller, D.; Zhou, D.; Rondeau-Gagné, S.; Gu, X. Probing the Viscoelastic Property of Pseudo Free-Standing Conjugated Polymeric Thin Films. *Macromolecular Rapid Communications* **2018,** *39*, 1800092.

(35) Zhang, L.; Kumar, K. S.; He, H.; Cai, C. J.; He, X.; Gao, H.; Yue, S.; Li, C.; Seet, R. C.; Ren, H.et al. Fully organic compliant dry electrodes self-adhesive to skin for long-term motion-robust epidermal biopotential monitoring. *Nat Commun* **2020,** *11*, 4683.

(36) Prominski, A.; Shi, J.; Li, P.; Yue, J.; Lin, Y.; Park, J.; Tian, B.; Rotenberg, M. Y. Porosity-based heterojunctions enable leadless optoelectronic modulation of tissues. *Nat Mater* **2022,** *21*, 647.

(37) Nielsen, C. B.; Giovannitti, A.; Sbircea, D. T.; Bandiello, E.; Niazi, M. R.; Hanifi, D. A.; Sessolo, M.; Amassian, A.; Malliaras, G. G.; Rivnay, J.et al. Molecular Design of Semiconducting Polymers for High-Performance Organic Electrochemical Transistors. *J Am Chem Soc* **2016,** *138*, 10252.

(38) Inal, S.; Malliaras, G. G.; Rivnay, J. Benchmarking organic mixed conductors for transistors. *Nat Commun* **2017,** *8*, 1767.

(39) Tringides, C. M.; Vachicouras, N.; de Lazaro, I.; Wang, H.; Trouillet, A.; Seo, B. R.; Elosegui-Artola, A.; Fallegger, F.; Shin, Y.; Casiraghi, C.et al. Viscoelastic surface electrode arrays to interface with viscoelastic tissues. *Nat Nanotechnol* **2021,** *16*, 1019.

(40) Zhang, M.; Müller, A. H. E. Cylindrical polymer brushes. *Journal of Polymer Science Part A: Polymer Chemistry* **2005,** *43*, 3461.

(41) Dashtimoghadam, E.; Fahimipour, F.; Keith, A. N.; Vashahi, F.; Popryadukhin, P.; Vatankhah-Varnosfaderani, M.; Sheiko, S. S. Injectable non-leaching tissue-mimetic bottlebrush elastomers as an advanced platform for reconstructive surgery. *Nat Commun* **2021,** *12*, 3961.

(42) Marblestone*, A.; Zamft*, B.; Maguire, Y.; Shapiro, M.; Cybulski, T.; Glaser, J.; Amodei, D.; Stranges, P. B.; Kalhor, R.; Dalrymple, D.et al. Physical principles for scalable neural recording. *Frontiers in Computational Neuroscience* **2013,** *7*.

(43) Du, J.; Riedel-Kruse, I. H.; Nawroth, J. C.; Roukes, M. L.; Laurent, G.; Masmanidis, S. C. High-Resolution Three-Dimensional Extracellular Recording of Neuronal Activity With Microfabricated Electrode Arrays. *Journal of Neurophysiology* **2009,** *101*, 1671.

(44) Herreras, O. Local Field Potentials: Myths and Misunderstandings. *Frontiers in Neural Circuits* **2016,** *10*.

(45) Pérez-Prieto, N.; Delgado-Restituto, M. Recording Strategies for High Channel Count, Densely Spaced Microelectrode Arrays. *Frontiers in Neuroscience* **2021,** *15*.

(46) Chen, A. X.; Kleinschmidt, A. T.; Choudhary, K.; Lipomi, D. J. Beyond Stretchability: Strength, Toughness, and Elastic Range in Semiconducting Polymers. *Chemistry of Materials* **2020,** *32*, 7582.

(47) Capuani, S.; Malgir, G.; Chua, C. Y. X.; Grattoni, A. Advanced strategies to thwart foreign body response to implantable devices. *Bioeng Transl Med* **2022,** *7*, e10300.

(48) Biran, R.; Martin, D. C.; Tresco, P. A. Neuronal cell loss accompanies the brain tissue response to chronically implanted silicon microelectrode arrays. *Exp Neurol* **2005,** *195*, 115.

(49) Matsuhisa, N.; Chen, X.; Bao, Z.; Someya, T. Materials and structural designs of stretchable conductors. *Chem Soc Rev* **2019,** *48*, 2946.

(50) Lee, Y.; Chung, J. W.; Lee, G. H.; Kang, H.; Kim, J.-Y.; Bae, C.; Yoo, H.; Jeong, S.; Cho, H.; Kang, S.-G.et al. Standalone real-time health monitoring patch based on a stretchable organic optoelectronic system. *Science Advances* **2021,** *7*, eabg9180.

Chapter 4. Immune-compatible designs of semiconducting polymers for suppressed foreign-body response

4.1 Introduction

For bioimplants, including bioelectronic implants, foreign-body response (FBR) is the major biocompatibility issue that limits the functional longevity of the implants and causes side effects for patients[1-3]. As a type of immune-mediated reaction to foreign/synthetic materials, FBR typically starts from nonspecific protein absorption, which triggers the cascade of immune cell (e.g., macrophages, fibroblasts) recruitment, foreign body giant cell (FBGC) formation, collagen deposition, and eventually encapsulates the functional implants[4] (**Figure 4-1**). For bioelectronic devices in particular, this often leads to a substantial increase of device-tissue interface impedance and decreased signal amplitude for the transduction of electrical or chemical signals[3,5-7]. With FBR being a material-initiated process, immunology studies have found that both the chemical (wettability, functional groups, etc.)[1,8] and physical (stiffness, size, tomography, etc.)[9-11] properties of implanted materials influence FBR outcomes.

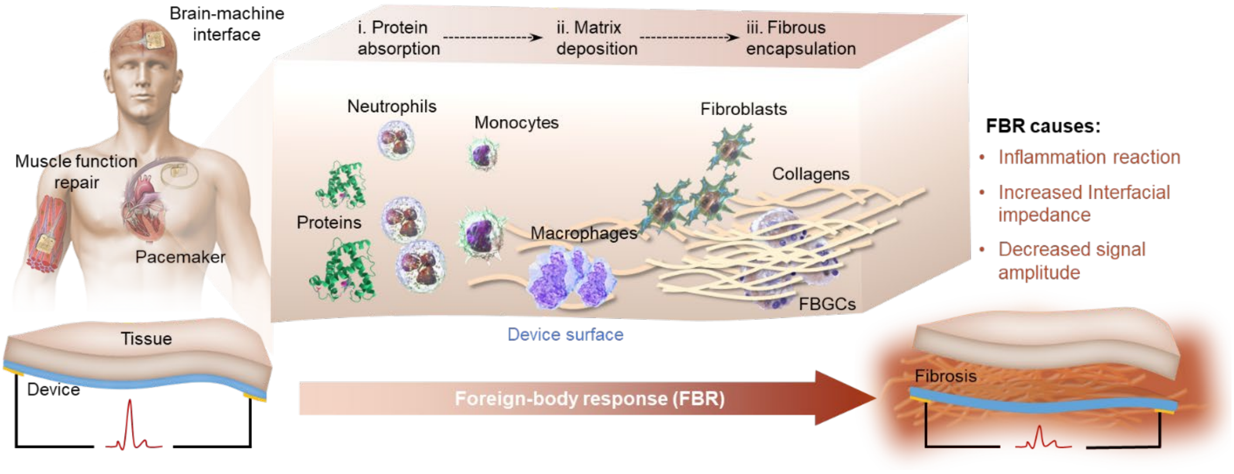

Figure 4-1. Schematics illustrating the development of foreign-body response on implantable devices and the influences.

To date, substantial efforts and progress have been made on the designs of non-electronic biomaterials to achieve suppressed FBR. For example, for hydrogels for drug delivery and tissue engineering applications, the strategies of incorporating anti-biofouling[12-14] and immunomodulatory[15-17] moieties have been shown to be highly effective in suppressing FBR. However, for electronic materials, in particular semiconductors which, in a lot of bioelectronic devices, need to be exposed on surfaces for signal transduction[18,19], very few efforts have been made in FBR-suppressing designs. Despite the possibility of mitigating this material-originated issue by applying immune-compatible surface coating[20-22] or releasing anti-inflammatory drugs[21,23,24], achieving intrinsic immune-compatible properties on implantable semiconductors is more desirable in avoiding increased surface impedance and limited efficacy period.

To interface with biological systems, semiconducting polymers have been shown as one of the most promising electronic materials for simultaneously providing amplified biosensing, tunable optoelectronic response, mechanical flexibility, and chemical versatility[18,19,25]. Recently, significant efforts have been made to achieve tissue-like mechanical properties (i.e., softness[26-28] and stretchability[29,30]), which indeed could help to suppress FBR. However, major gaps still exist in developing immune-compatible semiconducting polymers. First, there have not been any rigorous characterizations of FBR behaviors for semiconducting polymers. So far, the reported biocompatibility test often just focuses on *in vitro* cytotoxicity or cell adhesion[19,31-33]. As such, the influences of different chemical designs and physical properties of semiconducting polymers on FBR behaviors remain elusive. Second, for the molecular designs of semiconducting polymers, which is generally the primary factor dictating FBR, there has not been any design strategy reported for suppressing FBR. Compared to non-electrical polymers, creating such immune-compatible designs for semiconducting polymers is even more challenging with the need to minimize the sacrifice of electrical performance.

Here, we present a suite of design strategies for incorporating immunomodulatory moieties into both the backbones and side chains of semiconducting polymers, which substantially suppress the elicited FBR as indicated by as high as a 68% decrease in collagen density. By further carrying out a suite of systematic and rigorous immunological assays that are of little precedence for semiconducting polymers, which include PCR-based collagen quantification, cytokine assays, combined with an *in vitro* mechanistic study of anti-inflammatory effect, we obtained a relatively complete and mechanistic picture of the suppression effect on the FBR. Through measurement in OECT devices, these designs are shown to cause little sacrifice to the electrical performance of semiconducting polymers, with charge-carrier mobility maintaining ~1 $cm^2\ V^{-1}\ s^{-1}$.

4.2 Experimental section

Materials and characterizations

The chemicals used in the study, including tetra(ethylene glycol), copper (I) iodide, copper (I) bromide, potassium *tert*-butoxide, iodine, triphenylphosphine, imidazole, *N*-bromosuccinimide, sodium azide, selenophene, *n*-butyllithium, trimethyltin chloride, *N,N,N,N,N*-pentamethyldiethylenetriamine, 2,5-bis(trimethylstannyl)thiophene, trimethyl(phenyl)tin, bromobenzene, anhydrous dichloromethane (DCM), anhydrous chloroform, anhydrous dimethylformamide (DMF), and anhydrous chlorobenzene were purchased from Sigma-Aldrich and used without further purification. 3,3′-Dibromo-2,2′-bithiophene was purchased from Chemscene. 4-Propargylthiomorpholine 1,1-dioxide was purchased from TCI. Tetrahydro-2-(2-propynyloxy)-2H-pyran was purchased from Oakwood Chemical. 5,5'-Dibromo-3,3'-bis(2-(2-(2-

methoxyethoxy)ethoxy)ethoxy)-2,2'-bithiophene was purchased from SunaTech Inc. SEBS was obtained from Asahi Kasei.

Microwave polymerization was conducted using a Biotage Initiator +. Nuclei magnetic resonance (NMR) spectra were recorded on a Bruker Avance III HD console spectrometer (^{1}H 400 MHz, ^{13}C 100 MHz) at 293 K. Chemical shifts are given in parts per million (ppm) with respect to tetramethylsilane as an internal standard, and coupling constants (J) are given in Hertz (Hz). High-resolution mass spectra (HR-MS) were recorded on an Agilent 6530 LC Q-TOF mass spectrometer using electrospray ionization with fragmentation voltage set at 70 V and processed with an Agilent MassHunter Operating System. Number average molecular weight (M_n), weight average molecular weight (M_w), and polydispersity index (PDI) were evaluated by Tosoh EcoSEC size exclusion chromatography system (GPC) using DMF + 0.01 M LiBr as eluent (50 ºC) calibrated with polystyrene standards. The UV-Vis absorption spectra were recorded on the Shimadzu UV-3600 Plus UV-VIS-NIR spectrophotometer. The atomic force microscope (AFM) imaging was done with the Bruker Multimode 8 AFM. The depth-profiling X-ray photoelectron spectroscopy (XPS) was done with Kratos AXIS Nova with a monochromatic Al Kα X-ray source and a delay line detector (DLD) system with Ar1000+ with 5 keV to etch. Grazing-incidence X-ray diffraction (GIXD) was performed at the Advanced Photon Source at Argonne National Laboratory on beamline 8-ID-E[34], with photon energy 10.92 keV and collimated beam 200 μm x 10 μm (H x V) incident on the sample at an incident angle of 0.13°. GIXD samples were prepared by transferring thin films from OTS-treated substrates to Si wafer pieces. Samples were maintained in a rough vacuum environment (10^{-3} mbar) during measurements, 217 mm away from a pixel array detector (Pilatus 1M, Dectris). Pairs of exposures of 5 seconds each with different detector heights were captured and combined to fill in gaps between the detector modules, demonstrating that the scattering pattern did not change during the measurement. The Matlab package GIXSGUI[35] was used to apply all necessary corrections and combine the images, as well as to compute integrations (linecuts). The relative degree of crystallinity (rDoC) for each sample was computed from the sine-weighted integration of the partial pole figure for the (100) lamellar feature in each pattern and normalized by the sample thickness. The lamellar spacing was calculated for the out-of-plane (100) peak. The 2D images are displayed on the same (logarithmic) false color intensity scale.

Synthesis of azide-functionalized g2T monomer (4)

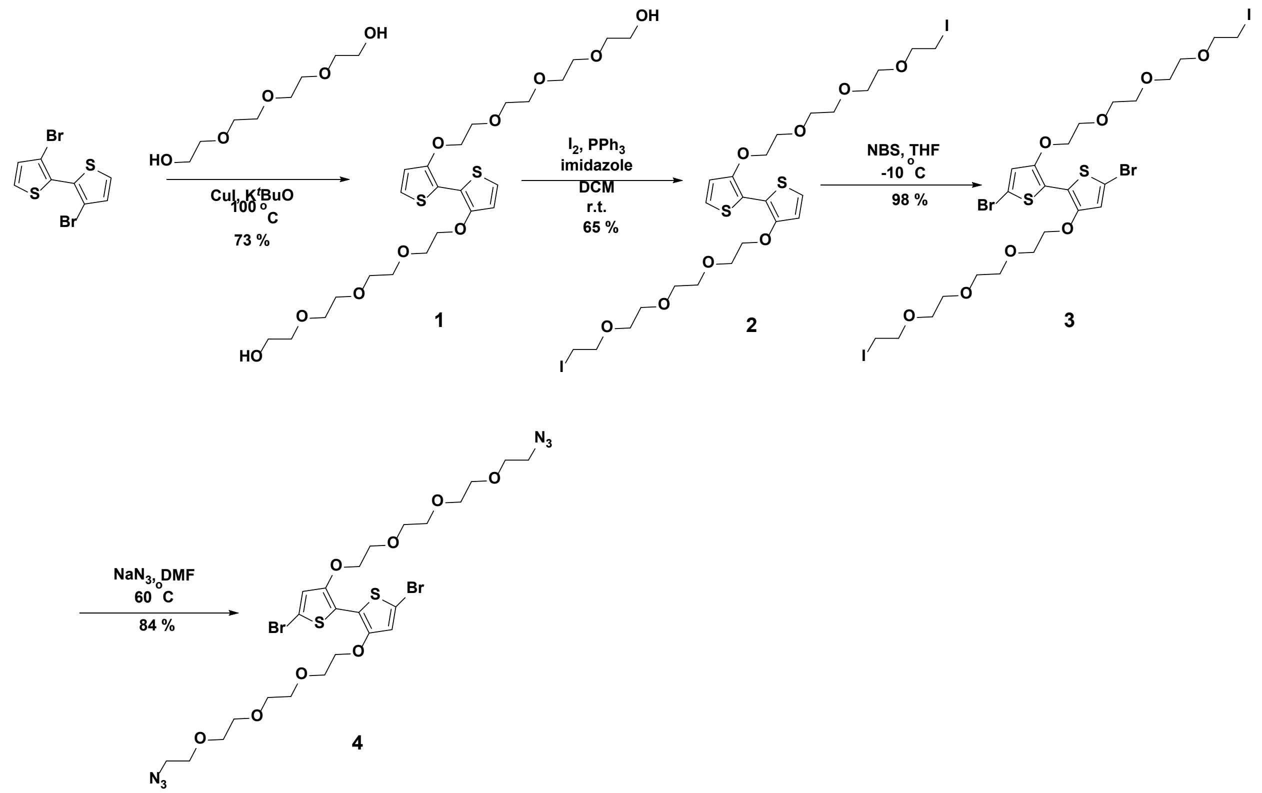

2,2'-((((((([2,2'-bithiophene]-3,3'-diylbis(oxy))bis(ethane-2,1-diyl))bis(oxy))bis(ethane-2,1-diyl))bis(oxy))bis(ethane-2,1-diyl))bis(oxy))bis(ethan-1-ol) (1)

To a nitrogen gas filled round bottom flask (RBF) with a stirring bar, potassium *tert*-butoxide (37.3 mmol, 4.2 g), copper (I) iodide (5 mmol, 0.95 g), 3,3′-dibromo-2,2′-bithiophene (12.4 mmol, 4 g), and tetra(ethylene glycol) (12.4 mmol, 24 g) were added. The mixture was heated to 100 °C for 20 h. Then the mixture was cooled to room temperature and filtered. The solid was washed with DCM and the organic phase was washed with 1M HCl and brine successively. The solvent was removed using rotary evaporation and purified by column chromatography (silica gel, EA). The final solid was isolated as a yellow oil (5 g, 73 %). ^{1}H NMR (400 MHz, $CDCl_3$) δ 7.07 (d, *J* = 5.5 Hz, 2H), 6.85 (d, *J* = 5.5 Hz, 2H), 4.25 (t, *J* = 4.8 Hz, 4H), 3.90 (t, *J* = 4.8 Hz, 4H), 3.79 – 3.72 (m, 4H), 3.72 – 3.62 (m, 16H), 3.62 – 3.55 (m, 4H), 2.46 (s, 2H); ^{13}C NMR (101 MHz, $CDCl_3$) δ 151.74, 121.94, 116.59, 115.00, 114.72, 72.47, 71.40, 70.93, 70.67, 70.38, 70.06, 61.76. HRMS (ESI) Calcd for $C_{24}H_{39}O_{10}S_2$ [M+H]+ : 551.1979, found 551.1989.

3,3'-bis(2-(2-(2-(2-iodoethoxy)ethoxy)ethoxy)ethoxy)-2,2'-bithiophene (2)

To a nitrogen gas filled RBF with I_2 (14.2 mmol, 3.6 g), imidazole (16.4 mmol, 1.1 g), and **1** (5.4 mmol, 3 g) in 40 mL DCM, PPh_3 (13.1 mmol, 3.4 g) in DCM was added at 0 °C. The mixture was stirred at room temperature overnight. After that, the organic phase was washed with brine. The solvent was removed using rotary evaporation and purified by column chromatography (silica gel, EA/hexane = 1/1). The final solid was isolated as a yellow oil (2.4 g, 65 %). ^{1}H NMR (400 MHz, $CDCl_3$) δ 7.08 (d, *J* = 5.6 Hz, 2H), 6.85 (d, *J* = 5.6 Hz, 2H), 4.29 – 4.19 (m, 4H), 3.96 – 3.86 (m, 4H), 3.74 (dt, J = 9.5, 5.8 Hz, 8H), 3.71 – 3.60 (m, 12H), 3.30 – 3.18 (m, 4H). ^{13}C NMR (101 MHz, $CDCl_3$) δ 150.21, 119.65, 115.85, 110.06, 71.71, 70.95, 70.79, 70.73, 70.04, 69.89, 50.70. HRMS (ESI) Calcd for $C_{24}H_{37}I_2O_8S_2$ [M+H]+ : 771.0014, found 771.0022.

5,5'-dibromo-3,3'-bis(2-(2-(2-(2-iodoethoxy)ethoxy)ethoxy)ethoxy)-2,2'-bithiophene (3)

To a nitrogen gas filled RBF, **2** (2.2 mmol, 1.5 g) was dissolved in 30 mL THF and cooled to -10 °C. NBS (4.6 mmol, 0.81 g) in 10 mL THF was added to the solution dropwise. The mixture was stirred at room temperature for 2 h. Then the mixture was quenched with sodium sulfite aqueous solution. The mixture was washed with brine and extracted with DCM. The solvent was removed using rotary evaporation and purified by column chromatography (silica gel, EA/hexane = 1/1). The final solid was isolated as a yellow oil (1.8 g, 98 %). ^{1}H NMR (400 MHz, $CDCl_3$) δ 6.85 (s, 2H), 4.25 – 4.13 (m, 4H), 3.93 – 3.83 (m, 4H), 3.72 (ddd, *J* = 15.0, 13.3, 8.4 Hz, 20H), 3.25 (t, *J* = 6.9 Hz, 4H); ^{13}C NMR (101 MHz, $CDCl_3$) δ 150.20, 119.65, 115.85, 110.07, 72.00, 71.72, 70.97, 70.80, 70.72, 70.27, 69.92. HRMS (ESI) Calcd for $C_{24}H_{35}Br_2I_2O_8S_2$ [M+H]+ : 926.8224, found 926.8225.

3,3'-bis(2-(2-(2-(2-azidoethoxy)ethoxy)ethoxy)ethoxy)-5,5'-dibromo-2,2'-bithiophene (4)

To a nitrogen gas filled RBF, **3** (1.2 mmol, 1 g) was dissolved in 30 mL DMF. NaN_3 (7.2 mmol, 0.47 g) in 10 mL DMF was added to the solution dropwise. The mixture was stirred at 60 °C overnight. The mixture was washed with brine and extracted with DCM. The solvent was removed using rotary evaporation and purified by column chromatography (silica gel, EA/hexane = 1/1). The final solid was isolated as a yellow oil (0.76 g, 84 %). ^{1}H NMR (400 MHz, $CDCl_3$) δ 6.85 (s, 2H), 4.20 (t, *J* = 4.7 Hz, 4H), 3.87 (t, *J* = 4.7 Hz, 4H), 3.78 – 3.61 (m, 20H), 3.38 (t, *J* = 4.9 Hz, 4H); ^{13}C NMR (101 MHz, $CDCl_3$) δ 150.21, 119.65, 115.85, 110.06, 71.71, 70.95, 70.79, 70.73, 70.04, 69.89, 50.70. HRMS (ESI) Calcd for $C_{24}H_{35}Br_2N_6O_8S_2$ [M+H]+ : 757.0319, found 757.0302.

Synthesis of 2,5-bis(trimethylstannyl)selenophene

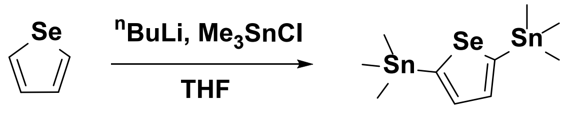

To a nitrogen gas filled RBF with selenophene (10 mmol, 1.3 g) in THF, *n*-butyllithium (21.8 mmol, 12.8 mL) was added dropwise at -78 ºC. The reaction was stirred at r.t. for 30 min. The mixture was cooled to -78 ºC. Trimethyltin chloride (25 mmol, 25 mL) was then added dropwise. The mixture was warmed to r.t and stirred overnight. After that, the mixture was poured into water and was extracted with diethyl ether. The organic phase was then concentrated. The final product was recrystallized from methanol as white solids (1.5 g, 33 %). ^{1}H NMR (400 MHz, $CDCl_3$) δ 7.68 (s, 2H), 0.47 – 0.27 (m, 18H). ^{13}C NMR (101 MHz, $CDCl_3$) δ 150.18, 138.70, -7.78.

Synthesis of p(g2T-T)-a and p(g2T-Se)-a polymers

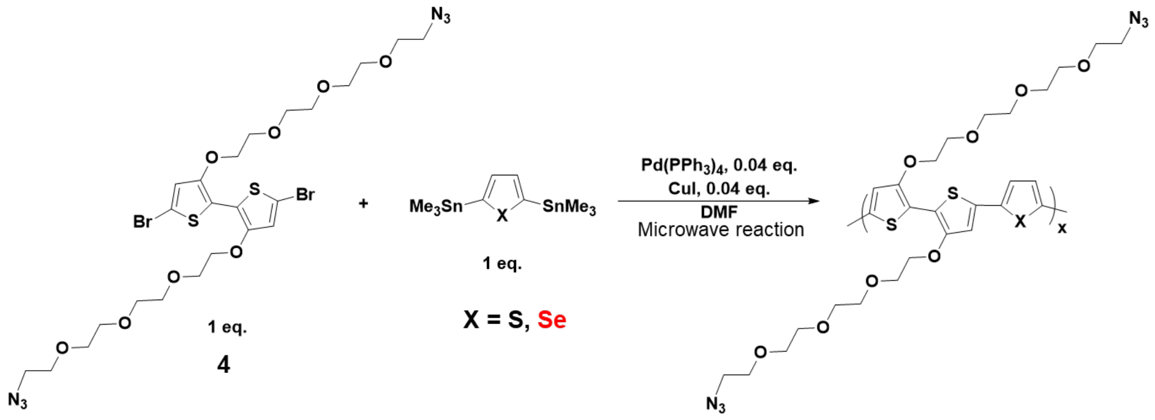

To a mixture of **4** (50 mg, 0.0774 mmol, 1.0 eq.), 2,5-bis(trimethylstannyl)thiophene (31.9 mg, 0.0774 mmol, 1.0 eq.), (or 2,5-bis(trimethylstannyl)selenophene (35.6 mg, 0.0774 mmol, 1.0 eq.)), $Pd(PPh_3)_4$ (3.6 mg, 0.0031 mmol, 0.04 eq.), and CuI (0.6 mg, 0.0031 mmol, 0.04 eq.) was added 2 mL of anhydrous DMF in a nitrogen filled glovebox. The reaction vial was sealed and submitted to a microwave reactor with the following temperature profile: 2 min at 80 °C and 6 min at 100 °C. After the reaction was cooled down, 10 mol% of trimethyl(phenyl)stannane were added and the crude polymer solution was heated again to 2 min at 80 °C. To complete the end-capping of the polymer, 10 mol% of bromobenzene were added and the reaction vessel submitted one last time to microwave heating (2 min at 80 °C). The crude polymer was then precipitated into methanol, filtered, loaded to a Soxhlet thimble and washed successively with hexane, ethyl acetate (each for 24 h). The polymer was finally collected from the thimble with chloroform. The chloroform solution was then concentrated to give the blue polymer named as p(g2T-T)-a or p(g2T-Se)-a. The molecular weights are listed in **Table 4-1**.

CLIP-method-based side chain functionalization

The semiconducting polymer p(g2T-T)-a or p(g2T-Se)-a was dissolved in chloroform. The solution was spin-coated on a *n*-octadecyltrimethoxysilane (OTS) layer modified substrate at 1000 rpm/min for 1 min and then annealed at 110 ºC for 1 min in a nitrogen-filled glovebox. The precursor solution was prepared by dissolving the alkyne-attached precursor molecules (4-propargylthiomorpholine 1,1-dioxide or tetrahydro-2-(2-propynyloxy)-2H-pyran) (~2 mM), copper (I) bromide (~0.2 mM), and *N,N,N,N,N*-pentamethyldiethylenetriamine (PMDETA, ~2 mM) in nitrogen gas-purged methanol in a vial in the glovebox. The solution was thoroughly mixed to become light blue color. The deposited conjugated polymer film on a substrate was submerged in the precursor solution overnight to allow the in-film side chain functionalization to happen. After that, the films were taken out from the vial outside the glovebox and washed with water and methanol for several cycles. The film was blown to dry using nitrogen gas.

OECT fabrication and characterization

First, a glass substrate was cleaned with acetone, isopropyl alcohol, and water, successively. After that, the source/drain gold electrodes (60-nm thick) were patterned via e-beam evaporation with a metal shadow mask. The channel length (*L*) and width (*W*) are 200 µm and 4 mm, respectively. The semiconducting polymer films were transferred onto the channel area using a PDMS stamp.

The electrolyte of 0.1 M NaCl in water was dropped on top of the channel. The gate electrode was served by Ag/AgCl. The performance of the fabricated OECTs was measured using Keithley 4200 in an ambient environment.

The charge-carrier mobility was measured using the constant gate current method[36,37].

Mice and cell line

Male C57BL/6 mice (6-8 weeks) were purchased from Charles River Laboratory. RAW 264.7 cell line was obtained from ATCC and was cultured according to instructions. RAW 264.7 cell line was routinely checked for mycoplasma contamination. All the animal experiments performed in this research were approved by the Institutional Animal Care and Use Committee for the University of Chicago.

In vitro cell viability assay

RAW 264.7 cells (60,000 cells per well) were incubated with various semiconducting polymer-coated SEBS substrates in a 48-well plate for 24 h. The cell culture media was DMEM (Gibco) containing 10 % heat-inactivated fetal bovine serum (FBS), 1 mM sodium pyruvate, 55 mM HEPES, and 1 % penicillin-streptomycin. Then, MTT assay and Live/Dead cell staining were conducted for cell viability assay. MTT assay was measured using a plate reader (Biotek). Live/dead cell imaging was taken using EVOSTM M7000 imaging system (Invitrogen).

In vivo implantation experiment

The semiconducting polymer films (thickness of ~150 nm) were transferred onto both sides of O_2-plasma-treated SEBS substrates (thickness of ~ 0.8 mm). Implants were prepared by punching the substrates into circular disks with a diameter of 5 mm. The implants were sterilized using 70 %

ethanol and UV sterilization for 20 min each. During the implantation, the back skin of the mouse was depilated with a razor and disinfected with isopropyl alcohol tissue and povidone-iodine tissue. The backside skin of the mouse was minimally incised, and the materials were implanted in the subcutaneous region. Then, the incise was closed by a skin clip.

Tissue staining and imaging

The harvested skins were incubated in 2 % PFA for 2 days at 4 ºC for fixation. The fixed skins underwent paraffin embedding process and were sectioned into 5 μm thickness. Masson's trichrome staining was conducted by Human Tissue Resource Center, The University of Chicago. Bright-field imaging was conducted using EVOSTM M7000 imaging system (Invitrogen).

For fluorescence staining, the sectioned slide was conducted deparaffination process and perm/blocking process in (0.3 % Triton X-100, 1 % BSA in PBS) for 3 h at room temperature. The slides were washed with PBS for 3 times and incubated in primary antibody solution (0.1 % tween 20 in PBS) for overnight at 4 ºC. Then, the slides were washed with PBS for 3 times and incubated in secondary antibody (solution) for 2 h at room temperature followed by washing with PBS for 3 times. The slides were stained with DAPI and covered by mounting solution. Antibody information: Anti-alpha smooth muscle Actin antibody (EPR5368, abcam), CD68 Monoclonal Antibody (FA-11, Invitrogen), Donkey anti-Rat IgG (H+L) Alexa FluroTM 594 Secondary Antibody, and Goat anti-Rabbit IgG Alexa FluorTM 647 Secondary Antibody (Invitrogen). The fluorescence imaging was conducted using Olympus confocal microscopy imaging system.

In vivo collagen mRNA expression level

The harvested mouse skin was chopped, and total RNA was isolated using a conventional RNA extraction kit (Qiagen). cDNA synthesis and polymerase chain reaction (PCR) process were conducted using conventional reverse transcriptase (Invitrogen) and PCR premix kit (Thermofisher).

In vivo cytokine/chemokine expression level

The harvested mouse skin was chopped and added to T-PER (Thermofisher Scientific) containing protease inhibitor (Thermofisher Scientific). The skin lysis was conducted using Lysis Matrix D (MP Biomedicals) and recommended protocol. The lysis solution was centrifuged at 20k rcf, 4 ºC for 20 min to remove tissue fragments. Cytokines or chemokines concentration in supernatants were measured using Legendplex (Biolegend) or ELISA (Invitrogen).

In vitro evaluation of the inhibitory effect on inflammation signals

RAW 264.7 cells (60,000 cells per well) were seeded to a 48-well plate and incubated in a cell incubator for 24 h. The cell media was carefully exchanged with the cell media (5 % DMSO) containing various doses of monomers or polymers for 6 h. Then, LPS (final concentration was 25 ng/mL) was added to this cell media, and the cells were incubated for 12 h for the stimulation of the inflammation signal. After the stimulation, the cells were fixed using BD Lyse/Fix buffer for 10 min at 37 ºC and subsequently permeabilized using BD Phosflow Perm Buffer III for 30 min at 4 ºC. The cells were stained with anti-pERK BV421 (clone: 6B8B69, Biolegend), anti-p-p38 PE (clone: A16016A, Biolegend), anti-iNOS Alexa FluroTM 488 (clone: CXNFT, Invitrogen), and anti-pJNK Alexa FluroTM 647 (clone: N9-66, BD) overnight at 4 ºC (dilution factor was 1:50). The cells were acquired using BD LSR flow cytometer and data was analyzed using FlowJo (TreeStar).

In vitro ROS evaluation

RAW 264.7 cells (30,000 cells per well) were seeded to a 96-well plate and incubated in a cell incubator for 24 h. The cell media was carefully exchanged with the cell media (5 % DMSO) containing polymers (final concentration was 20 μg/L) or monomers (final concentration was 1 mmol/L) for 6 h. Then, LPS (final concentration was 25 ng/mL) was added to the media, and the cells were incubated for 3 h for stimulation of the inflammation signal. After the stimulation, the cells were washed using PBS twice and incubated with PBS containing 2',7'-dichlorodihydrofluorescein diacetate (DCFH2-DA, finial concentration was 5 μM) for 30 min. Then, the cells were washed using PBS twice and resuspended in a flow buffer (PBS with 2 % FBS). The cells were acquired using BD LSR flow cytometer and data was analyzed using FlowJo (TreeStar).

4.3 Results and discussion

4.3.1 Synthesis and characterization of immune-compatible semiconducting polymers

The overall hypothesis of our design strategies is that the incorporation of immunomodulatory groups into either the backbone or the side chains (or both) of semiconducting polymers can serve to effectively suppress FBR induced by such polymers under implantation (**Figure 4-2**). For the backbone design, aromatic structures are the most preferred for keeping conjugation and efficient charge transport. Our inspiration was drawn from immunology studies[38-43] that report antioxidant (and immunomodulatory) effects of selenium-containing agents, possibly through the capability to scavenge reactive oxygen species (ROS). Based on this, we hypothesize that selenophene—a structure that has been utilized as a replacement for thiophene in semiconducting polymers to achieve higher performance[44,45]—may significantly suppress FBR.

Different from the backbone units, side chains of semiconducting polymers are better suited to accommodate non-aromatic structures without affecting charge transport. Taking advantage of this, our second design strategy is to incorporate two previously discovered immunomodulatory groups[15], namely, triazole-tetrahydropyran (THP) and triazole-thiomorpholine 1,1-dioxide (TMO), at the end of side chains. To the best of our knowledge, these two groups and their immunomodulatory effect have only been studied on non-electrical polymers and hydrogels.

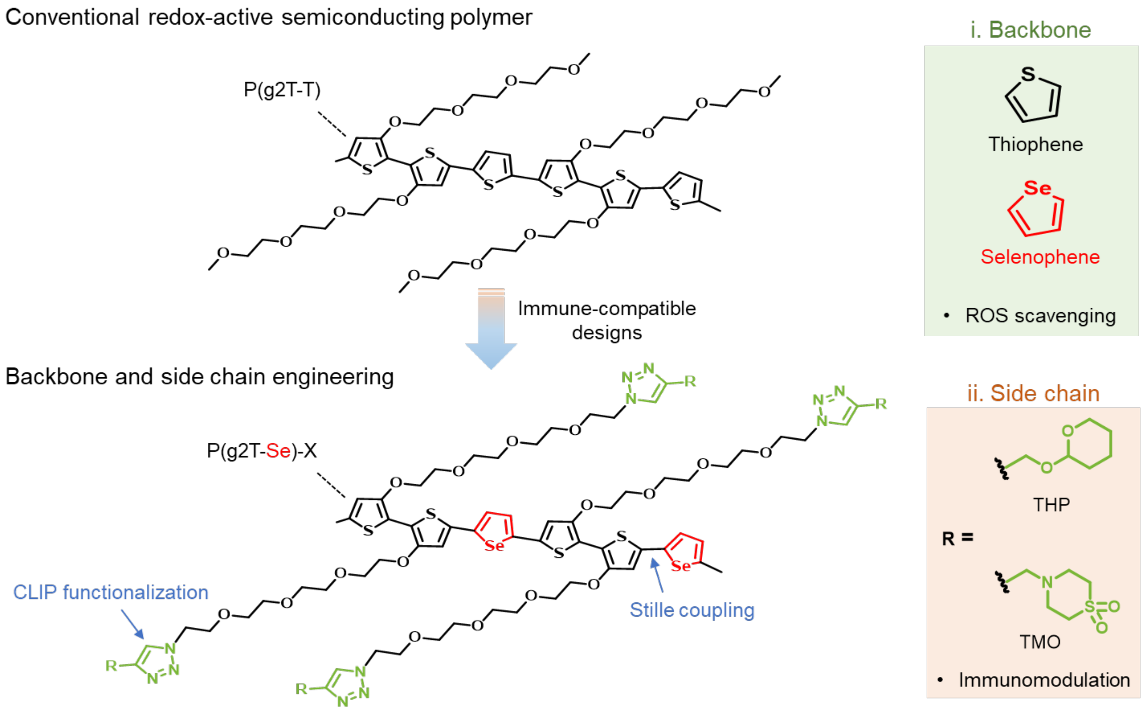

Figure 4-2. Immune-compatible designs of semiconducting polymers with suppressed FBR. Chemical structure of an existing type of redox-active semiconducting polymer p(g2T-T). For semiconducting polymers, immune-compatible design strategies include backbone engineering through selenophene substitution, which provides ROS-scavenging effect; and side-chain functionalization with immunomodulatory moieties of THP and TMO. Finally, applying these immune-compatible design strategies onto p(g2T-T), which generates p(g2T-Se)-X (X = THP or TMO).

To test these strategies, we utilize a base polymer structure of p(g2T-T). Our backbone design strategy is implemented by replacing one thiophene with a selenophene in every repeating unit and through Stille polymerization reaction, giving rise to the polymer p(g2T-Se). The side-chain engineering with THP and TMO groups is achieved through an in-film click-to-polymer (CLIP) method[46] with further optimization to achieve a 100% attachment ratio to the repeating units. To achieve this, semiconducting polymers with 100%-azide-terminated side chains p(g2T-T)-a and p(g2T-Se)-a were first synthesized through tuning the catalytic environment (Pd/Cu) for the Stille-based polymerization. Then the polymer p(g2T-T)-a and p(g2T-Se)-a was deposited from solution as thin films on a substrate. We then prepared the precursor solution including alkyne-attached THP/TMO groups together with copper catalyst in methanol, which shows great wettability on the conjugated polymer films but without dissolving the films (**Figure 4-3A**). We hypothesize that the oligo(ethylene glycol) side chain, taking advantage of the swellable property in polar solvent, can allow small precursor molecules to diffuse and transport in the polymer matrix. As a result, by incubating the polymer film in the precursor solution, we could achieve highly efficient click reaction between the alkyne groups on the precursor molecules and the terminal azide groups on the conjugated polymer.

Through FTIR (**Figure 4-3B**) and depth profiling XPS (**Figure 4-3C**) characterizations, we verified the successful conversion of the azide group from the initial polymer (p(g2T-T)-a or p(g2T-Se)-a) to the triazole bridge with corresponding functional units (THP, TMO), which proves the effectiveness of the strategy in functionalizing the side chains on a deposited film throughout the bulk.

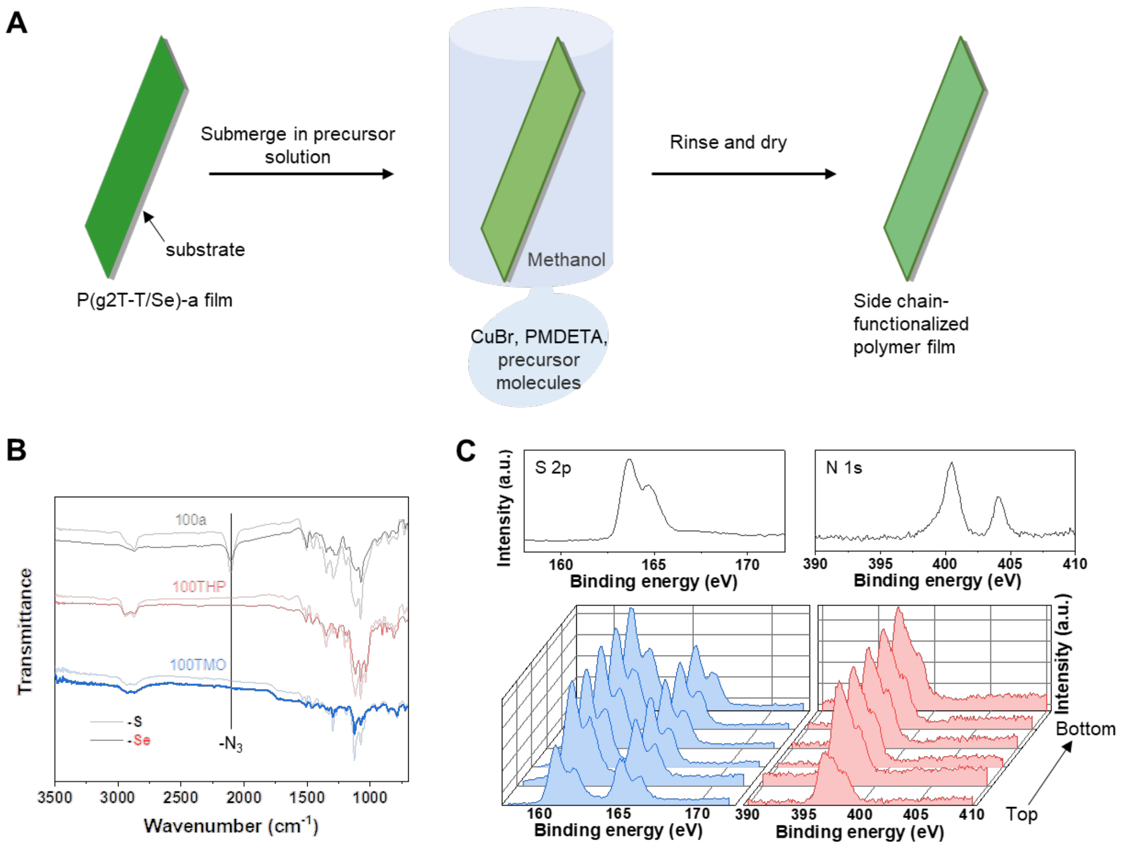

Figure 4-3. In-film side-chain functionalization on semiconducting polymer films using the CLIP method. (A) Scheme illustrating the side chain functionalization procedure on semiconducting polymers p(g2T-T)-a and p(g2T-Se)-a. (B) FTIR spectrum, verifying the disappearance of the azide peak after side chain functionalization. (C) Depth-profiling XPS spectra showing S 2p and N 1s peaks for p(g2T-T)-a (top) and p(g2T-T)-TMO (bottom).

Next, we use molecular dynamic (MD) simulation to understand the behaviors of chain solvation and molecular transport in our proposed in-film synthesis scheme. With the assistance of tetra(ethylene glycol) side chains, methanol molecules, when in contact with the polymer films, penetrate into the films in a facile way (**Figure 4-4A**). Our simulation results show that after 100 ns, an appreciable amount of methanol molecules penetrate from surface to the middle of the film, residing in the deep film location (**Figure 4-4B**). To understand how the precursor molecules move in the solvent and the dependence on molecular size, we simulated the diffusivity with hard spheres of different diameters. The molecular diffusivity of the spheres exhibits a generally decreasing trend with increasing diameters in the polymer matrix penetrated with 15 % methanol (**Figure 4-4C**). The simulated results also show that although the presence of the polymer matrix slows down the molecular movement than in pure methanol, the precursor molecules still show an appreciable diffusivity (~10^{-8} cm^2/s) compared to the solvent molecule to allow them to reach the deep film (**Figure 4-4, D and E**).

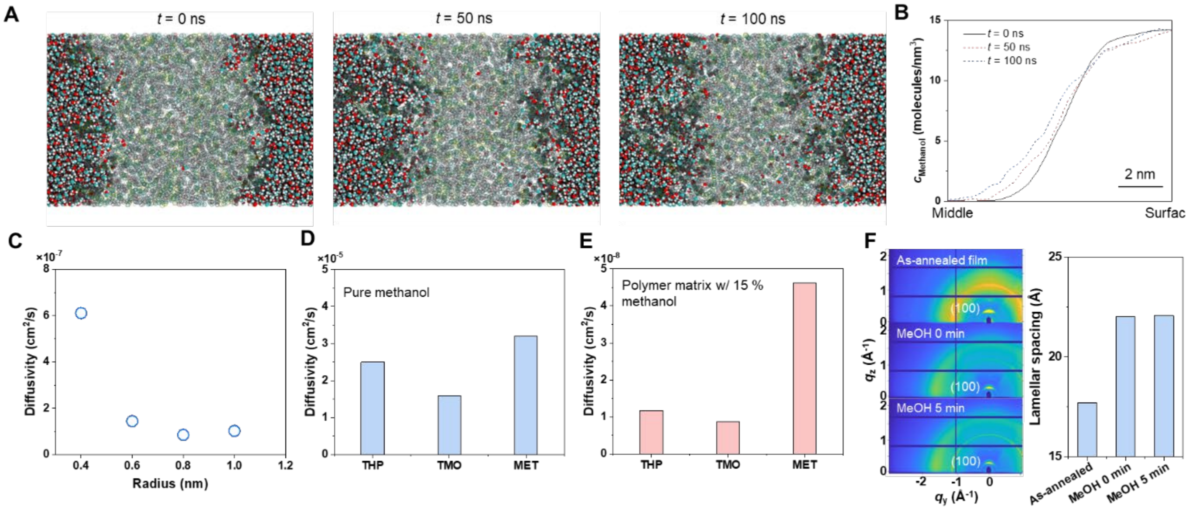

Figure 4-4. MD simulation of molecules transport in semiconducting polymer film penetrated with methanol. (A) Snapshots showing methanol molecules penetration in the conjugated semiconducting polymer films. (B) Simulated methanol molecules concentration profiles. (C) Simulated molecular diffusivity with different hard sphere radii. (D) Simulated molecular diffusivity in pure methanol. (E) Simulated molecular diffusivity in polymer matrix penetrated with 15 % methanol. (F) 2D GIXD images comparing the lamellar spacing with methanol treatment.

To illustrate the influence of methanol on polymeric packing, we showed by the in-situ GIXD measurement that, upon adding methanol to the conjugated polymer film, the lamellar spacing increases by 24 % almost instantaneously (**Figure 4-4F**). This further indicated the penetrated methanol could open up the lamellar space facilely and the possibility of solvent-assisted functional molecule transport to the reactive site, where the click reaction happens.

4.3.2 In vitro viability and inflammatory tests

We first tested the cytotoxicity of the functionalized semiconducting polymers. As shown by both MTT assay and Live/Dead cell staining (**Figure 4-5**), these polymer designs do not show significant cell toxicity, which ensures their potential as biomaterials and justifies the following tests of immune compatibility.

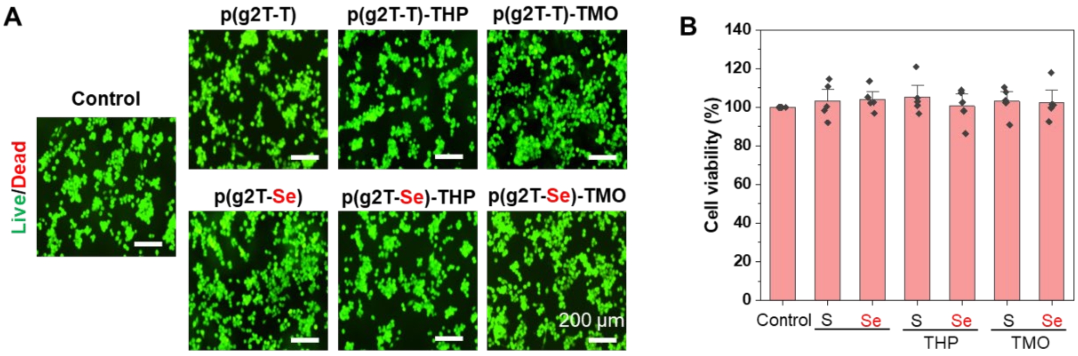

Figure 4-5. Cell viability test of the semiconducting polymers. (A) Live/dead test. (B) MTT assay. Uncoated SEBS substrates were used as the control. Values in (B) represent mean values ± s.e.m. (*n* = 5).

Despite the previous reports[38-43] of antioxidant properties from selenium-containing compounds, they were not studied for the effect in suppressing FBR. We conducted a group of *in vitro* tests by directly exposing selenophene (or thiophene) to macrophages (**Figure 4-6**). To activate the inflammatory behavior, lipopolysaccharide (LPS), an inflammatory activator of immune cells, was added into the cell culture media. In the first group tests, we incubated RAW 264.7 macrophages in media with selenophene (or thiophene) small molecules of different concentrations. During these cell culture processes over time, serious cell toxicity was not observed even at the maximum treatment dose in the two groups. After 12 hours, we tracked the inflammatory activities of macrophages by measuring the concentrations of several representative pro-inflammatory biomarkers in macrophages[47], including phospho-p38 (p-p38), phospho-extracellular signal-regulated kinases (p-ERK), nitric oxide synthase (iNOS), and phospho-c-Jun N-terminal Kinase (p-JNK) by flow cytometry.

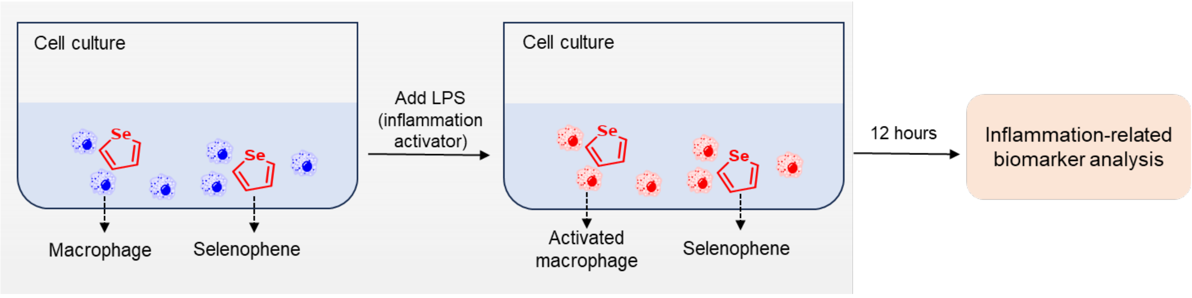

Figure 4-6. Schematics illustrating the *in vitro* test of the inhibitory effect of selenophene on inflammatory responses.

As shown in **Figure 4-7A**, the presence of selenophene indeed can suppress the expression of these inflammatory biomarkers in a dose-dependent way, in particular pERK, iNOS, and p-JNK. In contrast, no such effect can be observed from thiophene (**Figure 4-7B**). Similarly, the second group of *in vitro* tests comparing p(g2T-Se) with p(g2T-T) polymers also show such effect of selenophene in the polymer backbone in suppressing the inflammatory behavior of macrophages.

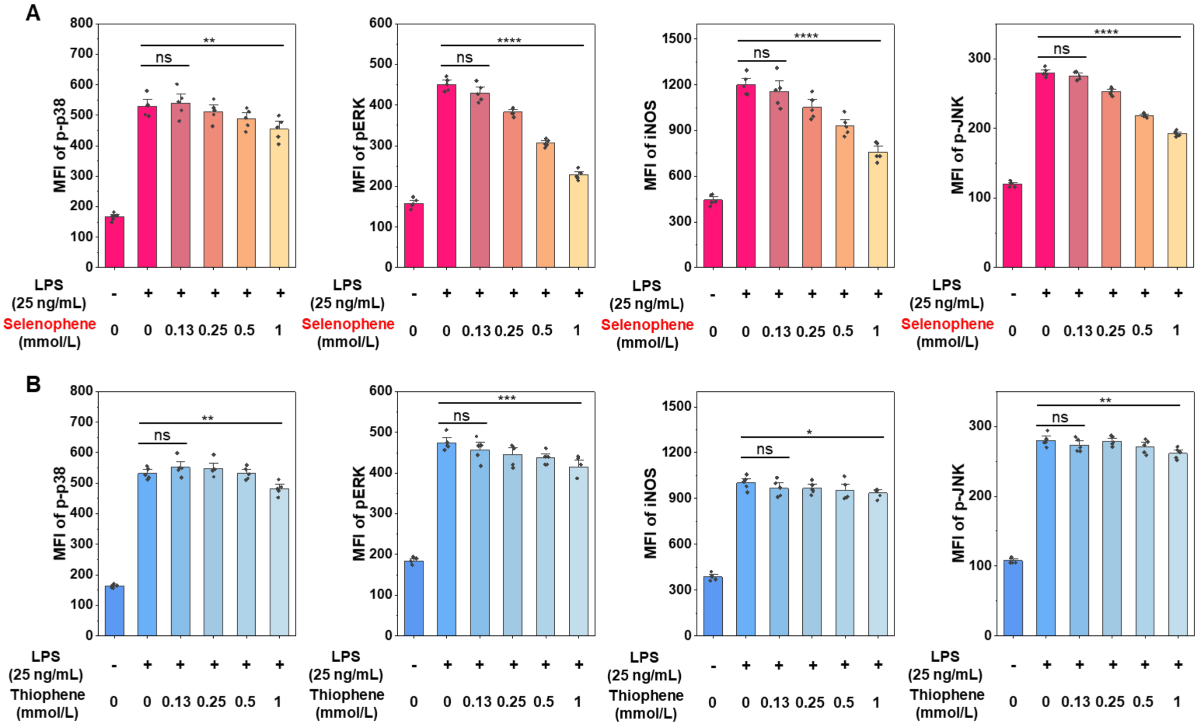

Figure 4-7. *In vitro* test of the inhibitory effect of selenophene on inflammatory responses. (A) Mean fluorescence intensity (MFI) of different inflammation-related biomarkers p-p38, p-ERK, iNOS, and p-JNK treated with selenophene showing suppressed expression in a dose-dependent way. LPS (-): no addition of LPS; LPS (+), with the addition of LPS. (B) MFI of different inflammation-related biomarkers p-p38, p-ERK, iNOS, and p-JNK treated with thiophene. The thiophene treatment had no effect on the inflammatory response. Values represent mean values ± s.e.m. ($n = 5$). Statistical significance and P values are determined by ordinary one-way ANOVA: $*P<0.05$; $**P<0.01$; $***P<0.001$; $****P<0.0001$; ns, not significant.

Furthermore, we tested the ROS generation from the treatment. Compared to p(g2T-T), p(g2T-Se) polymer treatment led to a more substantial decrease of ROS level (**Figure 4-8**). Overall, these results suggest that the selenophene's properties in scavenging the ROS, which is a type of key signaling molecules in inflammatory responses[48-50], could possibly suppress the pro-inflammatory macrophage activation, and thereby mitigating FBR.

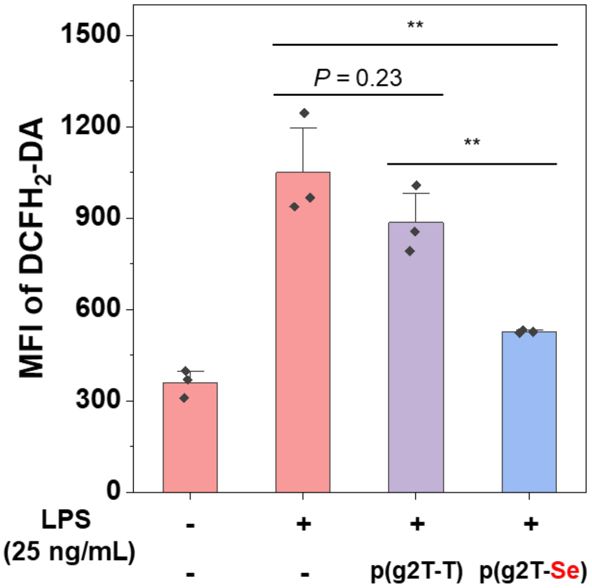

Figure 4-8. ROS levels after treatment with p(g2T-T) and p(g2T-Se) polymers. Values represent mean values ± s.e.m. (n = 3). Statistical significance and P values are determined by two-sided Student's t-tests: $^{**}P<0.01$.

4.3.3 In vivo foreign-body response study

To study the elicited FBR from these polymers *in vivo*, we implanted these semiconducting polymers (as thin films supported by thin circular SEBS substrates) subcutaneously into mouse dorsal regions, for periods of one and four weeks. We first evaluated the acute inflammatory response to the implants after one week of implantation. From Masson's trichrome (MT) staining (**Figure 4-9**), the collagen layer elicited by p(g2T-Se) polymer has a lower density (as measured by the blue pixel density) than that from the control p(g2T-T) polymer, which indicates less inflammation.

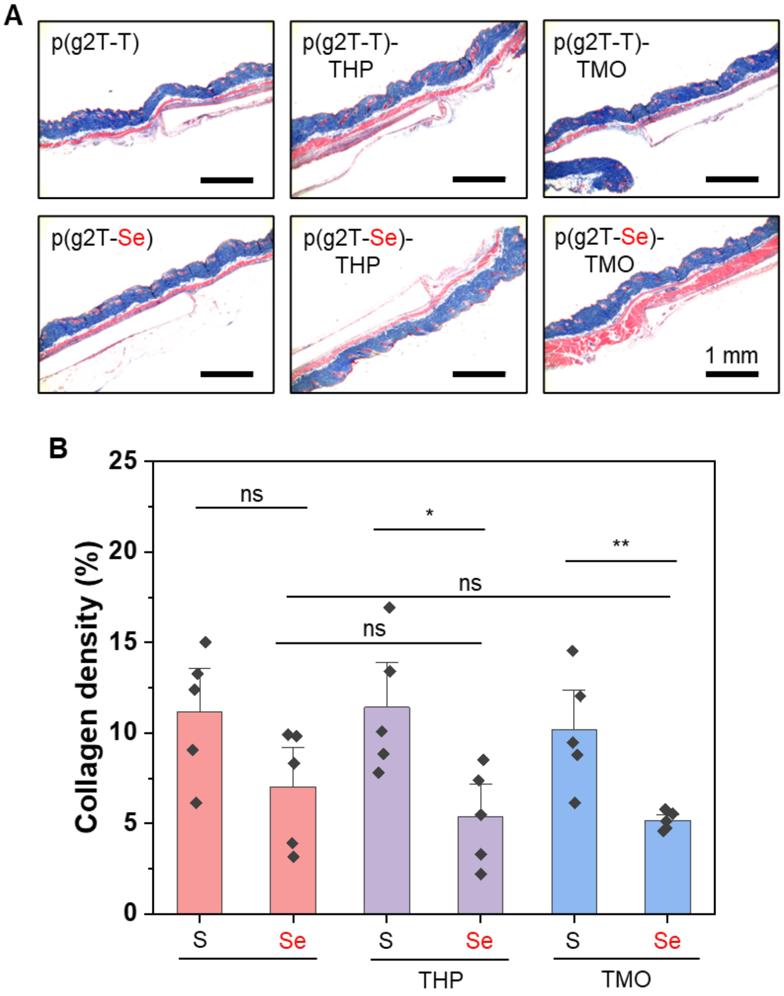

Figure 4-9. Reduced collagen deposition on the polymer films after 1-week subcutaneous implantation. (A) Masson's trichrome-stained tissue sections of p(g2T-T), p(g2T-Se), p(g2T-Se)-THP, and p(g2T-Se)-TMO polymers. (B) Extracted collagen densities. Values represent mean values ± s.e.m. (*n* = 5). Statistical significance and *P* values are determined by two-sided Student's t-test: *$P<0.05$; **$P<0.01$.

After four weeks of implantation with the fibrotic capsule fully developed, the MT staining results in **Figure 4-10, A and B** show a collagen density of ~13% at the p(g2T-Se) polymer-tissue interface, which marks a ~50% decrease from the collagen density of 25% from p(g2T-T).

Furthermore, the side-chain functionalization on p(g2T-Se) with the two immunomodulatory groups, i.e., THP and TMO, helps to further lower collagen density by another 35% and 39%, respectively.

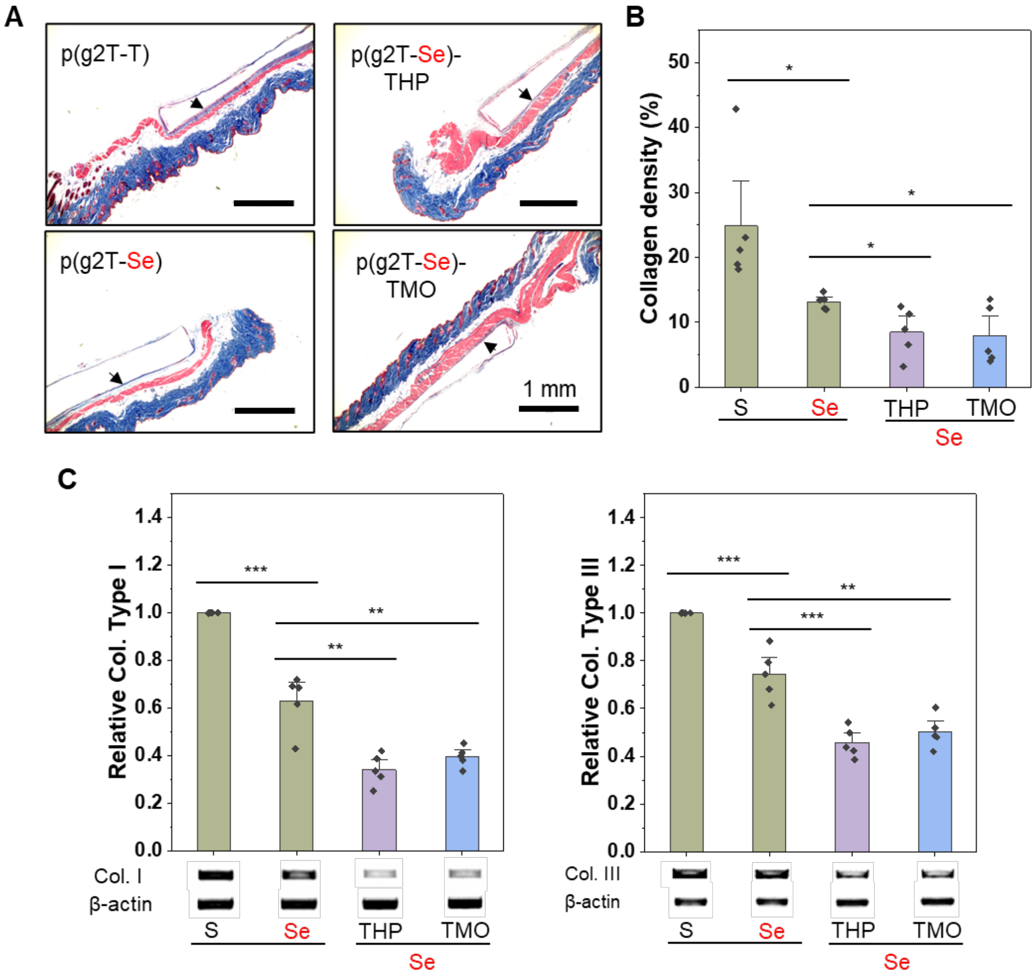

Figure 4-10. Reduced collagen deposition on the polymer films after 4-week subcutaneous implantation. (A) Masson's trichrome-stained tissue sections of p(g2T-T), p(g2T-Se), p(g2T-Se)-THP, and p(g2T-Se)-TMO polymers. (B) Extracted collagen densities showing decreased collagen deposition from the selenophene backbone and immunomodulatory side-chain engineering. (C) Relative collagen Type I and collagen Type III mRNA expression levels (i.e., fold changes) in the implanted region, further confirming the observed trend of collagen deposition. Values represent

mean values ± s.e.m. (*n* = 5). Statistical significance and *P* values are determined by two-sided Student's t-test: **P*<0.05; ***P*<0.01; ****P*<0.001.

As the collagen layer is mostly composed of type I and type III collagens[51,52], such a trend in the collagen density is further validated by quantifying mRNA expression levels for collagen types I and III in the tissue regions around the implants. As shown in **Figure 4-10C**, the selenophene backbone engineering alone decreases the levels of both collagen types by ~20-40%, and the further side-chain engineering by THP and TMO can further bring the decrease extents to ~50-70%. Overall, as collagen deposition is the final-stage outcome of FBR, such substantial decreases in collagen density reflect the effective suppression of the FBR by our immune-compatible designs.

To better understand the FBR suppression effect, we performed immunofluorescence imaging for macrophages (with CD68) and myofibroblasts (with α-smooth muscle actin, α-SMA) after 4-week implantation for the four polymers (i.e., p(g2T-T), p(g2T-Se), p(g2T-Se)-THP, and p(g2T-Se)-TMO). The results in **Figure 4-11** show that both the backbone and side-chain engineering strategies help suppress the immune cell recruitments. In particular, p(g2T-Se)-TMO achieved decreases in the populations of macrophages and myofibroblasts by ~68% and ~79%, respectively, compared to the control p(g2T-T).

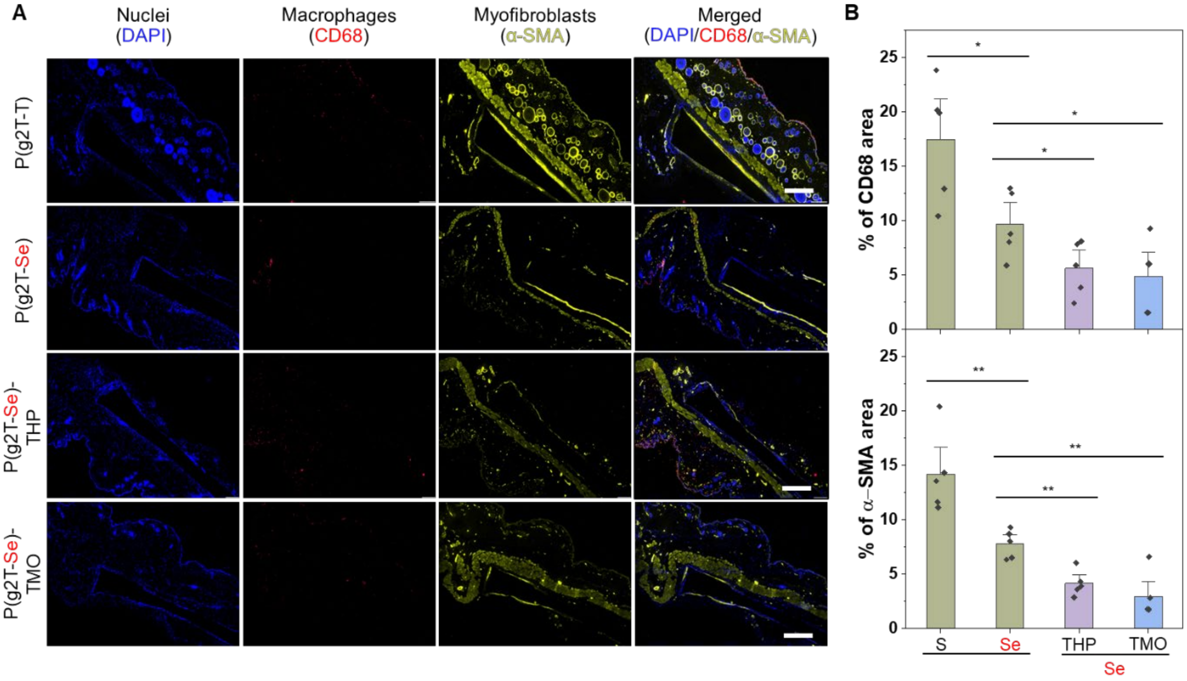

Figure 4-11. Reduced immune-cell populations on the polymer films with immune-compatible designs. (A) Immunofluorescence images showing cell nuclei (DAPI; blue), macrophages (CD68; red), and myofibroblasts (α-SMA; yellow) for the four polymers. Scale bars, 500 μm. (B) Quantification of CD68 (a marker of macrophages) (top), and α-SMA (a marker of myofibroblasts) (bottom) area at the tissue-polymer interface in the immunofluorescence images, which shows the suppression of macrophage and myofibroblast recruitment on the immune-compatible polymers.

To study the inflammatory signaling mechanism of the suppressed FBR, we further analyzed the expression levels of mouse inflammation-related markers (**Figure 4-12**) at the end of the four-week implantation. The results indicate that both the selenophene backbone engineering and the THP and TMO side-chain functionalization downregulate the pro-inflammatory biomarkers (including C-C chemokine receptor type 7 (CCR7), interferon-γ (IFN-γ), granulocyte-macrophage colony-stimulating factor (GM-CSF), monocyte chemoattractant protein-1 (MCP-1), interleukin (IL)-23, IL-6, IL-1β, IL-27, IL-12p70, and IL-1α). At the same time, upregulations are observed for the anti-inflammatory biomarkers (i.e., IL-10, IL-4). Together, these results suggest that the selenophene backbone and immunomodulatory side chains lead to the recruitment or differentiation of macrophages in anti-inflammatory phenotypes (Mϕ2) while suppressing pro-inflammatory phenotypes (Mϕ1), which, together, helps to mitigate the FBR.

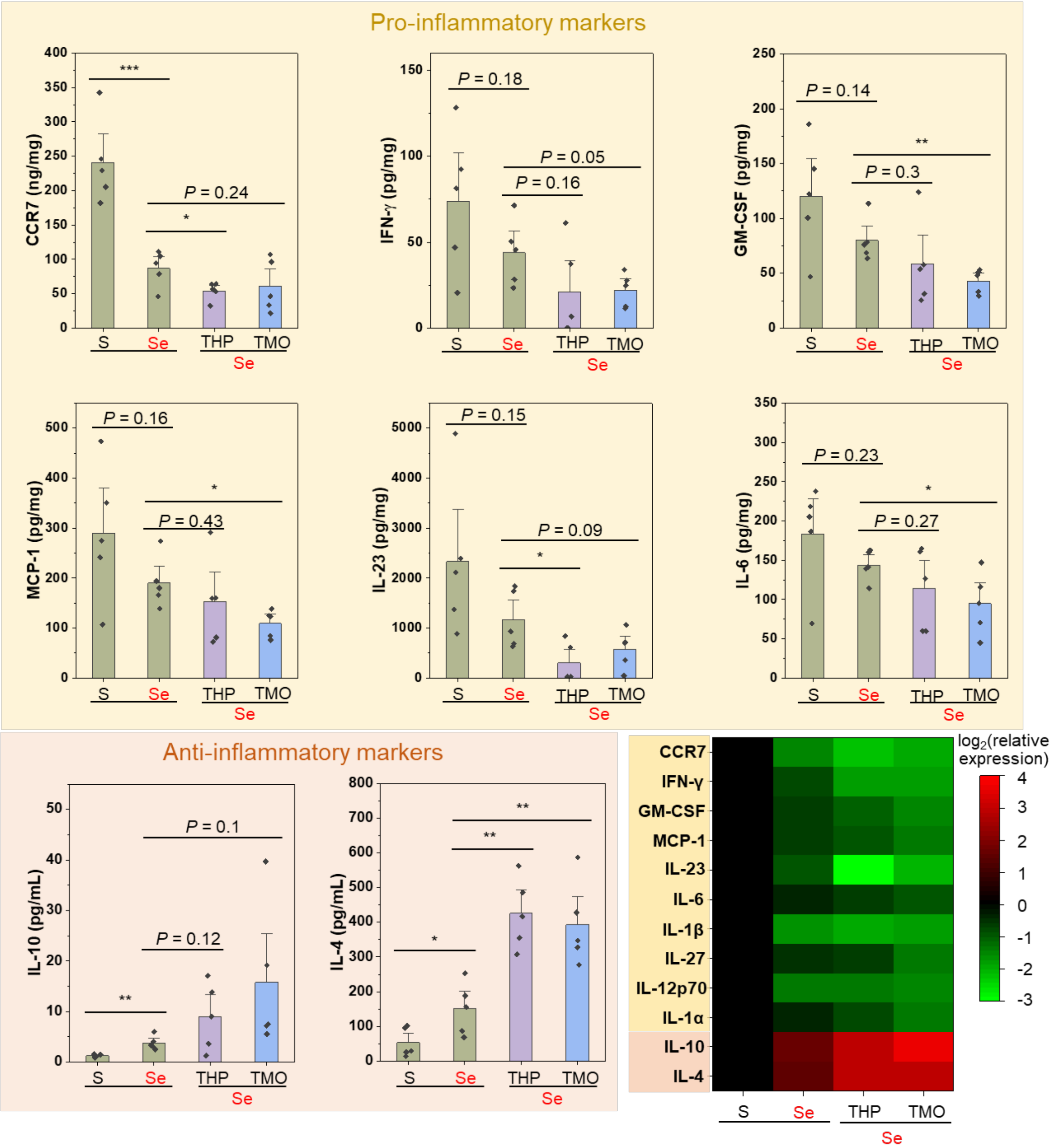

Figure 4-12. Pro- and anti-inflammatory markers analysis at 4-week post implantation.

Figure 4-12, continued. The expression levels of pro-inflammatory markers (including CCR7, IFN-γ, GM-CSF, MCP-1, IL-23, and IL-6) and anti-inflammatory markers (including IL-10 and IL-4) were analyzed. Values represent mean values ± s.e.m. ($n = 5$). Statistical significance and P values are determined by two-sided Student's t-test: $^{*}P<0.05$; $^{**}P<0.01$; $^{***}P<0.001$. The heat map summarized expression levels of all inflammation-related biomarkers (pro- and anti-). The selenophene backbone and THP (and TMO) side chains suppressed the expression of pro-inflammatory markers and promoted the expression of anti-inflammatory markers.

4.3.4 Electrical and structural characterization

Next, the electrical performance of these immune-compatible designs of semiconductors was tested in OECT devices (**Figure 4-13A**). All the polymers exhibit ideal transfer characteristics (**Figure 4-13B**). The figure-of-merit transistor parameters including transconductance (g_m) and charge-carrier mobility were calculated. The results show that selenophene in the backbone gives a higher transconductance and mobility compared to a full thiophene backbone (**Figure 4-13C**). This is consistent with the previous observations[44,45] of selenophene boosting mobility for donor-acceptor-type semiconducting polymers designed for organic field-effect transistors. For the side chain functionalization with THP and TMO that are relatively bulky in size, although the steric hindrance effect indeed leads to some minor decrease in the performance, the charge-carrier mobility still both stays around 1.0 $cm^2\ V^{-1}\ s^{-1}$ for selenophene-containing backbones, possibly benefiting from the buffer effect of the tetra-ethylene-glycol units in the side chains.

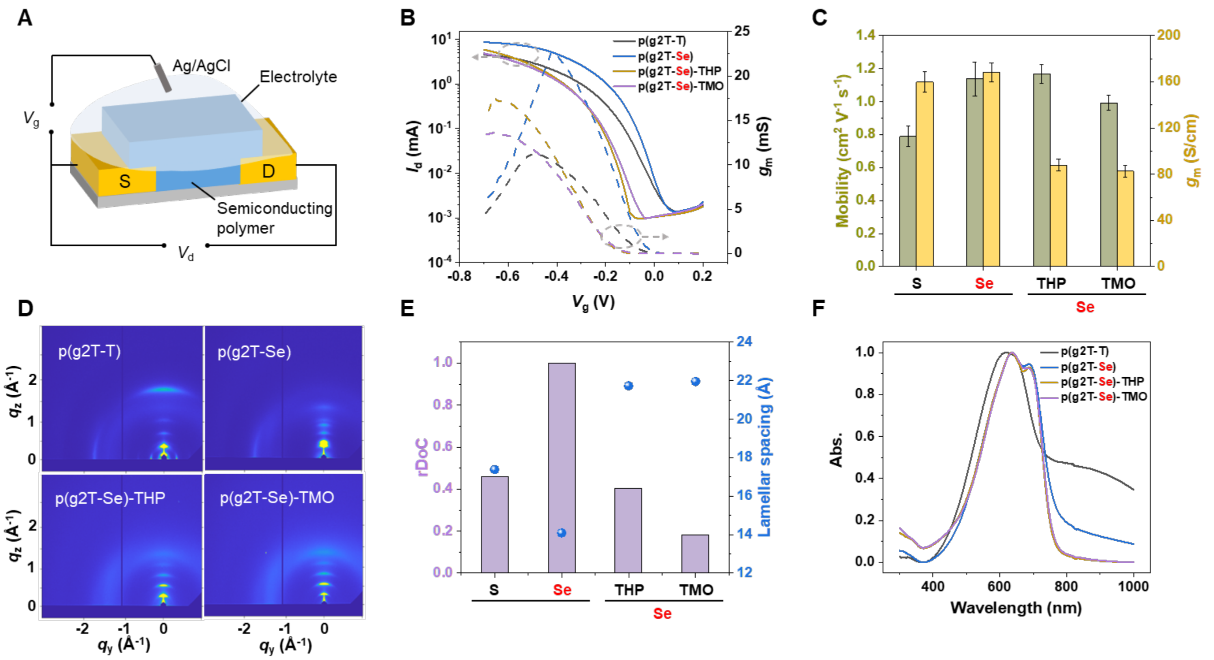

Figure 4-13. OECT and structural characterizations for the immune-compatible semiconducting polymers. (A) OCET device schematics. (B) Transfer characteristics of the four polymers as OECT channels. (C) Mobility and normalized transconductance. Values represent mean values ± s.d. (*n* = 5). (D) 2D GIXD images. (E) rDoC and lamellar spacing. (F) Normalized UV-Vis absorption.

To deepen the understanding of such structure-property relationships, we performed grazing incidence X-ray diffraction (GIXD) and UV-Vis spectra measurements on these polymers. The results show that selenophene in the backbone, compared to thiophene, gives a higher relative degree of crystallinity (rDoC) and smaller lamellar packing distances (**Figure 4-13, D and E**). From UV-Vis spectrum, a redshift for the absorption onset is observed (**Figure 4-13F**), which indicates the decrease of the bandgap coming from the improvement in structural ordering. After side chain functionalization, both p(g2T-Se)-THP and p(g2T-Se)-TMO display decreased rDoC and increased lamellar packing distances relative to p(g2T-Se), which possibly caused the slight decrease in electrical performance. However, UV-Vis spectra indicate that these two functionalized polymers still mostly preserve the short-range aggregation level. The AFM images also show similar surface morphology among the thin films of these polymers.

4.4 Conclusion

We demonstrated that the engineering of molecular structures for conjugated polymers can greatly suppress foreign-body responses elicited by such polymers as implants. Specifically, our work reveals the immunomodulatory effects of selenophene-based structures, presenting a promising design strategy that leverages immunomodulatory elements like selenide to construct conjugated units. By integrating these structures into the polymer backbone, we can achieve both immune compatibility and high electrical performance. This can be further coupled with side-chain installation of other immunomodulatory structures (for instance, THP and TMO) to achieve even lower FBR (**Figure 4-14**). The versatility of these design principles makes them readily applicable to other functional categories of conjugated polymers, such as those used in biochemical sensing and fluorescence imaging.

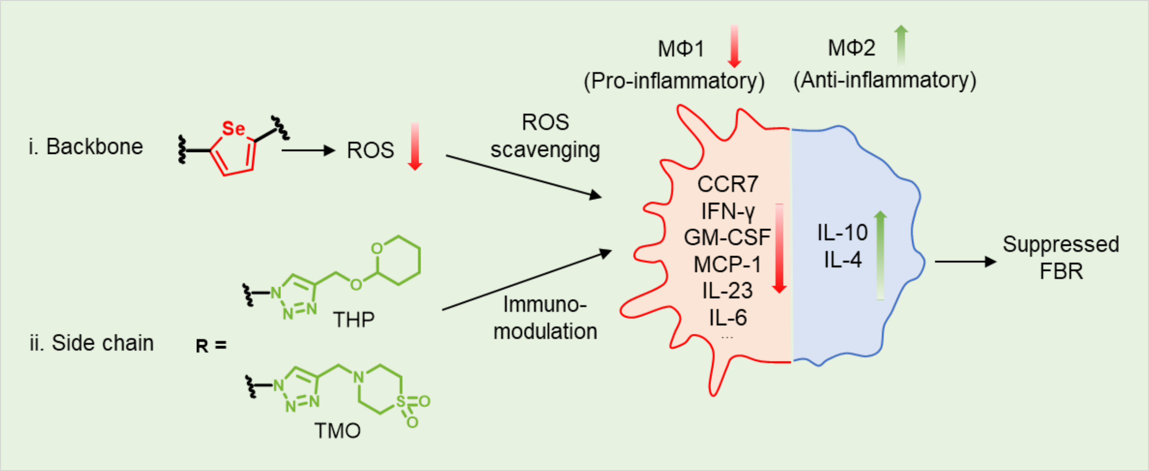

Figure 4-14. Summary of the proposed immunomodulation mechanism of functionalized semiconducting polymers.

Figure 4-14, continued. The selenophene in the backbone with the effect of ROS scavenging, together with immunomodulatory side chain groups (THP and TMO), modulate the differentiation of macrophage towards an anti-inflammatory phenotype, which leads to suppressed FBR.

4.5 Appendix

1D ^{1}H NMR spectrum for 1

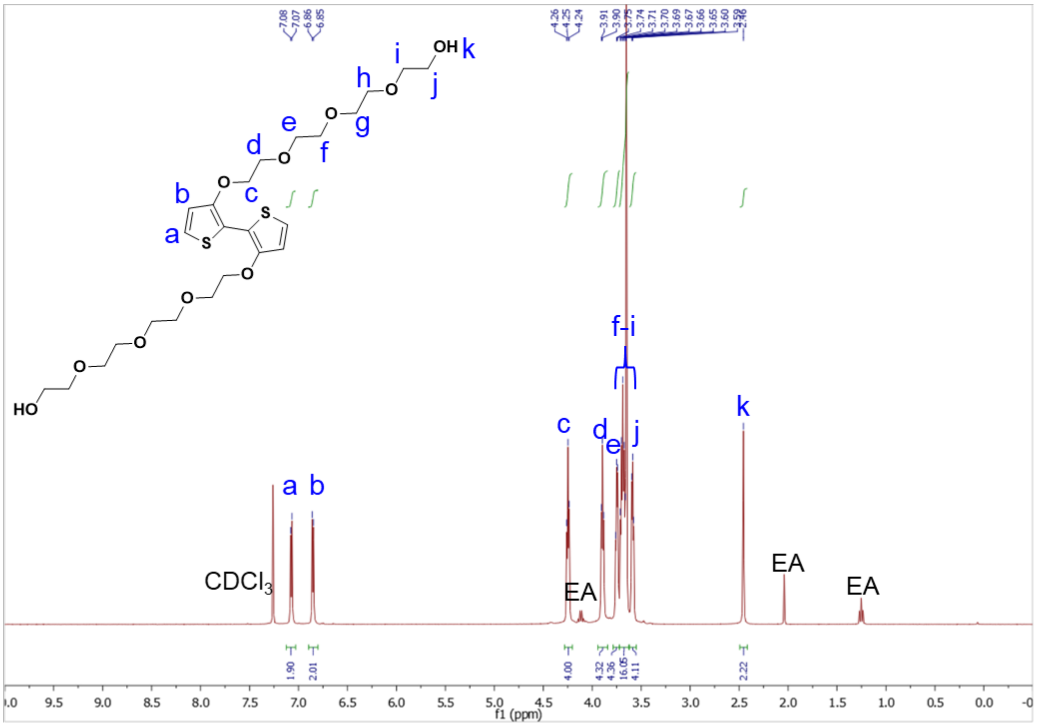

Figure 4-15. 1D ^{1}H NMR spectrum for 1

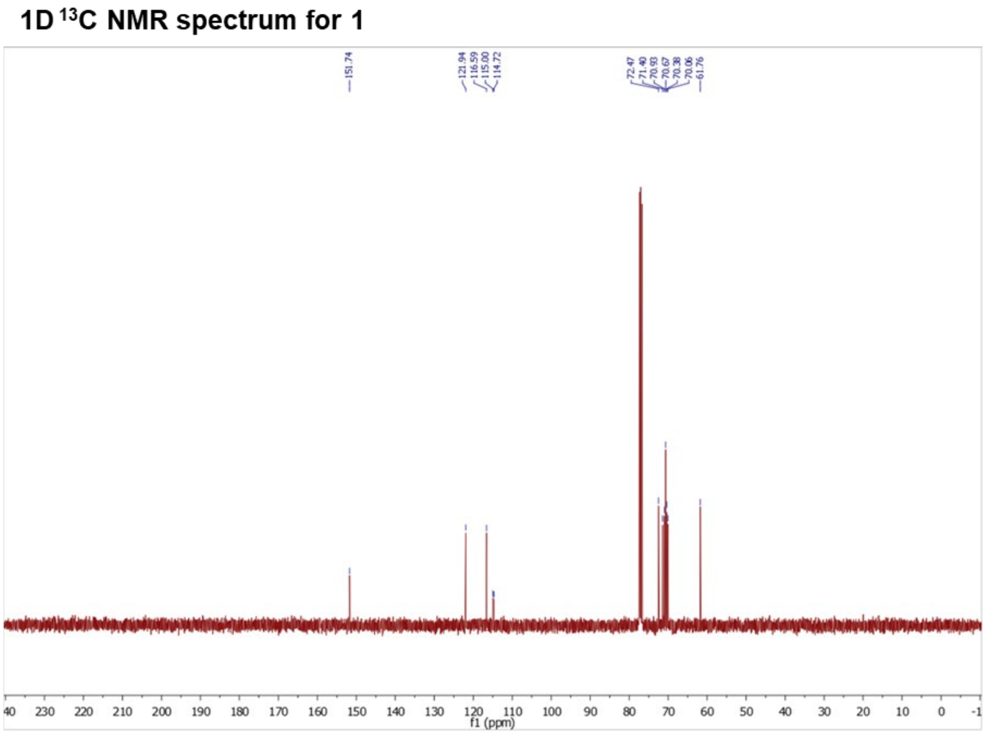

Figure 4-16. 1D ^{13}C NMR spectrum for 1

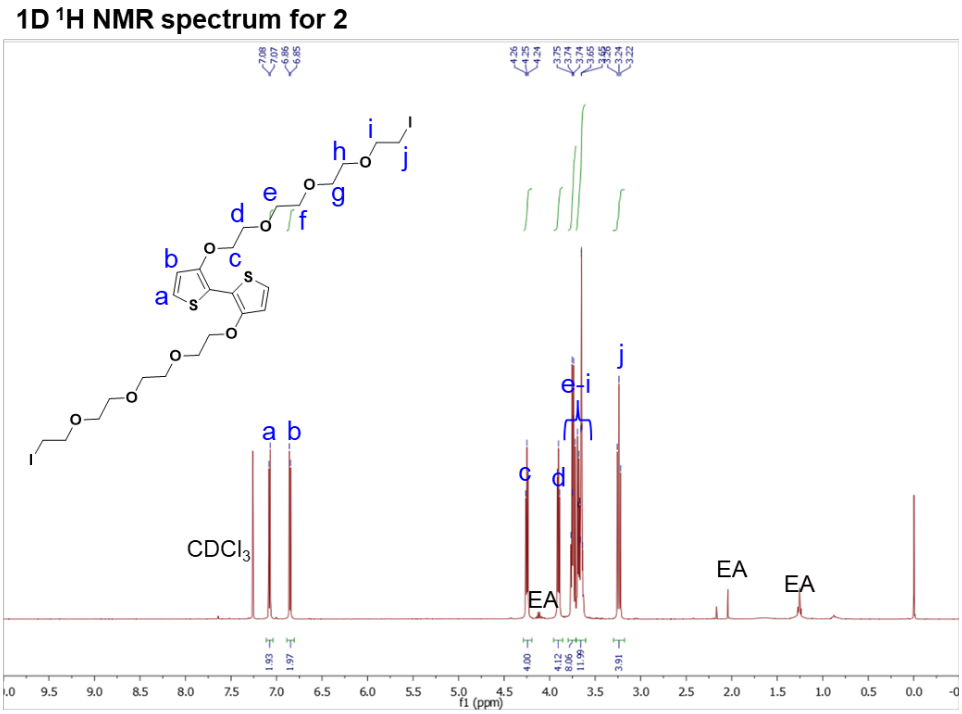

Figure 4-17. 1D ^{1}H NMR spectrum for 2

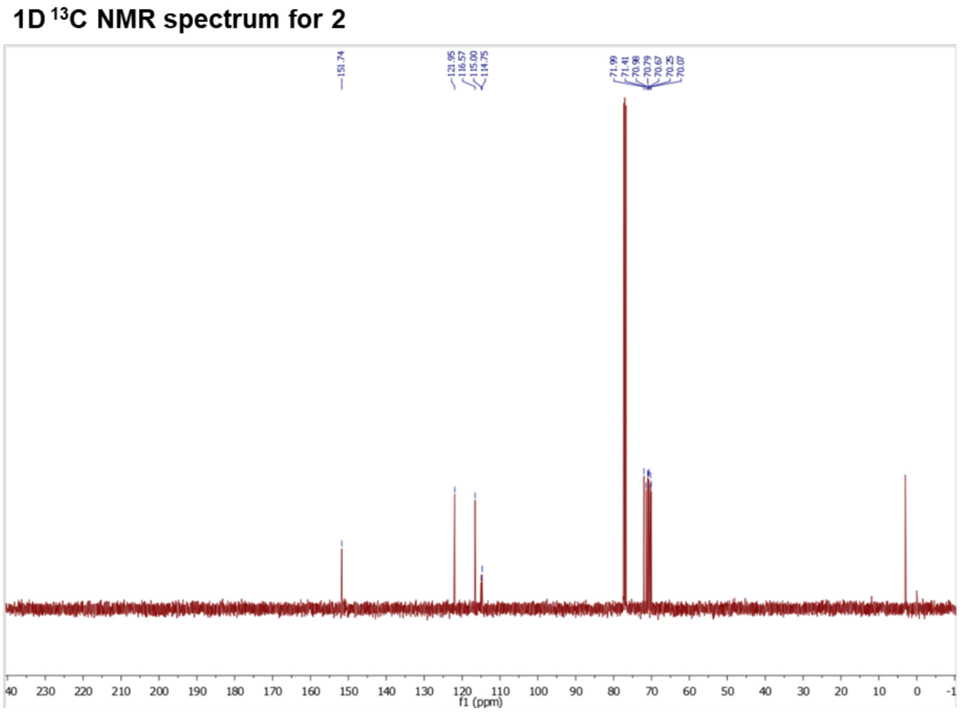

Figure 4-18. 1D ^{13}C NMR spectrum for 2

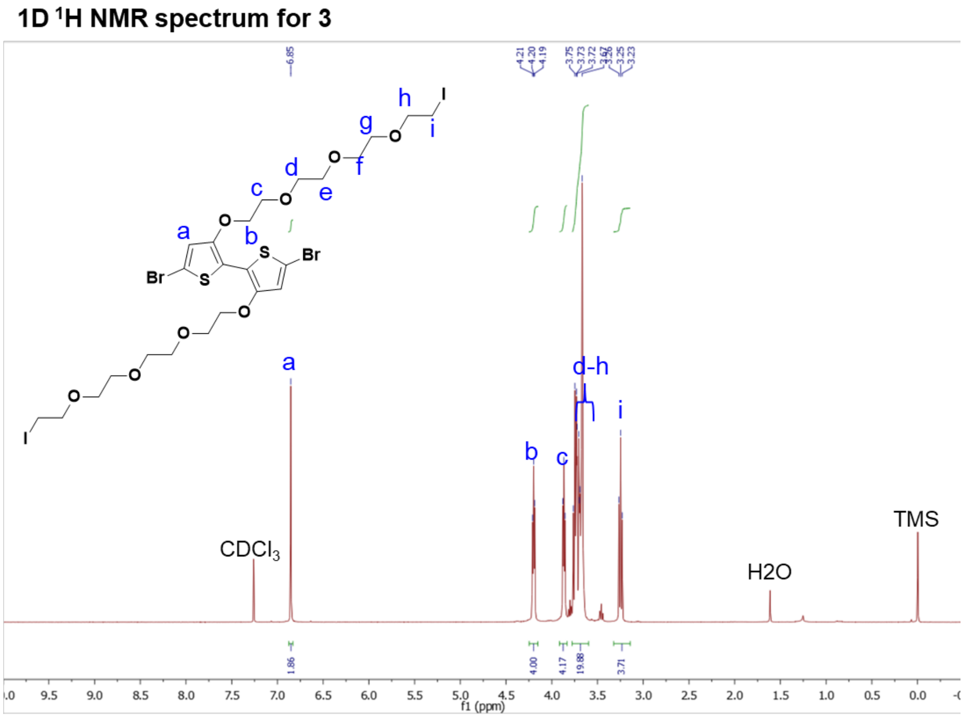

Figure 4-19. 1D ^{1}H NMR spectrum for 3

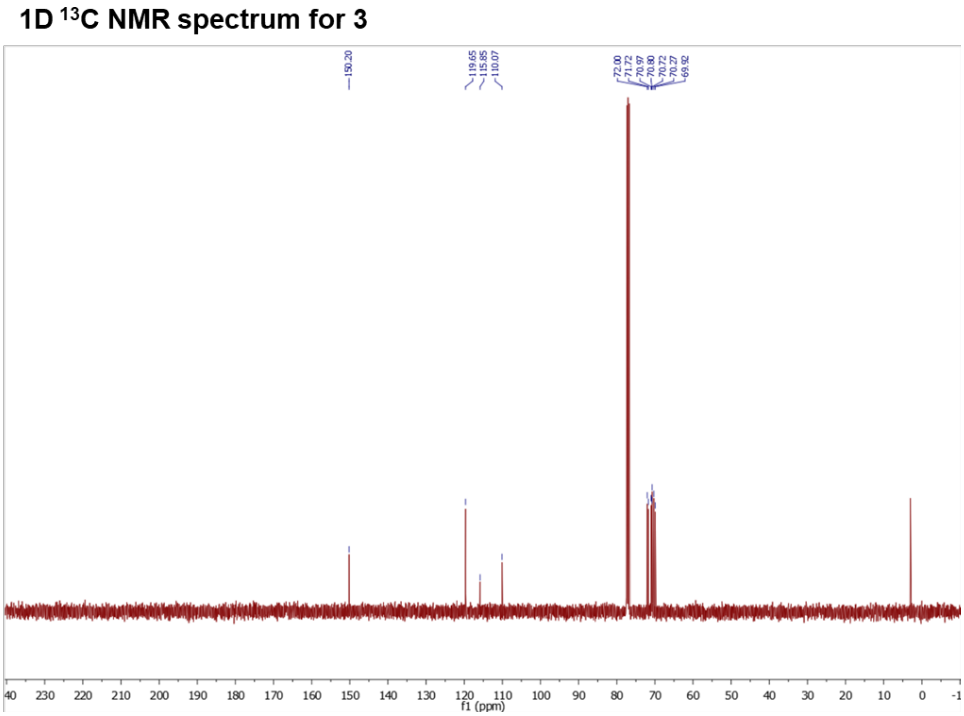

Figure 4-20. 1D ^{13}C NMR spectrum for 3

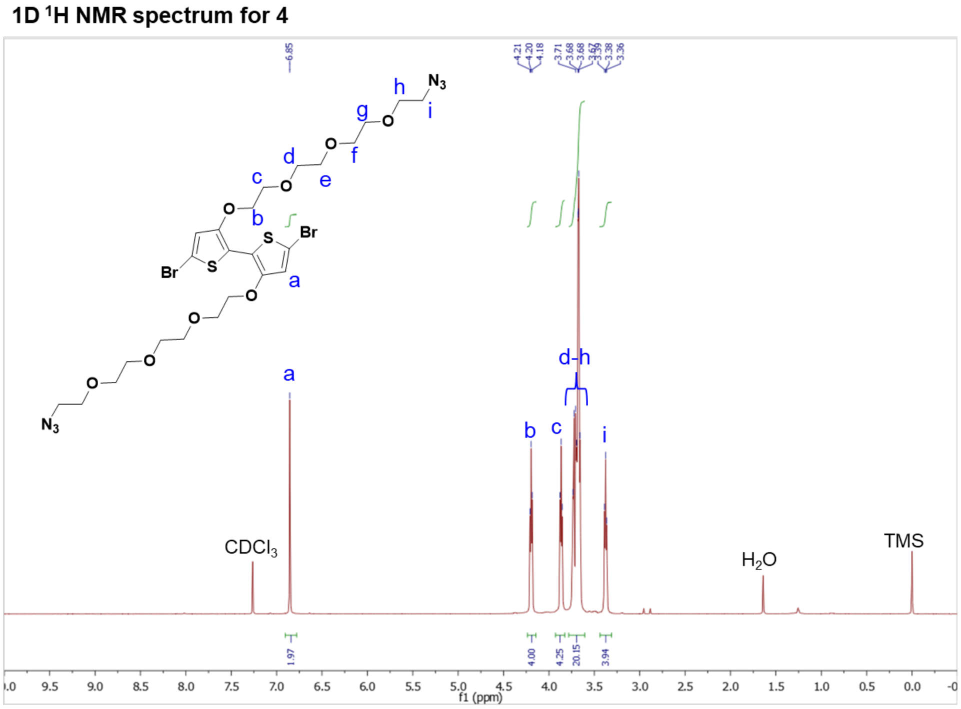

Figure 4-21. 1D ^{1}H NMR spectrum for 4

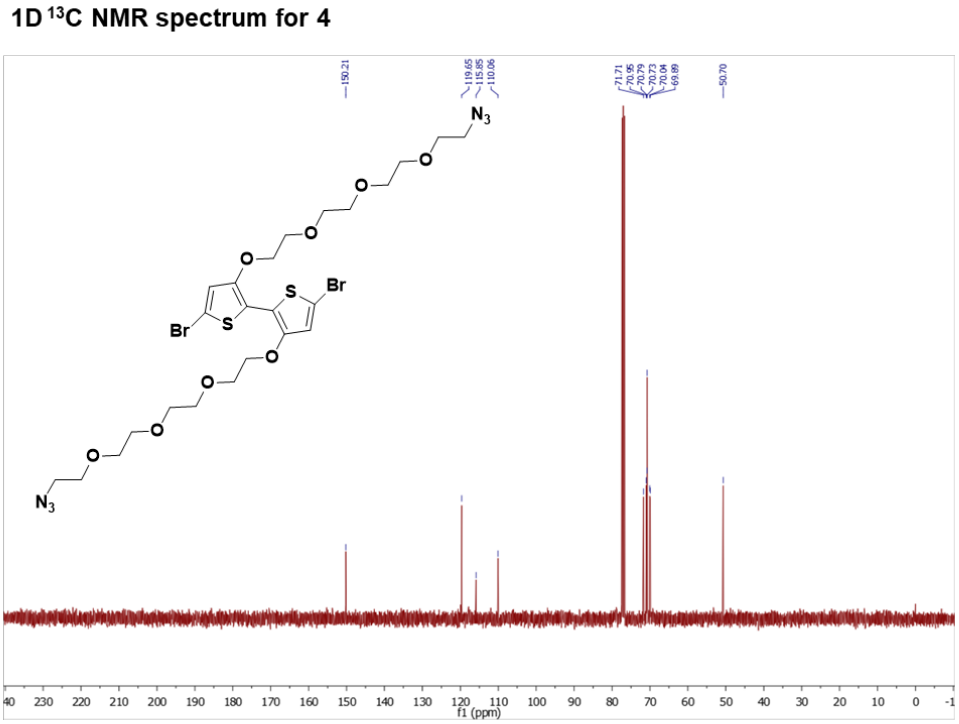

Figure 4-22. 1D ^{13}C NMR spectrum for 4

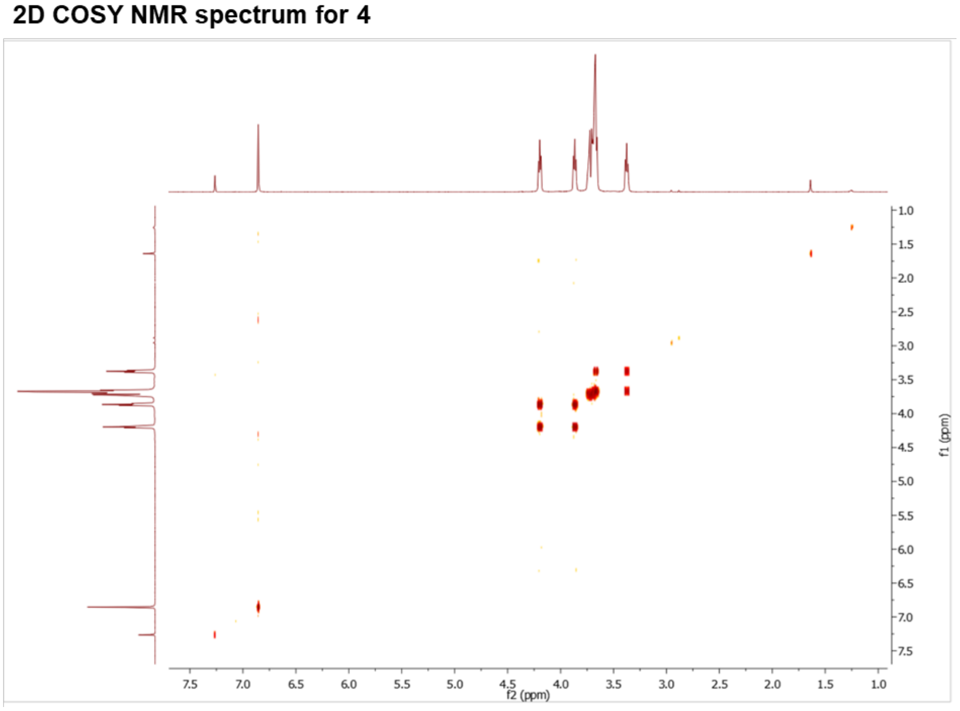

Figure 4-23. 2D COSY NMR spectrum for 4

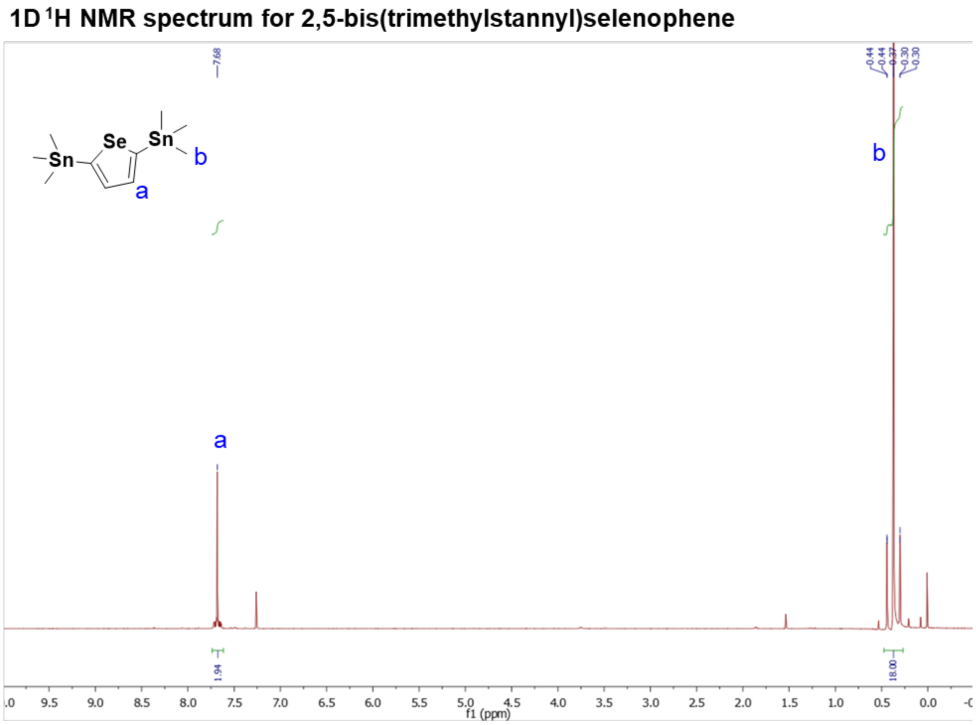

Figure 4-24. 1D ^{1}H NMR spectrum for 2,5-bis(trimethylstannyl)selenophene

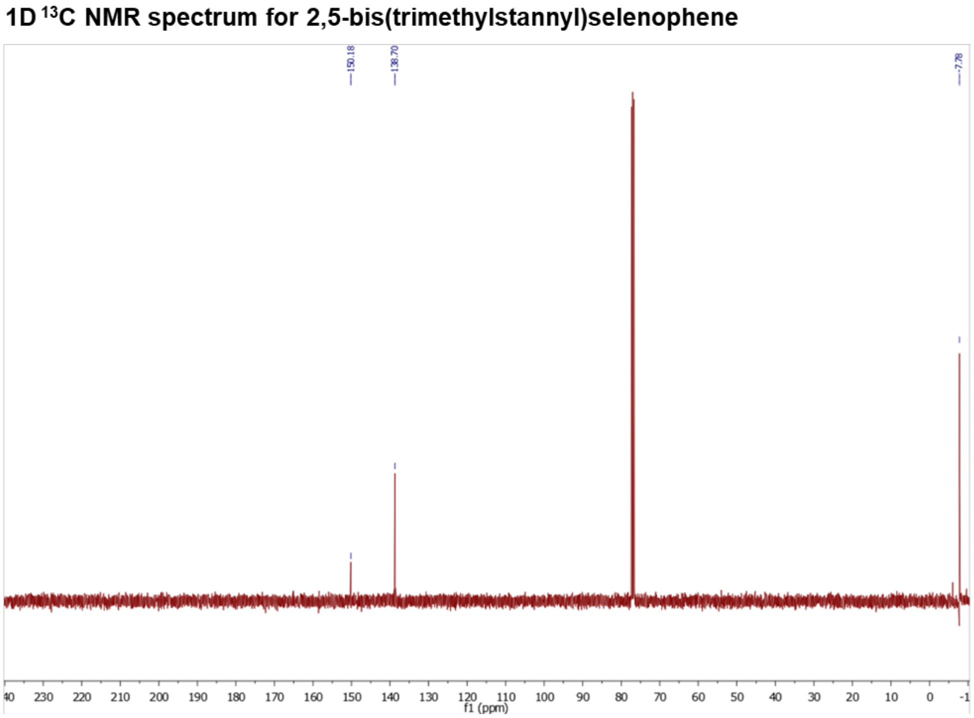

Figure 4-25. 1D ^{13}C NMR spectrum for 2,5-bis(trimethylstannyl)selenophene

Table 4-1. Molecular weights of functionalized conjugated polymers

Polymers	M_n (kDa)	M_w (kDa)	PDI
p(g2T-T)-a	30	62	2.1
p(g2T-Se)-a	52	130	2.5

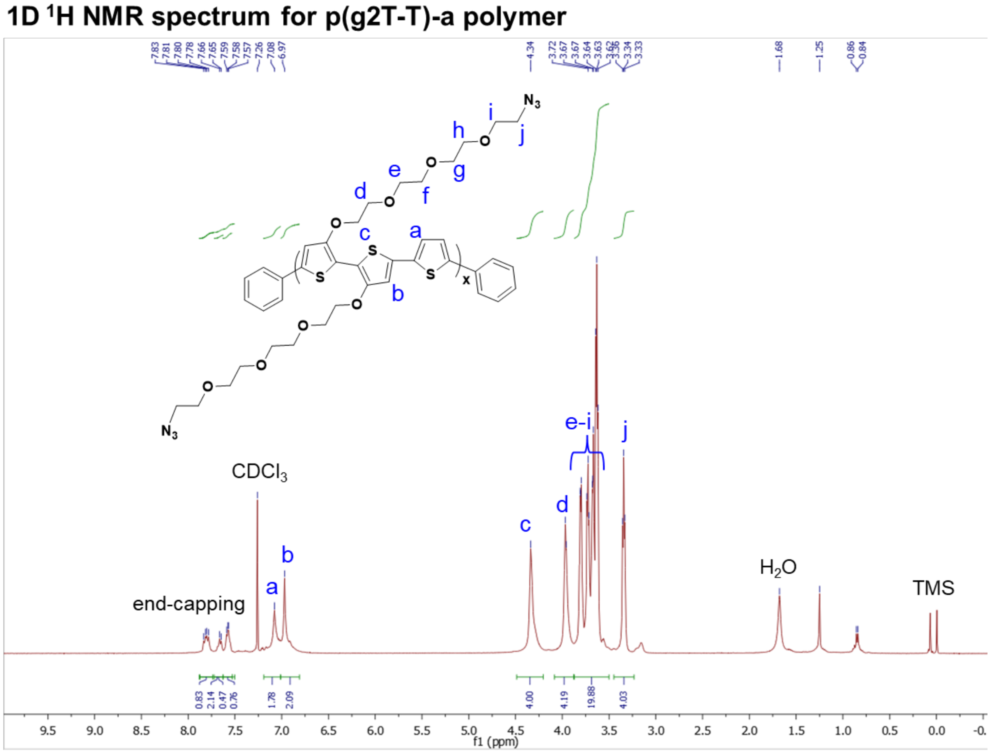

Figure 4-26. 1D ^{1}H NMR spectrum for p(g2T-T)-a polymer

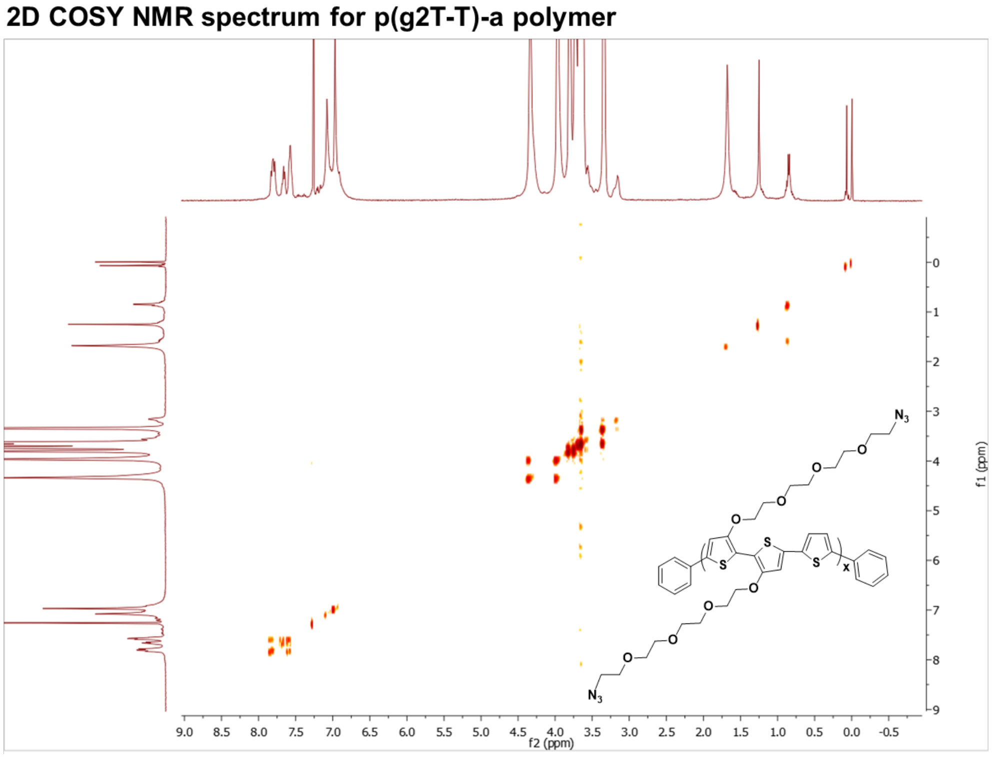
2D COSY NMR spectrum for p(g2T-T)-a polymer

Figure 4-27. 2D COSY NMR spectrum for p(g2T-T)-a polymer

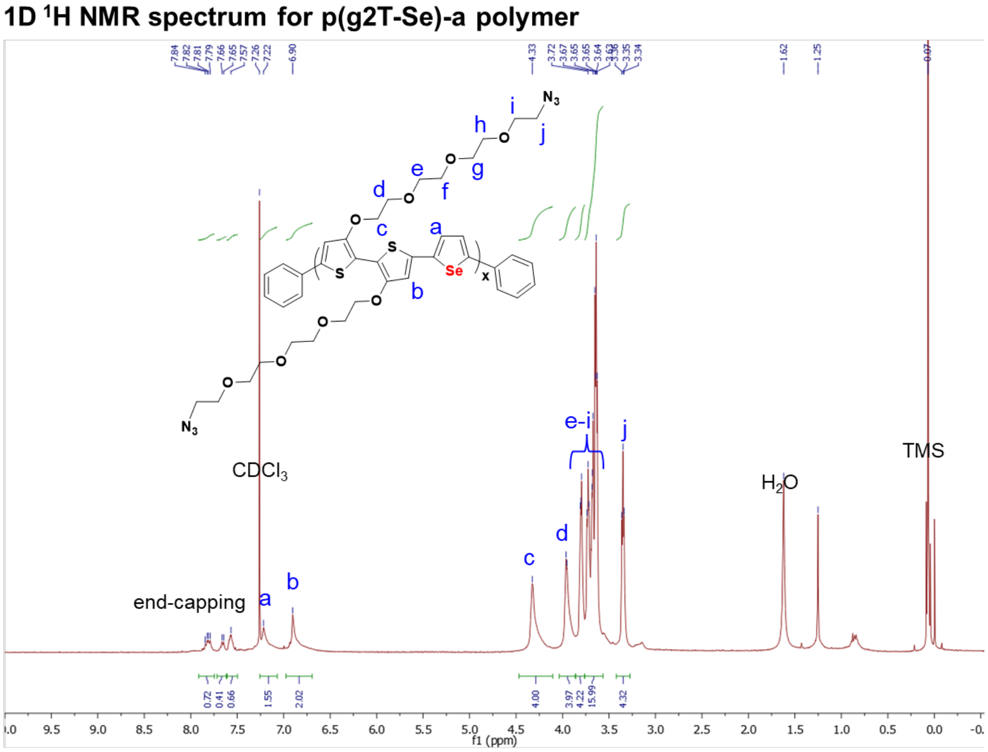
1D ^{1}H NMR spectrum for p(g2T-Se)-a polymer

Figure 4-28. 1D ^{1}H NMR spectrum for p(g2T-Se)-a polymer

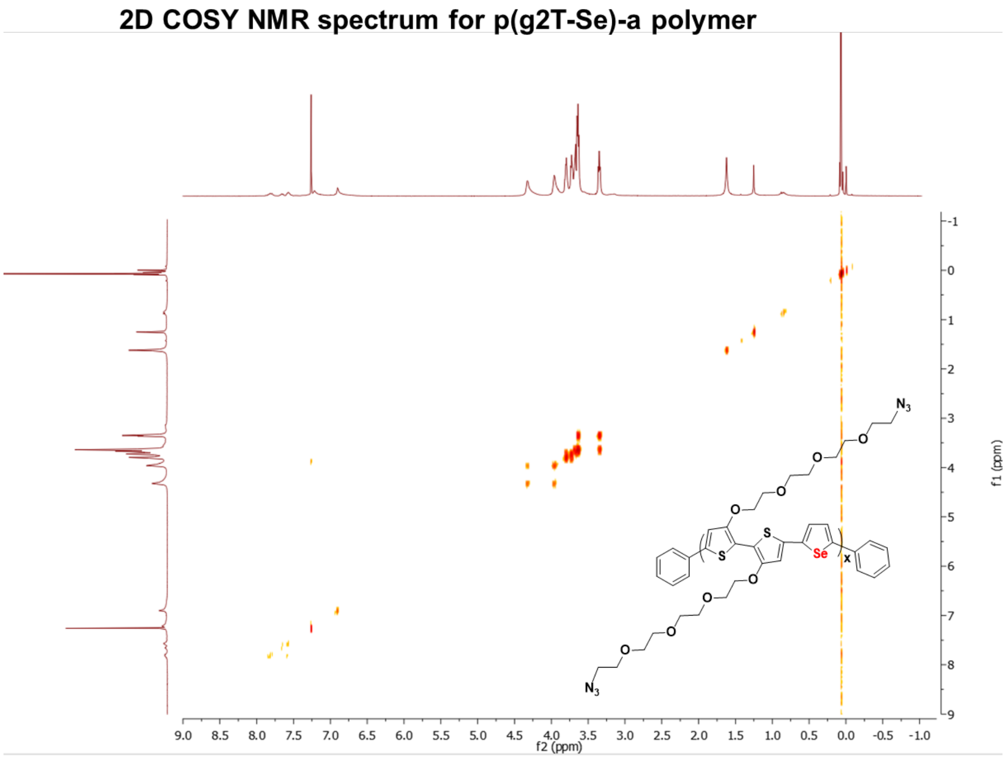

Figure 4-29. 2D COSY NMR spectrum for p(g2T-Se)-a polymer

4.6 References

(1) Capuani, S.; Malgir, G.; Chua, C. Y. X.; Grattoni, A. Advanced strategies to thwart foreign body response to implantable devices. *Bioeng Transl Med* **2022,** *7*, e10300.

(2) Zhang, D.; Chen, Q.; Shi, C.; Chen, M.; Ma, K.; Wan, J.; Liu, R. Dealing with the Foreign-Body Response to Implanted Biomaterials: Strategies and Applications of New Materials. *Advanced Functional Materials* **2020,** *31*.

(3) Welch, N. G.; Winkler, D. A.; Thissen, H. Antifibrotic strategies for medical devices. *Adv Drug Deliv Rev* **2020,** *167*, 109.

(4) Anderson, J. M.; Rodriguez, A.; Chang, D. T. Foreign body reaction to biomaterials. *Seminars in Immunology* **2008,** *20*, 86.

(5) Barrese, J. C.; Aceros, J.; Donoghue, J. P. Scanning electron microscopy of chronically implanted intracortical microelectrode arrays in non-human primates. *J Neural Eng* **2016,** *13*, 026003.

(6) Biran, R.; Martin, D. C.; Tresco, P. A. Neuronal cell loss accompanies the brain tissue response to chronically implanted silicon microelectrode arrays. *Experimental Neurology* **2005,** *195*, 115.

(7) Venkatraman, S.; Hendricks, J.; King, Z. A.; Sereno, A. J.; Richardson-Burns, S.; Martin, D.; Carmena, J. M. In vitro and in vivo evaluation of PEDOT microelectrodes for neural stimulation and recording. *IEEE Trans Neural Syst Rehabil Eng* **2011,** *19*, 307.

(8) Rahmati, M.; Silva, E. A.; Reseland, J. E.; C, A. H.; Haugen, H. J. Biological responses to physicochemical properties of biomaterial surface. *Chem Soc Rev* **2020,** *49*, 5178.

(9) Carnicer-Lombarte, A.; Chen, S.-T.; Malliaras, G. G.; Barone, D. G. Foreign Body Reaction to Implanted Biomaterials and Its Impact in Nerve Neuroprosthetics. *Frontiers in Bioengineering and Biotechnology* **2021,** *9*.

(10) Veiseh, O.; Doloff, J. C.; Ma, M.; Vegas, A. J.; Tam, H. H.; Bader, A. R.; Li, J.; Langan, E.; Wyckoff, J.; Loo, W. S.et al. Size- and shape-dependent foreign body immune response to materials implanted in rodents and non-human primates. *Nat Mater* **2015,** *14*, 643.

(11) Doloff, J. C.; Veiseh, O.; de Mezerville, R.; Sforza, M.; Perry, T. A.; Haupt, J.; Jamiel, M.; Chambers, C.; Nash, A.; Aghlara-Fotovat, S.et al. The surface topography of silicone breast implants mediates the foreign body response in mice, rabbits and humans. *Nat Biomed Eng* **2021,** *5*, 1115.

(12) Zhang, L.; Cao, Z.; Bai, T.; Carr, L.; Ella-Menye, J. R.; Irvin, C.; Ratner, B. D.; Jiang, S. Zwitterionic hydrogels implanted in mice resist the foreign-body reaction. *Nat Biotechnol* **2013,** *31*, 553.

(13) Liu, Q.; Chiu, A.; Wang, L. H.; An, D.; Zhong, M.; Smink, A. M.; de Haan, B. J.; de Vos, P.; Keane, K.; Vegge, A.et al. Zwitterionically modified alginates mitigate cellular overgrowth for cell encapsulation. *Nat Commun* **2019,** *10*, 5262.

(14) Li, Q.; Wen, C.; Yang, J.; Zhou, X.; Zhu, Y.; Zheng, J.; Cheng, G.; Bai, J.; Xu, T.; Ji, J.et al. Zwitterionic Biomaterials. *Chemical Reviews* **2022,** *122*, 17073.

(15) Vegas, A. J.; Veiseh, O.; Doloff, J. C.; Ma, M.; Tam, H. H.; Bratlie, K.; Li, J.; Bader, A. R.; Langan, E.; Olejnik, K.et al. Combinatorial hydrogel library enables identification of materials that mitigate the foreign body response in primates. *Nat Biotechnol* **2016,** *34*, 345.

(16) Bose, S.; Volpatti, L. R.; Thiono, D.; Yesilyurt, V.; McGladrigan, C.; Tang, Y.; Facklam, A.; Wang, A.; Jhunjhunwala, S.; Veiseh, O.et al. A retrievable implant for the long-term encapsulation and survival of therapeutic xenogeneic cells. *Nat Biomed Eng* **2020,** *4*, 814.

(17) Veiseh, O.; Vegas, A. J. Domesticating the foreign body response: Recent advances and applications. *Advanced Drug Delivery Reviews* **2019,** *144*, 148.

(18) Inal, S.; Rivnay, J.; Suiu, A. O.; Malliaras, G. G.; McCulloch, I. Conjugated Polymers in Bioelectronics. *Acc Chem Res* **2018,** *51*, 1368.

(19) Dimov, I. B.; Moser, M.; Malliaras, G. G.; McCulloch, I. Semiconducting Polymers for Neural Applications. *Chem Rev* **2022,** *122*, 4356.

(20) Xie, X.; Doloff, J. C.; Yesilyurt, V.; Sadraei, A.; McGarrigle, J. J.; Omami, M.; Veiseh, O.; Farah, S.; Isa, D.; Ghani, S.et al. Reduction of measurement noise in a continuous glucose monitor by coating the sensor with a zwitterionic polymer. *Nat Biomed Eng* **2018,** *2*, 894.

(21) Kutner, N.; Kunduru, K. R.; Rizik, L.; Farah, S. Recent Advances for Improving Functionality, Biocompatibility, and Longevity of Implantable Medical Devices and Deliverable Drug Delivery Systems. *Advanced Functional Materials* **2021,** *31*.

(22) Bridges, A. W.; García, A. J. Anti-Inflammatory Polymeric Coatings for Implantable Biomaterials and Devices. *Journal of Diabetes Science and Technology* **2008,** *2*, 984.

(23) Farah, S.; Doloff, J. C.; Muller, P.; Sadraei, A.; Han, H. J.; Olafson, K.; Vyas, K.; Tam, H. H.; Hollister-Lock, J.; Kowalski, P. S.et al. Long-term implant fibrosis prevention in rodents and non-human primates using crystallized drug formulations. *Nat Mater* **2019,** *18*, 892.

(24) Barone, D. G.; Carnicer-Lombarte, A.; Tourlomousis, P.; Hamilton, R. S.; Prater, M.; Rutz, A. L.; Dimov, I. B.; Malliaras, G. G.; Lacour, S. P.; Robertson, A. A. B.et al. Prevention

of the foreign body response to implantable medical devices by inflammasome inhibition. *Proceedings of the National Academy of Sciences* **2022,** *119*, e2115857119.

(25) Zhou, Y.; Liu, E.; Yang, Y.; Alfonso, F. S.; Ahmed, B.; Nakasone, K.; Forro, C.; Muller, H.; Cui, B. Dual-Color Optical Recording of Bioelectric Potentials by Polymer Electrochromism. *J Am Chem Soc* **2022,** *144*, 23505.

(26) Someya, T.; Bao, Z.; Malliaras, G. G. The rise of plastic bioelectronics. *Nature* **2016,** *540*, 379.

(27) Li, N.; Li, Y.; Cheng, Z.; Liu, Y.; Dai, Y.; Kang, S.; Li, S.; Shan, N.; Wai, S.; Ziaja, A.et al. Bioadhesive polymer semiconductors and transistors for intimate biointerfaces. *Science* **2023,** *381*, 686.

(28) Strakosas, X.; Biesmans, H.; Abrahamsson, T.; Hellman, K.; Ejneby, M. S.; Donahue, M. J.; Ekström, P.; Ek, F.; Savvakis, M.; Hjort, M.et al. Metabolite-induced in vivo fabrication of substrate-free organic bioelectronics. *Science* **2023,** *379*, 795.

(29) Zheng, Y.; Zhang, S.; Tok, J. B.; Bao, Z. Molecular Design of Stretchable Polymer Semiconductors: Current Progress and Future Directions. *J Am Chem Soc* **2022,** *144*, 4699.

(30) Dai, Y.; Dai, S.; Li, N.; Li, Y.; Moser, M.; Strzalka, J.; Prominski, A.; Liu, Y.; Zhang, Q.; Li, S.et al. Stretchable Redox-Active Semiconducting Polymers for High-Performance Organic Electrochemical Transistors. *Advanced Materials* **2022,** *34*, 2201178.

(31) Du, W.; Ohayon, D.; Combe, C.; Mottier, L.; Maria, I. P.; Ashraf, R. S.; Fiumelli, H.; Inal, S.; McCulloch, I. Improving the Compatibility of Diketopyrrolopyrrole Semiconducting Polymers for Biological Interfacing by Lysine Attachment. *Chemistry of Materials* **2018,** *30*, 6164.

(32) Lei, T.; Guan, M.; Liu, J.; Lin, H.-C.; Pfattner, R.; Shaw, L.; McGuire, A. F.; Huang, T.-C.; Shao, L.; Cheng, K.-T.et al. Biocompatible and totally disintegrable semiconducting polymer for ultrathin and ultralightweight transient electronics. *Proceedings of the National Academy of Sciences* **2017,** *114*, 5107.

(33) Krauss, G.; Meichsner, F.; Hochgesang, A.; Mohanraj, J.; Salehi, S.; Schmode, P.; Thelakkat, M. Polydiketopyrrolopyrroles Carrying Ethylene Glycol Substituents as Efficient Mixed Ion-Electron Conductors for Biocompatible Organic Electrochemical Transistors. *Advanced Functional Materials* **2021,** *31*.

(34) Jiang, Z.; Li, X.; Strzalka, J.; Sprung, M.; Sun, T.; Sandy, A. R.; Narayanan, S.; Lee, D. R.; Wang, J. The dedicated high-resolution grazing-incidence X-ray scattering beamline 8-ID-E at the Advanced Photon Source. *J Synchrotron Radiat* **2012,** *19*, 627.

(35) Jiang, Z. GIXSGUI: a MATLAB toolbox for grazing-incidence X-ray scattering data visualization and reduction, and indexing of buried three-dimensional periodic nanostructured films. *Journal of Applied Crystallography* **2015,** *48*, 917.

(36) Bernards, D. A.; Malliaras, G. G. Steady-State and Transient Behavior of Organic Electrochemical Transistors. *Advanced Functional Materials* **2007,** *17*, 3538.

(37) Inal, S.; Malliaras, G. G.; Rivnay, J. Benchmarking organic mixed conductors for transistors. *Nat Commun* **2017,** *8*, 1767.

(38) Tavadyan, L. A.; Manukyan, Z. H.; Harutyunyan, L. H.; Musayelyan, M. V.; Sahakyan, A. D.; Tonikyan, H. G. Antioxidant Properties of Selenophene, Thiophene and Their Aminocarbonitrile Derivatives. *Antioxidants (Basel)* **2017,** *6*.

(39) Lu, X.; Mestres, G.; Singh, V. P.; Effati, P.; Poon, J. F.; Engman, L.; Ott, M. K. Selenium- and Tellurium-Based Antioxidants for Modulating Inflammation and Effects on Osteoblastic Activity. *Antioxidants (Basel)* **2017,** *6*.

(40) Hariharan, S.; Dharmaraj, S. Selenium and selenoproteins: it's role in regulation of inflammation. *Inflammopharmacology* **2020,** *28*, 667.

(41) Mal'tseva, V. N.; Goltyaev, M. V.; Turovsky, E. A.; Varlamova, E. G. Immunomodulatory and Anti-Inflammatory Properties of Selenium-Containing Agents: Their Role in the Regulation of Defense Mechanisms against COVID-19. *International Journal of Molecular Sciences* **2022,** *23*, 2360.

(42) Chen, D.; Liang, Z.; Su, Z.; Huang, J.; Pi, Y.; Ouyang, Y.; Luo, T.; Guo, L. Selenium-Doped Mesoporous Bioactive Glass Regulates Macrophage Metabolism and Polarization by Scavenging ROS and Promotes Bone Regeneration In Vivo. *ACS Applied Materials & Interfaces* **2023,** *15*, 34378.

(43) Filipović, N.; Ušjak, D.; Milenković, M. T.; Zheng, K.; Liverani, L.; Boccaccini, A. R.; Stevanović, M. M. Comparative Study of the Antimicrobial Activity of Selenium Nanoparticles With Different Surface Chemistry and Structure. *Frontiers in Bioengineering and Biotechnology* **2021,** *8*.

(44) Kang, I.; Yun, H. J.; Chung, D. S.; Kwon, S. K.; Kim, Y. H. Record high hole mobility in polymer semiconductors via side-chain engineering. *J Am Chem Soc* **2013,** *135*, 14896.

(45) Marsh, A. V.; Heeney, M. Conjugated polymers based on selenophene building blocks. *Polymer Journal* **2022,** *55*, 375.

(46) Li, N.; Dai, Y.; Li, Y.; Dai, S.; Strzalka, J.; Su, Q.; De Oliveira, N.; Zhang, Q.; St. Onge, P. B. J.; Rondeau-Gagné, S.et al. A universal and facile approach for building multifunctional conjugated polymers for human-integrated electronics. *Matter* **2021,** *4*, 3015.

(47) Hu, T. Y.; Zhang, H.; Chen, Y. Y.; Jiao, W. H.; Fan, J. T.; Liu, Z. Q.; Lin, H. W.; Cheng, B. H. Dysiarenone from Marine Sponge Dysidea arenaria Attenuates ROS and Inflammation via Inhibition of 5-LOX/NF-kappaB/MAPKs and Upregulation of Nrf-2/OH-1 in RAW 264.7 Macrophages. *J Inflamm Res* **2021,** *14*, 587.

(48) Rusetskaya, N. Y.; Fedotov, I. V.; Koftina, V. A.; Borodulin, V. B. Selenium Compounds in Redox Regulation of Inflammation and Apoptosis. *Biochemistry (Moscow), Supplement Series B: Biomedical Chemistry* **2019,** *13*, 277.

(49) Mittal, M.; Siddiqui, M. R.; Tran, K.; Reddy, S. P.; Malik, A. B. Reactive oxygen species in inflammation and tissue injury. *Antioxid Redox Signal* **2014,** *20*, 1126.

(50) Forrester, S. J.; Kikuchi, D. S.; Hernandes, M. S.; Xu, Q.; Griendling, K. K. Reactive Oxygen Species in Metabolic and Inflammatory Signaling. *Circ Res* **2018,** *122*, 877.

(51) Akilbekova, D.; Bratlie, K. M. Quantitative Characterization of Collagen in the Fibrotic Capsule Surrounding Implanted Polymeric Microparticles through Second Harmonic Generation Imaging. *PLoS One* **2015,** *10*, e0130386.

(52) Mariani, E.; Lisignoli, G.; Borzi, R. M.; Pulsatelli, L. Biomaterials: Foreign Bodies or Tuners for the Immune Response? *Int J Mol Sci* **2019,** *20*.

Chapter 5. Conclusions and future perspective

5.1 Conclusions

Polymer semiconductors are promising materials for interfacing with biological tissues due to their soft mechanical property, solution processability, and chemical versatility. In the dissertation, functional designs of polymer semiconductors are discussed and demonstrated to achieve multifunctional and biocompatible bioelectronic-tissue interfaces.

To design multifunctional conjugated polymers from a universal polymer structure, the CLIP functionalization strategy was proposed (Li et al., *Matter*, 4, 1, 2021). The facile click reaction based on the azide group on the side chain of a conjugated polymer allows the compatible grafting with various sensitive yet important alkyne-attached functional groups. The electrical performance evaluation proves the effectiveness of the strategy in preserving the charge transport. For achieving a stable and intimate bioelectronic-tissue interface, the design of bioadhesive polymer semiconductors (BASC) was proposed (Li et al., *Science*, 381, 686, 2023). Through the interpenetrated double network formed from a brush bioadhesive polymer and a redox-active semiconducting polymer, the BASC achieved significantly enhanced adhesion on wet biotissues while maintaining high charge transport property. Moreover, the BASC film exhibits abrasion resistance, high stretchability, and good biocompatibility, which are highly desired for interfacing with tissues. For the long-term use of semiconducting polymers, the immune compatibility is of high significance for resisting the formation of foreign-body fibrous capsule around the implant. We proposed the immune-compatible designs of semiconducting polymers for bioelectronics. Both selenophene substitution on the backbone and immunomodulatory side chains led to the decrease of collagen deposition and immune population recruitment on the implant surface. The discovery of the ROS-scavenging property of selenophene in suppressing FBR is encouraging for using conjugated immunomodulatory moieties for boosting both the electrical performance and the immune compatibility.

5.2 Future perspective

Despite the promising development of polymer semiconductors for bioelectronic-tissue interfaces, there are still challenges regarding both the fundamental understanding of the structure-property relationship and material-bio interactions and their long-term application in implantable bioelectronics. Although 100% functionalization on the side chain of the semiconducting polymer has been demonstrated, the inevitable sacrifice of the electrical performance indicates that there is still room to improve. To further build functional polymer semiconductors that require the incorporation of large-sized molecules, the challenges will be escalated. The investigation of polymer synthesis, processing, microstructure, and device fabrication as a closely related loop might give valuable insights. In addition, more understandings of the functional material designs and their interactions with biological systems are highly necessary for ensuring the biosafety and broadening the bioelectronic functions.

Polymer semiconductors are known for their susceptibility to degradation by oxygen, water, and light. Biological systems include diverse tissue conditions and biofluids containing enzymes, ions, reactive oxygen species, etc. The oxidative environment poses significant challenges for the semiconducting polymers' stability and function. How to design electronically stable polymer semiconductors that can function over extended periods is an important question and will greatly expedite the integration of organic bioelectronics with biological systems.

Further work also needs to translate the functional polymer semiconductors into practical applications to address tangible biomedical problems. This requires multidisciplinary skills including materials, chemistry, electrical engineering, and biomedical engineering. I am confident that polymer semiconductors-based organic bioelectronics hold the great promise for interfacing with soft biological tissues.